Graphene based coatings for corrosion protection

Yu, Feng

Publication date:
2018

Document Version
Publisher's PDF, also known as Version of record

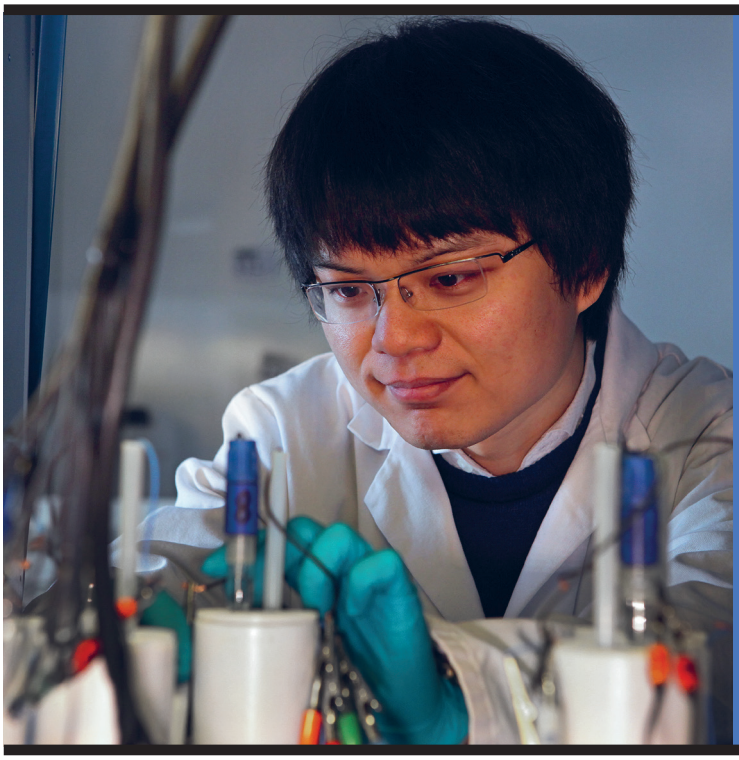

Graphene based coatings for corrosion protection

Feng Yu
PhD Thesis January 2018

DTU Nanotech
Department of Micro- and Nanotechnology

DTU Nanotech
Department of Micro- and Nanotechnology

Ph.D. thesis

Graphene based coatings for corrosion protection

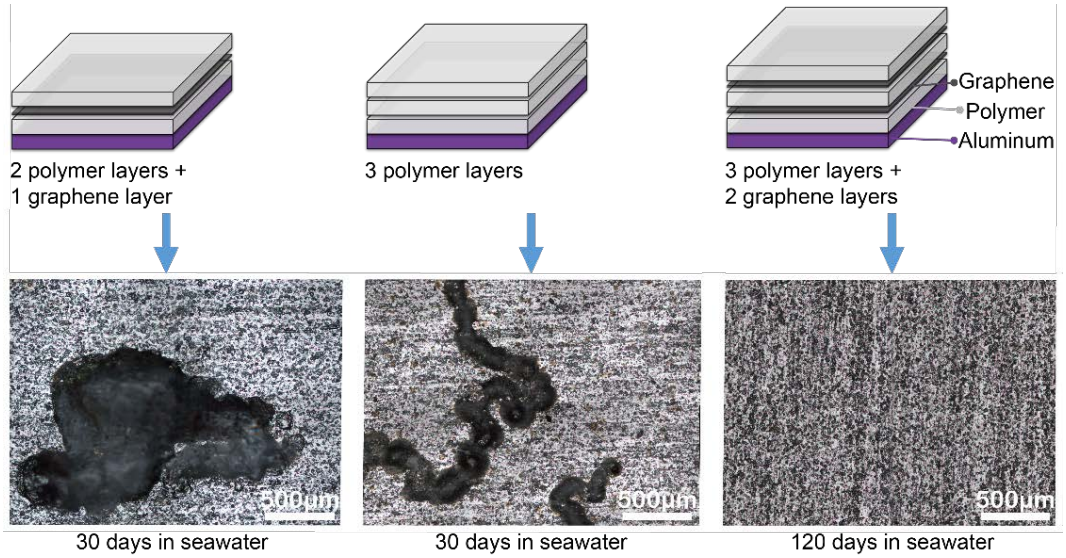

Candidate: Feng Yu

Supervisor: Prof. Peter Bøggild
Co-supervisor: Dr. Luca Camilli

Department of Micro- and Nanotechnology
Technical University of Denmark

January 2018

Front-page image: (Top) Schematic illustration of the coating structure on aluminum substrate and (bottom) optical images showing corrosion morphology after immersion in simulated seawater for hybrid polymer-graphene coatings with (left) one graphene and two polymer layers and (right) two graphene and three polymer layers and (mid) bare three-layer polymer coating.

Abstract

Owing to its impermeable nature, graphene is an excellent candidate as a barrier material for application in anticorrosive coatings. Although, graphene is reported to be able to reduce the corrosion rate of metals, enhanced corrosion due to the galvanic coupling between the conductive graphene layer and metal substrate is also well-established. Corrosion can initiate from graphene defects, which emphasizes the importance of the graphene layer to be of high quality. The weak adhesion of graphene on metals influences its practical use in anticorrosive coatings, especially at long-term exposure to corrosive environments. Furthermore, large-scale high-quality chemical vapor deposited (CVD) graphene can only be grown effectively on a few metal substrates and is difficult to apply onto rough surfaces, both of which significantly limit the universal use of graphene on substrates in practical use. Furthermore, industrially relevant alloys such as steel cannot withstand the high temperature (~1000°C) required for traditional CVD graphene growth process, without compromising the structural and mechanical integrity.

To address these common challenges of most graphene based anticorrosive coatings, both multilayer graphene (MLG) coatings and a polymer-graphene hybrid coating are reported in this thesis. Our results show that MLG coatings provide effective long-term protection for stainless steel in boiling seawater because of prolonged diffusion pathway for corrosion species. However, the MLG coating grown on Ni substrate fails in acidic media, due to hydrogen bubbles formation at the coating-substrate interface, which eventually lead to delamination of the coating. The hybrid coating, on the other hand, is prepared through a layer-by-layer transfer process with alternating polymer and graphene layers. Results show that graphene enhanced coatings consistently exhibit far better corrosion protection performance than both reference polymer coatings with same thickness, and bare graphene layers directly on metal. The number of graphene layers in the hybrid coating plays an important role in the overall performance. The hybrid coating with only one graphene layer cannot effectively protect aluminum alloys after 30 days of immersion in simulated seawater, while the hybrid coating with two graphene layers completely inhibits corrosion even at 120 days of immersion. The polymer graphene hybrid coating is also effective for corrosion protection on brass and steel substrates and it is anticipated to provide high performance anticorrosive coatings for various metals and alloys.

Resume

På grund af sin uigennemtrængelighed er grafen en fremragende kandidat som barrierematerialе til anvendelse i korrosionsbelægninger. Skønt grafen er kendt for at kunne reducere korrosionshastigheden for metaller, kan tilstedeværelsen af grafen uheldigvis også accelerere korrosion på grund af den galvaniske kobling mellem det ledende grafenlag og metalsubstratet. Der kan være fejl i grafenlaget, hvor korrosive væsker trænger igennem til metaloverfladen. Den svage vedhæftning af grafen på metaller har også uhensigtsmæssige konsekvenser for grafens praktiske anvendelse i korrosionsbelægninger. Grafen af høj kvalitet kan dyrkes på metal overflader ved chemical vapor deposition (CVD), men antallet af velegnede katalytiske materialer begrænser sig i praksis til nikkel og kobber, mens for eksempel rustfrist stål er langt vanskeligere at have med at gøre. Ru metaloverflader som man finder i realistiske metalemner, er også en udfordring for at dannelsen af ubrudte lag af grafen. Endeligt kan mange industrielle relevante legeringer som for eksempel stål og inconel ikke tåle den høje temperatur (~ 1000 °C), der normalt kræves til CVD-dyrkning af grafen, uden at miste de mekaniske egenskaber.

I dette projekt arbejdes med flere strategier til at imødegå disse udfordringer. Barrierelag bestående af mange lag grafen kan dyrkes på nikkel, der er plateret på stål for at forbedre både de mekaniske egenskaber og korrosionsbeskyttelsen. MLG-belægninger viser sig at kunne beskytte metaloverflader yderst effektivt selv ved ugevis påvirkning fra kogende havvand. . Derimod viser MLG-belægningen sig uegnet til sure medier; her vil selv den mindste defekt i laget føre til gennemtrængning af væske til overfladen, der så igen omdannes til hydrogen-bobler mellem metaloverfladen og grafen-lagene. Dette fører hurtigt til huller i grafenlaget og endeligt delaminering af belægningen. En ny type hybrid coating bestående af skiftevis polymerlag og grafen er også undersøgt til beskyttelse af aircraft aluminium, som er bruges til mange industrielle anvendelser. Idet polymerlaget både isolerer grafenlaget elektrisk fra overfladen, og øger vedhæftningen, resulterer det i en markant forbedret performance, der til forskel for størstedelen af den videnskabelige literatur på området, holdes uændret i op til 4 måneder. Her spiller antallet af grafenlag en central rolle; med et enkelt grafenlag holder coatingen mindre en 30 dage, hvor blot to lag er nok til at give næsten fuldstændig elimination af korrosion selv efter 120 dages nedsænkning i saltvand. Hybridbelægningen er også effektiv til beskyttelse af messing- og stål.

Preface

This thesis is submitted to the Technical University of Denmark (DTU) for obtaining the PhD degree. The work included in the thesis was mainly carried out in NanoCarbon Group, DTU Nanotech and under supervision of Professor Peter Bøggild and Dr. Luca Camilli. The research was financially supported by The Strategic Danish Research Collaboration (DSF) with the DA-GATE project (12-131827), the High Technology Foundation (HTF) with the NIAGRA project (058-2012-4) and additional support from the Danish National Research Foundation, Center for Nanostructured Graphene and the EU Graphene Flagship.

Feng Yu

DTU Nanotech, 14th January 2018

Acknowledgments

I would like to express my sincerest appreciation to my main supervisor Professor Peter Bøggild and co-supervisor Dr. Luca Camilli for their great help during the past three years. Collaboration with them was really an enjoyable experience for me and their advices always provide me with strong support.

I would like to thank both present and former NanoCarbon group members for their help during the whole project of my PhD. Thanks Dr. Adam C. Stoot for his close collaboration, especially for his help on graphene growth process and discussions on experiments and results. Thanks Dr. Patrick R. Whelan for his help with the graphene transfer process and Dr. Birong Luo for his help on the copper electropolishing process. Thanks Dr. David Mackenzie for his help on collecting and processing of Raman spectra. Thanks Associate Professor Tim J. Booth, Dr. Lene Gammelgaard, Dr. Bjarke S. Jessen, Joakim D. Thomsen and Abhay Shivayogimath for all their helpful support in the laboratory. I would like to thank my mater students Vincent Trole and Ting Wang for their collaboration with me on exploring the use of graphene for anticorrosive coatings. Thanks all the administration support at DTU Nanotech and all kinds of support from both DTU CEN and Danchip.

I also would like to thank my previous colleagues in the University of Manchester of both Professor Robert Akid and Dr. Michele Curioni for their great support on corrosion knowledge in my studies.

Finally, I would sincerely appreciate the support at all aspects from my parents, brother, girlfriend and close friends for their continuous accompany and encouragements during my PhD studies.

Contents

Chapter 1. Introduction

1.1. Background and motivation

Corrosion is a natural phenomenon which leads to deterioration of materials and economic loss of approximately 3~4% Gross Domestic Product in many countries. To protect materials from corrosion, barrier coatings are widely used to physically isolate the substrate from environment.[1] Graphene, being an atomically thin impermeable material to all molecules and gases,[2] is therefore an outstanding candidate for application in barrier coatings to prevent corrosion. Compared to the widely used traditional anticorrosive coatings such as polymer coatings, graphene exhibits superior impermeability. On the other hand, graphene is environmental-friendly, and therefore offers green, alternative solutions to the hazardous coatings, such as chromium-based coatings.

Chemical vapor deposition (CVD) is a successful technique to synthesize large-scale high-quality continuous graphene thin film, especially on Cu[3] and Ni[4] substrates. Although graphene has been reported to be effective in corrosion inhibition for Cu and Ni,[5-7] it is however reported that corrosion of Cu is actually enhanced at long-term due to galvanic coupling between the substrate and graphene coating.[8,9] Moreover, direct corrosion attack to metal substrates can take place through graphene defects (Figure 1.1a),[5,10-12] which significantly limit the corrosion protection performance of graphene coatings. The weak adhesion of graphene on metal substrates also influences its practical use, especially under friction and wear working conditions. Because of these difficulties, effective long-term corrosion protection by graphene coatings has not yet been reported to the author's best knowledge. Moreover, direct growth of high-quality graphene on various industrial relevant metals and alloys (e.g. Fe, Al and Mg) is also quite challenging due to their poor catalytic activity, which greatly limits the universal use of graphene as anticorrosive coatings. Moreover, standard CVD graphene growth process requires high temperature (~1000°C), which many metals and alloys cannot withstand, leading to degradation of their functional properties. Usually, rough metallic surfaces are difficult to be coated with atomically thin graphene films. Although graphene can be transferred to these substrates, due to weak adhesion and galvanic corrosion issues, it is difficult to preserve graphene coatings on these metallic substrates and effectively protect them from corrosion at long-term.

Besides the use of bare graphene coatings for corrosion protection, it is also widely reported that polymer-graphene composite coatings are effective for corrosion protection.[13-17] In these composite coatings, graphene nanoplatelets are dispersed in the coating matrix to provide tortuous diffusion path for corrosion species and enhance the barrier properties, as shown in Figure 1.1b. However, it is difficult to well disperse the graphene nanoplatelets in the coating matrix due to agglomeration. Even though the graphene nanoplatelets were well dispersed, the orientation of the flakes is still challenging to be well controlled. It is important to note that both the dispersion and orientation of graphene nanoplatelets in the coating matrix are highly relevant to the barrier properties of the coating.[18,19] Moreover, the graphene nanoplatelets dispersed in the coating matrix can lead to pinholes in the coating and loss of adhesion.[13]

Motivated by its superior impermeable nature, graphene is used as a coating to protect metals from corrosion in this study. However, the focus of this work is to address the above-mentioned challenges of graphene anticorrosive coating using both multilayer graphene (MLG) coatings (Figure 1.1c) and polymer-graphene hybrid coatings (Figure 1.1d). The hypothesis is that the diffusion pathway of corrosion species through MLG is greatly enhanced than that in single layer graphene (SLG).[20] For the polymer-graphene hybrid coatings, large-scale high-quality CVD graphene sheets are used rather than graphene nanoplatelets in the composites coatings, since the graphene barrier layer in the hybrid coating is better controlled with CVD graphene, which may provide better and more controllable barrier properties. Moreover, compared with bare CVD graphene coating directly coated on metal substrates, the polymer primer in the hybrid coating can electrically insulate the graphene from substrates to avoid galvanic corrosion and may provide adequate adhesion for the hybrid coating to be persevered on the substrate at long-term. With the graphene transfer technique, the polymer-graphene hybrid coating can also be applied on the surface of various metals and alloys without high temperature treatment involved in traditional CVD graphene growth process, which may deteriorate the mechanical properties of metal substrates. The soft polymer layer can also help graphene to coat rough surfaces.

1.2. Aims and objectives

The aim of this project is to develop advanced graphene anticorrosive coatings, which can be applied on various metals and alloys and provide long-term effective corrosion protection. The main objective is to protect commercially available stainless steel and aluminum alloys from corrosion at long-term with either a multilayer CVD graphene coating or a polymer-graphene hybrid coating.

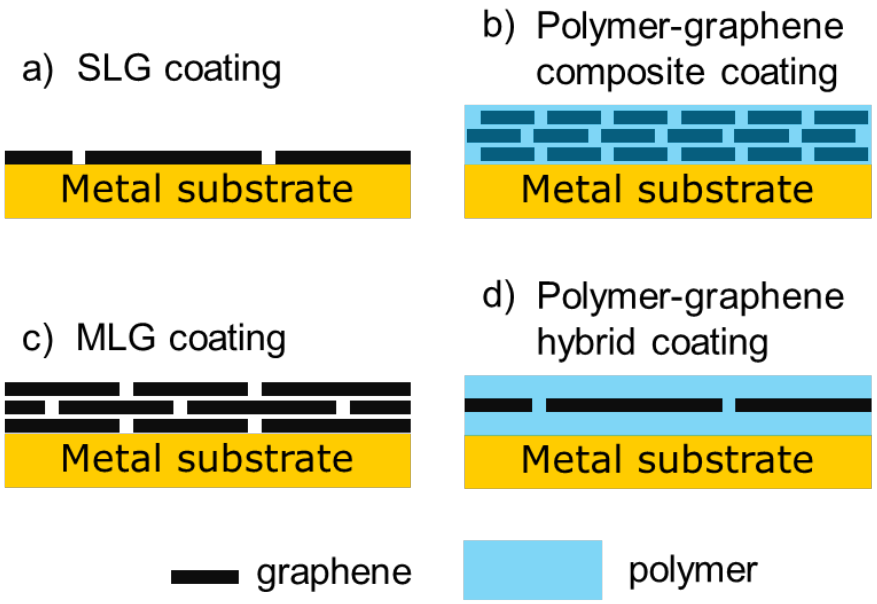

Figure 1.1 Schematic illustration of (a) single layer graphene (SLG), (b) polymer-graphene composite, (c) multilayer graphene (MLG) and (d) polymer-graphene hybrid coatings covered on metal substrates

1.3. Research approach

The thesis is divided into two parts to cover the aims and objectives. In the first part, a MLG coating is CVD grown on a Ni electroplated seed layer and used for corrosion protection of 304 stainless steel in simulated seawater (i.e. 3.5 wt% NaCl solution). Moreover, corrosion protection for a Ni foil by high-quality MLG coating in acidic media (e.g. 0.5 M HCl solution) is also investigated. The work in this part is mainly to address the challenges for CVD graphene anticorrosive coatings in (i) direct corrosion attack from

graphene defects; (ii) applying CVD graphene coatings on industrial relevant alloys that are poor catalysts for direct graphene growth (e.g. steel).

In the second part, a single layer graphene (SLG) is CVD grown on Cu and used together with polyvinyl butyral (PVB) to prepare polymer-graphene hybrid coatings for corrosion protection of aluminum alloy 2024 (AA2024) and other alloys (e.g. brass and steel) at long-term immersion in simulated seawater. The work in this part is mainly to address the following issues of CVD graphene anticorrosive coatings: (i) direct corrosion attack from graphene defects; (ii) galvanic coupling between metals and graphene; (iii) weak adhesion of graphene coatings on metal substrates; (iv) applying graphene coatings on industrial relevant alloys that are poor catalyst for direct graphene growth (e.g. aluminum alloy); (v) applying graphene coatings on rough surfaces; (vi) applying graphene coatings on metal surfaces at low temperature.

Raman spectroscopy, optical microscopy, secondary electron microscopy (SEM) and transmission electron microscopy (TEM) are used to study the properties of graphene and polymer layers, such as quality (in terms of density of defects) and thickness. Electrochemical impedance spectroscopy (EIS) and potentiodynamic polarization curves (PPC) are applied to evaluate the corrosion performance of various samples, mainly based on values of corrosion impedance and corrosion rate. Moreover, both optical microscopy and secondary electron microscopy are used to characterize the morphology of samples before and after corrosion tests.

1.4. Scope of the thesis

There are 9 chapters included in this thesis. Chapter 1 includes brief introduction to the background, motivation, aims, objectives and research approach of this project and outline of the thesis. Chapter 2 provides a mini review of literature on the corrosion process and methods used for corrosion protection. The properties of graphene are reviewed in Chapter 3 mainly focused on its electronic, thermal, optical and mechanical properties along with its superior impermeability. Main methods to obtain graphene are reviewed in Chapter 4 with a focused discussion on chemical vapor deposited (CVD) graphene and its transfer technique. Chapter 5 mainly discusses the use of CVD graphene coating for corrosion protection. Chapter 6 introduces the main experimental techniques used in the thesis, including CVD synthesis of graphene and transfer, materials characterization

techniques of Raman spectroscopy, scanning electron microscopy (SEM), transmission electron microscopy (TEM), and electrochemical corrosion testing methods of electrochemical impedance spectroscopy (EIS) and potentiodynamic polarization curves (PPC). In Chapter 7, results of using multilayer graphene coatings for corrosion protection in both simulated seawater and acidic media are presented after a short introduction on the background of the project and preparation of the coatings. The results on the polymer-graphene hybrid coatings are presented in Chapter 8, including fabrication of the coating, electrochemical corrosion performance, corrosion morphology and corrosion protection mechanisms. Chapter 8 summarized the thesis and discuss the future work that may extend the research beyond the contents included in this thesis.

There are six appendices included in this thesis. Appx. A includes a publication titled "Multilayer graphene for long-term corrosion protection of stainless steel bipolar plates for polymer electrolyte membrane fuel cell", which is related to the results of MLG coatings for long-term corrosion protection in simulated seawater. Appx. B contains a publication titled "Failure of multi-layer graphene coatings in acidic media", which is related to the results on the use of MLG coating for corrosion protection in acidic media. Appx. C is a submitted manuscript titled " Complete long-term corrosion protection with chemical vapor deposited graphene", which is related to the work on polymer-graphene hybrid anticorrosive coatings. Appx. D includes a EU patent application titled "A coated metal product and a method to produce a coated metal product", which is also related to the polymer-graphene hybrid anticorrosive coatings. Appx. E contains a prepared manuscript titled “CVD graphene/Ni Interface Evolution in Sulfuric Electrolyte”, which is a work exploring the failure mechanism of multilayer CVD graphene on Ni in acidic media. Appx. F includes a prepared manuscript titled “Low-temperature synthesis of a graphene-based, corrosion-inhibiting coating on an industrial grade alloy”, which is a study about applying graphene coatings directly on industrial alloys at low temperature for corrosion protection.

Chapter 2. Corrosion and corrosion protection

2.1. Impact of corrosion on society

Corrosion is generally described as chemical or electrochemical reactions of metals or alloys with the environment, reactions which undesirably deteriorate the properties of the materials in a way that may lead to failure to perform their function.[21] Degradation and failure of metals due to corrosion not only lead to direct economic loss (e.g. loss of metals and leakage of oil or gas) but also indirect catastrophic disasters (e.g. breakdown of bridges and leakage of nuclear power plants), as shown in Figure 2.1. According to reported studies,[22-24] cost of corrosion can be up to 5% of Gross Domestic Product (GDP) in USA, UK, and China.

Figure 2.1 Examples of failures induced by corrosion of (a) corroded pipeline[25] and (b) collapsed bridge.[26]

2.2. Principles of corrosion

There are generally two types of corrosion, including “dry” corrosion and ”wet” corrosion.[21] “Dry” corrosion is normally used for metal-gas or metal-vapor reactions, where oxidation of metals and reduction of non-metals take place at the same area. This form of corrosion is more commonly termed as “oxidation” of metals as direct chemical reactions between metals and environment are normally involved. On the other hand, in the case of “wet” corrosion, oxidation (or dissolution) of metals (anodic reaction) and reduction of non-metals (cathodic reaction) can occur at different places with corresponding electron transfer processes to complete electrochemical reactions. In this thesis, the term “corrosion” refers to “wet” corrosion unless otherwise specified.

As corrosion is essentially a chemical reaction process, its thermodynamics follows the Second Law of Thermodynamics,[27] which can be expressed as in Equation 1.1.

$$\Delta G = \Delta H - T\Delta S \quad (1.1)$$

- ΔG is the change of Gibbs free energy at constant pressure (P) and temperature (T) ($J \cdot mol^{-1}$)
- ΔH is the change of enthalpy (i.e. the heat change) ($J \cdot mol^{-1}$)
- ΔS is the change of entropy ($J \cdot mol^{-1} \cdot K^{-1}$)
- T is the absolute temperature (K)

For a corrosion process, ΔG must be negative to allow the reactions to spontaneously take place. Besides, as corrosion includes electron transfer processes, Faraday's Law can be applied to express Gibbs free energy, as shown in Equation 1.2.

$$\Delta G = -nEF \quad (1.2)$$

- n is the number of electrons transferred in a reaction
- E is the reversible electrode potential at constant P and T (V)
- F is the Faraday's constant ($96{,}485\ C \cdot mol^{-1}$)

Therefore, the overall potential ($E_{cathode} - E_{anode}$) for electrochemical reactions should be positive in a corrosion process. Values of potential in electrochemistry are normally referred to standard hydrogen electrode (SHE), which is defined with a potential value of 0 V and forms the basis for scaling of potential for other redox half reactions, which are partly listed in Table 2.1. When the reduction potential of a metal is more negative, it is more likely to serve as an anode to be oxidized and allow cathodic reaction to be coupled and initiate corrosion process. For example, an anode of Fe (-0.44 V) can be corroded in water with a corresponding cathodic oxygen reduction process (0.40 V).

As the potentials listed in Table 2.1 are potential values at standard conditions (e.g. 25 °C, 1 atm, 1 mol/L for aqueous species), these standard potential values need to be transformed to actual potential values using the Nernst equation, as expressed in Equation 1.3.

$$E = E° - \frac{RT}{nF} \ln \frac{\alpha_{Red}}{\alpha_{Ox}} \quad (1.3)$$

- E is the reduction potential of interest (V)

- $E°$ is the standard reduction potential (V)
- R is the universal gas constant (8.314 J·K^{-1}·mol^{-1})
- α_{Red} is the chemical activity of species in reduced state
- α_{Ox} is the chemical activity of species in oxidized state

Half-Reaction	$\mathscr{E}°$ (V)	Half-Reaction	$\mathscr{E}°$ (V)
$F_2 + 2e^- \rightarrow 2F^-$	2.87	$O_2 + 2H_2O + 4e^- \rightarrow 4OH^-$	0.40
$Ag^{2+} + e^- \rightarrow Ag^+$	1.99	$Cu^{2+} + 2e^- \rightarrow Cu$	0.34
$Co^{3-} + e^- \rightarrow Co^{2-}$	1.82	$Hg_2Cl_2 + 2e^- \rightarrow 2Hg + 2Cl^-$	0.27
$H_2O_2 + 2H^- + 2e^- \rightarrow 2H_2O$	1.78	$AgCl + e^- \rightarrow Ag + Cl^-$	0.22
$Ce^{4+} + e^- \rightarrow Ce^{3+}$	1.70	$SO_4^{2-} + 4H^+ + 2e^- \rightarrow H_2SO_3 + H_2O$	0.20
$PbO_2 + 4H^+ + SO_4^{2-} + 2e^- \rightarrow PbSO_4 + 2H_2O$	1.69	$Cu^{2+} + e^- \rightarrow Cu^+$	0.16
$MnO_4^- + 4H^+ + 3e^- \rightarrow MnO_2 + 2H_2O$	1.68	$2H^+ + 2e^- \rightarrow H_2$	0.00
$2e^- + 2H^+ + IO_4^- \rightarrow IO_3^- + H_2O$	1.60	$Fe^{3+} + 3e^- \rightarrow Fe$	−0.036
$MnO_4^- + 8H^+ + 5e^- \rightarrow Mn^{2+} + 4H_2O$	1.51	$Pb^{2+} + 2e^- \rightarrow Pb$	−0.13
$Au^{3+} + 3e^- \rightarrow Au$	1.50	$Sn^{2+} + 2e^- \rightarrow Sn$	−0.14
$PbO_2 + 4H^+ + 2e^- \rightarrow Pb^{2+} + 2H_2O$	1.46	$Ni^{2+} + 2e^- \rightarrow Ni$	−0.23
$Cl_2 + 2e^- \rightarrow 2Cl^-$	1.36	$PbSO_4 + 2e^- \rightarrow Pb + SO_4^{2-}$	−0.35
$Cr_2O_7^{2-} + 14H^+ + 6e^- \rightarrow 2Cr^{3+} + 7H_2O$	1.33	$Cd^{2+} + 2e^- \rightarrow Cd$	−0.40
$O_2 + 4H^+ + 4e^- \rightarrow 2H_2O$	1.23	$Fe^{2+} + 2e^- \rightarrow Fe$	−0.44
$MnO_2 + 4H^+ + 2e^- \rightarrow Mn^{2+} + 2H_2O$	1.21	$Cr^{3+} + e^- \rightarrow Cr^{2+}$	−0.50
$IO_3^- + 6H^+ + 5e^- \rightarrow \frac{1}{2}I_2 + 3H_2O$	1.20	$Cr^{3+} + 3e^- \rightarrow Cr$	−0.73
$Br_2 + 2e^- \rightarrow 2Br^-$	1.09	$Zn^{2+} + 2e^- \rightarrow Zn$	−0.76
$VO_2^+ + 2H^+ + e^- \rightarrow VO^{2+} + H_2O$	1.00	$2H_2O + 2e^- \rightarrow H_2 + 2OH^-$	−0.83
$AuCl_4^- + 3e^- \rightarrow Au + 4Cl^-$	0.99	$Mn^{2+} + 2e^- \rightarrow Mn$	−1.18
$NO_3^- + 4H^+ + 3e^- \rightarrow NO + 2H_2O$	0.96	$Al^{3+} + 3e^- \rightarrow Al$	−1.66
$ClO_2 + e^- \rightarrow ClO_2^-$	0.954	$H_2 + 2e^- \rightarrow 2H^-$	−2.23
$2Hg^{2+} + 2e^- \rightarrow Hg_2^{2+}$	0.91	$Mg^{2+} + 2e^- \rightarrow Mg$	−2.37
$Ag^+ + e^- \rightarrow Ag$	0.80	$La^{3+} + 3e^- \rightarrow La$	−2.37
$Hg_2^{2+} + 2e^- \rightarrow 2Hg$	0.80	$Na^+ + e^- \rightarrow Na$	−2.71
$Fe^{3+} + e^- \rightarrow Fe^{2+}$	0.77	$Ca^{2+} + 2e^- \rightarrow Ca$	−2.76
$O_2 + 2H^+ + 2e^- \rightarrow H_2O_2$	0.68	$Ba^{2+} + 2e^- \rightarrow Ba$	−2.90
$MnO_4^- + e^- \rightarrow MnO_4^{2-}$	0.56	$K^+ + e^- \rightarrow K$	−2.92
$I_2 + 2e^- \rightarrow 2I^-$	0.54	$Li^+ + e^- \rightarrow Li$	−3.05
$Cu^+ + e^- \rightarrow Cu$	0.52		

Table 2.1 Standard reduction potentials at 25 °C for common half-reactions.[21]

2.3. Types of corrosion

There are many types of corrosion and corrosion-induced effects, including uniform corrosion, localized corrosion, galvanic corrosion, intergranular corrosion, dealloying, stress corrosion cracking and so on.[21] However, in this thesis, the focus is to discuss the first three types of corrosion.

Uniform corrosion, also termed as “general corrosion”, is the most common type of corrosion, which takes place at the entire exposed surface of metals. Although uniform

corrosion attack contributes to most of metal destruction, it is often considered as a relatively safe type of corrosion because it is predictable, preventable and manageable.

Localized corrosion, on the other hand, attacks specific areas of metals and includes pitting (e.g. cavities on surfaces), crevice (e.g. gaps between two joining surfaces) and filiform (e.g. under painted surfaces) corrosion. Localized corrosion is more insidious than uniform corrosion, because it is generally faster, harder to prevent and causes more serious damage to metals.

Galvanic corrosion or “bimetallic corrosion”, is defined by NACE International[28] as ”corrosion associated with the current resulting from an electrical coupling of dissimilar electrodes in an electrolyte’’. Galvanic corrosion accelerates existing corrosion processes and can be mostly prevented by a proper corrosion design. Figure 2.2 presents the galvanic corrosion of iron coupling with tin, which is more noble than iron hence less susceptible to corrosion. When iron is oxidized, Fe^{2+} ions from the electrolyte react with oxygen in the water to form iron hydroxides or iron oxides and precipitate on the surface as rust. Electrons from iron are transferred from iron to tin, driven by the difference in individual corrosion potential between the two metals. The tin surface can act as a large cathode and greatly increases the rate of cathodic oxygen reduction reaction, which spontaneously accelerates the corrosion rate of iron.[21,29]

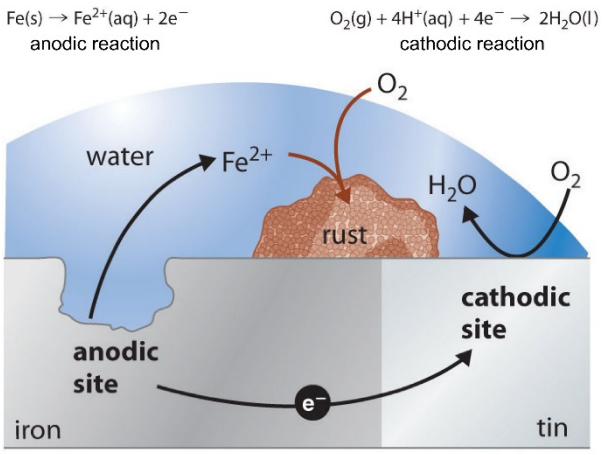

Figure 2.2 Schematic illustration of galvanic corrosion of iron coupled with tin.[29]

2.4. Corrosion protection

Metals and alloys are important structural materials for various industries, it is therefore of vital importance that these materials are protected from corrosion not only to increase the lifetime of industrial systems and decrease economic loss, but also to reduce its adverse impact on the environment and society (e.g. pollution or explosion). So far, many different types of corrosion protection strategies have been developed,[21] including surface pretreatment, anticorrosive coatings, cathodic protection, anodic protection, corrosion inhibitors and corrosion-resistant materials, just to name a few.[21,30,31]

According to a recent study on cost of corrosion[24], expenditures on coatings, corrosion resistant materials and surface treatments dominates the direct cost of corrosion in China, as presented in Figure 2.3, indicating that these strategies are currently of great importance in corrosion protection.

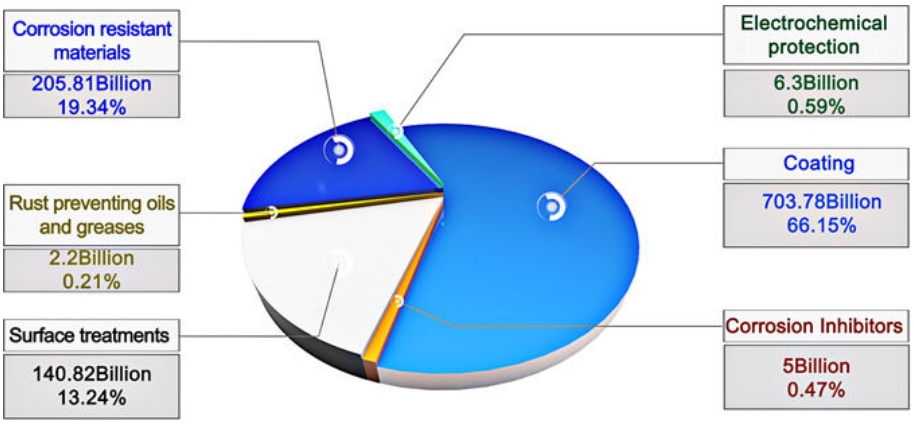

Figure 2.3 The direct costs of corrosion (RMB) in China in 2014 by protection strategies.[24]

Surface treatment is applied to change the state, chemical composition and/or microstructure of metal surfaces so as to make it more stable (e.g. plasma ablation, chemical etching).[21,32,33] On the other hand, Corrosion-resistant materials, such as stainless steels and titanium alloys, are used in various applications (e.g. deep-sea and aerospace equipment) to provide sufficient corrosion resistance in specific working conditions.[24,34]

Coatings, including metallic (e.g. noble Cr and sacrificial Zn coating), inorganic (e.g. zinc silicate and SiO_2 coating) and organic coatings (e.g. resins and latexes), are widely used to protect metals from corrosion via barrier, inhibition (i.e. surface passivation) or

galvanic (i.e. sacrificial protection) effects.[1,35] Anticorrosive coatings normally consist of multiple layers with different functions for each individual layer. Structure of typical anticorrosive coatings for marine and aerospace applications consists of three layers, including pretreatment, primer and topcoat, as shown in Figure 2.4.[33] Pretreatment is the layer in direct contact with the metal substrate and its important function is to provide essential mechanical or chemical adhesion of the coating to the substrate, thus avoiding direct exposure of the substrate to the environment, which can eventually promote failure of the coating. The pretreatment layer is also termed as “conversion layer” and is usually a thin inorganic layer with nanoscale thickness. The key function of the primer layer is to provide adequate corrosion protection and it is much thicker than pretreatment layer, up to few hundreds of microns. The topcoat layer is normally used to adapt the properties of surface, such as color and gloss, and improve the survivability of the coating system to altering environment conditions (e.g. UV radiation and impact from objects, friction and wear).[1]

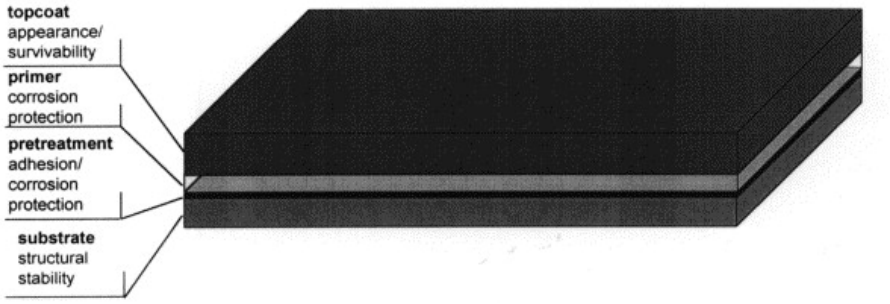

Figure 2.4 Schematic illustration of typical structure of anticorrosive coatings for aerospace applications.[33]

Chapter 3. Properties of graphene

3.1. Graphene: the forerunner of the 2D material family

Graphene is a one-atom-thick layer of sp^2-bonded carbon atoms densely packed in a honeycomb crystal lattice. It is the forerunner of the 2D materials that was isolated for the first time in 2004 by Prof. Andre Geim and Kostya Novoselov via mechanical cleavage of highly oriented pyrolytic graphite (HOPG).[36] The two scientists were both awarded the Nobel Prize in Physics in 2010 "for groundbreaking experiments regarding the two-dimensional material graphene." Graphene, from a topological point of view, can be regarded as the basic unit for carbon materials of all other dimensionalities,[37] such as 0D buckyballs, 1D nanotubes and 3D graphite, as illustrated in Figure 3.1. Moreover, the isolation of graphene led to an enormous interest towards other two-dimensional systems,[38,39] such as hexagonal boron nitride (hBN) and transition metal dichalcogenides (TMDs).

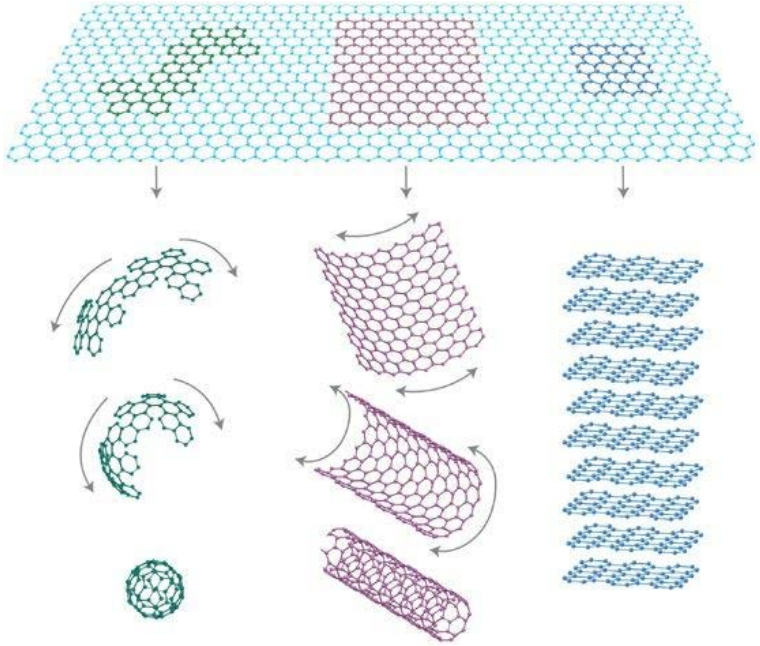

Figure 3.1 Schematic illustration on how other carbon allotropes can be formed by graphene.[37]

3.2. Electronic properties

Since its discovery, graphene has attracted enormous attention for its remarkable electronic, as well as mechanical, optical and chemical properties. In graphene, the

valence band and conduction band meet at the six discrete Dirac points of the Brillouin zone, resulting in zero band gap semiconductor, as illustrated in Figure 3.2. Due to the fact that charge carriers in graphene behave as massless relativistic particles (Dirac fermions),[40] graphene exhibits anomalous integer quantum Hall effect,[41] high electron mobility at room temperature (>200,000 cm^2/V)[42] as well as numerous other remarkable electronic characteristics.[43] Moreover, ballistic transport of charge carriers is available at micron-scale at room temperature.[44] The resistivity of graphene can be as low as 1×10^{-8} Ω·m, which is even lower than that of Ag (1.59×10^{-8} Ω·m), Cu (1.68×10^{-8} Ω·m), Au (2.44×10^{-8} Ω·m) and Al (2.82×10^{-8} Ω·m),[45] testifying graphene as a better conductor than these metals. Although the unique electronic properties of graphene make it promising in application of electronic devices, they are generally not beneficial when it comes to application in anticorrosive coatings. This is because galvanic corrosion is introduced when the noble and highly conductive graphene layer is in direct contact with the metal substrates, as it will be explained in more details later in Chapter 5.[8,9,46]

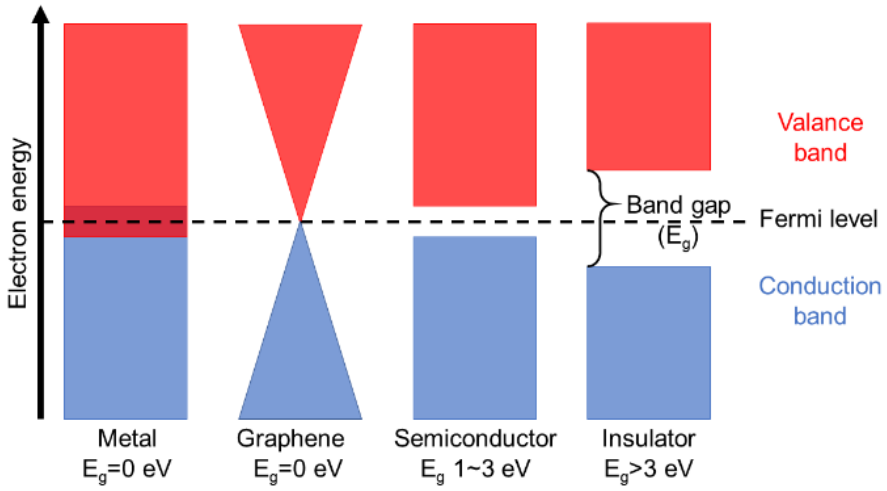

Figure 3.2 Band structures of metal, graphene, semiconductor and insulator.

3.3. Thermal properties

Initial measurement of thermal conductivity of graphene is conducted on a suspended single-layer graphene with a value of 5300 $W\cdot m^{-1}\cdot K^{-1}$.[47] The value of thermal conductivity of graphene is higher than those reported for carbon nanotubes (CNTs) (3000 $W\cdot m^{-1}\cdot K^{-1}$ for multi wall CNT[40] and 3500 $W\cdot m^{-1}\cdot K^{-1}$ for single wall CNT[48]). Later studies propose the initial results on graphene's ultrahigh thermal conductivity to be overestimated, however, a range between 1500–2500 $W\cdot m^{-1}\cdot K^{-1}$ was still obtained,[49,50] indicating that

graphene is an excellent thermal conductor. Graphene's superior thermal conductivity makes it an outstanding material for thermal management applications, such as condensation heat transfer system[51] and heat spreaders.[52]

3.4. Optical properties

Single layer graphene is reported to have an opacity of 2.3% and negligible reflectance (<0.1%) to incident white light,[53] as presented in Figure 3.3. The absorption of light increases linearly with the number of graphene layers, which is 2.3% for each additional graphene layer. Due to interference effects that strongly enhance the optical contrast, graphene supported on Si/SiO_2 substrate can be imaged with the contrast scaling linearly with the number of graphene layers.[54] Moreover, the combined optical and electrical properties of graphene pave the way for its application in photonics and optoelectronics,[55] such as transparent conductors,[56] infrared photodetectors,[57] light-emitting devices,[58] touch screens,[59] solar cells[60] and THz devices[61] etc.

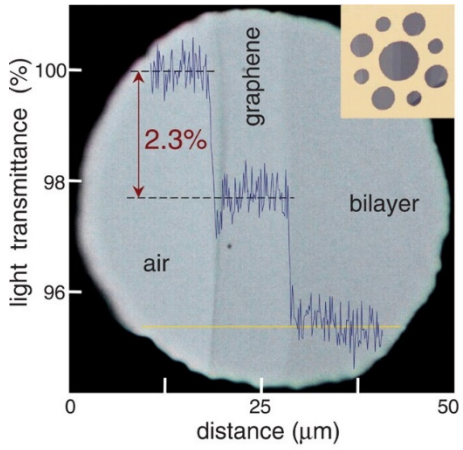

Figure 3.3 First measurement on graphene's opacity.[53]

3.5. Mechanical properties

Graphene is the strongest known material, up to 200 times stronger than steel of the same weight.[62] Measurements on the mechanical properties of monolayer graphene was initially carried out with an atomic force microscope (AFM),[63] as presented in Figure 3.4. Results showed an intrinsic tensile strength of 130 GPa, a Young's modulus of 1 TPa and

a failure strain up to 12%.[63] Moreover, compressive and tensile strain in graphene have been measured using Raman spectroscopy via monitoring the change of G and 2D peaks under stress, and their results showed that graphene can sustain tensile strains over 1.3%, whereas in compression the maximum load is 0.7%.[64] Moreover, defects in graphene have been proved to lower the mechanical strength of pristine graphene.[65]

Furthermore, the remarkable mechanical properties of graphene have been exploited to reinforce polymer matrix. For instance, it is reported that when graphene nanoplatelets are loaded with a fraction of 0.1% in a polymer matrix, the overall mechanical properties of the composite structure, in terms of Young's modulus and tensile strength, are greatly enhanced with respect to the starting polymer matrix.[66,67]

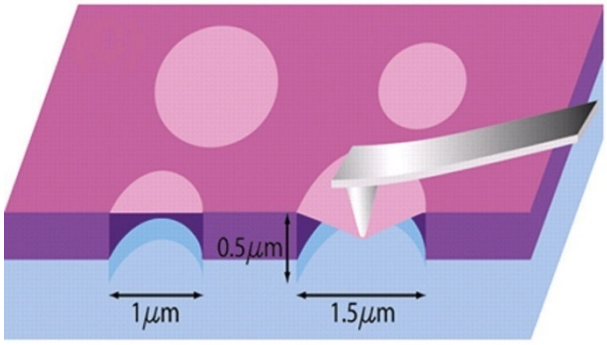

Figure 3.4 Schematic illustration on the nanoindentation experiment for initial measurement of graphene's mechanical properties.[63]

3.6. Impermeability

Graphene has been experimentally demonstrated to be impermeable to all gases including helium (Figure 3.5a).[2] Furthermore, a perfect single layer graphene is also impermeable to hydrogen atoms at ambient conditions, due to the high energy barrier for tunneling through graphene's dense electronic cloud.[68] However, it has been experimentally proved that defect-free pristine graphene is instead highly permeable to thermal protons at ambient conditions, as illustrated in Figure 3.5b.[69] For AB-stacked bilayer graphene, where carbon atoms are centered on the hexagonal rings of the next layer, protons are, however, not able to penetrate through.[69] Moreover, protons can also be transported through graphene in aqueous solution through atomic defects via the Grotthuss mechanism (Figure 3.5c).[70]

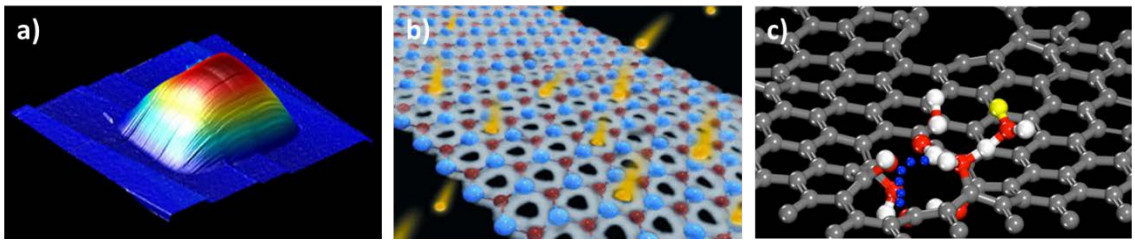

Figure 3.5 (a) A graphene balloon that is impermeable to helium.[2] (b) Schematic illustration on thermal protons passing through graphene.[71] (c) Density functional theory calculations showing aqueous protons transport through atomic defects in graphene.[70]

3.7. Other properties

Graphene has a large theoretical specific surface area of 2630 m^2/g from reported results[72] as well as high aspect ratio (i.e., the ratio of lateral size to thickness). The wettability and surface free energy of graphene is reported by Wang, S et al.[73] From their results, graphene is hydrophobic with a water contact angle of 127°, which is higher than that of graphite (98.3°). The surface energy of graphene in dry nitrogen, which implies the interaction strength between graphene and nitrogen, is reported to be about 115 mJ/m^2.[74] Moreover, experimentally measured results for the adhesion energy of chemical vapour deposited graphene on Cu and Ni are 12.8 and 72.7 $J \cdot m^{-2}$, respectively.[75]

Chapter 4. Methods to obtain graphene

4.1. Mechanical exfoliation

Since graphene is the basic building unit of graphite, it is therefore possible to obtain single layer graphene through exfoliation of graphite. In this case, it is necessary to overcome the van der Waals forces between the graphene layers in graphite. A representative method for this technique is the mechanical cleavage with scotch tape that was used by Prof.s Andre Geim and Kostya Novoselov when they firstly obtained graphene.[36] Although this method produces high-quality pristine graphene, the preparation process is time-consuming and the result is only micrometer-scale graphene flakes. Therefore, this method is only for research prototyping in the laboratory, but is not scalable and therefore not relevant for any practical applications.

4.2. Liquid-phase exfoliation

Liquid-phase high-yield exfoliation of defect-free graphene from graphite[76] is also proved to be very successful with the assist of sonication[77-79] and high-shear mixing,[80] as illustrated in Figure 4.1a. It is a far more practical method and enables graphene production on large-scale with a production rate exceeding 100 grams per hour.[81]

Another method to exfoliate graphene from graphite in liquid environment is to use an intercalant, which helps to increase the distance between adjacent graphene layers therefore decreasing the interaction between adjacent graphene layers, as presented in Figure 4.1b. Reported intercalants molecules used for this technique include $FeCl_3$,[82] $(NH_4)_2S_2O_8$,[83] and CrO_3[84] etc.

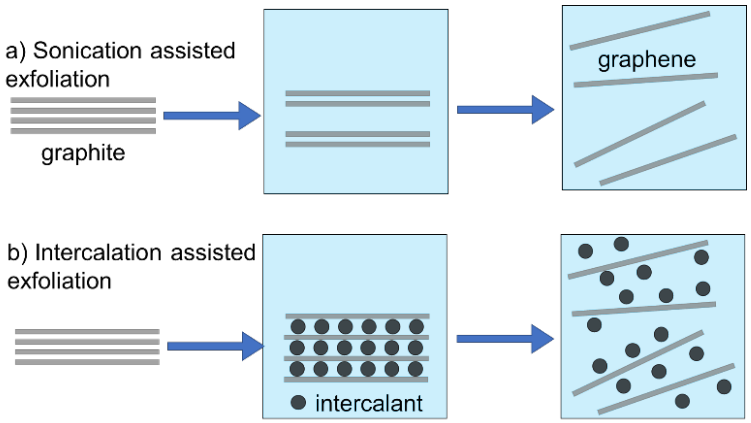

Figure 4.1 Schematic illustration of (a) sonication and (b) intercalation assisted exfoliation of graphene from graphite.

4.3. Chemical vapor deposition (CVD)

4.3.1. CVD synthesis of graphene

Chemical vapor deposition (CVD) process is normally used in semiconductor industry to produce high quality solid materials, such as silicon dioxide, silicon nitride and diamond etc. In a CVD process, gaseous precursors decompose at high temperature on the surface of a substrate to form new solid materials.[85] CVD synthesis of graphene was initially reported on Cu and Ni with methane and acetylene as gaseous precursors.[3,4,86,87] This technique has become the most popular and promising method of obtaining high-quality graphene at large-scale.[88] Later research revealed that the graphene formation mechanism is different on Cu and Ni substrates, as illustrated in Figure 4.2. mainly due to the difference in carbon solubility for these two metals,[89] which are still the two most commonly used metals for graphene growth. When Cu is used as catalyst substrate, the growth occurs via a surface absorption reaction. During the process hydrocarbon precursor can be catalytically decomposed into carbon atoms. Due to the ultra-low solubility of carbon in Cu, these carbon atoms are absorbed on the surface of Cu and form small grains that then coalesce into graphene, as illustrated in Figure 4.2a.[90] On the other hand, when Ni is used, graphene growth process occurs via a segregation and precipitation mechanism. Namely, carbon atoms dissolve into Ni bulk at high temperature and, during the cool down process, diffuse onto the surface and precipitate to form graphene, since the solubility of carbon atoms in Ni significantly decreases when temperature is lowered.[89,91] The difference of graphene formation between Cu and Ni is

schematically represented in Figure 4.2b and c.[91] Moreover, the number of graphene layers formed on the surface of both metals is generally different, mainly due to the difference in the mechanism of CVD process on both substrates. In the case of Cu, once the first layer of graphene is formed, further formation of graphene is suppressed (or, at least, dramatically slowed down), so that graphene synthesized on Cu is primarily of monolayer nature (this kind of growth is generally called self-limiting growth). On the other hand, when Ni is the growth substrate, as the carbon atoms segregate from the bulk where they had diffused and precipitate onto the surface, the graphene is generally of multilayer nature, especially when polycrystalline Ni is used.[89] It is found that the deposition parameters during the CVD process have little influence on the physical and electrical properties of as-grown graphene on Cu substrate.[92] However, the pre-treatment of the Cu foils has been demonstrated to play an important role in obtaining high-quality graphene layers,[3,59] mainly due to the fact that native oxides (CuO and Cu_2O) on the Cu surface can reduce the catalytic activity for graphene growth.[92] Sufficient growth time is also required to obtain continuous graphene layer because small graphene grains normally start to form at nucleation sites on Cu surface (such as step edges, defects and impurities[93]) and increase in size as the growth time increased before coalescing into a continuous layer.[92] The density of defects in as-grown graphene layer on Cu has been proved to be greatly influenced by the pressure of the chamber[94] and methane partial pressure[95] during the growth process, where low pressure of both are beneficial for obtaining high-quality graphene. On the other hand, the thickness and quality of graphene film synthesized on Ni substrate is strongly depend on the cooling rate, since graphene growth on Ni is via a carbon segregation and precipitation process.[86,89,93] The optimal cooling rate has been reported to be 10°C/s for high-quality few layer graphene growth on Ni.[86] Large size of single-crystalline Ni grain can also help improving the quality of graphene.[86] The thickness of graphene grown on Ni is also influenced by the growth time and hydrocarbon concentration since both parameters affect the amount of carbon dissolved in the Ni substrate.[89] Beyond these, more details of CVD synthesis of graphene are reviewed by Munoz et al.[96]

Although Cu and Ni are the most widely used catalysts, mainly due to the combination of relatively low price and easy graphene growth, various other substrates can be used to grow graphene via CVD process, such as other metal substrates of Pt,[97] Ir,[98] Ru,[99] Pd,[100] and Al.[101] Moreover, insulating substrates, such as sapphire,[102,103] SiC,[104] Si/SiO_x,[105] SiO_2,[106,107] Si_3N_4,[108] hBN[109,110] and have also been reported to be successful for

CVD growth of graphene. Moreover, the large-scale high-quality continuous CVD graphene films has been demonstrated to be promising in various applications, such as field effect transistors,[111,112] sensors,[113-115] transparent conductive films,[56,59,116] energy devices[117,118] and anticorrosive coatings,[5,10] which is the focused application studied in this thesis.

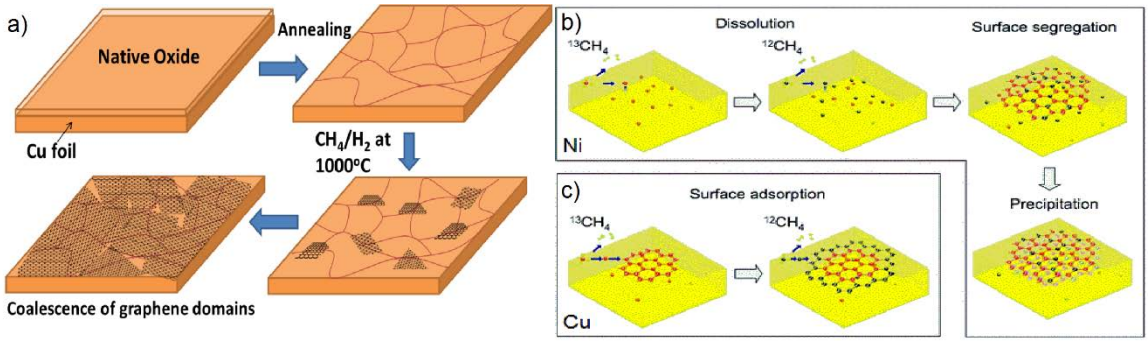

Figure 4.2 Schematic illustration of (a) CVD graphene growth process on Cu[90] and graphene formation mechanism on (b) Ni and (c)Cu.[91]

4.3.2. Transfer of CVD graphene

When CVD graphene is to be used on a substrate where direct high-quality graphene growth is not feasible, a transfer process is required. There are various types of methods to transfer CVD graphene, due to its utmost importance for many applications and the inherent difficulty for transferring an atomically thin graphene layer without damaging it. Several reviews[119,120] cover this topic, reporting on popular graphene transfer methods, such as polymer-assisted etching transfer,[3,4,59,87] electrochemical delamination transfer,[121-123] and mechanical peeling transfer, etc.

The first widely used graphene transfer method is the polymer-assisted etching transfer. In a typical polymer-assisted etching transfer method, as presented in Figure 4.3a,[90] a protective polymer layer (e.g. poly-methyl methacrylate (PMMA)[3,4]) is coated on graphene film, followed by etching of underneath metal substrate in oxidizing solutions, such as iron chloride ($FeCl_3$)[87,124] or ammonium persulfate solution ($(NH_4)_2S_2O_8$)[59]. The obtained graphene-polymer hybrid film is then transferred onto the surface of target substrate and the polymer layer is subsequently removed with a solvent (e.g. acetone)[4]

and thermal annealing (e.g. 150-300°C).[125] Although this method is simple, the cost of graphene production is increased due to the loss of metal substrates and production of chemical waste during the etching step.[126] The quality of graphene is decreased as well because the polymer residues on the surface of graphene are difficult to be completely removed.[125]

Electrochemical delamination transfer is an efficient and nondestructive method developed in recent years, which allows the metal catalyst substrate to be reused for successive graphene growth. A typical example of electrochemical delamination transfer is the "bubbling transfer" method, which is illustrated in Figure 4.3b. Before the "bubbling transfer" process, a protective polymer layer is coated on the surface of graphene/metal. Then the polymer/graphene/metal electrode is used as cathode and a noble material (e.g. glassy carbon[122] or Pt [121]) is used as anode in an electrochemical cell. When the cathode is polarized with large negative potential (e.g. -5V)[122], water molecules in the electrolyte are reduced at cathode and hydrogen bubbles start to form at metal-graphene interface. These hydrogen bubbles eventually detach the graphene layer from the metal substrate. The delaminated graphene/polymer hybrid film is then transferred onto target substrate with the polymer layer being subsequently removed by suitable solvents.

For mechanical peeling transfer method, a polymer layer is normally applied onto graphene as well, such as poly(vinyl alcohol) (PVA)[127] or poly(lactide acid) (PLA).[128] As shown in Figure 4.3c, the Cu substrate can be directly peeled off from graphene after the polymer/graphene/Cu is treated under controlled temperature and pressure. The polymer/graphene hybrid film is then obtained without use of etching solution and consequent loss of metal substrates. Although this technique is versatile, it is less efficient than the other two techniques, since successful graphene transfer with this technique is highly dependent on fine-tuning of transfer conditions.[126]

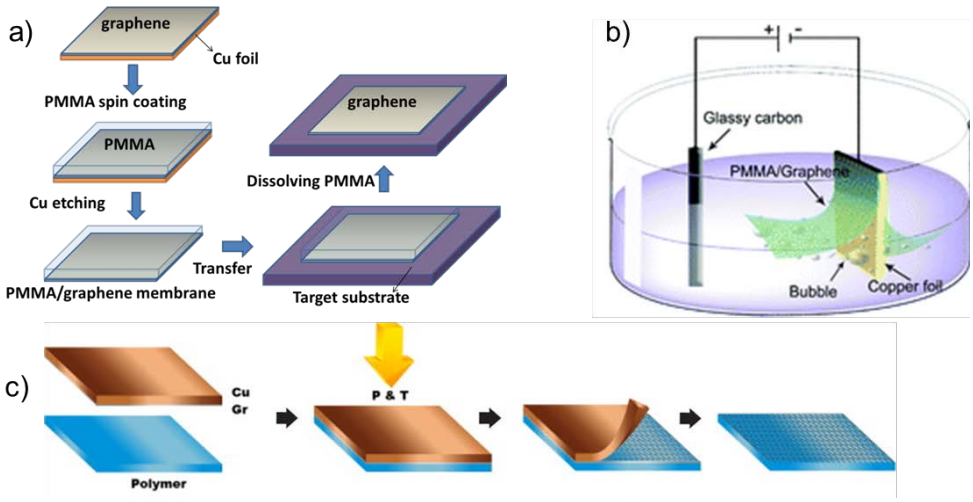

Figure 4.3 Schematic illustration of typical examples of (a) polymer-assisted etching transfer,[90] (b) electrochemical delamination transfer[122] and (c) mechanical peeling transfer[128] of CVD graphene.

4.4. Chemically derived graphene

Graphene oxide (GO) and reduced graphene oxide (rGO or chemical converted graphene) are the two most common types of chemically derived graphene. Chemical oxidation and exfoliation of graphite is the main route to produce GO, using approaches developed by Brodie,[129] Staudenmaier,[130] Hummers[131] and other methods derived from these three. The structure of graphene, GO and rGO are illustrated in Figure 4.4a.[132]. Various functional groups, such as epoxy and hydroxyl groups, are found in GO and these functional groups are mainly introduced during the oxidation process. In the oxidation process, as presented in Figure 4.4b,[132] graphite is oxidized to graphite oxide using a mixture of acid and oxidizing agent (e.g. potassium permanganate ($KMnO_4$) and sulfuric acid (H_2SO_4) in Hummers method[131]). Graphene oxide platelets can then be exfoliated from graphite oxide with the aid of stirring or sonication in solvents. These functional groups can be removed by a reduction process from GO to obtain rGO. Several effective methods are reported for reduction of GO to rGO, including chemical reagent reduction (e.g., with one of the following chemicals, hydrazine,[133] vitamin C,[134] hydriodic acid[135]), thermal reduction (e.g. thermal annealing,[136-138] microwave irradiation[139,140] and laser irradiation)[136] and a combination thereof (e.g. chemical reduction followed by thermal annealing[141,142] and gentle reduction[143]).

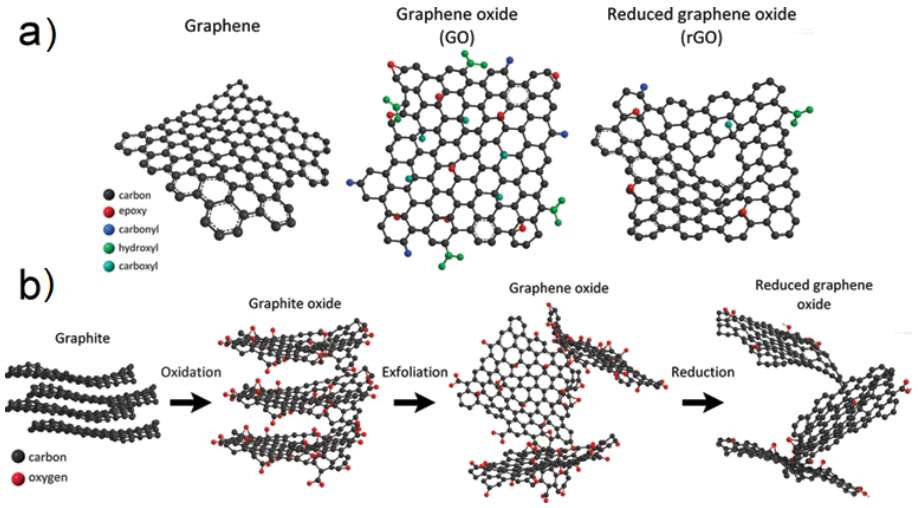

Figure 4.4 Schematic illustration of (a) structure of graphene, graphene oxide, reduced graphene oxide and (b) process of preparation of graphene oxide, reduced graphene oxide from chemical oxidation and exfoliation of graphite.[132]

4.5. Other methods for graphene preparation

Besides the above-mentioned methods of obtaining graphene, there are some other routes for preparation of graphene, including epitaxial growth,[144,145] total organic synthesis,[146-148] un-zipping of carbon nanotubes (CNTs)[149-151].

A typical epitaxial growth of graphene is heating up silicon carbide (SiC) in ultra-high vacuum (UHV) at high temperature (e.g. 1300°C) to enable desorption of Si atoms from the crystal and leave C atoms on the surface to form graphene layer,[152] as illustrated in Figure 4.5a. Although this technique produces large-area, continuous graphene, which is attractive for industrial applications, especially in semiconductor industries, it is limited by several unsolved issues, such as thickness and quality control and repeated production for graphene films.[153]

In a total organic synthesis of graphene, polycyclic aromatic hydrocarbon molecules are normally used as precursors (e.g. pentacene[146] and coronene[147]) for chemical reactions and the as-synthesized product is generally in a form of graphene nanoribbons (GNRs), as presented in Figure 4.5b using pentacene as an example. Although this approach produces GNRs with precise control of composition and structure, it is only at very small quantities and therefore may not be suitable for industrial applications.[88]

CNTs, from a morphological point of view, can be regarded as rolled GNRs. It is therefore possible to obtain graphene by un-zipping CNTs. The mechanism process resembles that of chemical synthesis of graphene from graphite, including both oxidation and exfoliation steps but for CNTs, as presented in Figure 4.5c using multiwall carbon nanotubes (MWCNTs) as an example.[149] This technique appears to be promising for mass production of graphene since mass quantities of CNTs can be produced. However, control over the morphologies of synthesized GNRs still needs to be improved in mass production.[154]

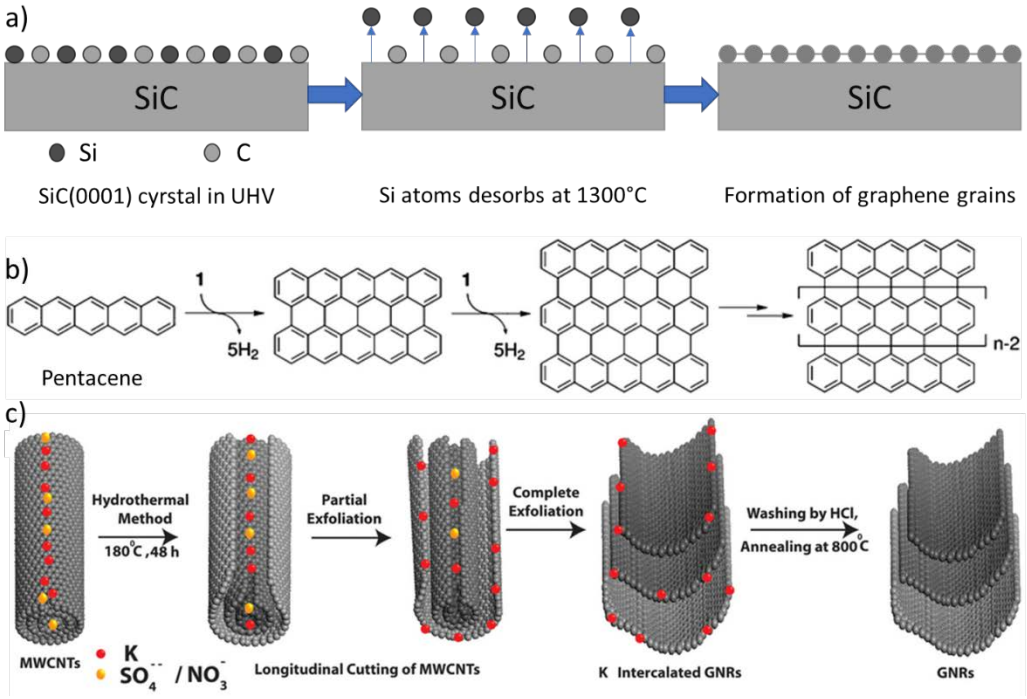

Figure 4.5 Schematic illustration of (a) epitaxial growth process of graphene on SiC, (b) total organic synthesis of GNRs using pentacene as a precursor,[146] (c) synthesis of GNRs via un-zipping MWCNTs.[149]

4.6. Discussion on graphene synthesis methods for application in coatings

As various methods to produce graphene have been developed, a comparison between these methods is therefore important so that we can find the production method that is more suitable for application in coatings. In Figure 4.6, Novoselov et al,[155] compared the price and quality of graphene obtained from various methods. Sukang Bae et al,[156]

listed features of graphene films produced from four representative methods in Table 3.1. Based on their views of the graphene produced from various methods, the correlation between production methods of graphene and its applications is therefore clear. Both CVD synthesis and liquid-phase exfoliation are the two most promising and robust methods to produce graphene for application in coatings, mainly because both methods are scalable and show relative higher cost-efficiency than other methods.

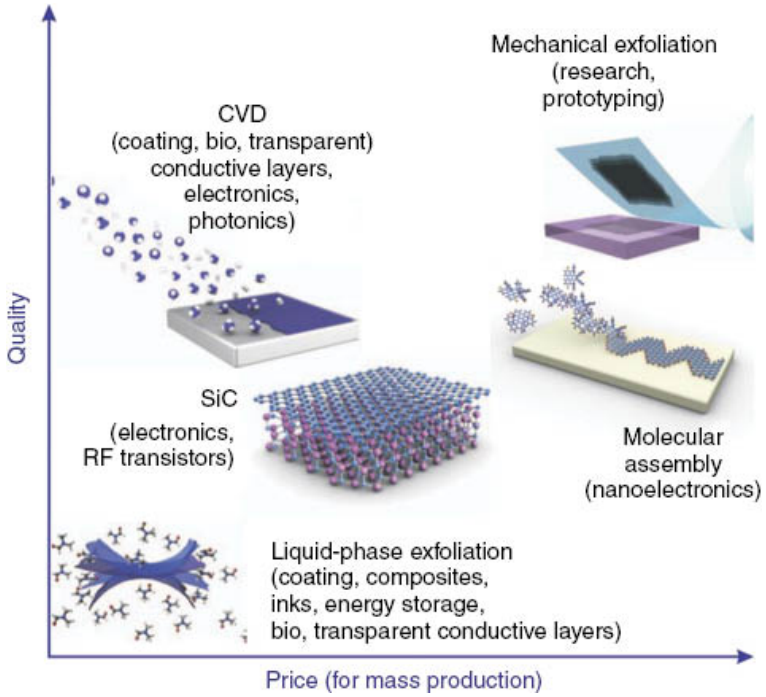

Figure 4.6 A comparison between various methods for production of graphene regarding to the price and quality.[155]

Method	Mechanical exfoliation	Chemical reduction from graphene oxide	Epitaxial growth on SiC	CVD based graphene growth on Ni, Cu, Fe, Co
Size	10~100 μm	> 6 inch	< 4 inch	> 6 inch
Mobility	best	bad	high	high
Transfer	yes	yes	no	yes
Applications	no	yes	little	most
Scalable	no	yes	not yet	yes
	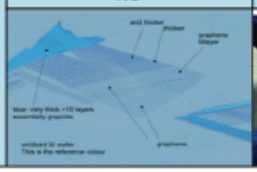		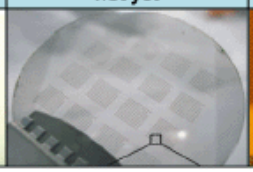	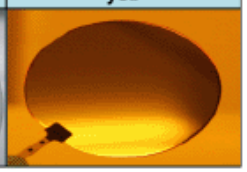

Table 4.1 Features of graphene produced from four representative methods.[156]

Chapter 5. Graphene for corrosion protection

5.1. Graphene as a corrosion barrier

Due to the fact that graphene exhibits unique impermeability and exceptional chemical inertness to corrosive species,[157] such as water and oxygen, graphene is an excellent candidate for corrosion barrier and promising in the application of corrosion protection. The excellent barrier properties of graphene principally stem from its structure, exceptional high stability and strength. As illustrated in Figure 5.1a,[158,159] the size of the geometric pore is only 0.064 nm, smaller than the van der Waals (vdw) diameter of helium (0.140 nm), hydrogen (0.120 nm), oxygen (0.152 nm), sodium (0.227 nm) and chlorine (0.175 nm) etc.[160] Therefore, an energy barrier exists for atoms passing through the graphene lattice. The value of the energy barrier is 16.34 eV for oxygen atom for passing the graphene lattice through the fixed vertical path as illustrated in Figure 5.1b.[161] This energy barrier excludes diffusion for oxygen through graphene. Although the energy barrier can be lower when oxygen atoms take reaction paths, the energy barrier is still high enough to block the diffusion of oxygen through graphene lattice.[161]

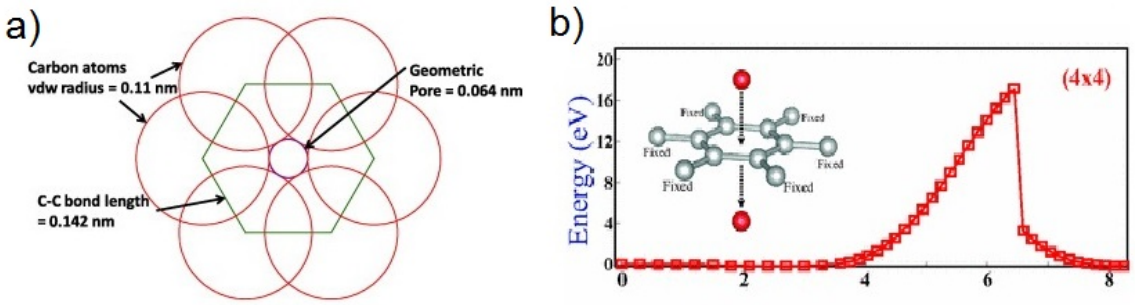

Figure 5.1 (a) Schematic illustration of geometric pore of graphene lattice[158] and (b) energy barrier for an oxygen atom to pass through graphene lattice from top to bottom with the fixed vertical path.[161]

Although graphene exhibits impermeability to all molecules, it is however demonstrated that a single layer of graphene can be permeable to protons.[69,70] As shown in Figure 5.2a, the geometric pore of graphene has an area of about 0.32Å^2, considering its diameter of 64 pm. Protons, with a ion radius of 0.000875 pm,[162] can theoretically penetrate through graphene lattice.[70] In Figure 5.2b, Hu et al,[69] reported their results on the proton transport through a graphene membrane by measuring the hydrogen flow rate. As seen from the top inset, when a negative bias is applied on the graphene membrane,

protons from the PdH_x electrode can diffuse through both Nafion and graphene layer to produce a steady H_2 flux into the vacuum chamber while the flow rate is measured by a mass spectrometer. Their experimental results (scattered dots) agree with theoretically expected results (red line). Nevertheless, they also reported that no proton penetration was detected for bilayer graphene. In an another study, Achtyl et al,[70] found that protons in aqueous solutions can transfer across single layer graphene through rare, naturally occurring atomic defects via a Grotthuss mechanism.[163] After all, the knowledge that that protons can pass through single layer graphene should be taken into consideration when graphene is used as a corrosion barrier to protect metals in acidic media.

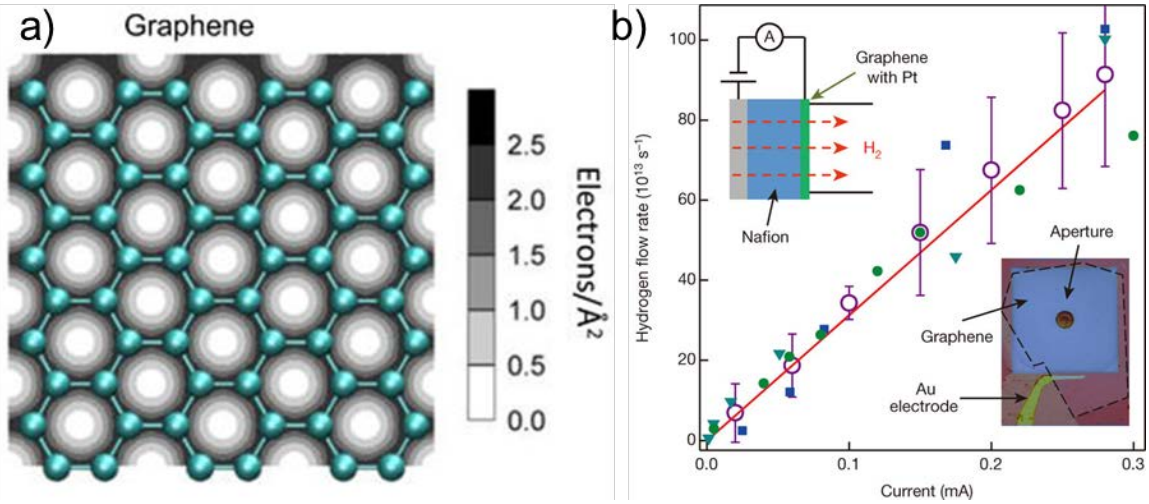

Figure 5.2 (a) Integrated charge densities for graphene and (b) current-controlled hydrogen flux through a graphene membrane.[69]

5.2. Atomically thin CVD graphene anticorrosive coatings

CVD graphene seems to be the ideal example of large-area graphene thin film for corrosion protection. Initial qualitative proof of CVD graphene's ability to protect against corrosion was reported by Chen et al.[10] Graphene sheet is an inert physical barrier which blocks corrosive species, as illustrated in Figure 5.3a. A single sheet of graphene was shown to protect a US penny from corrosion when immersed in 30% H_2O_2 for 2 minutes (Figure 5.3b). Later report from Prasai et al[5] managed to quantify the corrosion inhibition efficiency of CVD graphene coatings on Cu and Ni, as presented in Figure 4.3. With the CVD graphene coatings on metal surfaces, the corrosion rates of Cu and Ni are reduced by 7 and 20 times, respectively. When CVD graphene layers are transferred to the surface

of Ni, the corrosion rates are reduced by just a few times. However, the reduction of corrosion rate by CVD graphene coatings on Cu has also been reported to be at most of 100 times,[7] due to the higher quality of graphene synthesized on Cu. Kirkland et al,[6] explained that the reduction of corrosion rate for CVD graphene coated Ni and Cu are primarily due to the slowdown of anodic dissolution process for Ni and cathodic oxygen reduction reactions for Cu.

Besides its corrosion inhibition effects on metals, the superior thermal conductivity and transparency of atomically thin graphene may be beneficial for its application as anticorrosive coatings. Due to its high thermal conductivity, graphene may help dissipate heat thus reducing local heating of metal substrates, which may otherwise lead to heavier corrosion or oxidation at those regions with higher temperature. Moreover, being transparent, graphene makes it possible to directly monitor through visual inspection the effect of corrosion on the surface of metal substrates (and therefore, also the corrosion morphology) without indirect characterization techniques (e.g. electrochemical tests).

Although the unique impermeability of graphene alongside the high inertness, stability and strength make it an outstanding candidate as a corrosion barrier, there are some factors significantly limiting the application of CVD graphene for anticorrosive coatings.

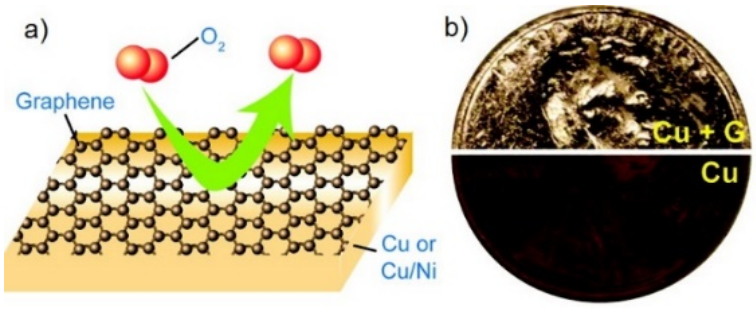

Figure 5.3 (a) Schematic illustration on CVD graphene as a noble physical barrier and (b) an image showing graphene covered (upper) and uncovered (lower) US penny after immersion in H_2O_2 for 2 minutes.[10]

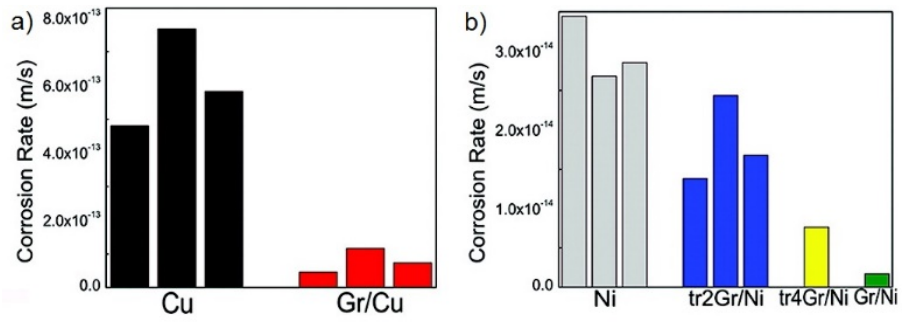

Figure 5.4 Corrosion rate values of (a) bare Cu and graphene coated Cu (Gr/Cu) samples and (b) bare Ni and graphene (both transferred and as-grown) coated Ni samples in 0.1 M Na_2SO_4 solution.[5] Note the values are extracted from polarization curves.

Firstly, corrosion can be induced directly on metals at defective area of the atomically thin graphene layer, such as cracks,[5,12] grain boundaries[10,34,164] and wrinkles[11,165], as presented in Figure 5.5. In this scenario, continuous, uniform, high-quality, single crystal large-domain graphene or high-fidelity transfer of graphene is a possible solution to improve the corrosion protection properties of graphene. Besides, deposition of another materials to passivate the defects can also increase the corrosion inhibition efficiency of CVD graphene coatings.[166] However, these methods will most likely increase the cost of graphene coatings and greatly decrease their potential for real applications.

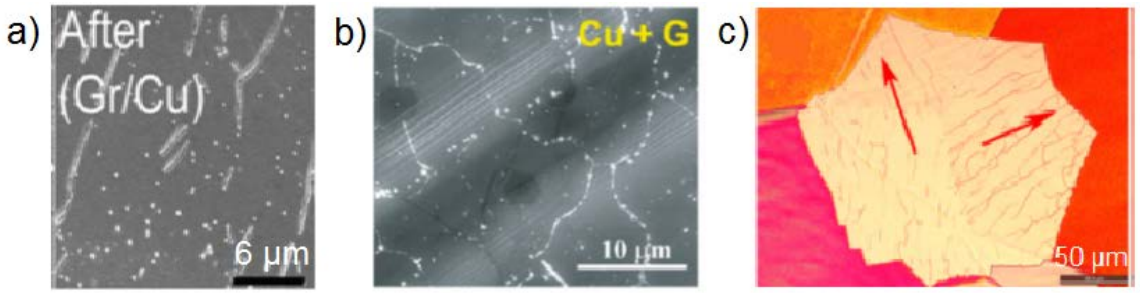

Figure 5.5 SEM images of Cu corrosion at graphene (a) cracks[5] and (b) grain boundaries[10] and optical image of Cu copper at graphene wrinkles.[11]

Secondly, the high nobility and electrical conductivity of graphene make graphene act as a cathode when in direct contact with metals, inducing galvanic corrosion and increase of corrosion rate.[27] Therefore, graphene should be used with caution as an anticorrosive coating especially in this regard. According to results reported by Schriver et al[8] and Zhou et al,[9] corrosion of graphene coated Cu is accelerated at long-term (6 or 18

months) exposure in air. As presented in Figure 5.6a, c and e, when Cu corrosion takes places at graphene defects, the electrons lost from Cu due to oxidation are transferred from graphene, which is a more efficient conductive pathway than Cu, to react with oxygen for cathodic reaction. In aqueous solution (e.g. seawater), graphene on the surface will also serve as a cathode with large area for cathodic oxygen reduction and increase the corrosion rate of Cu. Therefore, the insulating hexagonal boron nitride (hBN) can be a promising candidate to replace graphene as a more effective corrosion barrier,[167-171] due to the insulating nature of hBN and thus the lack of galvanic corrosion issues, as shown in Figure 5.6b,d and f.

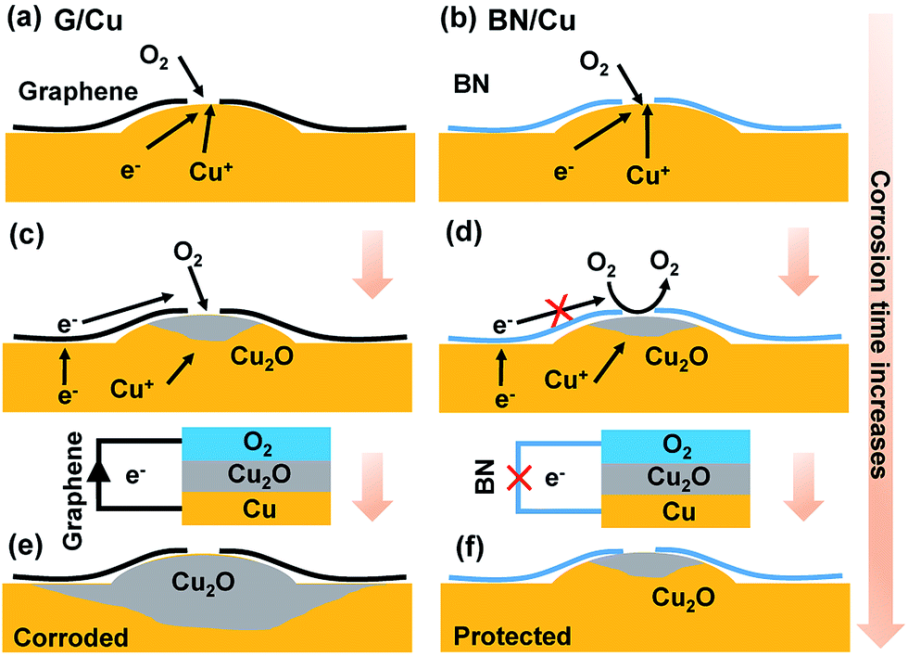

Figure 5.6 Schematic illustration of the corrosion mechanism of (a,c,e) graphene coated Cu (G/Cu) and (b,d,f) hexagonal boron nitride coated Cu (BN/Cu).[167]

Thirdly, the adhesion of graphene coatings on metal substrates is weak, which explains why it is relatively easy to transfer CVD-grown graphene.[121,122,127,128] According to reported results,[75] the adhesion energy of CVD as-grown graphene on Cu and Ni are 12.8 and 72.7 $J \cdot m^{-2}$, respectively. The adhesion strength of graphene on metal substrates can strongly influence the corrosion protection properties, especially at long-term, as presented in Figure 5.7.[172] When graphene is covered on weakly interacting metals (e.g. Cu and Pt), due to the impermeability of graphene, oxygen is not able to pass through defect-free area of graphene grains. However, oxygen can attack metals at defective sites

at short-term exposure to air. Oxygen can diffuse at the metal-substrate interface and oxidize the whole surface of metals at long-term exposure, due to weak interaction energy of graphene to substrates. For metals like Ni, Co and Fe, where graphene interacts strongly with these substrates, oxygen is not able to diffuse at the interface. In most cases, the metals are barely oxidized at sites covered with defective graphene. At long-term exposure, continuous protection is provided by graphene and oxide at whole surface of metals (e.g. Ni and Co) for long-term exposure, as the oxides formed at defective sites are dense and can passivate the metal surface. While the oxides are porous, continuous corrosion is not available at defective sites at long-term exposure for metals like Fe. From a practical application point of view, weak adhesion of graphene on metals does not only affect its long-term corrosion protection properties but may also lead to delamination of graphene layer under realistic wear and friction in working conditions. Moreover, adhesion is important to be considered when transferred graphene is used as anticorrosive coatings directly on metals, as transferred graphene is reported to be easily delaminated from metal substrate even under normal working conditions at short-term.[173] In addition, it is also important to note that the atomically thin graphene film could be difficult to be applied on rough surfaces, especially for those metals not available for direct high-quality graphene growth. In this case, the excellent corrosion protection performance by CVD graphene may be hard to achieve if the graphene coating cannot properly cover and adhere the metal surface.

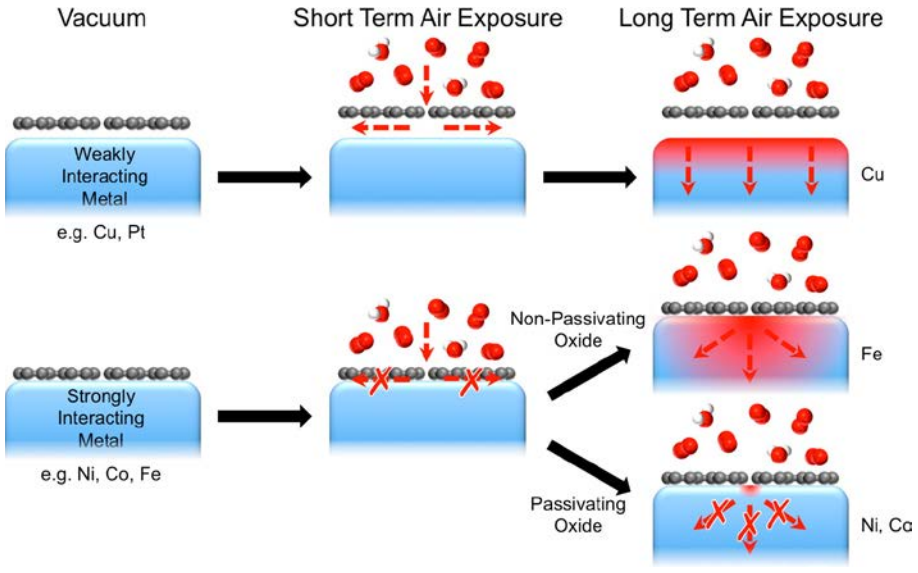

Figure 5.7 Schematic illustration of the passivation behavior of graphene on different metals.[172]

Furthermore, many important industrial-relevant metals and alloys (e.g. Fe, Mg and Al alloys pose additional challenges because (i) large-scale high-quality continuous graphene layers are difficult to directly synthesize by CVD on them, (ii) they cannot withstand the high temperature (~1000 °C) required by standard CVD process and may suffer degradation of their functional properties. This shortcoming of CVD graphene would significantly decrease its potential for universal applications as atomic-thin anticorrosive coatings for metals and alloys. However, in these cases, transferred graphene can provide a solution. Indeed, studies have shown successful corrosion protection for Al alloys with transferred graphene.[174] In addition, reported results have shown that the use of solid and liquid carbon sources[175,176] and design of alloy catalysts[177] can be an efficient to prepare high-quality CVD graphene at low temperatures (as low as 300°C[176]).

In summary, although CVD graphene has the potential as a coating for corrosion protection of metals and alloys, graphene defects, galvanic coupling issues, weak adhesion on metallic substrates, the high temperature required for conventional growth processes and the roughness of the metal surface need to be considered.

Chapter 6. Experimental techniques

6.1. CVD graphene growth and transfer

Generally, graphene used in this thesis is synthesized via CVD; on Cu substrate for single-layer graphene (SLG) and on Ni substrate for multi-layer graphene (MLG). Before the CVD growth process, both Ni and Cu are cleaned in acetone to remove organic residues and Cu is subject to another electropolishing process to remove native oxide on the surface and reduce its surface roughness.[175] MLG is synthesized on Ni with both a home-built CVD system (details are included in reference[178]) and a commercial available cold-wall based rapid thermal CVD system (AS-ONE from Annealsys). Four main steps are included in the CVD graphene synthesis process: (i) heating up, (ii) annealing, (iii) growth and (iv) cooling down. Briefly, for MLG growth on Ni with home-built CVD system, as presented in Figure 6.1a, the substrate is firstly heated up to 850 °C and annealed with 100 sccm H_2 under 5 mbar for 10 minutes, then subject to the growth process with a co-flow of 24 sccm H_2 and 12 scm C_2H_2 for 10 minutes before cooling down to room temperature. When MLG growth on Ni was processed with AS-ONE CVD system (Figure 6.1b), the substrate was heated up to 950 °C, annealed with a co-flow of 100 sccm H_2 and 120 sccm Ar at 1 atm for 15 minutes, and then subject to the growth process for 5 minutes with a co-flow of 100 sccm H_2 and 2 sccm C_2H_2 before cooling down.[4] It is important to note that the growth temperature was increased from 850 °C for MLG growth on Ni with home-built CVD system to 950 °C for the growth process with AS-ONE CVD system. This is because, according to Chae et al,[179] with the increase in growth temperature, the defect density in graphene decreases while the number of layers increases. Therefore, it seems that high-quality, thick graphene layer may be obtained at higher temperature. The SLG growth on Cu with the AS-ONE CVD system (Figure 6.1c) was processed with annealing at 1000 °C with 1000 sccm Ar at 25 mbar for 10 minutes and then synthesis with a co-flow of 900 sccm Ar, 60 sccm H_2, 2 sccm CH_4 at 1 atm for 15 minutes.

For the transfer of as-grown SLG from Cu to other substrates, a polymer-assisted etching transfer method is used as illustrated in Figure 6.2. Firstly, 12 wt% polyvinyl butyral (PVB) ethanol solution is drop-casted onto SLG and then subject to spin coating process at 1000 rpm for 1 minute and curing at 60 °C for 2 hours. The Cu substrate is then chemically etched in a mixed solution of 5 wt% HCl and 30 wt% H_2O_2 for overnight so that a freestanding SLG/PVB hybrid thin film can be obtained. A polydimethylsiloxane (PDMS)

stamp is used to transfer the hybrid film to the target substrate and PVB is dissolved with acetone so that SLG is finally transferred from Cu to other substrates. The transfer of MLG from Ni to target substrate is carried out with the same process as for SLG.

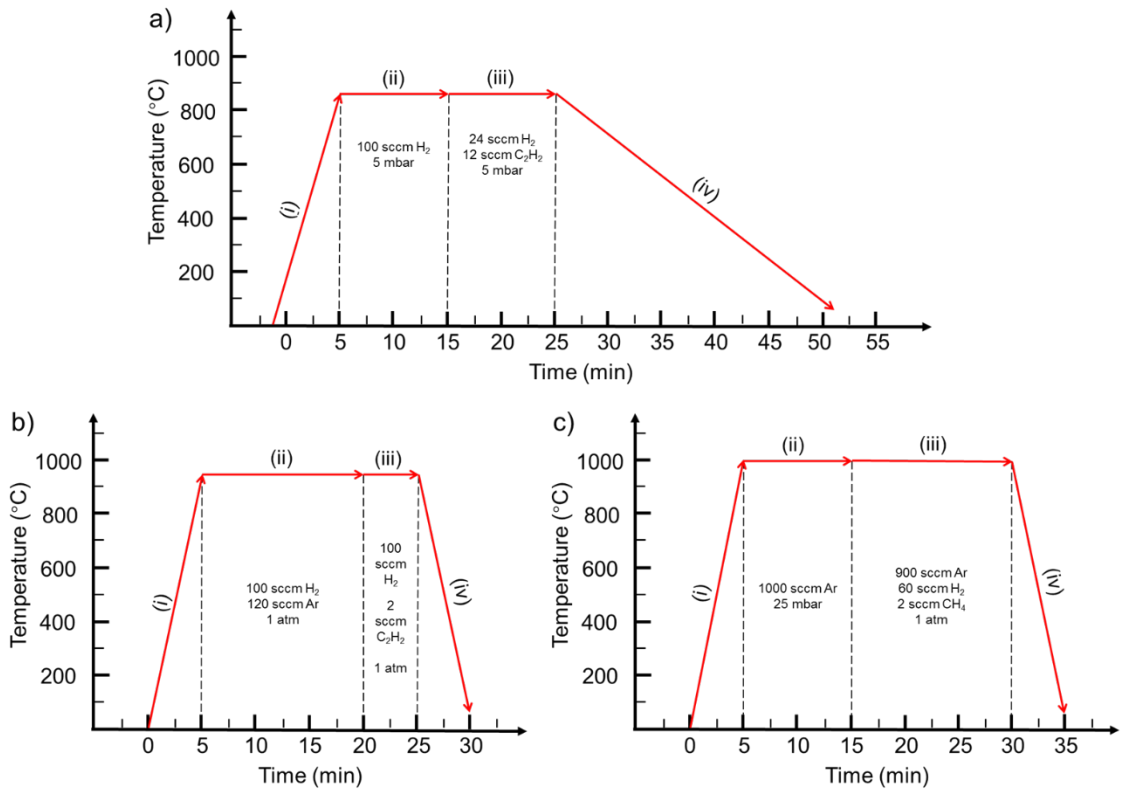

Figure 6.1 Temperature profiles of MLG growth process on Ni with (a) home-built CVD system and (b) AS-ONE CVD system, and (c) SLG growth process on Cu with AS-ONE CVD system. The four steps in the CVD process are (i) heating up, (ii) annealing, (iii) growth and (iv) cooling down.

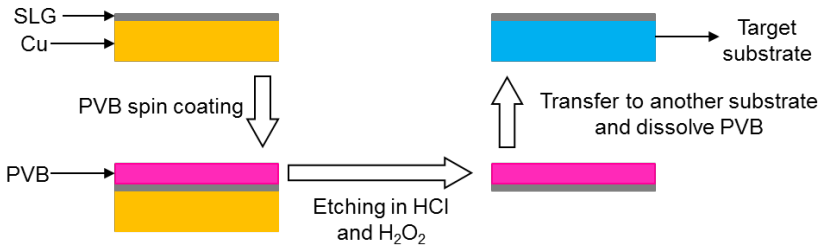

Figure 6.2 Schematic illustration of SLG transfer process from Cu to target substrate.

6.2. Raman spectroscopy

Raman spectroscopy studies the inelastic scattering of light by materials and can be used to obtain information on the structure and properties of molecules or solids based on their vibrational transitions.[180] When it is applied on graphene research, information on the layer numbers, stacking orders and quality of a graphene sheet can be obtained quickly in a non-destructive way.[181,182] In a typical measurement, a laser light is irradiated on graphene, due to inelastic collisions between incident photons and graphene, the photon scattered, which is one out of a million scattered photons, involve a change of the photon energy. This energy change is recorded as a Raman shift of the wavelength of incident light, which depends on the vibrational and rotational modes of the graphene sample being studied. The Raman spectrum of graphene contains abundant information on defects and disorders,[183] doping,[184] number and relative orientation of layers[181] and mechanical strain[185] in a graphene thin film. G and 2D peaks are the main peaks used for characterizing graphene by Raman spectroscopy among all the Raman peaks that exist in graphene samples.[181,186] The Raman spectra of both pristine and defective graphene are presented in Figure 6.3.[187] The D peak (~1350 cm^{-1}) is due to the breathing modes of sp^2 bonded atoms in rings,[183] which can be detected by Raman spectroscopy only when defects or disorders exist in the graphene layers.[181,186] The G peak (~1580 cm^{-1}) originates from the stretching modes of all pairs of sp^2 bonded atoms in both rings and chains, thus can be observed from many other carbon based materials such as carbon nanotubes and graphite.[183] The 2D peak is a double resonance and overtone of D peak and is located at around 2700 cm^{-1}.[179] It is important to note that the peak intensity ratio of D to G peak (I(D)/I(G)) and 2D to G peak (I(2D)/I(G)) are the two parameters of utmost importance for characterization of graphene with Raman spectroscopy. I(D)/I(G) is related to the average distance between graphene defects and its value increases with more defects present in graphene layer.[188] I(2D)/I(G) is related to the number of graphene layers, which is about 2 for single graphene layer supported on SiO_2 substrate and this value drops with the increase of graphene layers.[4] Moreover, the Raman Spectroscopy of graphene greatly depends on the supporting substrate. When graphene is supported on SiO_2 substrate with a proper thickness, due to the interference of light, the signal is multiplied by many times.[189] When graphene is supported on Cu, the Raman spectra of graphene are similar to those of free standing graphene or graphene supported on SiO_2,[190] since graphene weakly interacts with Cu. However, when single-layer graphene is supported on a Ni substrate, no Raman single can be obtained,[191] since graphene is strongly interacting with

Ni surface, which strongly influence the electron-phonon coupling in graphene and suppress Raman signals.[189] Raman spectrum collected in this thesis are using a 455-nm laser with a Thermo Fisher DXR Raman spectrometer at 8 mW power and 50X objective. Peaks of graphene are determined via Maltab as described by Larsen et al.[192]

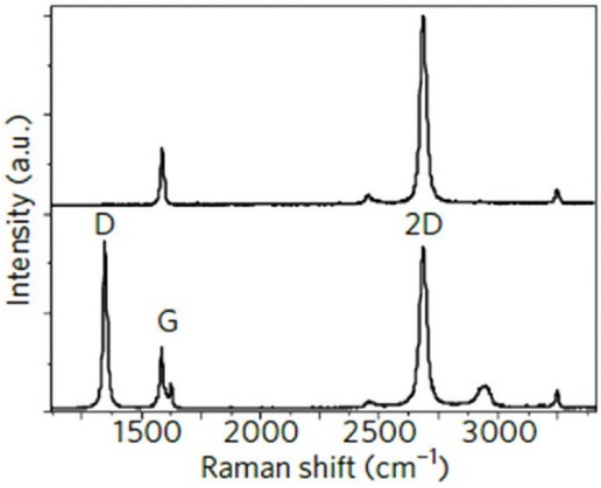

Figure 6.3 Raman spectra of pristine (top) and defective (bottom) of a graphene layer. [187]

6.3. Scanning electron microscopy (SEM)

Scanning electron microscopy (SEM) is used to obtain the information on morphology, structure and, if coupled with a EDX analyzer, composition of the studied solid materials. When a focused electron beam with high acceleration voltage (e.g. 5 to 30 kV) is irradiated on the surface of a materials, secondary electrons can be knocked out from the atoms in the materials via inelastic scattering as illustrated in Figure 6.4a. Moreover, the incoming electrons can rebound as backscattered electrons due to elastic scattering as shown in Figure 6.4b.[193,194] The signals from both these two types of electrons can then be collected by separate detectors to form SEM images for the characterization of samples. SEM images based on secondary electrons primarily provide topographical information of the sample, while information on chemical composition can be obtained from backscattered electron based images.[193] In this thesis, SEM is mainly used to characterize the morphology of graphene, structure of graphene coatings and corrosion morphology of metallic substrates.

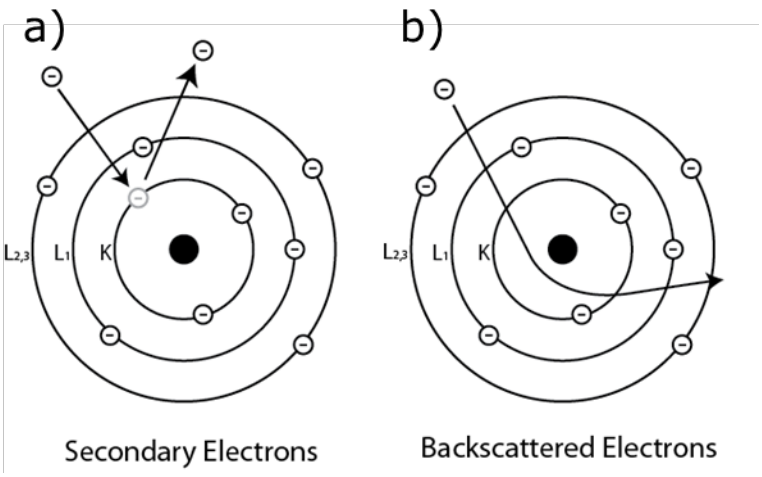

Figure 6.4 Schematic illustration on the emission of (a) secondary electrons and (b) backscattered electrons.[195]

6.4. Transmission electron microscopy (TEM)

Transmission electron microscopy (TEM) is a powerful technique used to characterize the structure of small specimens especially at atomic resolution.[196] During the TEM characterization, the sample is irradiated with a focused electron beam with high acceleration voltage (e.g. 60 to 300 kV) so that the electrons are transmitted through the thin specimen and then collected for imaging rather than secondary or backscattered electrons as in SEM. The TEM imaging formation mechanism in bright field imaging mode is schematic illustrated in Figure 6.5a.[197] For graphene research, TEM is very useful for the observation of graphene's atomic structure, regarding to layer numbers[59,198] (Figure 6.5b) and structural defects.[199] Due to the mass-induced contrast in TEM,[200] the carbon atoms in graphene, when compared with heavier atoms of Cu and Ni, will exhibit lighter contrast and it is difficult to image individual atom. In this study, TEM is used to characterize the thickness of graphene thin film grown on Ni substrate. For the manipulation of thickness measurement, the cross-section TEM technique is used. A lamella structure in the graphene film is firstly shaped using Focus Ion Beam (FIB) technique and then lifted on a TEM grid for observation.

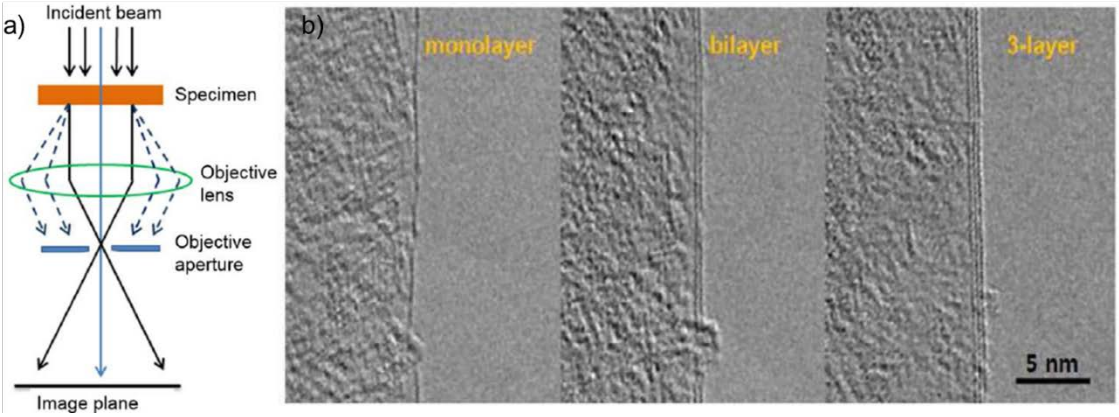

Figure 6.5 (a) Schematic illustration showing the mechanism of image formation in TEM[197] and (b) TEM images showing number of layers for graphene.

6.5. Setting up for electrochemical corrosion tests

Electrochemical corrosion tests, such as electrochemical impedance spectroscopy (EIS) and potentiodynamic polarization curves (PPC) measurements, are mainly used in this thesis to study the corrosion performance of graphene coated metallic samples. Both tests are carried out with a typical three electrode electrochemical cell, as illustrated in Figure 6.6. Teflon is the material used to fabricate the bottom, body and lid of the cell. The working electrode of graphene coated metal specimen is fixed by the groove in the cell bottom. Testing area of the sample (~1 cm^2) is controlled by the O-ring between the sample and cell body. The hollow body of the cell is filled with electrolyte and sealed by the O-ring when screws between the bottom and body are fastened. The lid is used to hold the Pt counter electrode and Ag/AgCI reference electrode as well as preventing electrolyte being contaminated and evaporated. Three electrodes are then connected with a Gamry Reference 3000 potentiostat and an ECM8 Electrochemical Multiplexer for EIS and PPC tests in a Faraday cage.

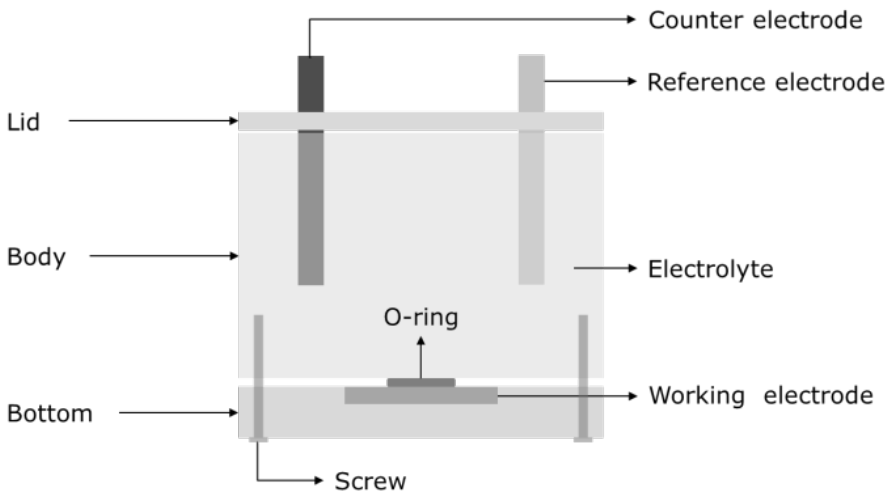

Figure 6.6 Schematic illustration on cross-section of the three-electrode cell.

6.6. Electrochemical impedance spectroscopy (EIS)

Electrochemical impedance spectroscopy (EIS) is a powerful tool to study corrosion, especially for coated metallic samples.[201,202] EIS can be measured by applying a small sinusoidal AC potential perturbation (e.g. ±10 mV) to the metal near its open circuit potential (OCP) in the testing electrolyte. The AC potential perturbation of the OCP is so small for any change on most studied samples that the EIS can be used as a non-destructive tool for corrosion study. With the applied sinusoidal AC potential perturbation, the primary output signal for EIS tests is therefore sinusoidal AC current. Electrochemical impedance is therefore obtained from the applied potential and generated current, together with both the sinusoidal characteristics from the two parameters, as explained by Equation 6.1.[203]

$$Z(t) = \frac{E(t)}{I(t)} = \frac{E_0 \cos(\omega t)}{I_0 \cos(\omega t - \varphi)} = Z_0 \frac{\cos(\omega t)}{\cos(\omega t - \varphi)} \qquad 6.1$$

Therefore, the impedance ($Z_{(t)}$) is expressed with a magnitude (Z_0) and a phase angle (ϕ). The phase angle of ϕ refers to shift on the signals, as charging-time is often required for capacitors in the electrochemical system to be fully charged. Moreover, the impedance can be transferred to another complex expression as shown in Equation 6.2.[203] The vectorial nature of impedance is expressed with a real and an imaginary part.

$$Z = \frac{E}{I} = Z_0 \exp(i\varphi) = Z_0(\cos\varphi + i\sin\varphi) \qquad 6.2$$

Typical EIS spectra can be expressed with three types of graph, including Bode plot (Figure 6.7a), phase diagram (Figure 6.7b), both of which are based on Equation 6.1, and Nyquist plot (Figure 6.7c), which is based on Equation 6.2. Bode plot and phase diagram are usually displayed together, while Nyquist plots can be given alone.

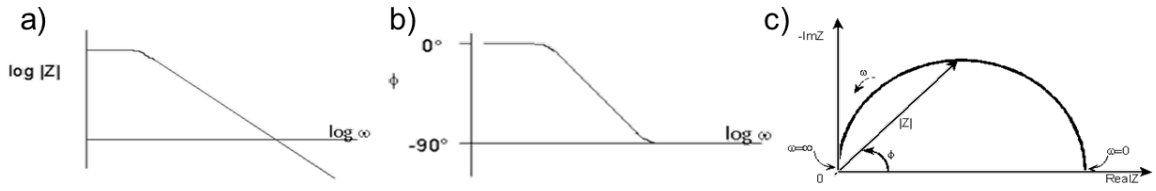

Figure 6.7 Typical example of (a) Bode plot, (b) phase angle diagram and (c) Nyquist plot. Adapted from reference [203].

After the EIS spectra is measured, appropriate equivalent electrical circuits (EEC) are usually used to fit the spectra to get the parameters for individual elements, including resistance and capacitance components in a corrosion system. Randles circuit, as shown in Figure 6.8, is a very basic EEC in corrosion study with paralleled charge transfer resistance (R_{ct}) (sometimes in series with a diffusion-control induced Warburg resistant element (Z_w)) and double layer capacitance (C_{dl}), together with the solution resistance (R_s) in series.[204] Moreover, the shape characteristics in Nyquist plot could provide the information on the components included in the EEC. For example, in Figure 6.8, the starting point of the half circle at high frequencies on Z' (or Z_{real}) indicates a solution resistance (R_s); the half circle suggests a couple of paralleled R_{ct} and C_{dl} (i.e. one time constant) due to kinetics controlled process, a straight line with a slope of 45° at low frequencies is usually related to a Warburg resistant element due to diffusion controlled process.[203] After mathematic fitting of the EIS spectra with the EEC model in Figure 6.8, values of R_s, R_{ct}, C_{dl} and Z_w can be obtained. It is therefore possible to analyze the corrosion process or corrosion protection mechanisms via a time-dependent evolution of the values of both the resistance and capacitance with a suitable EEC, which should be related to the real physical structure of the working electrode. Moreover, it is possible that different EECs may be used to fit the EIS spectra at different stages of corrosion, which can be defined from either characterization on samples (e.g. pits, corrosion products) or the EIS spectra generated during the tests. To conclude, EIS technique is a non-destructive tool for corrosion study, providing useful time-dependent and quantitative data on corrosion behaviors of metals, especially for those covered with high resistance

materials such as paints and coatings. Therefore, the EIS technique is used as the main electrochemical method to study the corrosion of graphene coated metallic samples to provide insight of the function of graphene in the corrosion protection process.

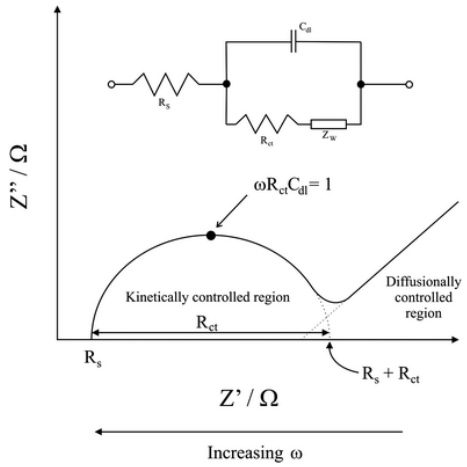

Figure 6.8 Example of the Nyquist plot for a Randles circuit in an electrochemical system.[205]

6.7. Potentiodynamic polarization curves (PPC)

Along with the AC technique of EIS, the DC technique of potentiodynamic polarization curves (PPC) is another important tool for corrosion study. In practice, a potentiodynamic scan is normally applied to the metal samples so that the response of current signal is collected as a curve, reflecting the relationship between potential and current during the electrochemical polarization process. In Figure 6.9, an example of PPC for aluminum alloy 2024 (AA2024) in 3.5% NaCl solution is presented.[206] During both the anodic and cathodic polarization process, due to activation control by charge transfer process, the corrosion behavior of cathode (reduction of oxygen) and anode (oxidation of aluminum) follows Tafel's law and is given by a linear line in the plot of E-Log*i*.[207] An extrapolation of the portions of the two linear lines could produce an intersection at corrosion potential (E_{corr}) and corrosion current density (i_{corr}). According to the value of obtained i_{corr}, the corrosion rate (CR, mm/year) of the metal sample can be calculated according to Faraday's law expressed in Equation 6.3.[208]

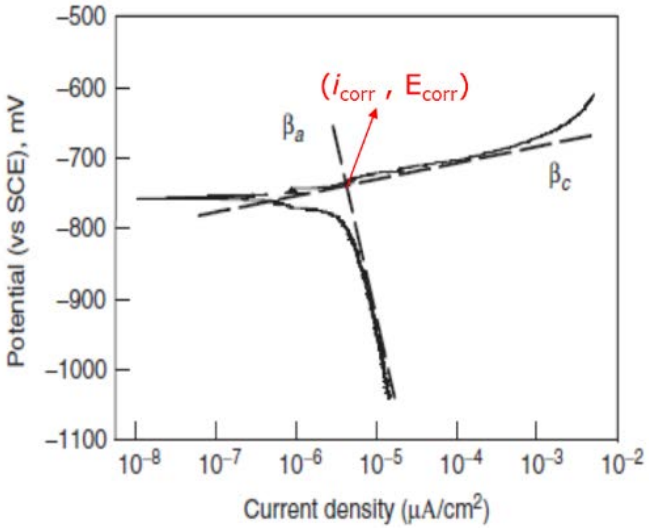

Figure 6.9 An example of PPC for AA2024 in 3.5% NaCl solution at room temperature.[206]

$$CR = \frac{i_{corr} \cdot K \cdot E_w}{\rho} \qquad 6.3$$

- CR is the corrosion rate (mm·year^{-1})
- i_{corr} is the corrosion current density (A·cm^{-2})
- K is the corrosion rate constant (3272 mm·A^{-1}·cm^{-1}·year^{-1})
- E_w is the equivalent weight (g)
- ρ is the density of the studied material (g·cm^{-3})

Although PPC measurements is widely used for the quantitative study of corrosion kinetics of metals,[6,209,210] this technique should be used with caution when the sample is coated with high resistance coatings (e.g. insulating polymeric coatings). This is because the PPC measurements on coated metals mainly reflects the barrier effects and resistance of the coatings rather than the corrosion kinetics of the metals, it is however widely reported on coated samples [5,14,211] and useful to reveal its barrier nature.[6,212] While PPC measurements are used in this thesis to analyze the corrosion protection performance by graphene based coatings, it is important to note that these results cannot stand alone for coated samples.

Chapter 7. Multilayer graphene coatings for corrosion protection

7.1. Background

Since the use of single layer graphene (SLG) as an anticorrosive coating exhibits significant limitations, notably direct corrosion attack at graphene defects,[5,10-12,34,164,165] the application of thicker multilayer graphene (MLG) coatings on the surface of metals and alloys can improve the barrier and corrosion protection performance. According to the results reported by Prasai et al,[5] when a SLG is synthesized on Cu and then transferred onto Ni substrate, the corrosion rate of Ni is not significantly reduced. However, when 2 and 4 SLG are transferred, the corrosion rate is decreased by around 1.6 and 4 times, respectively, as shown in Figure 5.4b. A similar result is also reported by Hsieh et al,[166] the corrosion rate of Cu is still only reduced by 2 times when they transfer up to three graphene layers Cu substrate, due to extremely fast mass transport (meters per second) both across and parallel to the atomically thin graphene layers. Using atomic layer deposition (ALD) of Al_2O_3, they selectively passivate graphene defects and reduced the corrosion rate of Cu by more than 100 times. Huh et al[213] also prove that the increase of graphene layers can reduce the corrosion rate of Cu substrate in seawater by blocking the diffusion path of dissolved oxygen and chloride ions through graphene defects to the substrate. Roy et al[214] and Hong et al[215] also propose that besides stacking multiple graphene layers, increasing the grain size of graphene is also efficient in improving the barrier performance of graphene coatings. Zhao et al[20] propose that the decrease of mass transport through MLG barrier can be explained by the reduction of porosity. When the coverage of SLG is defined as γ, the porosity of SLG can be described as (1- γ). When the SLG are layer-by-layer stacked and defects in each layer are independent and can be covered by adjacent graphene layer, the porosity of MLG is subject to an exponential decay and be described as $(1- \gamma)^n$, as presented in Figure 7.1.

Compared with layer-by-layer transferred MLG barrier coatings, the defects in MLG CVD grown on Cu and Ni substrates are more likely to be overlapped[215,216] because the MLG graphene growth process normally starts from the same nucleation sites.[179,217] In this case, the defects in adjacent layers are not completely independent and the porosity estimation for transferred MLG is not applicable. The barrier properties of transferred MLG is also reported to be better than CVD grown MLG.[218] However, from a practical use point

of view, when used as anticorrosive coatings, MLG CVD grown on Ni is more versatile than transferred MLG, because there is no need for multiple graphene growth and transfer processes, which can significantly increase the cost. Besides, in addition to the high costs, although transferred MLG coatings can be applied onto any metallic substrates, the weak adhesion should also be considered.

Based on the abovementioned facts, CVD grown MLG can be promising as a barrier coating to protect metals from corrosion and the aim of this chapter is therefore to present our results on the study of CVD MLG coatings for corrosion protection in both neutral and acidic media. Our results generally revealed that the MLG coating can offer long-term effective corrosion protection for stainless steel in stimulate seawater with prolonged diffusion pathway of corrosion species. However, when MLG is coated on Ni surface, it fails to protect Ni in acids (e.g. 0.5M HCl) because hydrogen bubbles form and grow at Ni-MLG interface, eventually leading to delamination of MLG coating.

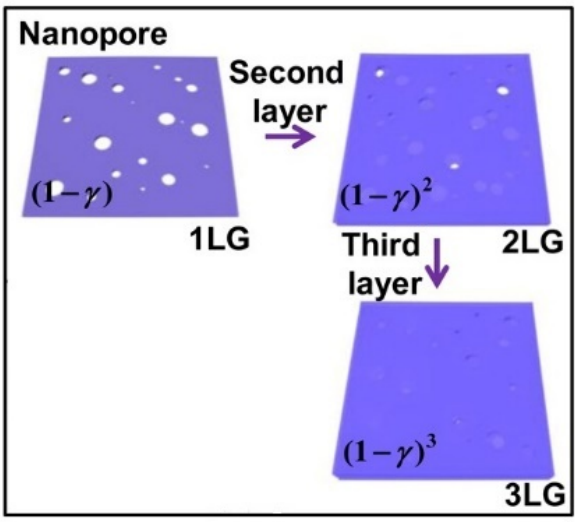

Figure 7.1 Schematic of the porosity for single, double and triple layer graphene.[20]

7.2. Preparation of multilayer graphene coatings

Firstly, we prepared MLG coatings to test their corrosion protection performance when applied on 304-stainless steel (SS) in neutral media of simulated seawater (3.5% NaCl solution). Detailed results are presented in publication 1.[219] Since the CVD graphene growth on stainless steel has been proved to be enhanced in some regions and retarded in other areas, due to the inconsistency and variety of element species distributed in

stainless steel,[220,221] direct growth of high-quality large-scale graphene films is not possible through CVD process on stainless steel. Therefore, a Ni seed layer is firstly electroplated on the surface of SS and then used as catalyst for MLG growth. The preparation steps of MLG/Ni/SS are illustrated in Figure 7.2. After cleaning by Triton X, SS is electroplated with a Ni seed layer using a Technotrans electroplating system.[178,219] The thickness of the Ni seed layer is 150 µm as controlled by the parameters of the electroplating process. The Ni/SS sample is then subject to CVD growth process in a home-built CVD system, as detailed in Section 6.1. The thickness of as synthesized MLG coating on Ni/SS is 25-40 nm, corresponding to 75-120 layers of graphene, as characterized by the SEM image after Fast Ion Beam milling (image not shown here, see more details in reference [219]).

Figure 7.2 Preparation steps of the MLG/Ni/SS sample.

MLG coating is also grown on a commercial Ni foil in the AS-ONE CVD system (see details in Section 6.1) to test the corrosion protection performance of the MLG coating for Ni substrate in acidic media. The thickness of the MLG coating is around 100 nm (~300 layers of graphene) with a constant interlayer distance of ~ 0.33 nm, as seen from cross-section TEM images of MLG on Ni presented in Figure 7.3a. Moreover, both A-B stacking and turbostratic regions are found on the MLG coating, as seen from the Raman spectra presented in Figure 7.3b.[222]

Besides the difference in thickness of both MLG coatings, the quality of MLG synthesized with AS-ONE CVD system turns to be higher than that of home-built CVD system, as shown from the Raman spectra of both MLG films shown in Figure 7.4. While the I(D)/I(G) ratio is around 0.2 for MLG grown with home-built CVD system,[219] this value is only 0.04 for the MLG grown with AS-ONE CVD system,[222] suggesting that the MLG from the commercial system has a much lower density of structural defects, which may due to the temperature for graphene growth increased from 850 °C in the home-built CVD system to 950 °C in AS-ONE CVD system, as discussed in Section 6.1.

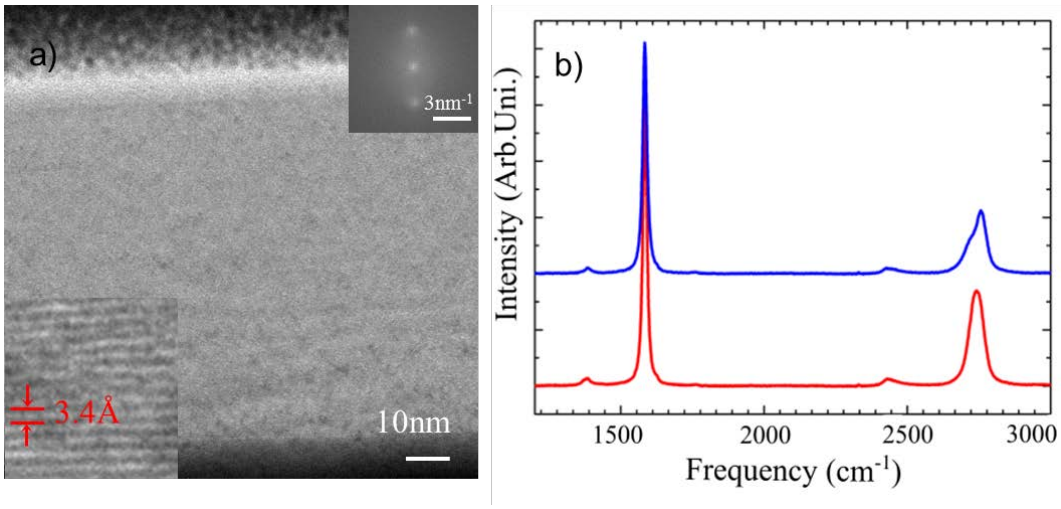

Figure 7.3 (a) Cross-section TEM image of MLG on Ni foil. Inset: (top right corner) Fourier transform and (bottom left corner) high-resolution image. (b) Two typical Raman spectra at different regions of the MLG layer on Ni foil showing the coexistence of both AB-stacking (blue curve at top) and turbostratic stacking (red curve at bottom) in the MLG film.

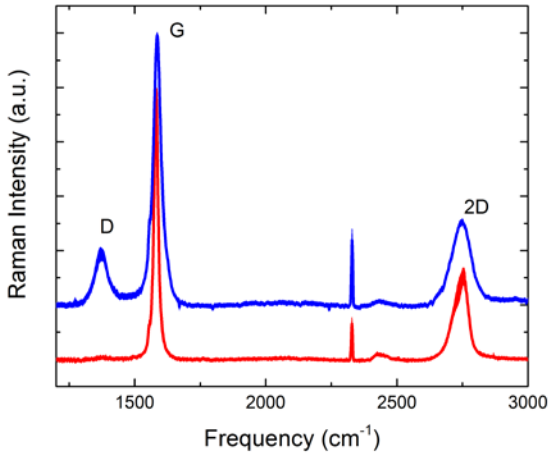

Figure 7.4 Typical Raman spectra of MLG film on Ni synthesized with the home-built (blue curve at top) and the AS-ONE (red curve at bottom) CVD systems.[178]

7.3. Corrosion protection of stainless steel in seawater

To test the corrosion protection performance of the MLG coating for stainless steel, both the graphene coated sample (MLG/Ni/SS) and the reference sample (Ni/SS) are half immersed in boiling simulated seawater for 504 hours. In this test, called the Atlas cell test, the lower half of the sample is immersed in the liquid phase, while the upper one is exposed to the air. In addition, to test the adhesion of the coating, the back of the substrate

is exposed to room temperature, so as to create a temperature gradient through the specimen.

The optical images of both samples before and after the corrosion test are presented in Figure 7.5. It is evident that the surface of Ni/SS sample is heavily corroded with signs of Ni oxides in both green and black color. It appears that the Ni/SS sample exposed to the air (upper part) is corroded more than the other part in the liquid phase. This can be mainly attributed to the difference in oxygen concentration in the air and liquid phases, since the oxygen concentration in the boiling simulated seawater is much lower than that in the air. On the other hand, no sign of corrosion is found on MLG/Ni/SS sample after the corrosion test. Both MLG/Ni/SS and Ni/SS samples are also characterized with energy dispersive x-ray spectroscopy (EDS) after the Atlas cell test and results have shown the presence of oxygen in Ni/SS and absence of oxygen in MLG/Ni/SS (results not shown here, see more details in reference [219]). It is important to note that the dark areas that can be seen optically on the sample are formed during the CVD process. Moreover, the quality of MLG coating after the corrosion test is investigated by Raman spectroscopy. As shown in Figure 7.6a, the Raman spectra of MLG after corrosion tests remains comparable to that before test, suggesting that the MLG coating is still preserved on Ni, without any evident sign of damage after 504 hours immersion in boiling seawater (i.e., the D peak for the sample after test has the same intensity than the one before the test).

By comparing the outcomes of our tests with the works in the literature, our study strongly suggests the superiority of MLG coating over that SLG coating for corrosion protection. According to reported results,[5-7,166,167] metal substrates coated with SLG suffered from corrosion in mild corrosion environment (e.g. Na_2SO_4 and NaCl solution) at room temperature and short-term of up to few hours. One of the main reasons responsible for the failure of SLG coated metals is that direct corrosion attack occurs at the defects in the atom-thin SLG film,[11,12,223] as illustrated in Figure 7.6b. However, the metal substrate coated with MLG remains uncorroded even after 504 hours of immersion in boiling seawater. This is because corrosive species must diffuse through a longer and more tortuous pathway in the case of thick MLG film before reaching the metal surface and initiate corrosion, as illustrated in Figure 7.6c.

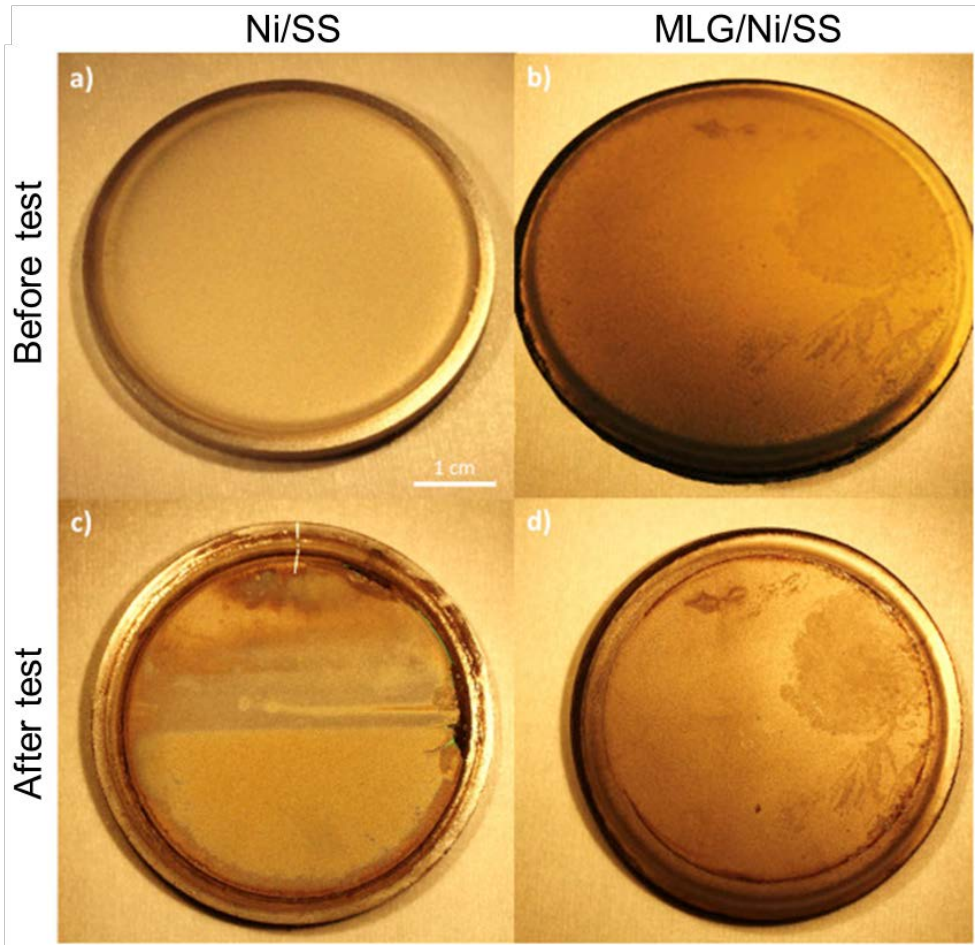

Figure 7.5 Optical images of both (a,c) Ni/SS and (b,d) MLG/Ni/SS sample (a,b) before and (c,d) after half immersion in boiling simulated seawater for 504 hours.[219]

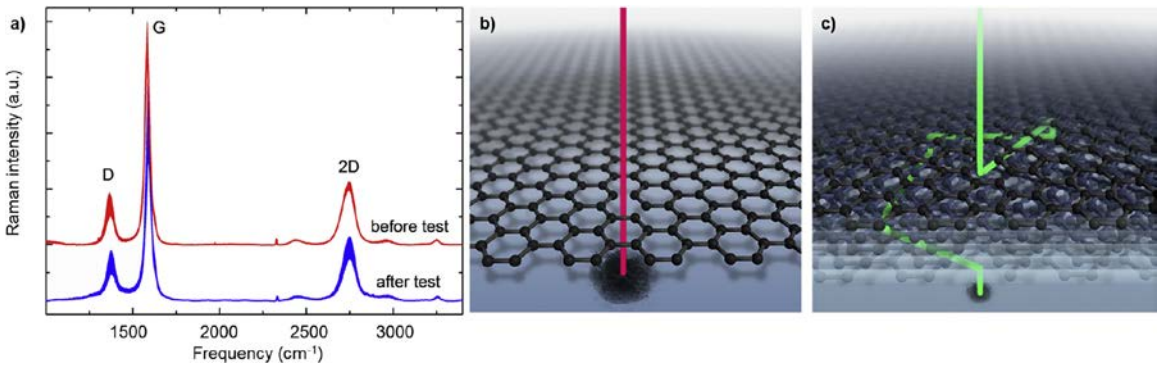

Figure 7.6 (a) Raman spectra of MLG coating on Ni/SS sample before and after corrosion test and schematic illustration on the diffusion pathway for (b) SLG and (c) MLG coating.[219] Note that the Raman spectra plotted is the average value and the thickness of the two lines represent standard deviation error bars.

7.4. Corrosion protection of nickel in acidic media

Being impermeable to all molecules, graphene is therefore expected to be able to protect metal substrates in harsher corrosive environment than simulated seawater such as acids. In this section, the behavior of MLG coating on Ni when immersed in acidic media is discussed and detailed results are included in publication 2.[222]

To begin with, both bare Ni and MLG coated Ni samples are tested with potentiodynamic polarization curves (PPC) and electrochemical impedance spectroscopy (EIS) measurements in 0.5 M HCl solution. From the results in PPC measurements (Figure 7.7a), the corrosion rate is found to decrease from 0.226 mm/year for bare Ni to 0.097 mm/year for MLG coated Ni, suggesting that MLG is efficient in corrosion inhibition within the tested timeframe of 1 hour. EIS results (Figure 7.7b) showed that the magnitude of impedance at 0.01 Hz for MLG coated Ni is 2700 Ω·cm^2, which is 5 times higher than that of bare Ni (536 Ω·cm^2), indicating that MLG is a good barrier layer within the short-term even to acidic media.

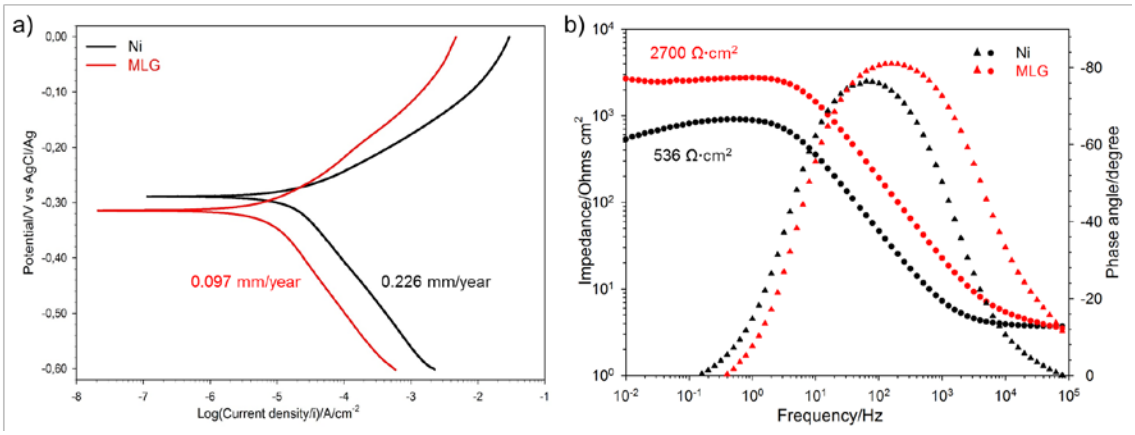

Figure 7.7 Results of (a) PPC and (b) EIS measurements of both bare Ni (black) and MLG coated Ni in 0.5 M HCl solution.[222]

However, after the PPC measurements (from -0.6 V to 0 V (vs. Ag/AgCl) with a scan rate of 0.5 mV/s), MLG coating has been observed to be heavily damaged as the MLG is delaminated from the substrate, as shown in Figure 7.8a. When a constant negative potential of -0.6 V is applied to the MLG coated Ni for 30 mins so that cathodic reactions are accelerated, MLG coating is also observed to be locally delaminated from the substrate as evidenced from Figure 7.8b. Raman spectra reveal that no graphene is observed on Ni substrate at the regions where MLG was delaminated, as shown in Figure

7.8. Moreover, the formation of hydrogen bubble is observed when negative potentials are applied on MLG coated Ni, according to reaction:

$$2H_3O^+ + 2e^- \rightarrow H_2 + 2\,H_2O$$

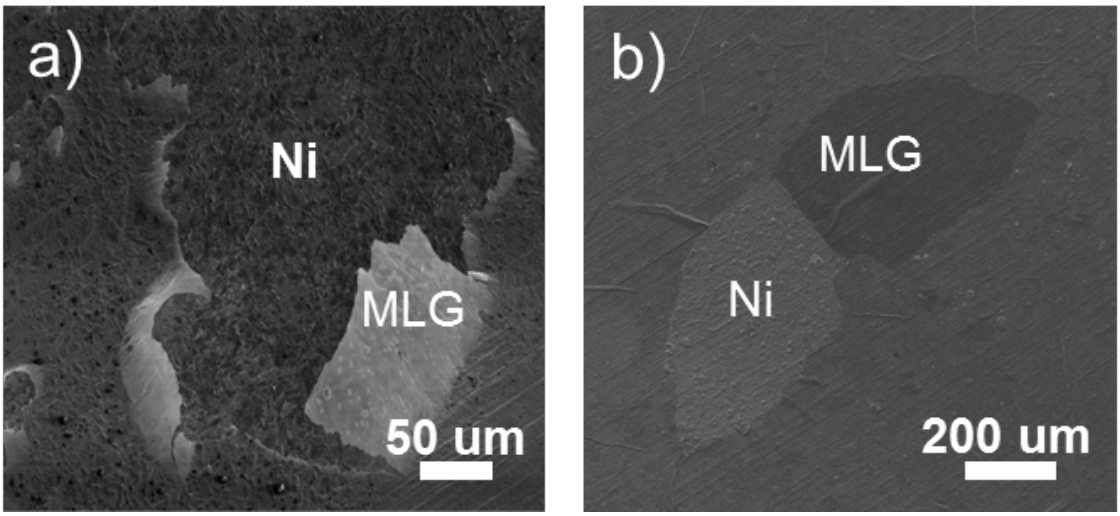

Figure 7.8 SEM images of MLG coated Ni sample after (a) PPC measurements and (b) a constant negative potential of -0.6 V (vs. Ag/AgCl) is applied for 30 minutes.

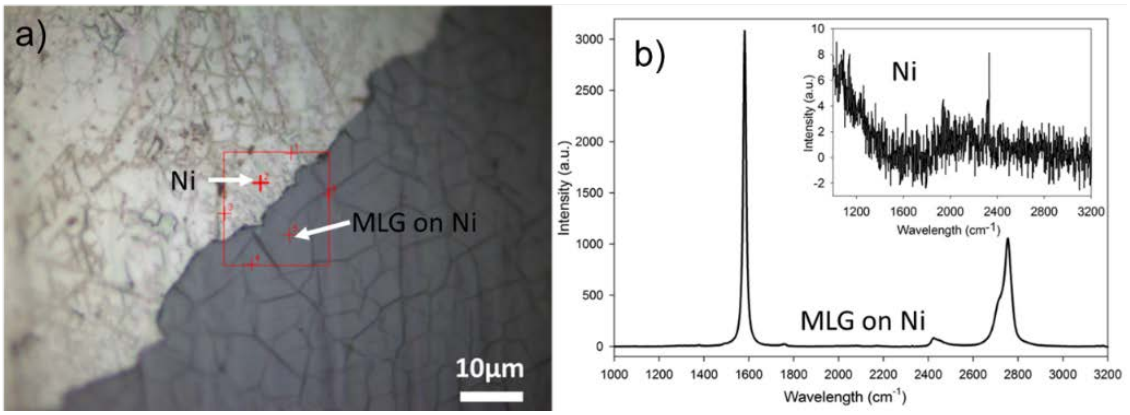

Figure 7.9 (a) Optical image of partially delaminated MLG on Ni and (b) Raman spectra of the area covered with MLG and (inset) without MLG after applying a constant negative potential in 0.5 M HCl for 30 minutes.

Besides the hydrogen bubble formation when either a scanning or constant potential is applied on MLG/Ni sample, it is also found that the bubbles are generated at the interface spontaneously without applying any potential. As shown in Figure 7.10, when a droplet of 0.5 M HCl is placed on the surface of MLG/Ni sample, few blisters (10 to 20 µm in diameter) are found under optical microscope after 5 minutes. These small blisters grow up in size over time and merge to form large blisters of up of few hundreds of microns

after 2 hours. This continuous formation, growth and merging of blisters, due to spontaneously formation of hydrogen bubbles generated at the interface, eventually lead to complete delamination of MLG from Ni substrate after 18 hours,[222] suggesting the failure of MLG coating on Ni in 0.5 M HCl. When other types of acid (such as H_2SO_4 and HNO_3) are placed on MLG coated Ni instead of HCl, as shown in Figure 7.11, blisters of different size are also found after 4 hours of exposure, suggesting that the hydrogen bubble formation is independent on the type of acid used.

SEM is also used to study the real-time hydrogen bubble formation but with higher spatial resolution than optical microscope. In this experiment, a droplet of 0.5 M HCl is placed on top of the MLG coated Ni sample and then dried with a tissue before the SEM observation. For initial observation on the area of MLG coated Ni previously wetted by acid, no change of the MLG coating is visible from SEM as seen from Figure 7.12a. However, when the electron beam is zoomed in and irradiated only on a local part of the area seen in Figure 7.12a, a blister-like protrusion around few tens of microns in diameter is observed, as presented in Figure 6.11b. During imaging of this area, more blisters are formed (Figure 7.12c). At lower magnifications (Figure 7.12d), it is observed that these blisters are only found in the area that was previously irradiated with the electron beam. We explained this process by saying that the electron beam can accelerate the diffusion of acid residues through defects in MLG through local heating and provide energy for the formation of hydrogen at the coating substrate interface. It is important to note that the fact that hydrogen bubbles are trapped at the interface in the vacuum environment of the SEM chamber indicates the superior gas-tight properties of the high-quality MLG coating.

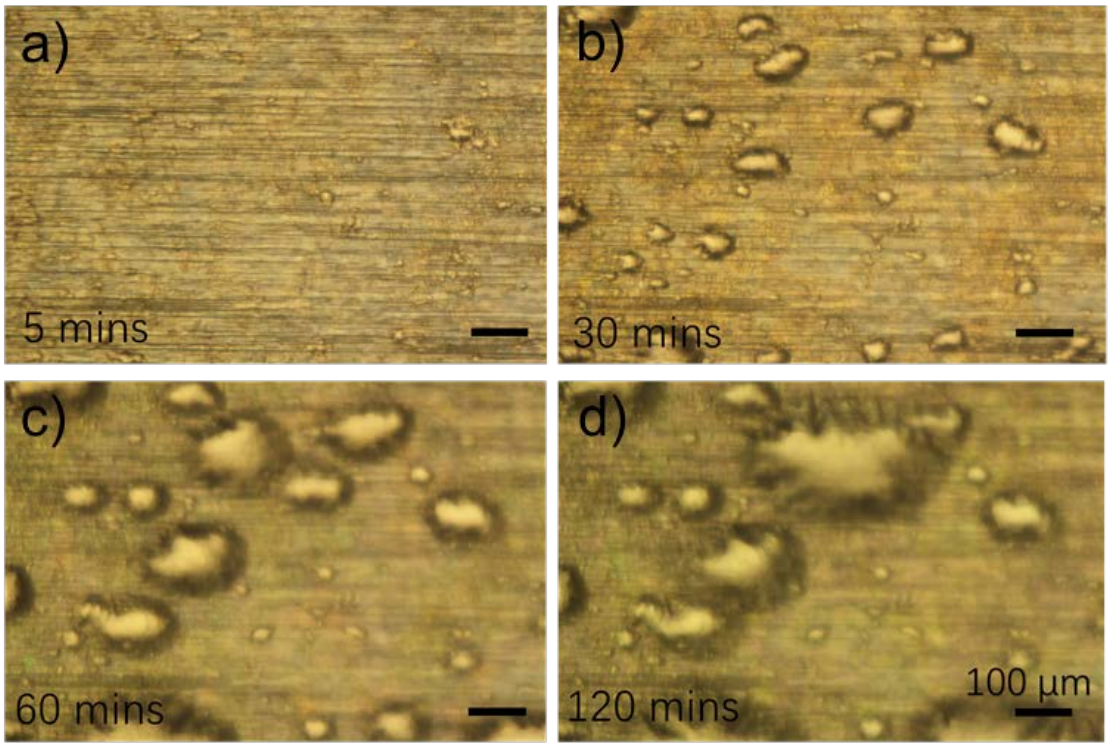

Figure 7.10 Optical images of MLG coated Ni sample after a droplet of 0.5 M HCl is placed on the surface for (a) 5, (b) 30, (c) 60 and (d) 120 minutes.

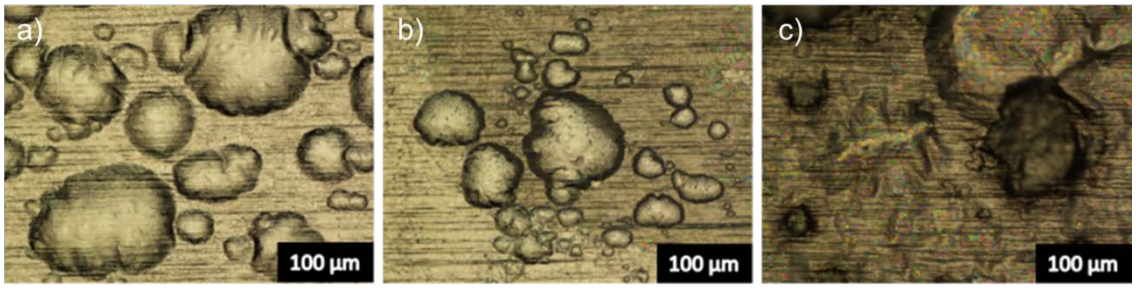

Figure 7.11 Optical images of MLG coated Ni sample after a droplet of 0.5 M (a) HCl, (b) H_2SO_4 and (c) HNO_3 is placed on the surface for 240 minutes.

To explain the reason of hydrogen formation at MLG-Ni interface, which eventually leads to delamination and failure of the MLG coating in acids, a mechanism is proposed as illustrated in Figure 7.13. When the MLG-Ni sample is exposed to acids, protons are carried by water and can shuttle from the bulk solution through the defective areas in MLG film (e.g. grain boundaries and wrinkles) to the surface of Ni substrate via the Grotthuss mechanism.[70,163] Spontaneous reaction of hydrogen evolution is then initiated in such a low pH environment (0.3 for 0.5 M HCl) at the Ni surface.[224] The gas-tight property of the MLG coatings prevents as-formed hydrogen bubbles from escaping the coating. These

continuously generated hydrogen bubbles eventually lead to delamination of the MLG coating from Ni substrate or mechanical damage to the MLG film. In this scenario, the hydrogen bubbles probably do not deflate because the few defective areas within the graphene film are clogged by the acidic media.

Although these results showed the failure of high-quality MLG coating when used for the protection of Ni substrate in acids, it also implies that the coating may be subject to such similar failure when impermeable materials like graphene is used for anticorrosive coatings to protect electroactive metals in corrosive environment, where hydrogen evolution is the dominant cathodic process (e.g. Mg in water and Fe in acids).

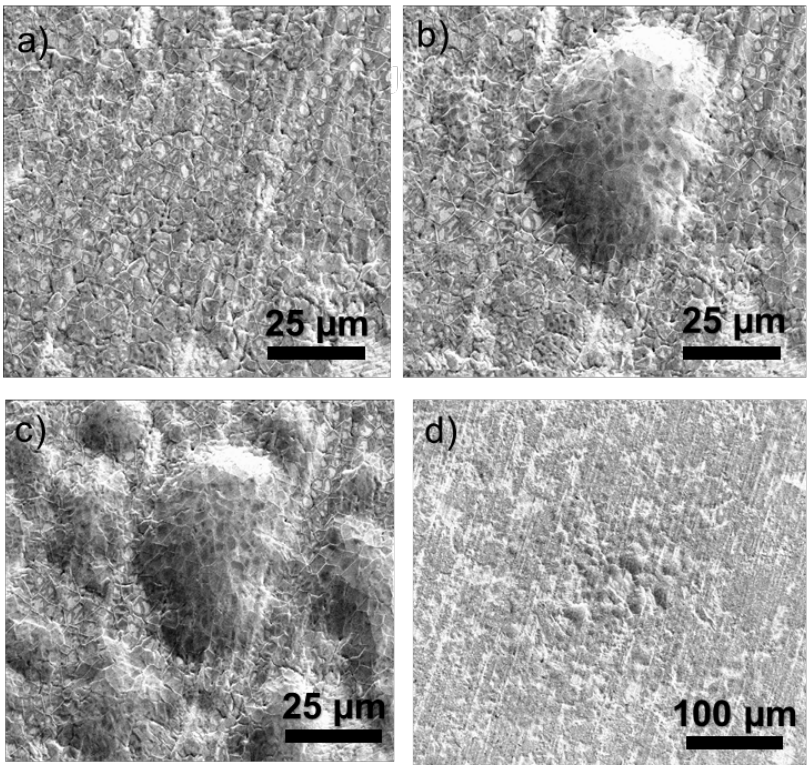

Figure 7.12 SEM images of (a) initial observation of MLG coated Ni sample after wetted by a droplet of 0.5 M HCl, (b) single-blister and (c) multiple-blister formed at MLG-Ni interface and (d) local blister formed at electron beam irradiated area.

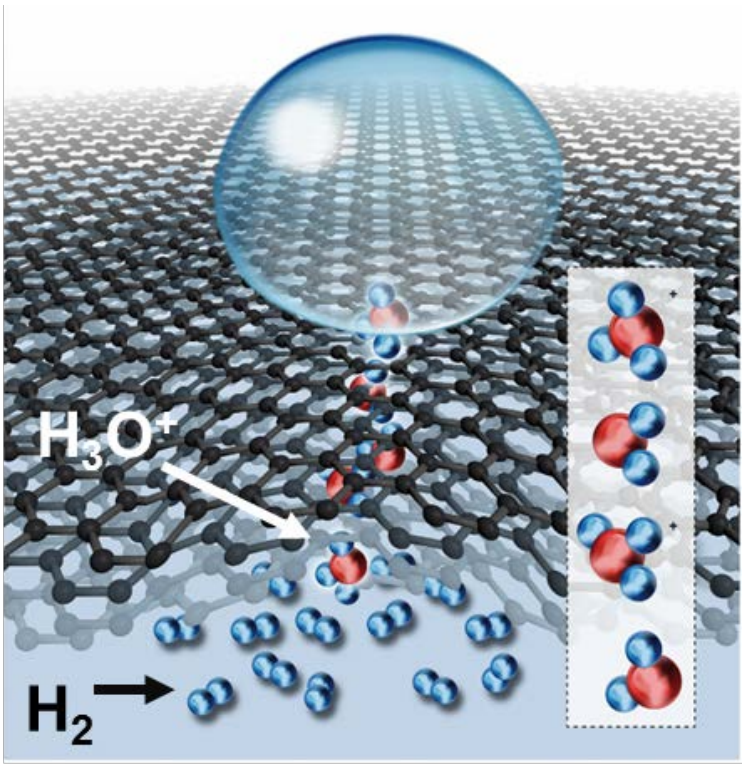

Figure 7.13 Schematic illustration on the proposed mechanism for hydrogen bubbles formation at MLG-Ni interface in acids with oxygen and hydrogen atoms shown as red and blue spheres, respectively.

Chapter 8. Polymer-graphene hybrid coatings for corrosion protection

8.1. Background

Besides the use of large-scale continuous CVD graphene sheet for anticorrosive coatings, the application of graphene-based nanoplatelets (GNPs) (e.g. graphene oxide (GO) or reduced graphene oxide (rGO)), which are dispersed in a coating matrix to enhance the barrier properties, are widely reported.[13,14,225,226] Aneja et al[14] reported that high shear liquid-phase exfoliated GNPs, upon functionalization, can be used to prepare a nearly impermeable barrier coating which provides excellent corrosion protection for steel and is promising candidate to replace chromate conversion coatings. Sun et al[13] reported that a polymer-graphene coating, where modified rGO flakes are dispersed in the polymer matrix, can effectively inhibit both the corrosion of Cu substrate and the corrosion promotion activity of graphene due to galvanic coupling. Other reported results also demonstrated effective corrosion protection offered by graphene-polymer composite coatings, due to improved barrier properties to water[17] and oxygen[16] with well dispersed GNPs in the coating matrix.

Although these composite coatings are robust, versatile and easy to scale up for industrial applications with relatively low cost, there are some challenges significantly limiting their corrosion protection performance. The most important challenge is that the stacking of graphene nanoplatelets (GNPs) in the coating matrix is difficult to control, which strongly influences the overall barrier properties of the coating. As illustrated in Figure 8.1a,[227] when GNPs are poorly dispersed in the coating matrix, agglomeration can lead to significant decline of the barrier properties of the coating.[19] On the other hand, in case of well-dispersed and horizontally stacked GNPs, the diffusion pathway of molecules through the coating matrix is prolonged and the barrier properties of the coatings in improved, as illustrated in Figure 8.1b.[227] In addition to the influence of GNPs stacking on the barrier properties of anticorrosive coatings, it is also reported that graphene added in the coating matrix can introduce pinholes and weaken the adhesion between the coating and substrate with inappropriate loading of GNPs.[13]

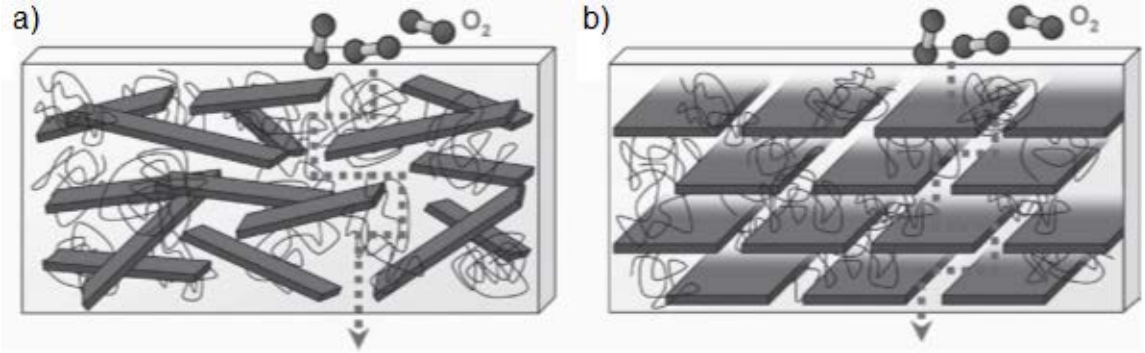

Figure 8.1 Schematic illustration of diffusion pathway for oxygen molecule through polymer-graphene composite films when graphene nanoplatelets are (a) randomly dispersed with agglomeration and (b) well-dispersed with horizontally stacked structure.[227]

Although the use of CVD graphene films as anticorrosive coatings also involves intrinsic limitations, such as galvanic corrosion, weak adhesion and limiting substrates, as discussed in Chapter 5, the stacking of CVD graphene layers is much easier to control than GNPs with graphene transfer techniques (see Section 4.3). In this case, a polymer-CVD graphene hybrid coating is proposed, and this structure could be considered as the limit case of GNP-polymer hybrids, where the quality of GNPs is significantly improved as well as their lateral size. Moreover, the polymer used in the hybrid coatings can (i) contribute to electrically insulating the graphene from metal substrate to reduce or avoid galvanic corrosion, (ii) provide adequate adhesion for the coating on metal substrates and (iii) make it easier to transfer CVD graphene on various metal substrates to be used for corrosion protection. Based on these facts, our results on the corrosion protection performance of polymer-graphene hybrid will be discussed in this chapter and more details on this part are included in Appendix C.[228]

8.2. Fabrication of polymer-graphene hybrid anticorrosive coatings

To prepare the polymer-graphene hybrid coating, three main steps are involved including graphene growth, transfer and coating fabrication, as illustrated in Figure 8.2. Single layer graphene is firstly grown on Cu with the AS-ONE CVD system. A polymer of polyvinyl butyral (PVB) is then spin coated on the surface of graphene. Both the graphene growth and transfer process are following the details described in Section 6.1. After Cu substrate is chemically etched, a PVB supported graphene (P-G) hybrid film is obtained.

The metal substrate coated with the polymer-graphene hybrid coating is aluminum alloy 2024 (AA), which is widely used in aerospace applications and quite susceptible to corrosion.[229] As presented in Figure 8.2, when the obtained PVB-graphene hybrid film is directly transferred onto the surface of AA, both structure of AA/graphene/PVB (AA-G-P) and AA/PVB/graphene (AA-P-G) are fabricated. The P-G hybrid film is also transferred onto the surface of a PVB coated AA to obtain a sandwich structure of AA/PVB/graphene/PVB (AA-P-G-P) and AA/PVB/graphene/PVB/graphene/PVB (AA-P-G-P-G-P) when two layers of P-G hybrid film are transferred. After each transfer process, the sample is thermal annealed at 100 °C for 5-10 minutes to fuse together the different layers. Moreover, both two and three layers of PVB are coated on the surface of AA for reference and are denoted as AA-P-P and AA-P-P-P, respectively. The thickness of the PVB layer is 4 to 5 µm for both directly spin coated on AA and transferred from Cu substrate, as shown from cross-section SEM micrographs provided in Figure 8.3. When SLG is transferred onto a SiO_2 substrate, micro size pinholes are observed (Figure 8.4), which may be due to either the transfer or CVD growth process. Raman spectroscopy is used to study the quality of graphene and results are shown in Figure 8.5 and Figure 8.6. The as-grown graphene on Cu substrate present extremely low level of defects as the D-peak is not detectable within our measurements. The graphene sheet becomes defective after transferred to SiO_2 most likely due to the damage during the transfer process. However, the graphene layer supported by PVB in the P-G hybrid film still shows ~99% coverage and 8% area being defective.

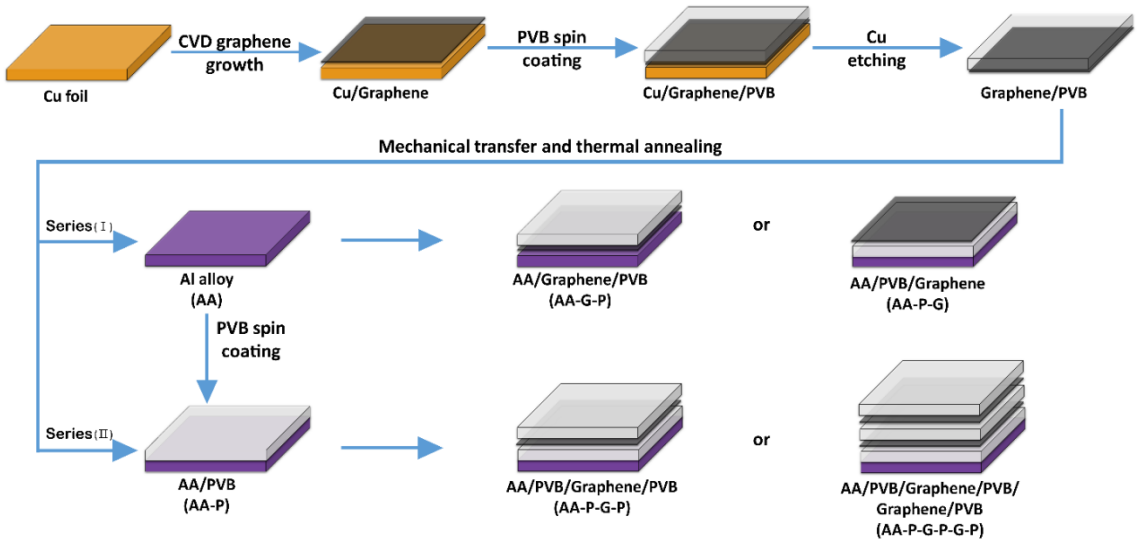

Figure 8.2 Schematic illustration of the fabrication process of polymer-graphene hybrid coatings on AA2024 alloy. [228]

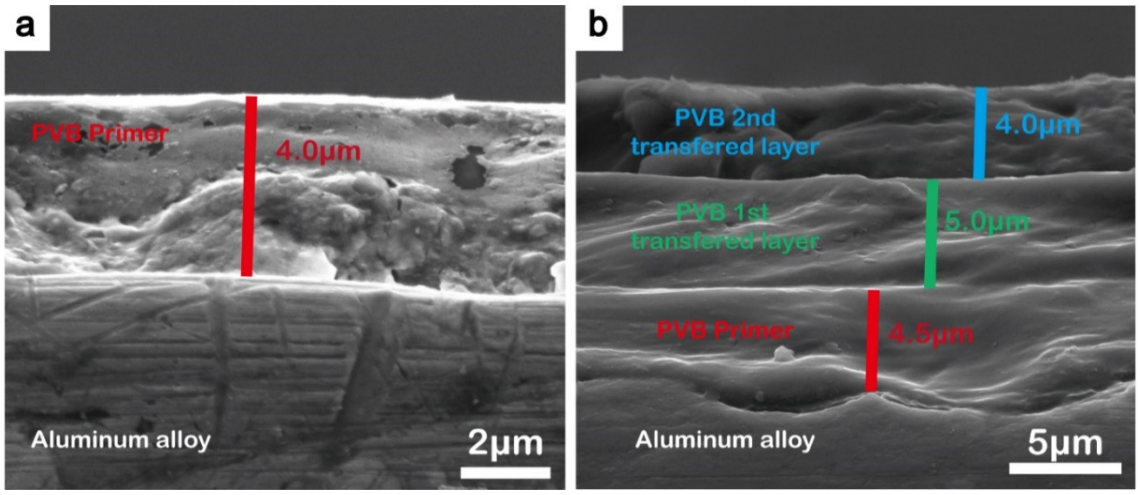

Figure 8.3 SEM images of (a) one and (b) three layers of PVB coated on AA2024 alloy. [228]

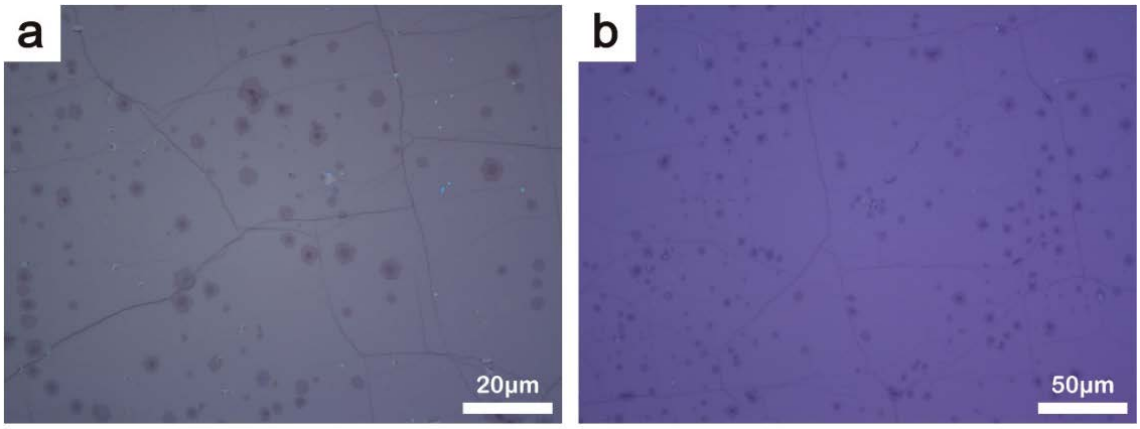

Figure 8.4 Optical images of single layer graphene transferred onto SiO_2 substrate at (a) high and (b) low magnification. Note that dark areas represent seeds of second or third graphene layers. [228]

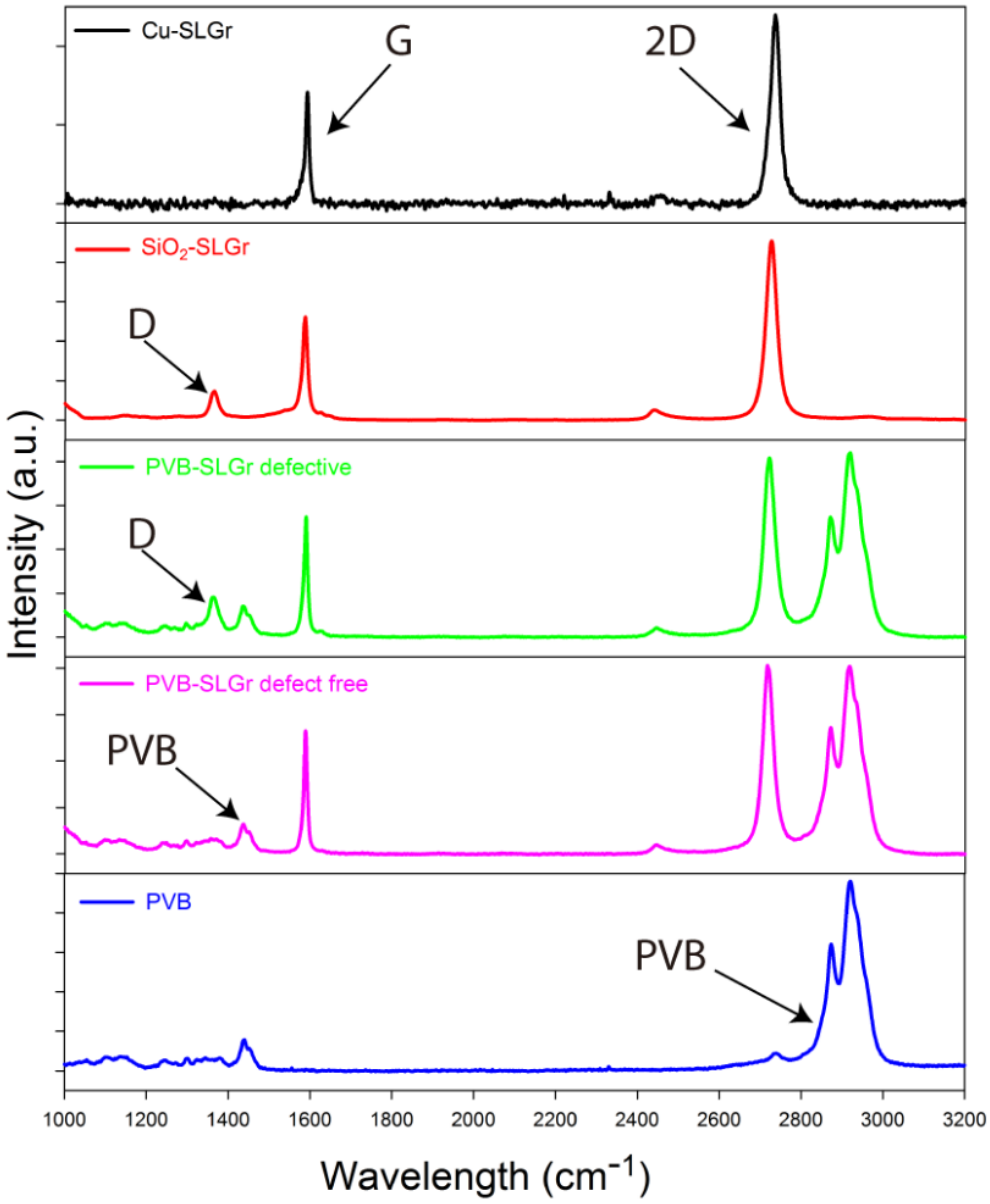

Figure 8.5 Raman spectra of SLG on Cu (black), SiO_2 (red), PVB (green and pink) and bare PVB (blue). [228]

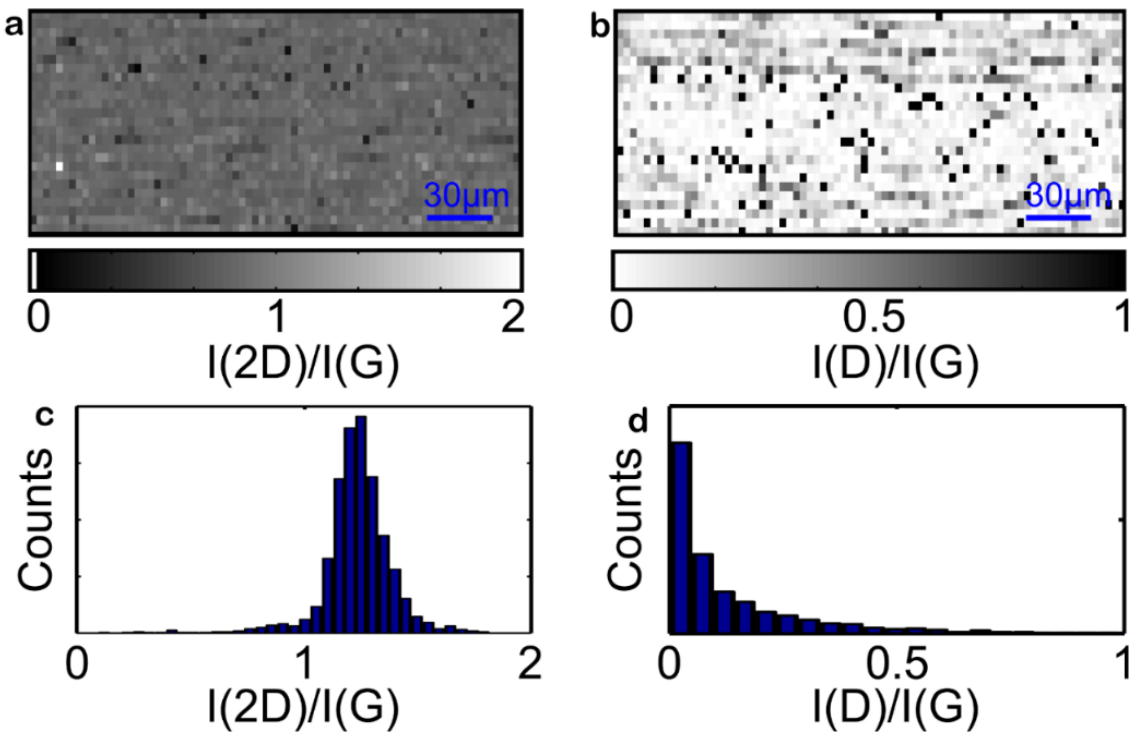

Figure 8.6 Raman spectroscopic maps of the (a) I(2D)/I(G) and (b) I(D)/I(G) peak ratios of PVB supported SLG. Statistical distribution of (c) I(2D)/I(G) and (d) I(D)/I(G) peak ratios. [228]

8.3. Electrochemical corrosion performance

To investigate the corrosion protection performance of polymer-graphene hybrid coatings, both electrochemical impedance spectroscopy (EIS) and potentiodynamic polarization curves (PPC) measurements are used. EIS results were obtained by applying ±10 mV sinusoidal perturbation (respect to the measured open circuit potential (OCP)) on the sample during a frequency range of 100,000 Hz to 0.01 Hz with 10 points per decade. PPC tests were carried out by scanning the potential from -500 mV to 500 mV or -300 mV to 300 mV (vs. OCP or Ag/AgCl reference electrode) with a scan rate of 1mV/s.

Figure 8.7 presents representative EIS spectra with both Bode plot and phase angle for bare metal substrate (AA), polymer-graphene hybrid coatings (AA-P-G, AA-G-P, AA-P-G-P and AA-P-G-P-G-P) and polymer reference coatings (AA-P-P and AA-P-P-P) at different days of immersion in 3.5% NaCl solution. Generally, higher values of impedance at low frequencies (e.g. $|Z|_{0.01Hz}$) indicate better corrosion protection performance of the coating and slow decrease of $|Z|_{0.01Hz}$ over immersion time suggests its high resistance to

degradation.[230] At 1 day of immersion, it is observed that both AA and AA-G-P exhibit low values of $|Z|_{0.01Hz}$ (~2×10^4 Ω·cm^2), suggesting that AA-G-P leads to little improvement on the corrosion resistance of AA. This is attributed to graphene being in direct contact with AA, which introduces galvanic corrosion. In contrast, a two-order improvement in $Z|_{0.01Hz}$ is observed for AA-P-G (~2×10^6 Ω·cm^2) with respect to that of bare AA. This can be explained by the double advantage introduced by the PVB layer, which not only electrically isolates SLG from AA substrate, but also provides adhesion of the coating to the substrate. Furthermore, when an additional layer of PVB is placed on top of AA-P-G, the magnitude of $|Z|_{0.01Hz}$ is further increased to 1×10^7 Ω·cm^2 for AA-P-G-P. It is worth mentioning that, although the coating thickness is doubled from AA-P-G to AA-P-G-P sample, the improvement on the impedance module is not due to the coating thickness, since the AA-P-P reference sample showed an impedance value (8×10^5 Ω·cm^2) lower than that of AA-P-G. This fact also strongly suggests the superior barrier property of a 0.3 nm thick SLG layer than a 5 µm thick PVB layer. When two P-G layers are transferred, nearly five orders of improvement are observed for sample AA-P-G-P-G-P (1×10^9 Ω·cm^2) over that of bare AA, two orders over that of AA-P-G-P sample and one order over that of the graphene-free reference sample, AA-P-P-P. These results clearly indicate that the CVD graphene in the polymer matrix can significantly enhance the barrier properties of the hybrid coating. Moreover, an additional time constant (as seen from the peak in the medium frequency range) is observed for both AA-P-G and AA-P-G-P sample from the phase diagram. This time constant may be attributed to the presence of polymer-graphene interface. This time constant is not shown for AA-P-G-P-G-P sample, which contains two graphene layers, maybe due to the fact that this sample is significantly more resistive than both AA-P-G and AA-P-G-P samples, and therefore the additional time constant is not resolved.

Both AA-P-G-P and AA-P-G-P-G-P samples along with reference sample of AA-P-P-P and bare AA are tested after 30 days of immersion. The magnitude of impedance of AA-P-G-P-G-P maintains above 1×10^9 Ω·cm^2, while the impedance value drops to 7% for AA-P-G-P (from 1.4×10^7 Ω·cm^2 to 9.2×10^5 Ω·cm^2) and 3% for AA-P-P-P (from 8.3×10^7 Ω·cm^2 to 2.4×10^6 Ω·cm^2) from 1 day to 30 days of immersion. These observations are clear signs of the heavy degradation of both AA-P-P-P and AA-P-G-P sample and, on the other hand, the high resistance to degradation of AA-P-G-P-G-P sample at medium-term immersion. Moreover, the impedance value for AA-P-G-P-G-P sample remains around 10^9 Ω·cm^2 after 120 days of immersion, indicating its excellent barrier properties over long-term (Figure 8.7).

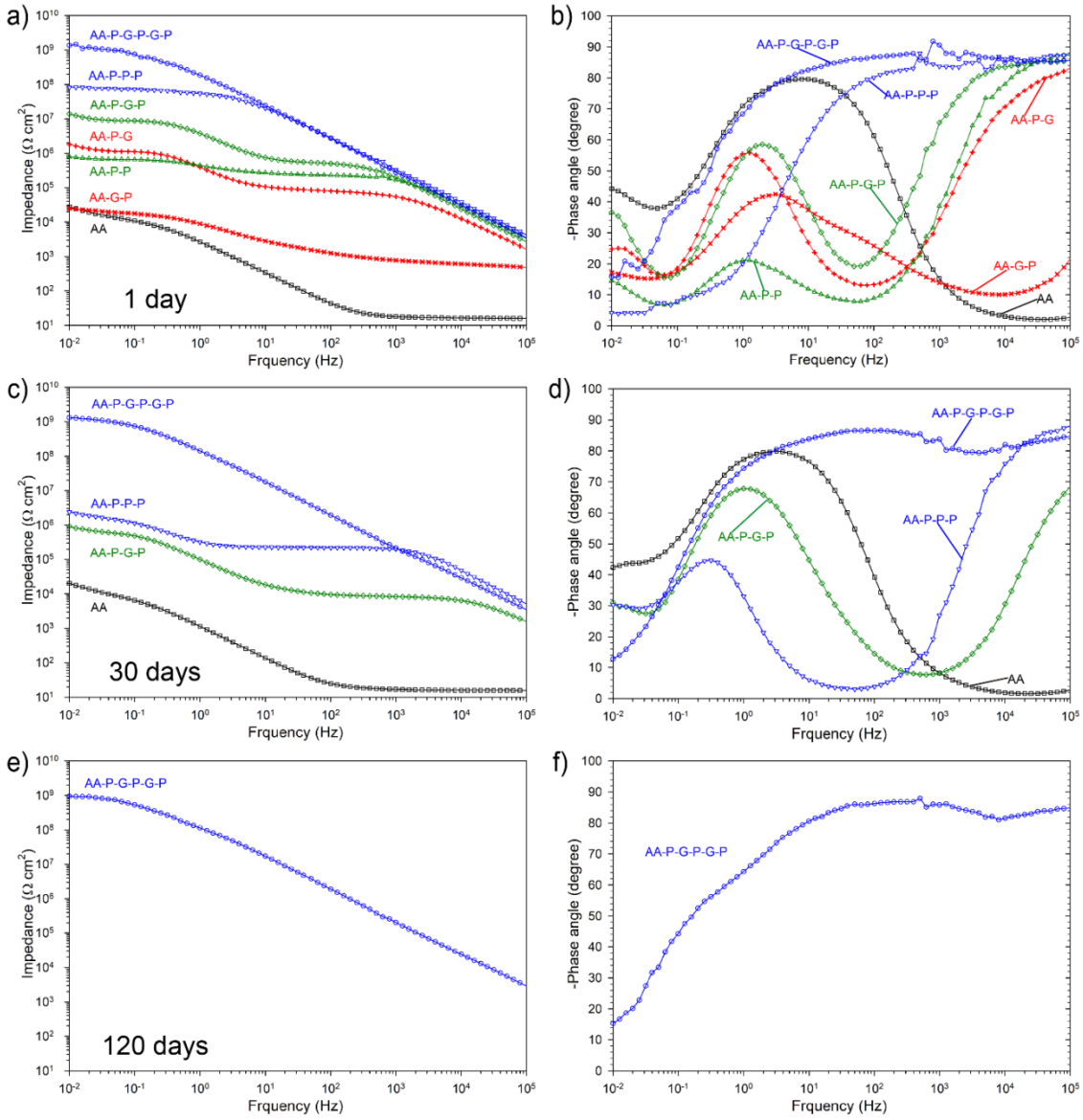

Figure 8.7 (a,c,e) Bode plots and (b,d,f) phase diagram for polymer-graphene hybrid coatings (AA-P-G, AA-G-P, AA-P-G-P and AA-P-G-P-G-P), polymer reference coatings (AA-P-P and AA-P-P-P) and bare AA after (a,b) 1 day, (c,d) 30 days and (e,f) 120 days of immersion in 3.5% NaCl solution. [228]

Table 8.1 lists the values of both OCP and $|Z|_{0.01Hz}$ for three individual samples of each type at different time of immersion. It is important to note that an additional sample, specifically AA-P-P-G-G-P, is also studied, which shares the same number of graphene and polymer layers as that of AA-P-G-P-G-P. It can be seen that the values of OCP and $|Z|_{0.01Hz}$ for AA-P-P-G-G-P and AA-P-G-P-G-P samples differ only slightly between each other and are consistently significantly higher than other samples at all time of immersion.

This clearly proves the excellent barrier performance at long-term of the hybrid coatings with two graphene layers, regardless of the coating structure (i.e., the order in which the graphene and polymer layers are alternated). Moreover, EIS results of all tested samples are very reproducible and the values for 3 individual samples of each kind are comparable. Therefore, the conclusions drawn from Figure 8.7 are convincing.

Sample	Open circuit potential OCP (mV vs Ag/AgCl)				Low frequency impedance $\|Z\|_{0.01Hz}$ (MOhms cm^2)			
	1	2	3	average	1	2	3	average
AA 1d	-623	-706	-697	-675	0.03	0.03	0.03	0.03
AA 30d	-732	-722	-738	-731	0.02	0.02	0.02	0.02
AA-G-P 1d	-817	-825	-810	-817	0.02	0.02	0.03	0.02
AA-P-G 1d	-591	-672	-693	-652	1.82	1.67	1.75	1.75
AA-P-P 1d	-820	-780	-797	-799	0.74	0.85	0.80	0.80
AA-P-G-P 1d	-635	-621	-657	-638	13.8	14.5	12.3	13.5
AA-P-G-P 30d	-751	-797	-732	-760	0.92	0.29	1.08	0.76
AA-P-P-P 1d	-750	-486	-501	-579	39	40	83	54
AA-P-P-P 30d	-787	-758	-747	-764	1.5	2.3	3.9	2.6
AA-P-G-P-G-P 1d	870	694	618	727	1364	1505	1077	1315
AA-P-G-P-G-P 30d	731	660	771	721	1319	1318	1408	1348
AA-P-G-P-G-P 120d	587	727	676	663	952	1709	1240	1300
AA-P-P-G-G-P 1d	746	487	686	640	2551	1830	2998	2460
AA-P-P-G-G-P 30d	230	448	405	361	1720	1408	1521	1550
AA-P-P-G-G-P 120d	401	204	337	314	1928	888	1073	1296

Table 8.1 Values of OCP and $|Z|_{0.01Hz}$ for all test samples at different days of immersion in 3.5% NaCl solution. [228]

Figure 8.8 displays representative PPC measurements of bare AA after 1 day, AA-P-P-P after 1 day and 30 days, and AA-P-G-P-G-P after 1 day, 30 days and 120 days of immersion in 3.5% NaCl solution. According to the calculated corrosion rate, bare AA shows the highest value of 4 µm/year and AA-P-G-P-G-P sample presents lowest corrosion rate below 2 nm/year, which is 10 times lower than its graphene-free reference sample of AA-P-P-P (20 nm/year) after 1 day of immersion. However, the corrosion rate for AA-P-P-P is increased by 15 times to 0.3 µm/year from 1 day to 30 days of immersion, while graphene enhanced hybrid coating of AA-P-G-P-G-P showed consistently low corrosion rate below 2 nm/year up to 120 days of immersion.

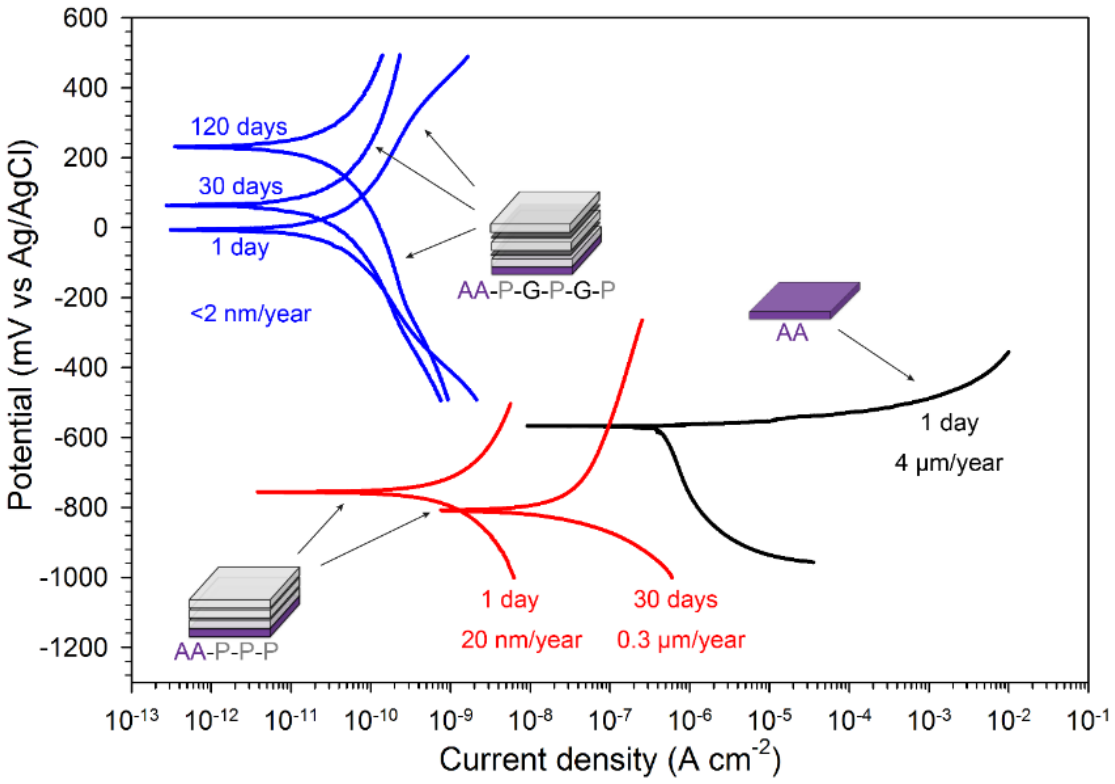

Figure 8.8 Representative potentiodynamic polarization curves of bare AA (black), AA-P-P-P (red) and AA-P-G-P-G-P (blue) after different days of immersion in 3.5% NaCl solution. [228]

Sample	Corrosion potential E_{corr} (mV vs Ag/AgCl)				Corrosion current density i_{corr} (nA cm^{-2})				Corrosion rate CR (µm/year)
	1	2	3	average	1	2	3	average	average
AA 1d	-567	-567	-576	-570	425	390	319	378	4
AA 30d	-1100	-1100	-1110	-1103	17700	19800	18200	18567	203
AA-G-P 1d	-936	-889	-953	-926	651	1020	837	836	9
AA-P-G 1d	-723	-762	-674	-720	38	75	35	49	0.54
AA-P-P 1d	-802	-799	-821	-807	52	195	206	151	1.6
AA-P-G-P 1d	-619	-564	-627	-603	0.39	0.53	0.34	0.42	0.005
AA-P-G-P 30d	-894	-912	-800	-869	124	182	12	106	1.2
AA-P-P-P 1d	-755	-736	-551	-680	1.3	1.9	3.2	2.1	0.02
AA-P-P-P 30d	-823	-808	-798	-810	15	43	22	27	0.29
AA-P-G-P-G-P 1d	-9	-219	-59	-96	0.08	0.27	0.09	0.15	0.0016
AA-P-G-P-G-P 30d	18	-158	-12	-51	0.13	0.04	0.28	0.15	0.0016
AA-P-G-P-G-P 120d	412	120	191	241	0.29	0.02	0.12	0.14	0.0016
AA-P-P-G-G-P 1d	-47	-115	32	-43	0.23	0.22	0.11	0.19	0.0020
AA-P-P-G-G-P 30d	-55	-36	26	-22	0.29	0.16	0.22	0.22	0.0024
AA-P-P-G-G-P 120d	371	234	461	355	0.01	0.15	0.32	0.16	0.0017

Table 8.2 Values of corrosion potential (E_{corr}), corrosion current density (i_{corr}) and corrosion rate (CR) for all test samples at different days of immersion in 3.5% NaCl solution. [228]

PPC measurements are performed on at least three individual samples for all the tested structures. Corrosion potential and corrosion rate data extracted from PPC results are listed in Table 8.2. It can be seen that the corrosion rate of AA-G-P (9 µm/year) is more than 2 times higher than that of bare AA (4 µm/year) after 1 day of immersion, indicating enhanced corrosion due to galvanic coupling between graphene and AA substrate. While the corrosion rate for AA-P-G-P increased by 3 orders of magnitude from 0.005 µm/year at 1 day to 1.2 µm/year at 30 days of immersion, the hybrid coatings with two graphene layers (both AA-P-G-P-G-P and AA-P-P-G-G-P) consistently show low corrosion rate at around 0.002 µm/year. This fact once again highlights the superior barrier properties of hybrid coating with two graphene layers over that with one graphene layer.

In Figure 8.9, electrochemical results for various samples tested are summarized, regarding to values of OCP, corrosion current density and impedance. Firstly, the samples can be clustered into three groups based on their data. In group 1, the data for all samples are in the area where the magnitude of $|Z|_{0.01Hz}$ are small (10^5 to 10^8 $\Omega \cdot cm^2$), corrosion current density are high (10^{-4} to 10^{-6} $A \cdot cm^{-2}$) and OCP are in a range between -600 to -800 mV. Both AA and AA-G-P samples are in this group characterized by poor corrosion performance with direct corrosion attack at AA surface for bare AA sample and enhanced corrosion for AA-G-P sample due to galvanic corrosion. Compared with group 1, the samples in group 2 are characterized with higher values of $|Z|_{0.01Hz}$ (10^5 to 10^8 $\Omega \cdot cm^2$) and lower corrosion current density (10^{-6} to 10^{-9} $A \cdot cm^{-2}$), suggesting a somewhat improved corrosion performance. However, the OCP values in the group 2 are still in the same range as those in group 1, which suggests that the electrolyte has reached the surface of AA despite the presence of the coating. Group 2 consists of 4 samples including AA-P-G, AA-P-G-P, AA-P-P and AA-P-P-P. Al these samples share the presence of the polymer primer, which seems to be an important factor to improve the corrosion performance over that of the samples in group 1.

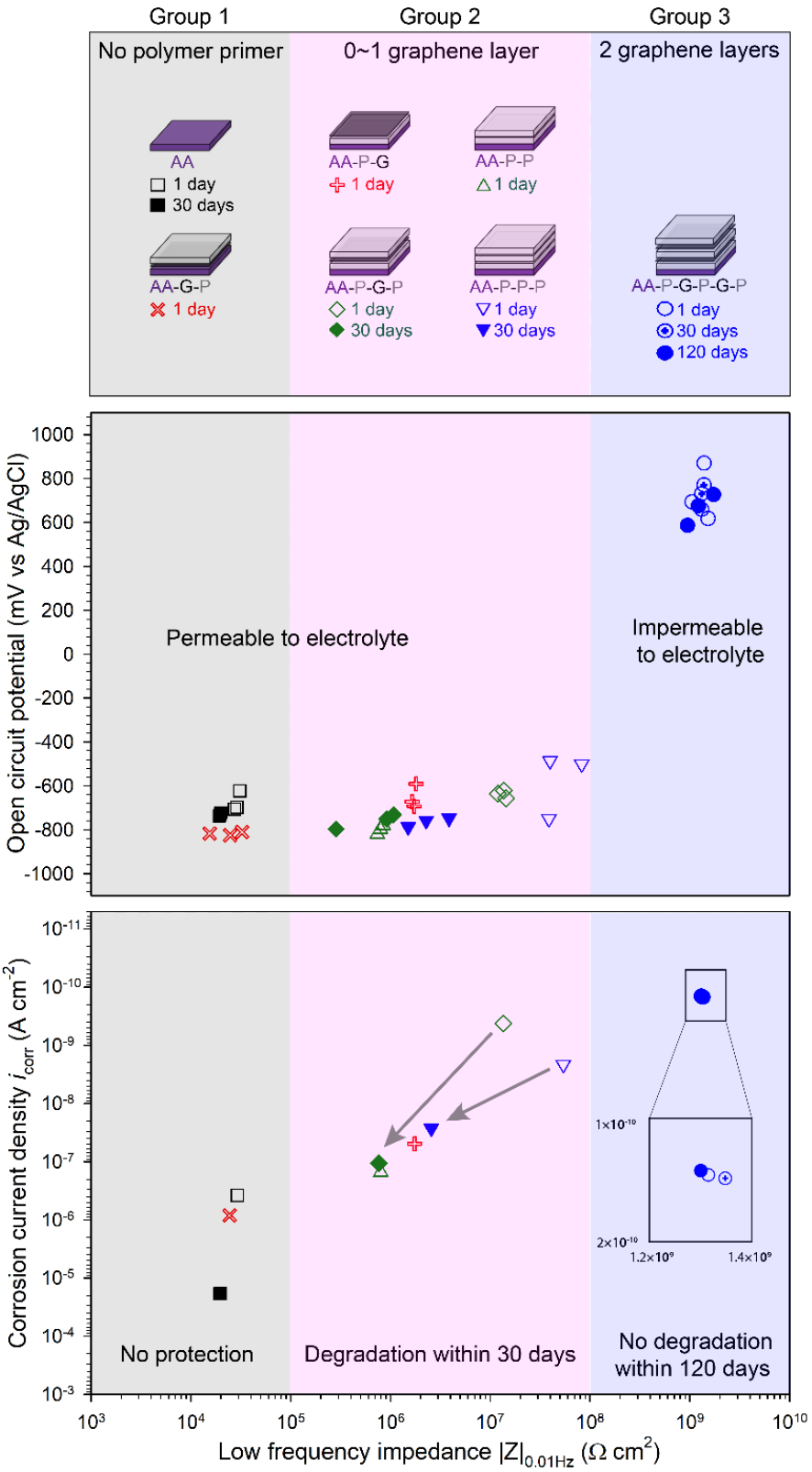

Figure 8.9 Summary of electrochemical testing results for all tested samples. [228]

Nevertheless, both sample of AA-P-G-P and AA-P-P-P are significantly degraded after 30 days of immersion, as seen from the increase of corrosion current density and decrease of impedance. Although these two samples are thick (between 10 and 15 µm) and with good corrosion protection performance at 1 day of immersion, only 1 layer of graphene is present in the coating, therefore significantly limiting its barrier performance at long-term of immersion. In group 3, we find samples that have high values of $|Z|_{0.01Hz}$ ($10^{9}\,\Omega\cdot cm^{2}$), low values of corrosion current densities ($10^{-10}\,A\cdot cm^{-2}$) and OCP between 600 to 800 mV. The two-layer graphene hybrid coatings, including both AA-P-G-P-G-P and AA-P-P-G-G-P (not presented in Figure 8.9, but it is of little difference to AA-P-G-P-G-P for all measurement results). The improvement on OCP of about 1.5 V over the other groups indicates the increased barrier properties, which make the coating impermeable to electrolyte. As the data for all three measurements keep almost unchanged during the 120 days of immersion, the high resistance to environmental degradation for both AA-P-G-P-G-P and AA-P-P-G-G-P are demonstrated.

Moreover, the polymer graphene hybrid coating with one graphene layer (P-G-P) is also applied on brass and steel substrates. Figure 8.10 present the EIS results for P-G-P coating and its graphene-free P-P reference coating covered on both brass and steel substrate after 1 day and 7 days of immersion in 3.5% NaCl solution. From the Bode plots, it can be seen that the P-G-P coating on both substrates exhibit higher values of $|Z|_{0.01Hz}$ than P-P coating at 1 day of immersion. However, after 7 days of immersion, no significant difference is observed between the two coatings when coated on steel substrate, while the value of $|Z|_{0.01Hz}$ for P-G-P coating is one order higher than P-P coating on brass. This result suggests that the polymer-graphene hybrid coating is robust and can provide effective corrosion protection for various metals and alloys.

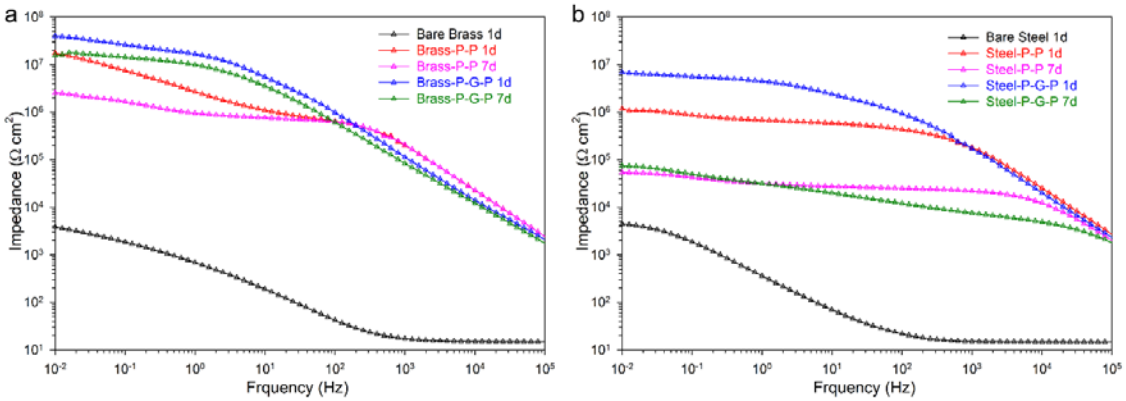

Figure 8.10 Bode plots of (a) brass, P-P coated brass and P-G-P coated brass and (b) steel, P-P coated steel and P-G-P coated steel after 1 day and 7 days of immersion in 3.5% NaCl solution. [228]

8.4. Corrosion morphology

Apart from the electrochemical measurements used to investigate the corrosion performance, optical microscopy and scanning electron microscopy (SEM) are also used to provide more information about the nature of corrosion for all samples. Figure 8.11 presents both the optical and SEM images of fresh uncorroded AA and AA after 1 day and 30 days of immersion in 3.5% NaCl solution. As shown in Figure 8.11d, the surface morphology of uncorroded AA shows many cavities, which are due to the loss of second phase particles during cleaning process on as-received AA (de-smutted in 10wt% NaOH for 1 minute and etched in 50% HNO_3 for 1 minute).[228] After 1 day of immersion in 3.5% NaCl solution, multiple pits are observed as dark points in Figure 8.11b and dissolution of the alloy matrix is seen from the SEM image in Figure 8.11e. At 30 days of immersion, the whole surface of AA exposed to solution is corroded (Figure 8.11c) and the surface is covered with corrosion products as seen from the SEM image in Figure 8.11f.

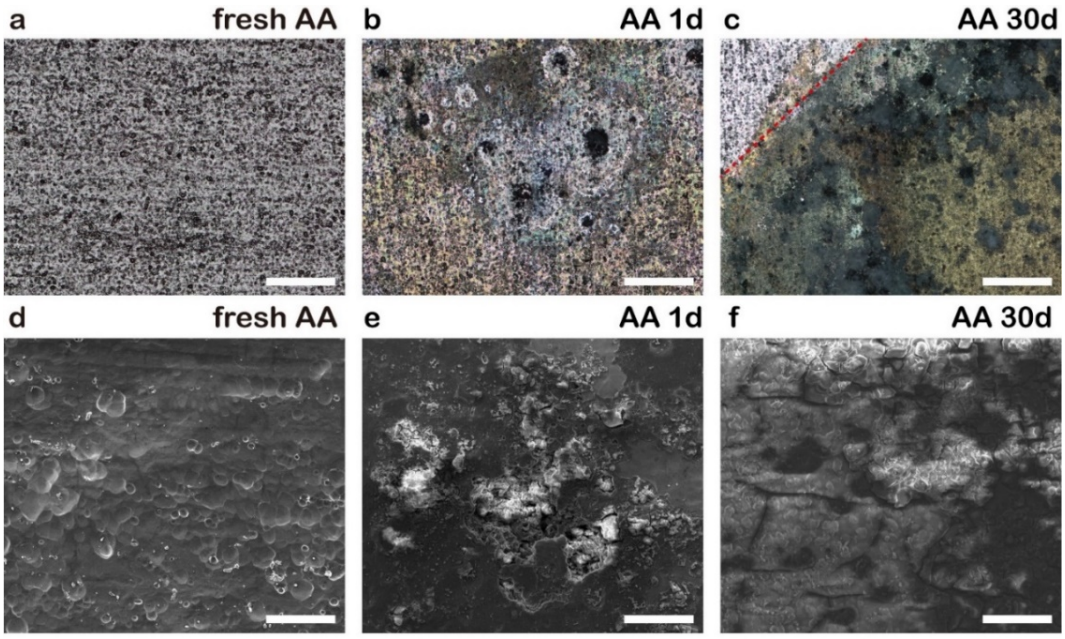

Figure 8.11 (a,b,c) Optical and (d,e,f) SEM images of (a,d) fresh uncorroded AA, (b,e) AA at 1 day and (c,f) 30 days of immersion in 3.5% NaCl solution. Red dashed line in (c) is to sign the edge of the sealing O-ring. Scale bars represents 500 μm in (a,b,c) and 50 μm in (d,e,f). [228]

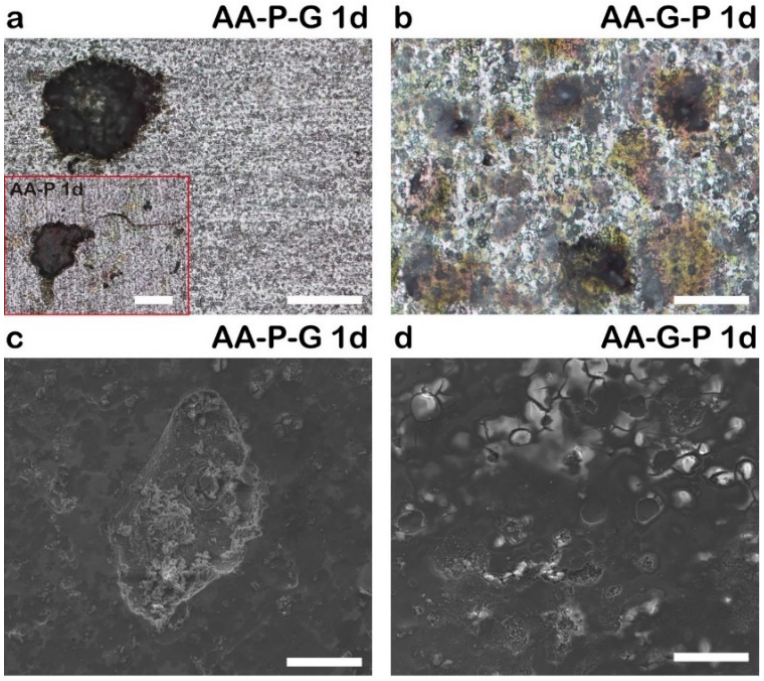

Figure 8.12 (a,b) Optical and (c,d) SEM images of (a,c) AA-P-G, (b,d) AA-G-P at 1 day of immersion in 3.5% NaCl solution. Inset image in (a) shows the optical corrosion morphology of AA-P sample at 1 day of immersion. Scale bars represents 500 μm in (a,b,) and 50 μm in (c,d). [228]

When AA is coated with a polymer-graphene hybrid film, both AA-P-G and AA-G-P samples are corroded after 1 day of immersion, as shown from Figure 8.12. Compared with reference sample of AA-P (inset image in Figure 8.12a), AA-P-G sample showed only a large dark corrosion pit without visible corroded area around. However, when graphene is not present in AA-P sample, many small corrosion pits (in black or brown) are found near a large dark corrosion pit. This may be due to the focused corrosion attack at graphene defective area in AA-P-G sample with the other areas being protected by the impermeable graphene (clearly seen from Figure 8.12c with local dissolution of the AA), while the bare porous polymer coating of AA-P suffered from electrolyte penetration and corrosion attack at all areas. When graphene is in directly contact with AA in AA-G-P sample, from both optical and SEM images, it is clear that AA is more uniformly corroded than bare AA and AA-P samples. This is because the galvanic coupling between the AA and graphene significantly increases the area for cathodic oxygen reduction from some local sites on AA (bare AA and AA-P samples) to the whole surface of AA (AA-G-P sample), which correspondingly enhances the anodic metal oxidation at the whole surface.

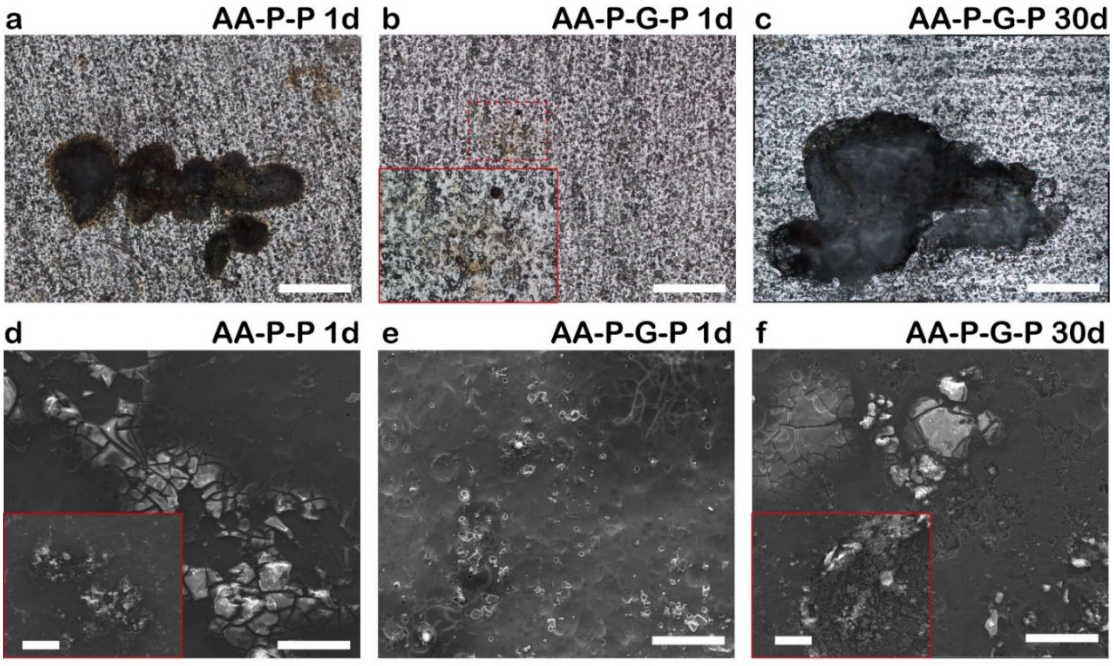

Figure 8.13 (a,b,c) Optical and (d,e,f) SEM images of (a,d) AA-P-P, (b,e) AA-P-G-P at 1 day and (c,f) AA-P-G-P at 30 days of immersion in 3.5% NaCl solution. Red dashed line in (b) is magnified in the inset. Red line highlighted images in (d) and (f) are from other areas on the same sample. Scale bars represents 500 μm in (a,b,c) and 50 μm in (d,e,f).[228]

For bare polymer coating of two polymer layers coated on AA (AA-P-P), heavily localized filiform corrosion is observed (Figure 8.13), due to the porous nature of PVB. On the other hand, when a graphene enhanced coating (P-G-P) is coated on AA, only a small part of the sample is corroded after 1 day of immersion, indicating good barrier properties of the coating at short-term. However, the sample is heavily corroded at long-term immersion of 30 days with large corrosion pits and severe dissolution of AA. This suggests that although the P-G-P coating provides good corrosion protection for AA at short-term, it is however degraded and insufficient to maintain the barrier properties at long-term of immersion. The corrosion protection performance is improved when two layers of P-G film are transferred onto AA-P. As seen from Figure 8.14, both AA-P-G-P-G-P and AA-P-P-G-G-P samples are free from corrosion after 30 days of immersion, while the reference sample of AA-P-P-P suffered from heavy filiform corrosion. Furthermore, the hybrid coatings with two graphene layers remain uncorroded even after 120 days of immersion as seen from both optical and SEM images in Figure 8.15.

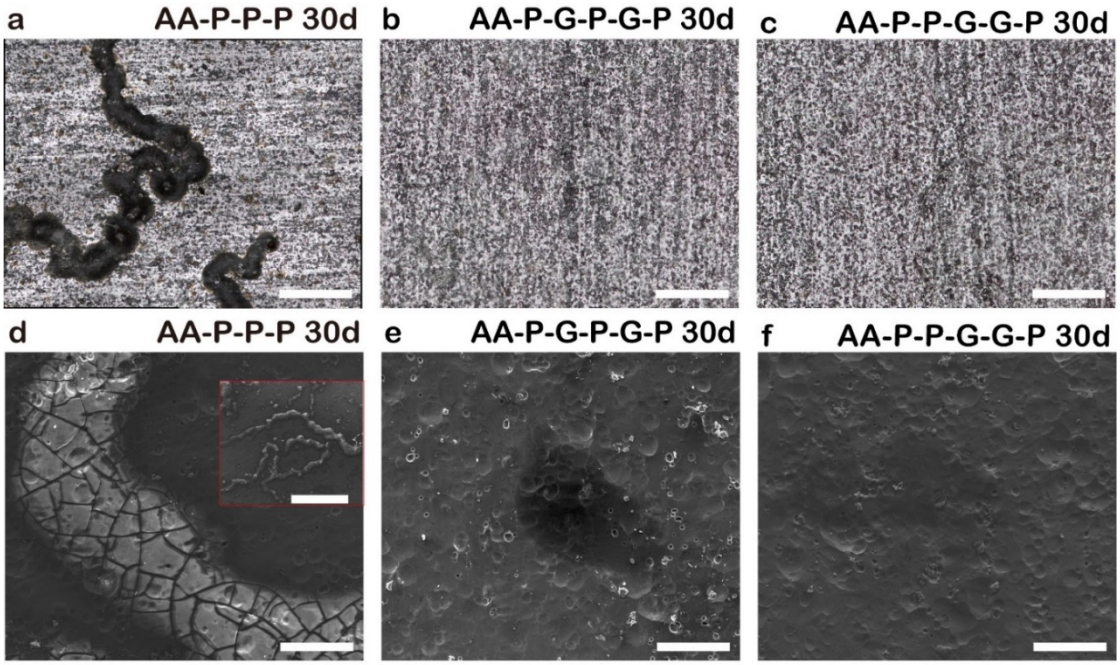

Figure 8.14 (a,b,c) Optical and (d,e,f) SEM images of (a,d) AA-P-P-P, (b,e) AA-P-G-P-G-P and (c,f) AA-P-P-G-G-P at 30 days of immersion in 3.5% NaCl solution. Inset image in (d) highlighted by red line is a low magnification image. Scale bars are 500 μm in (a,b,c) and inset image in (d) and 50 μm in (d,e,f). [228]

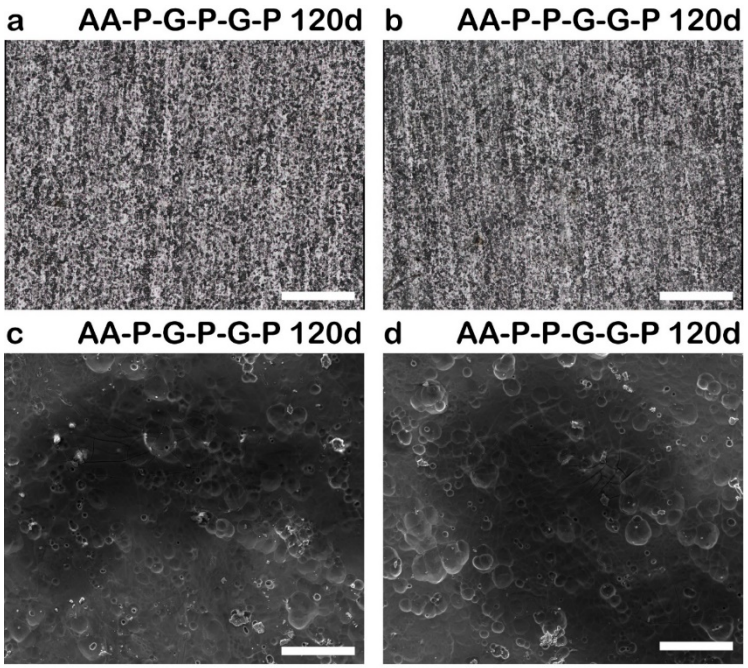

Figure 8.15 (a,b) Optical and (c,d) SEM images of (a,c) AA-P-G-P-G-P and (b,d) AA-P-P-G-G-P at 120 days of immersion in 3.5% NaCl solution. Scale bars are 500 µm in (a,b) and and 50 µm in (c,d). [228]

From the study of corrosion morphology with optical microscopy and scanning electron microscopy, it can be said that the results are in line with the those collected from electrochemical tests. Both these studies thus provide solid evidence for poor corrosion protection performance of bare polymer coatings and significantly improved performance on graphene enhanced coatings.

8.5. Corrosion protection mechanism

To explain the reason why the polymer graphene hybrid coating exhibits improved corrosion protection performance, the barrier structure of the coating is proposed in Figure 8.16 to discuss the corrosion protection mechanism of bare graphene, bare polymer and polymer graphene hybrid coating with one and two graphene layers. When a graphene thin film is directly covered on the surface of a metal substrate (Figure 8.16a), due to the defects in graphene layer, corrosion attack occurs at these defective sites, while other areas are protected by defect-free graphene. For bare polymer coatings (e.g. P-P-P in Figure 8.16b), the electrolyte penetrates from all areas due to the porous nature of polymers. The electrolyte therefore reaches eventually the surface of metal substrate and

initiate corrosion. When one graphene layer is inserted into the polymer matrix (Figure 8.16c), electrolyte penetration in the polymer matrix is significantly limited by the graphene layer, since the electrolyte is now able to pass only through the few graphene defects. Although this structure can provide excellent barrier performance at short-term, the polymer layer between the graphene and metal substrate will eventually be saturated by electrolyte passing slowly through the graphene layer, and this will induce heavy corrosion over time. By applying two graphene layers in the polymer matrix (Figure 8.16d), the barrier properties of the overall coating can be greatly enhanced even at long-term. This is because the electrolyte diffused through the defects in the first graphene layer needs to find the defective sites in the second graphene layer before being able to attack the metal substrate. The defects in these two graphene layers are generally not aligned so that the diffusion pathway for electrolyte is significantly increased than the hybrid coating with only one graphene layer.

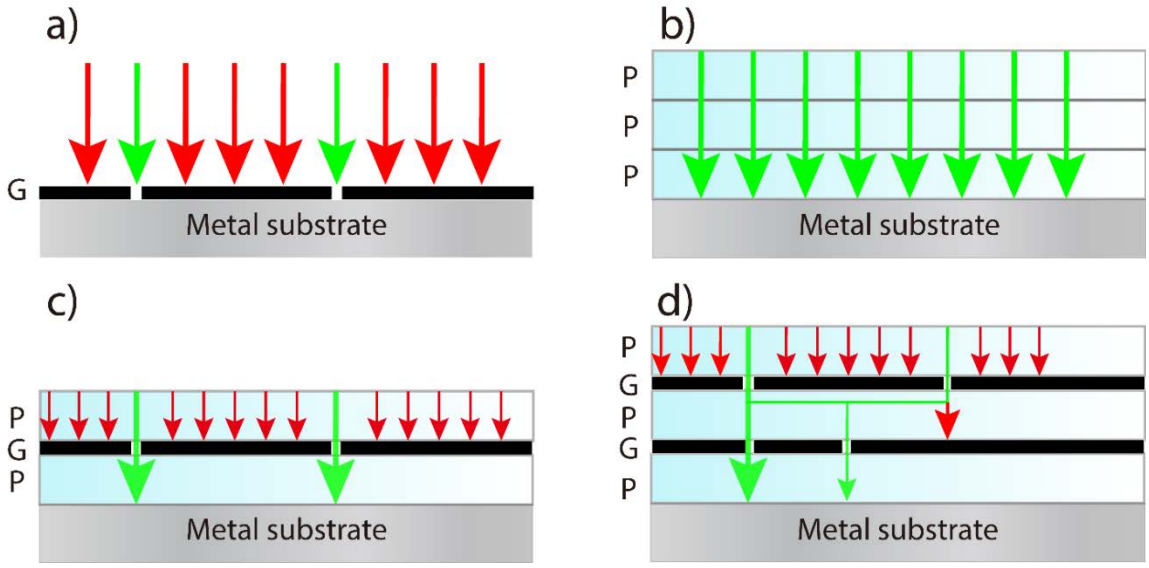

Figure 8.16 Schematic illustration of the barrier structure of (a) as-grown graphene coating (G), (b) bare polymer coating (P-P-P) and polymer graphene hybrid coating with (c) one (P-G-P) and (d) two (P-G-P-G-P) graphene layers coatings on metal substrate. [228]

Chapter 9. Conclusions and outlook

9.1. Conclusions

In the work presented in this thesis, the corrosion protection provided by graphene-based coatings is investigated. Particularly, both multilayered graphene (MLG) coatings and polymer-graphene hybrid coatings are used. When MLG is synthesized on an electroplated Ni seed layer and used to protect stainless steel in a neutral environment (i.e., simulated seawater), excellent corrosion protection at long-term is provided by MLG coating. This is evident when comparing both graphene-coated and graphene-free samples immersed in boiling simulated seawater at 504 hours. The main reason for enhanced corrosion protection with MLG in this case is because corrosion species need to transport through the defects in the MLG to reach the metal surface, and thus the diffusion pathway is significantly increased. Moreover, the strategy of using a Ni seed layer deposited on stainless steel for graphene growth can be applied on other metals and alloys, where direct high-quality CVD graphene growth is not possible.

Based on its outstanding barrier performance, the MLG coating with high-quality is expected to protect metals also in other environments, such as acidic media. However, based on the findings in this thesis, the MLG coating fails to protect Ni substrates shortly after immersion in acids, due to the spontaneous formation of hydrogen bubbles at MLG-Ni interface. This eventually leads to complete delamination of the MLG coating from the substrate. The main reason for the failure is caused by protons that are transported through defects in the MLG coating and react with metal substrate to produce hydrogen bubbles, which form and grow at the interface between MLG and Ni substrate. This fact suggests that graphene coating is not suitable for the corrosion protection of electroactive metals (e.g. Al, Fe, Mg) in aggressive corrosion environments, where cathodic process is dominated by hydrogen evolution. The MLG coating is however still promising for corrosion protection of metals in some applications such as deep sea and aerospace, due to its excellent barrier properties.

Besides the MLG coating, a polymer-graphene hybrid coating is also investigated for corrosion protection in this thesis. Complete corrosion inhibition at long-term is provided by a hybrid coating made of three polymer layers with two graphene layers inserted in the polymer matrix, in contrary to reported results on the enhanced corrosion by bare graphene coatings directly coated on metals at long-term.[8,9] A key reason

responsible for the difference between the results reported in the literature and this work is the polymer primer between the graphene layer and the metal substrate, which electrically insulate graphene layer from the metal, thus avoiding galvanic coupling between them. Furthermore, the soft polymer primer also enables the atomically thin graphene layer to coat flat and rough metal surfaces, which is very challenging for transferred graphene because of the weak adhesion to metals. Due to the presence of the multiple polymer and graphene layers in the hybrid coating, direct corrosion attacks to the metal substrate through graphene defects is also avoided. Moreover, the single graphene layers in the hybrid coating is protected by polymer layers from environmental damage (e.g., wear and friction) while the excellent barrier property of graphene is well preserved at long-term. Furthermore, the use of polymer expands the application of graphene on various metal and alloys for corrosion protection, especially for those substrates that do not allow for direct high-quality graphene growth. Additionally, the hybrid coating avoids the high temperature treatment of metals and alloys that would be otherwise necessary during the CVD growth process.

Although the polymer-graphene hybrid coating provides excellent corrosion protection performance, it is intrinsically limited by the nature of polymer and CVD graphene, and the fabrication process of coating structure. In particular, due to the relatively low glass transition and melting temperature of polymers, this hybrid coating cannot be used for high temperature applications. Besides, the high cost of CVD graphene significantly decreases the cost-efficiency of the hybrid coating. In addition, it is very hard to think of an effective way to apply coatings based on CVD graphene on large areas such as pipelines, ships and automobiles. However, it is worth noting that such coatings may still find promising applications for corrosion protection of small electronic components or metallic core parts of high-tech products, where traditional coatings do not meet the demands.

9.2. Outlook

The work of this thesis focuses on graphene based anticorrosive coatings, including a multilayered CVD graphene coating directly grown on metal substrates and a polymer-graphene hybrid coating using transferred CVD graphene. In this section, personal perspectives on the future work beyond this thesis are proposed.

Firstly, due to the conductive nature of graphene, galvanic corrosion is an issue for graphene anticorrosive coatings. In this case, insulating 2D materials such as hexagonal boron nitride (hBN) are a more suitable material for corrosion protection. Related reports show that hBN can effectively protect metals at longer term[167] and higher temperature[170] than graphene. Although production of large-scale high-quality continuous hBN film is very expensive (the hBN precursors are expensive and often toxic, so that additional precautions must be taken during the synthesis process), the use of hBN coatings for corrosion protection may be promising to investigate.

Secondly, the sandwich structure in the polymer-graphene hybrid coatings may be modified by replacing either layer with other materials, more suitable for specific applications, so that the concept of the sandwich coating can be extended. For example, ceramics rather than polymers may be used together with hBN for high temperature (~1000 °C) applications, while both the polymer and graphene cannot be used at such high temperatures.

Moreover, since the polymer-graphene hybrid coatings presented in this work are intrinsically without self-healing properties, which is of great importance to anticorrosive coatings when it is damaged, the addition of self-healing agents in the polymer matrix may be worth investigating.

Lastly, the mechanical properties and gas barrier properties of the polymer-graphene hybrid film can be interesting to explore, which is not only useful when it comes to anticorrosive coatings but also as free-standing films for applications such as packing materials and weather balloons. This is because graphene is expected to strongly enhance both impermeability and strength of the polymer matrix.

Chapter 10. Bibliography

10.1. References

1 Sørensen, P. A. *et al.* Anticorrosive coatings: a review. *Journal of Coatings Technology and Research* **6**, 135-176, (2009).

2 Bunch, J. S. *et al.* Impermeable atomic membranes from graphene sheets. *Nano Lett.* **8**, 2458-2462, (2008).

3 Li, X. *et al.* Large-area synthesis of high-quality and uniform graphene films on copper foils. *Science* **324**, 1312-1314, (2009).

4 Reina, A. *et al.* Large Area, Few-Layer Graphene Films on Arbitrary Substrates by Chemical Vapor Deposition. *Nano Lett.* **9**, 30-35, (2009).

5 Prasai, D. *et al.* Graphene: Corrosion-Inhibiting Coating. *ACS Nano* **6**, 1102-1108, (2012).

6 Kirkland, N. *et al.* Exploring graphene as a corrosion protection barrier. *Corros. Sci.* **56**, 1-4, (2012).

7 Raman, R. S. *et al.* Protecting copper from electrochemical degradation by graphene coating. *Carbon* **50**, 4040-4045, (2012).

8 Schriver, M. *et al.* Graphene as a long-term metal oxidation barrier: worse than nothing. *ACS nano* **7**, 5763-5768, (2013).

9 Zhou, F. *et al.* Enhanced room-temperature corrosion of copper in the presence of graphene. *ACS nano* **7**, 6939-6947, (2013).

10 Chen, S. *et al.* Oxidation resistance of graphene-coated Cu and Cu/Ni alloy. *ACS nano* **5**, 1321-1327, (2011).

11 Zhang, Y. *et al.* Role of wrinkles in the corrosion of graphene domain-coated Cu surfaces. *Appl. Phys. Lett.* **104**, 143110, (2014).

12 Wlasny, I. *et al.* Role of graphene defects in corrosion of graphene-coated Cu (111) surface. *Appl. Phys. Lett.* **102**, 111601, (2013).

13 Sun, W. *et al.* Inhibiting the corrosion-promotion activity of graphene. *Chem. Mater.* **27**, 2367-2373, (2015).

14 Aneja, K. S. *et al.* Graphene based anticorrosive coatings for Cr(vi) replacement. *Nanoscale* **7**, 17879-17888, (2015).

15 Yu, Y.-H. *et al.* High-performance polystyrene/graphene-based nanocomposites with excellent anti-corrosion properties. *Polym. Chem* **5**, 535-550, (2014).

16 Chang, K.-C. *et al.* Synergistic effects of hydrophobicity and gas barrier properties on the anticorrosion property of PMMA nanocomposite coatings embedded with graphene nanosheets. *Polym. Chem* **5**, 1049-1056, (2014).

17 Gu, L. *et al.* Facile Preparation of Water-Dispersible Graphene Sheets Stabilized by Carboxylated Oligoanilines and Their Anticorrosion Coatings. *ACS Appl. Mater. Interfaces* **7**, 17641-17648, (2015).

18 Du, H. *et al.* Enhancement of barrier properties of cement mortar with graphene nanoplatelet. *Cem. Concr. Res.* **76**, 10-19, (2015).

19 Yoo, B. M. *et al.* Graphene and graphene oxide and their uses in barrier polymers. *J. Appl. Polym. Sci.* **131**, n/a-n/a, (2014).
20 Zhao, Y. *et al.* Mass Transport Mechanism of Cu Species at the Metal/Dielectric Interfaces with a Graphene Barrier. *ACS nano* **8**, 12601-12611, (2014).
21 Cottis, R. Shreir's corrosion. (2010).
22 Bhaskaran, R. *et al.* Global cost of corrosion—A historical review. *Corrosion: Materials* **13**, 621-628, (2005).
23 Thompson, N. G. *et al.* Cost of corrosion and corrosion maintenance strategies. *Corros. Rev.* **25**, 247-262, (2007).
24 Hou, B. *et al.* The cost of corrosion in China. *npj Materials Degradation* **1**, 4, (2017).
25 http://careers-uk.dnvgl.com/asset-integrity/.
26 https://www.nace.org/CORROSION-FAILURES-Lowes-Motor-Speedway-Bridge-Collapse.aspx.
27 Ahmad, Z. *Principles of corrosion engineering and corrosion control*. (Butterworth-Heinemann, 2006).
28 *Standard Terminology for Corrosion, NACE Publications Style Manual, 2nd ed.*, (NACE International: Houston, TX, 1989).
29 Averill, B. A. *et al.* Principles of general chemistry. *Creative Commons*, (2012).
30 Uhlig, H. H. *et al.* Corrosion and Corrosion Control: an Introduction to Corrosion Science and Engineering. (Book). *John Wiley & Sons, Inc., 441*, 1985, (1985).
31 Boden, P. (Taylor & Francis, 1989).
32 Mathaudhu, S. N. *et al. Essential Readings in Magnesium Technology*. (Springer, 2016).
33 Twite, R. *et al.* Review of alternatives to chromate for corrosion protection of aluminum aerospace alloys. *Prog. Org. Coat.* **33**, 91-100, (1998).
34 Tamaki, S. *et al.* Advance in Corrosion Protection and Its Material. *Shinnittetsu Giho*, 2-5, (2002).
35 Revie, R. W. *Corrosion and corrosion control*. (John Wiley & Sons, 2008).
36 Novoselov, K. S. *et al.* Electric field effect in atomically thin carbon films. *Science* **306**, 666-669, (2004).
37 Geim, A. K. *et al.* The rise of graphene. *Nature materials* **6**, 183-191, (2007).
38 Butler, S. Z. *et al.* Progress, challenges, and opportunities in two-dimensional materials beyond graphene. *ACS nano* **7**, 2898-2926, (2013).
39 Gupta, A. *et al.* Recent development in 2D materials beyond graphene. *Prog. Mater Sci.* **73**, 44-126, (2015).
40 Novoselov, K. S. *et al.* Two-dimensional gas of massless Dirac fermions in graphene. *Nature* **438**, 197-200, (2005).
41 Zhang, Y. *et al.* Experimental observation of the quantum Hall effect and Berry's phase in graphene. *Nature* **438**, 201, (2005).
42 Bolotin, K. I. *et al.* Ultrahigh electron mobility in suspended graphene. *Solid State Commun.* **146**, 351-355, (2008).
43 Neto, A. C. *et al.* The electronic properties of graphene. *Reviews of modern physics* **81**, 109, (2009).

44 Baringhaus, J. *et al.* Exceptional ballistic transport in epitaxial graphene nanoribbons. *Nature* **506**, 349-354, (2014).
45 https://iupac.org/materialschemistryedu/computing/conductors/.
46 Cui, C. *et al.* A cautionary note on graphene anti-corrosion coatings. *Nat. Nanotechnol* **12**, 834-835, (2017).
47 Balandin, A. A. *et al.* Superior thermal conductivity of single-layer graphene. *Nano Lett.* **8**, 902-907, (2008).
48 Pop, E. *et al.* Thermal conductance of an individual single-wall carbon nanotube above room temperature. *Nano Lett.* **6**, 96-100, (2006).
49 Cai, W. *et al.* Thermal transport in suspended and supported monolayer graphene grown by chemical vapor deposition. *Nano Lett.* **10**, 1645-1651, (2010).
50 Xu, X. *et al.* Length-dependent thermal conductivity in suspended single-layer graphene. *Nature Communications* **5**, (2014).
51 Preston, D. J. *et al.* Scalable Graphene Coatings for Enhanced Condensation Heat Transfer. *Nano Lett.* **15**, 2902-2909, (2015).
52 Gao, Z. *et al.* Thermal chemical vapor deposition grown graphene heat spreader for thermal management of hot spots. *Carbon* **61**, 342-348, (2013).
53 Nair, R. *et al.* Fine structure constant defines visual transparency of graphene. *Science* **320**, 1308-1308, (2008).
54 Jung, I. *et al.* Simple Approach for High-Contrast Optical Imaging and Characterization of Graphene-Based Sheets. *Nano Lett.* **7**, 3569-3575, (2007).
55 Bonaccorso, F. *et al.* Graphene photonics and optoelectronics. *Nature photonics* **4**, 611-622, (2010).
56 Li, X. *et al.* Transfer of large-area graphene films for high-performance transparent conductive electrodes. *Nano Lett.* **9**, 4359-4363, (2009).
57 Mueller, T. *et al.* Graphene photodetectors for high-speed optical communications. *Nature photonics* **4**, 297-301, (2010).
58 Han, T.-H. *et al.* Extremely efficient flexible organic light-emitting diodes with modified graphene anode. *Nature Photonics* **6**, 105-110, (2012).
59 Bae, S. *et al.* Roll-to-roll production of 30-inch graphene films for transparent electrodes. *Nat. Nanotechnol* **5**, 574-578, (2010).
60 Wang, X. *et al.* Transparent, conductive graphene electrodes for dye-sensitized solar cells. *Nano Lett.* **8**, 323-327, (2008).
61 Sensale-Rodriguez, B. *et al.* Broadband graphene terahertz modulators enabled by intraband transitions. *Nature communications* **3**, ncomms1787, (2012).
62 Shinohara, H. *et al. Graphene: An Introduction to the Fundamentals and Industrial Applications*. (John Wiley & Sons, 2015).
63 Lee, C. *et al.* Measurement of the elastic properties and intrinsic strength of monolayer graphene. *science* **321**, 385-388, (2008).
64 Tsoukleri, G. *et al.* Subjecting a Graphene Monolayer to Tension and Compression. *Small* **5**, 2397-2402, (2009).
65 Zandiatashbar, A. *et al.* Effect of defects on the intrinsic strength and stiffness of graphene. *Nature Communications* **5**, 3186, (2014).

66 Rafiee, M. A. *et al.* Enhanced Mechanical Properties of Nanocomposites at Low Graphene Content. *ACS Nano* **3**, 3884-3890, (2009).
67 Fang, M. *et al.* Covalent polymer functionalization of graphene nanosheets and mechanical properties of composites. *J. Mater. Chem.* **19**, 7098-7105, (2009).
68 Miao, M. *et al.* First principles study of the permeability of graphene to hydrogen atoms. *PCCP* **15**, 16132-16137, (2013).
69 Hu, S. *et al.* Proton transport through one-atom-thick crystals. *Nature* **516**, 227-230, (2014).
70 Achtyl, J. L. *et al.* Aqueous proton transfer across single-layer graphene. *Nature communications* **6**, (2015).
71 http://www.manchester.ac.uk/discover/news/protons-fuel-graphene-prospects/.
72 Stoller, M. D. *et al.* Graphene-Based Ultracapacitors. *Nano Lett.* **8**, 3498-3502, (2008).
73 Wang, S. *et al.* Wettability and surface free energy of graphene films. *Langmuir* **25**, 11078-11081, (2009).
74 van Engers, C. D. *et al.* Direct Measurement of the Surface Energy of Graphene. *Nano Lett.* **17**, 3815-3821, (2017).
75 Das, S. *et al.* Measurements of the adhesion energy of graphene to metallic substrates. *Carbon* **59**, 121-129, (2013).
76 Coleman, J. N. Liquid exfoliation of defect-free graphene. *Acc. Chem. Res.* **46**, 14-22, (2012).
77 Hernandez, Y. *et al.* High-yield production of graphene by liquid-phase exfoliation of graphite. *Nat. Nanotechnol* **3**, 563-568, (2008).
78 Khan, U. *et al.* High‐Concentration Solvent Exfoliation of Graphene. *Small* **6**, 864-871, (2010).
79 Khan, U. *et al.* Solvent-exfoliated graphene at extremely high concentration. *Langmuir* **27**, 9077-9082, (2011).
80 Paton, K. R. *et al.* Scalable production of large quantities of defect-free few-layer graphene by shear exfoliation in liquids. *Nature materials* **13**, 624-630, (2014).
81 Hernandez, Y. *et al.* High-yield production of graphene by liquid-phase exfoliation of graphite. *Nat. Nanotechnol* **3**, 563, (2008).
82 Geng, X. *et al.* Interlayer catalytic exfoliation realizing scalable production of large-size pristine few-layer graphene. *Scientific Reports* **3**, 1134, (2013).
83 Dimiev, A. M. *et al.* Chemical Mass Production of Graphene Nanoplatelets in 100% Yield. *ACS Nano* **10**, 274-279, (2016).
84 Lin, S. *et al.* Room-Temperature Intercalation and 1000-Fold Chemical Expansion for Scalable Preparation of High-Quality Graphene. *Chem. Mater.* **28**, 2138-2146, (2016).
85 Park, J.-H. *et al. Chemical vapor deposition*. Vol. 2 (ASM international, 2001).
86 Yu, Q. *et al.* Graphene segregated on Ni surfaces and transferred to insulators. *Appl. Phys. Lett.* **93**, 113103, (2008).
87 Kim, K. S. *et al.* Large-scale pattern growth of graphene films for stretchable transparent electrodes. *nature* **457**, 706-710, (2009).
88 Singh, V. *et al.* Graphene based materials: Past, present and future. *Prog. Mater Sci.* **56**, 1178-1271, (2011).

89 Zhang, Y. *et al.* Review of chemical vapor deposition of graphene and related applications. *Acc. Chem. Res.* **46**, 2329-2339, (2013).
90 Kumar, A. *et al.* in *Advances in Graphene Science* (InTech, 2013).
91 Li, X. *et al.* Evolution of graphene growth on Ni and Cu by carbon isotope labeling. *Nano Lett.* **9**, 4268-4272, (2009).
92 Mattevi, C. *et al.* A review of chemical vapour deposition of graphene on copper. *J. Mater. Chem.* **21**, 3324-3334, (2011).
93 Hofmann, S. *et al.* CVD-Enabled Graphene Manufacture and Technology. *The Journal of Physical Chemistry Letters* **6**, 2714-2721, (2015).
94 Bhaviripudi, S. *et al.* Role of Kinetic Factors in Chemical Vapor Deposition Synthesis of Uniform Large Area Graphene Using Copper Catalyst. *Nano Lett.* **10**, 4128-4133, (2010).
95 Colombo, L. *et al.* Growth kinetics and defects of CVD graphene on Cu. *Ecs Transactions* **28**, 109-114, (2010).
96 Muñoz, R. *et al.* Review of CVD synthesis of graphene. *Chem. Vap. Deposition* **19**, 297-322, (2013).
97 Sutter, P. *et al.* Graphene on Pt (111): Growth and substrate interaction. *Physical Review B* **80**, 245411, (2009).
98 Coraux, J. *et al.* Structural coherency of graphene on Ir (111). *Nano Lett.* **8**, 565-570, (2008).
99 Sutter, E. A. *et al.* Epitaxial graphene on ruthenium. *Nature materials* **7**, 406, (2008).
100 Choucair, M. *et al.* Gram-scale production of graphene based on solvothermal synthesis and sonication. *Nat. Nanotechnol* **4**, 30-33, (2009).
101 Wang, M. *et al.* Graphene‐Armored Aluminum Foil with Enhanced Anticorrosion Performance as Current Collectors for Lithium‐Ion Battery. *Adv. Mater.*, (2017).
102 Hwang, J. *et al.* van der Waals Epitaxial Growth of Graphene on Sapphire by Chemical Vapor Deposition without a Metal Catalyst. *ACS Nano* **7**, 385-395, (2013).
103 Fanton, M. A. *et al.* Characterization of Graphene Films and Transistors Grown on Sapphire by Metal-Free Chemical Vapor Deposition. *ACS Nano* **5**, 8062-8069, (2011).
104 Strupinski, W. *et al.* Graphene epitaxy by chemical vapor deposition on SiC. *Nano Lett.* **11**, 1786-1791, (2011).
105 Pang, J. *et al.* Self-Terminating Confinement Approach for Large-Area Uniform Monolayer Graphene Directly over Si/SiOx by Chemical Vapor Deposition. *ACS Nano* **11**, 1946-1956, (2017).
106 Chen, Z. *et al.* One‐Step Growth of Graphene/Carbon Nanotube Hybrid Films on Soda‐Lime Glass for Transparent Conducting Applications. *Advanced Electronic Materials* **3**, (2017).
107 Chen, J. *et al.* Oxygen-Aided Synthesis of Polycrystalline Graphene on Silicon Dioxide Substrates. *J. Am. Chem. Soc.* **133**, 17548-17551, (2011).
108 Chen, J. *et al.* Two‐Stage Metal‐Catalyst‐Free Growth of High‐Quality Polycrystalline Graphene Films on Silicon Nitride Substrates. *Adv. Mater.* **25**, 992-997, (2013).
109 Gao, T. *et al.* Temperature-triggered chemical switching growth of in-plane and vertically stacked graphene-boron nitride heterostructures. *Nature communications* **6**, (2015).

110 Liu, C.-C. *et al.* Epitaxial growth of single-domain graphene on hexagonal boron nitride. *Nature materials* **12**, 792, (2013).
111 Lin, Y.-M. *et al.* 100-GHz transistors from wafer-scale epitaxial graphene. *Science* **327**, 662-662, (2010).
112 Kim, B. J. *et al.* High-performance flexible graphene field effect transistors with ion gel gate dielectrics. *Nano Lett.* **10**, 3464-3466, (2010).
113 Huang, Y. *et al.* Nanoelectronic biosensors based on CVD grown graphene. *Nanoscale* **2**, 1485-1488, (2010).
114 He, Q. *et al.* Graphene-based electronic sensors. *Chemical Science* **3**, 1764-1772, (2012).
115 Liu, Y. *et al.* Biological and chemical sensors based on graphene materials. *Chem. Soc. Rev.* **41**, 2283-2307, (2012).
116 Gomez De Arco, L. *et al.* Continuous, highly flexible, and transparent graphene films by chemical vapor deposition for organic photovoltaics. *ACS nano* **4**, 2865-2873, (2010).
117 Wang, Y. *et al.* Large area, continuous, few-layered graphene as anodes in organic photovoltaic devices. *Appl. Phys. Lett.* **95**, 209, (2009).
118 Wang, Y. *et al.* Interface engineering of Layer-by-Layer stacked graphene anodes for High-Performance organic solar cells. *Adv. Mater.* **23**, 1514-1518, (2011).
119 Kang, J. *et al.* Graphene transfer: key for applications. *Nanoscale* **4**, 5527-5537, (2012).
120 Chen, M. *et al.* Advances in transferring chemical vapour deposition graphene: a review. *Materials Horizons* **4**, 1054-1063, (2017).
121 Gao, L. *et al.* Repeated growth and bubbling transfer of graphene with millimetre-size single-crystal grains using platinum. *Nature Communications* **3**, 699, (2012).
122 Wang, Y. *et al.* Electrochemical Delamination of CVD-Grown Graphene Film: Toward the Recyclable Use of Copper Catalyst. *ACS Nano* **5**, 9927-9933, (2011).
123 Pizzocchero, F. *et al.* Non-destructive electrochemical graphene transfer from reusable thin-film catalysts. *Carbon* **85**, 397-405, (2015).
124 Lee, Y. *et al.* Wafer-Scale Synthesis and Transfer of Graphene Films. *Nano Lett.* **10**, 490-493, (2010).
125 Lin, Y.-C. *et al.* Graphene Annealing: How Clean Can It Be? *Nano Lett.* **12**, 414-419, (2012).
126 Lee, H. C. *et al.* Review of the synthesis, transfer, characterization and growth mechanisms of single and multilayer graphene. *RSC Adv* **7**, 15644-15693, (2017).
127 Yang, S. Y. *et al.* Metal-Etching-Free Direct Delamination and Transfer of Single-Layer Graphene with a High Degree of Freedom. *Small* **11**, 175-181, (2015).
128 Fechine, G. J. M. *et al.* Direct dry transfer of chemical vapor deposition graphene to polymeric substrates. *Carbon* **83**, 224-231, (2015).
129 Brodie, B. Sur le poids atomique du graphite. *Ann. Chim. Phys* **59**, e472, (1860).
130 Staudenmaier, L. Verfahren zur darstellung der graphitsäure. *Eur. J. Inorg. Chem.* **31**, 1481-1487, (1898).
131 Hummers Jr, W. S. *et al.* Preparation of graphitic oxide. *J. Am. Chem. Soc.* **80**, 1339-1339, (1958).
132 Amieva, E. J. C. *et al.* in *Recent Advances in Graphene Research* (InTech, 2016).

133 Stankovich, S. *et al.* Synthesis of graphene-based nanosheets via chemical reduction of exfoliated graphite oxide. *Carbon* **45**, 1558-1565, (2007).
134 Gao, J. *et al.* Environment-Friendly Method To Produce Graphene That Employs Vitamin C and Amino Acid. *Chem. Mater.* **22**, 2213-2218, (2010).
135 Moon, I. K. *et al.* Reduced graphene oxide by chemical graphitization. *Nature Communications* **1**, 73, (2010).
136 McAllister, M. J. *et al.* Single Sheet Functionalized Graphene by Oxidation and Thermal Expansion of Graphite. *Chem. Mater.* **19**, 4396-4404, (2007).
137 Wu, Z.-S. *et al.* Synthesis of high-quality graphene with a pre-determined number of layers. *Carbon* **47**, 493-499, (2009).
138 Grimm, S. *et al.* High-Quality Reduced Graphene Oxide by CVD-Assisted Annealing. *The Journal of Physical Chemistry C* **120**, 3036-3041, (2016).
139 Zhu, Y. *et al.* Microwave assisted exfoliation and reduction of graphite oxide for ultracapacitors. *Carbon* **48**, 2118-2122, (2010).
140 Voiry, D. *et al.* High-quality graphene via microwave reduction of solution-exfoliated graphene oxide. *Science*, (2016).
141 Gao, W. *et al.* New insights into the structure and reduction of graphite oxide. *Nature Chemistry* **1**, 403, (2009).
142 Eda, G. *et al.* Large-area ultrathin films of reduced graphene oxide as a transparent and flexible electronic material. *Nat. Nanotechnol* **3**, 270-274, (2008).
143 Overgaard, M. H. *et al.* Highly Conductive Semitransparent Graphene Circuits Screen-Printed from Water-Based Graphene Oxide Ink. *Advanced Materials Technologies*, (2017).
144 Zhou, S. Y. *et al.* Substrate-induced bandgap opening in epitaxial graphene. *Nature Materials* **6**, 770, (2007).
145 Cambaz, Z. G. *et al.* Noncatalytic synthesis of carbon nanotubes, graphene and graphite on SiC. *Carbon* **46**, 841-849, (2008).
146 Ishii, Y. *et al.* Facile bottom-up synthesis of graphene nanofragments and nanoribbons by thermal polymerization of pentacenes. *Nanoscale* **4**, 6553-6561, (2012).
147 Talyzin, A. V. *et al.* Coronene Fusion by Heat Treatment: Road to Nanographenes. *The Journal of Physical Chemistry C* **115**, 13207-13214, (2011).
148 Yang, X. *et al.* Two-dimensional graphene nanoribbons. *J. Am. Chem. Soc.* **130**, 4216-4217, (2008).
149 Shinde, D. B. *et al.* Counter-ion Dependent, Longitudinal Unzipping of Multi-Walled Carbon Nanotubes to Highly Conductive and Transparent Graphene Nanoribbons. *Scientific Reports* **4**, 4363, (2014).
150 Jiao, L. *et al.* Facile synthesis of high-quality graphene nanoribbons. *Nat. Nanotechnol* **5**, 321, (2010).
151 Kosynkin, D. V. *et al.* Longitudinal unzipping of carbon nanotubes to form graphene nanoribbons. *Nature* **458**, 872-876, (2009).
152 Sutter, P. How silicon leaves the scene. *Nature Materials* **8**, 171, (2009).
153 Choi, W. *et al.* Synthesis of graphene and its applications: a review. *Crit. Rev. Solid State Mater. Sci.* **35**, 52-71, (2010).

154 Jia, X. *et al.* Graphene edges: a review of their fabrication and characterization. *Nanoscale* **3**, 86-95, (2011).
155 Novoselov, K. S. *et al.* A roadmap for graphene. *Nature* **490**, 192, (2012).
156 Bae, S. *et al.* Towards industrial applications of graphene electrodes. *Phys. Scr.* **2012**, 014024, (2012).
157 Su, Y. *et al.* Impermeable barrier films and protective coatings based on reduced graphene oxide. *Nat Commun* **5**, (2014).
158 Berry, V. Impermeability of graphene and its applications. *Carbon* **62**, 1-10, (2013).
159 Nine, M. J. *et al.* Graphene: a multipurpose material for protective coatings. *J. Mater. Chem. A* **3**, 12580-12602, (2015).
160 Bondi, A. van der Waals Volumes and Radii. *The Journal of Physical Chemistry* **68**, 441-451, (1964).
161 Topsakal, M. *et al.* Graphene coatings: an efficient protection from oxidation. *Physical Review B* **85**, 155445, (2012).
162 Mohr, P. J. *et al.* CODATA recommended values of the fundamental physical constants: 2014. *J. Phys. Chem. Ref. Data* **45**, 043102, (2016).
163 Agmon, N. The grotthuss mechanism. *Chem. Phys. Lett.* **244**, 456-462, (1995).
164 Ding, D. *et al.* Grain Boundaries and Gas Barrier Property of Graphene Revealed by Dark-Field Optical Microscopy. *The Journal of Physical Chemistry C*, (2017).
165 Zhang, Y. H. *et al.* The distribution of wrinkles and their effects on the oxidation resistance of chemical vapor deposition graphene. *Carbon* **70**, 81-86, (2014).
166 Hsieh, Y.-P. *et al.* Complete corrosion inhibition through graphene defect passivation. *ACS nano* **8**, 443-448, (2013).
167 Shen, L. *et al.* A long-term corrosion barrier with an insulating boron nitride monolayer. *J. Mater. Chem. A* **4**, 5044-5050, (2016).
168 Mahvash, F. *et al.* Corrosion resistance of monolayer hexagonal boron nitride on copper. *Scientific Reports* **7**, 42139, (2017).
169 Zhang, J. *et al.* Investigation of hexagonal boron nitride as an atomically thin corrosion passivation coating in aqueous solution. *Nanotechnology* **27**, 364004, (2016).
170 Liu, Z. *et al.* Ultrathin high-temperature oxidation-resistant coatings of hexagonal boron nitride. *Nature Communications* **4**, 2541, (2013).
171 Galbiati, M. *et al.* Real-time oxide evolution of copper protected by graphene and boron nitride barriers. *Scientific reports* **7**, 39770, (2017).
172 Weatherup, R. S. *et al.* Long-Term Passivation of Strongly Interacting Metals with Single-Layer Graphene. *J. Am. Chem. Soc.* **137**, 14358-14366, (2015).
173 Ye, X. *et al.* Corrosion resistance of graphene directly and locally grown on bulk nickel substrate by laser irradiation. *RSC Adv* **5**, 35384-35390, (2015).
174 Mišković-Stanković, V. *et al.* Electrochemical study of corrosion behavior of graphene coatings on copper and aluminum in a chloride solution. *Carbon* **75**, 335-344, (2014).
175 Zhang, B. *et al.* Low-Temperature Chemical Vapor Deposition Growth of Graphene from Toluene on Electropolished Copper Foils. *ACS Nano* **6**, 2471-2476, (2012).
176 Li, Z. *et al.* Low-Temperature Growth of Graphene by Chemical Vapor Deposition Using Solid and Liquid Carbon Sources. *ACS Nano* **5**, 3385-3390, (2011).

177 Weatherup, R. S. *et al.* In Situ Characterization of Alloy Catalysts for Low-Temperature Graphene Growth. *Nano Lett.* **11**, 4154-4160, (2011).
178 Stoot, A. C. *Protective coatings based on 2D-materials*, DTU Nanotech, (2016).
179 Chae, S. J. *et al.* Synthesis of large-area graphene layers on poly-nickel substrate by chemical vapor deposition: wrinkle formation. *Adv. Mater.* **21**, 2328-2333, (2009).
180 Jayasooriya, U. A. *et al.* in *An Introduction to Laser Spectroscopy* 77-104 (Springer, 2002).
181 Ferrari, A. C. *et al.* Raman spectroscopy as a versatile tool for studying the properties of graphene. *Nat. Nanotechnol* **8**, 235, (2013).
182 Malard, L. M. *et al.* Raman spectroscopy in graphene. *Physics Reports* **473**, 51-87, (2009).
183 Ferrari, A. C. Raman spectroscopy of graphene and graphite: Disorder, electron–phonon coupling, doping and nonadiabatic effects. *Solid State Commun.* **143**, 47-57, (2007).
184 Das, A. *et al.* Monitoring dopants by Raman scattering in an electrochemically top-gated graphene transistor. *Nat. Nanotechnol* **3**, 210, (2008).
185 Mohiuddin, T. *et al.* Uniaxial strain in graphene by Raman spectroscopy: G peak splitting, Grüneisen parameters, and sample orientation. *Physical Review B* **79**, 205433, (2009).
186 Ferrari, A. C. *et al.* Raman spectrum of graphene and graphene layers. *Phys. Rev. Lett.* **97**, 187401, (2006).
187 Wu, Z. *et al.* Spectroscopic investigation of defects in two-dimensional materials. *Nanophotonics*, (2017).
188 Lucchese, M. M. *et al.* Quantifying ion-induced defects and Raman relaxation length in graphene. *Carbon* **48**, 1592-1597, (2010).
189 Usachov, D. Y. *et al.* Raman Spectroscopy of Lattice-Matched Graphene on Strongly Interacting Metal Surfaces. *ACS Nano* **11**, 6336-6345, (2017).
190 Frank, O. *et al.* Interaction between graphene and copper substrate: The role of lattice orientation. *Carbon* **68**, 440-451, (2014).
191 Dahal, A. *et al.* Graphene-nickel interfaces: a review. *Nanoscale* **6**, 2548-2562, (2014).
192 Larsen, M. B. B. S. *et al.* Transfer induced compressive strain in graphene: Evidence from Raman spectroscopic mapping. *Microelectron. Eng.* **121**, 113-117, (2014).
193 Goldstein, J. I. *et al. Scanning electron microscopy and X-ray microanalysis*. (Springer, 2017).
194 Seiler, H. Secondary electron emission in the scanning electron microscope. *J. Appl. Phys.* **54**, R1-R18, (1983).
195 https://sites.ualberta.ca/~ccwj/teaching/microscopy/.
196 Wang, Z. L. Transmission Electron Microscopy of Shape-Controlled Nanocrystals and Their Assemblies. *J. Phys. Chem. B* **104**, 1153-1175, (2000).
197 Reza, M. *et al.* Transmission electron microscopy for wood and fiber analysis− A review. *BioResources* **10**, 6230-6261, (2015).
198 Meyer, J. C. *et al.* The structure of suspended graphene sheets. *Nature* **446**, 60, (2007).
199 Banhart, F. *et al.* Structural Defects in Graphene. *ACS Nano* **5**, 26-41, (2011).
200 Egerton, R. F. *Physical principles of electron microscopy*. (Springer, 2005).

201 Walter, G. A review of impedance plot methods used for corrosion performance analysis of painted metals. *Corros. Sci.* **26**, 681-703, (1986).
202 Mansfeld, F. Electrochemical impedance spectroscopy (EIS) as a new tool for investigating methods of corrosion protection. *Electrochim. Acta* **35**, 1533-1544, (1990).
203 Loveday, D. *et al.* Evaluation of organic coatings with electrochemical impedance spectroscopy. *JCT coatings tech* **8**, 46-52, (2004).
204 Orazem, M. E. *et al. Electrochemical impedance spectroscopy*. Vol. 48 (John Wiley & Sons, 2011).
205 Randviir, E. P. *et al.* Electrochemical impedance spectroscopy: an overview of bioanalytical applications. *Analytical Methods* **5**, 1098-1115, (2013).
206 Wessel, J. K. *The handbook of advanced materials: enabling new designs*. (John Wiley & Sons, 2004).
207 Hughes, A. E. *et al.* Active Protective Coatings.
208 Jones, D. A. *Principles and prevention of corrosion*. (Macmillan, 1992).
209 Stern, M. *et al.* Electrochemical polarization I. A theoretical analysis of the shape of polarization curves. *J. Electrochem. Soc.* **104**, 56-63, (1957).
210 Oldham, K. B. *et al.* Corrosion rates from polarization curves: a new method. *Corros. Sci.* **13**, 813-819, (1973).
211 Galliano, F. *et al.* Evaluation of corrosion protection properties of additives for waterborne epoxy coatings on steel. *Prog. Org. Coat.* **44**, 217-225, (2002).
212 Gupta, G. *et al.* Polyaniline-lignosulfonate/epoxy coating for corrosion protection of AA2024-T3. *Corros. Sci.* **67**, 256-267, (2013).
213 Huh, J.-H. *et al.* Enhancement of seawater corrosion resistance in copper using acetone-derived graphene coating. *Nanoscale* **6**, 4379-4386, (2014).
214 Roy, S. S. *et al.* Improving graphene diffusion barriers via stacking multiple layers and grain size engineering. *Adv. Funct. Mater.* **23**, 3638-3644, (2013).
215 Hong, J. *et al.* Graphene as an atomically thin barrier to Cu diffusion into Si. *Nanoscale* **6**, 7503-7511, (2014).
216 Nguyen, B.-S. *et al.* 1-nm-thick graphene tri-layer as the ultimate copper diffusion barrier. *Appl. Phys. Lett.* **104**, 082105, (2014).
217 Wofford, J. M. *et al.* Graphene islands on Cu foils: the interplay between shape, orientation, and defects. *Nano Lett.* **10**, 4890-4896, (2010).
218 Li, L. *et al.* Vertical and Lateral Copper Transport through Graphene Layers. *ACS Nano* **9**, 8361-8367, (2015).
219 Stoot, A. C. *et al.* Multilayer graphene for long-term corrosion protection of stainless steel bipolar plates for polymer electrolyte membrane fuel cell. *J. Power Sources* **293**, 846-851, (2015).
220 Guermoune, A. *et al.* Chemical vapor deposition synthesis of graphene on copper with methanol, ethanol, and propanol precursors. *Carbon* **49**, 4204-4210, (2011).
221 John, R. *et al.* Single-and few-layer graphene growth on stainless steel substrates by direct thermal chemical vapor deposition. *Nanotechnology* **22**, 165701, (2011).
222 Yu, F. *et al.* Failure of multi-layer graphene coatings in acidic media. *RSC Adv* **6**, 21497-21502, (2016).

223 Zhu, Y. *et al.* Graphene coating for anti-corrosion and the investigation of failure mechanism. *J. Phys. D: Appl. Phys.* **50**, 114001, (2017).

224 Pourbaix, M. *et al.* in *Lectures on Electrochemical Corrosion* 83-183 (Springer US, 1973).

225 Li, J. *et al.* Reinforcement of graphene and its derivatives on the anticorrosive properties of waterborne polyurethane coatings. *Compos. Sci. Technol.* **129**, 30-37, (2016).

226 Mo, M. *et al.* Corrosion inhibition of functional graphene reinforced polyurethane nanocomposite coatings with regular textures. *RSC Adv* **6**, 7780-7790, (2016).

227 Compton, O. C. *et al.* Crumpled Graphene Nanosheets as Highly Effective Barrier Property Enhancers. *Adv. Mater.* **22**, 4759-4763, (2010).

228 Yu, F, et al. "Complete long-term corrosion protection with chemical vapor deposited graphene." Carbon 132 (2018): 78-84.

229 Yu, F. *et al.* Corrosion protection of AA2024-T3 alloy by modified hybrid titania-containing sol-gel coatings. *Prog. Org. Coat.* **102**, 120-129, (2017).

230 Amirudin, A. *et al.* Application of electrochemical impedance spectroscopy to study the degradation of polymer-coated metals. *Prog. Org. Coat.* **26**, 1-28, (1995).

10.2. List of publications

10.2.1. Peer reviewed publications

i. Stoot, A. C., Camilli, L., Spiegelhauer, S. A., Yu, F., & Bøggild, P. (2015). Multilayer graphene for long-term corrosion protection of stainless steel bipolar plates for polymer electrolyte membrane fuel cell. Journal of Power Sources, 293, 846-851. (Appendix A)

ii. Yu, F., Stoot, A. C., Bøggild, P., & Camilli, L. (2016). Failure of multi-layer graphene coatings in acidic media. RSC Advances, 6(26), 21497-21502. (Appendix B)

iii. Yu, F., Camilli, L., Wang, T., Mackenzie, D. M., Curioni, M., Akid, R., & Bøggild, P. (2018). Complete long-term corrosion protection with chemical vapor deposited graphene. Carbon, 132, 78-84. (Appendix C)

iv. Yivlialin, R., Bussetti, G., Duò, L., Yu, F., Galbiati, M., & Camilli, L. (2018). CVD Graphene/Ni Interface Evolution in Sulfuric Electrolyte. Langmuir: the ACS journal of surfaces and colloids, 34(11), 3413.

10.2.2. Manuscripts in preparation

i. *Low-temperature synthesis of a graphene-based, corrosion-inhibiting coating on an industrial grade alloy*. Susanne Halkjær, Jon Iversen, Line Kyhl, Jacques Chevallier, Federico Andreatta, Feng Yu, Adam Stoot, Luca Camili, Peter Bøggild, Liv Hornekær, Andrew M Cassidy.

10.2.3. Conference contributions

i. *Corrosion protection of nickel by multilayer CVD growth graphene in acidic media*. Feng Yu, Adam Stoot, Luca Camili, Peter Bøggild. Poster at 10th NANOSMAT 2015, Manchester, United Kingdom.

ii. *Corrosion protection of nickel by multilayered graphene coatings.* Feng Yu, Adam Stoot, Luca Camili, Peter Bøggild. Poster at Graphene China 2016, Qingdao, China.

iii. *CVD-grown graphene and its composite coatings for corrosion*. Feng Yu, Adam Stoot, Luca Camili, Ting Wang, David M. A. Mackenzie, Michele Curioni, Robert Akid, Peter Bøggild. Presentation at Graphene China 2017, Nanjing, China.

iv. *Multilayer hybrid graphene-polymer coatings for long term corrosion protection.* Robert Akid, Feng Yu, Peter Bøggild. Presentation at European Coatings Future Dialogue 2017, Berlin, Germany.

10.2.4. Patent applications

i. *A coated metal product and a method to produce a coated metal product*. Feng Yu, Luca Camili, Patrick R. Whelan, Peter Bøggild, Adam Stoot and Timothy J. Booth. EP16176135, 2016. (Appendix D)

Appendix A

Multilayer graphene for long-term corrosion protection of stainless steel bipolar plates for polymer electrolyte membrane fuel cell

Article published in Journal of Power Sources

Journal of Power Sources 293 (2015) 846–851

Contents lists available at ScienceDirect

Journal of Power Sources

journal homepage: www.elsevier.com/locate/jpowsour

Multilayer graphene for long-term corrosion protection of stainless steel bipolar plates for polymer electrolyte membrane fuel cell

Adam C. Stoot [a], Luca Camilli [a], Susie-Ann Spiegelhauer [b], Feng Yu [a], Peter Bøggild [a, *]

[a] Technical University of Denmark, Department of Micro- and Nanotechnology, Kgs. Lyngby, DK-2800, Denmark
[b] Accoat, SP-Group A/S, Kvistgård, DK-3490, Denmark

HIGHLIGHTS

- Nickel-coating on stainless steel enhances its short term anti-corrosion properties.
- Multi-layer graphene film on steel enhances long-term corrosion resistance.
- The effect of nickel in corrosion resistance of graphene/nickel/steel is important.
- Accelerated reaction kinetics are used to simulate effect of longer exposures.

GRAPHICAL ABSTRACT

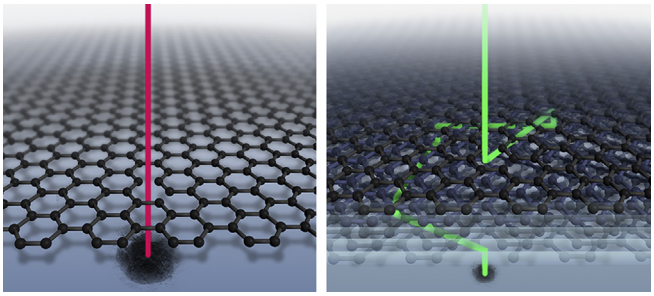

ARTICLE INFO

Article history:
Received 24 March 2015
Received in revised form
15 May 2015
Accepted 2 June 2015
Available online 12 June 2015

Keywords:
Graphene coating
Wet corrosion
Chemical vapour deposition
Raman spectroscopy
Stainless steel
Metal bipolar plate

ABSTRACT

Motivated by similar investigations recently published (Pu et al., 2015), we report a comparative corrosion study of three sets of samples relevant as bipolar plates for polymer electrolyte fuel cells: stainless steel, stainless steel with a nickel seed layer (Ni/SS) and stainless steel with Ni seed layer coated by a multi-layered graphene thin film (G/Ni/SS). The graphene film, synthesized by chemical vapour deposition (CVD), has a moderate amount of defects according to Raman spectroscopy. Short/medium-term corrosion test shows no significant advantage of using G/Ni/SS rather than Ni/SS, both samples exhibiting a similar trend, thus questioning the short-term positive effect of graphene coatings. However, partial immersion in boiling seawater for three weeks reveals a clear superiority of the graphene coating with respect to steel just protected by Ni. After the test, the graphene film is still intact with unchanged defect density. Our results show that even non-perfect multilayer graphene films can considerably increase the lifetime of future-generation bipolar plates for fuel cells.

1. Introduction

After the seminal works by Novoselov and Geim [1], the superior material properties of graphene has fuelled an intense search for practical applications of this planar honeycomb structure of carbon atoms. Graphene and related materials (*i.e.*, other two-dimensional crystals) are expected to have a major impact in several technological fields in the near future [2]. While graphene is chemically inert and impermeable to even hydrogen [3], the effectiveness of graphene as a protective coating is still subject to debate and controversy. While several studies have reported pronounced short- and medium-term protection performance of graphene coatings [4–6], Schriver et al. pointed out that graphene may in fact eventually accelerate corrosion and oxidation of metals over longer periods of time [7].

Very recently, Pu et al. proposed the use of graphene on stainless steel as a high-performance anti-corrosion coating for polymer

* Corresponding author.
E-mail address: peter.boggild@nanotech.dtu.dk (P. Bøggild).

http://dx.doi.org/10.1016/j.jpowsour.2015.06.009
0378-7753/

electrolyte membrane fuel cells bipolar plates [8]. As the growth of large-scale high-quality graphene directly on stainless steel (SS) has not yet been shown to be possible, the authors suggest using a nickel (Ni) seed layer on top of SS (Ni/SS) in order to catalyse the graphene growth. The authors then compare the anti-corrosion performance of three sets of specimens: (i) bare SS, (ii) graphene-coated SS and (iii) graphene-coated Ni/SS (G/Ni/SS). After repeating a potentiodynamic polarization test twenty times for each set of samples they conclude that while the corrosion rate of bare SS and graphene-coated SS increases by almost 50 and 15 times, respectively, the corrosion rate of G/Ni/SS remains almost constant. Since in the case of graphene-coated SS specimen the graphene coverage is non-uniform and incomplete, while for the G/Ni/SS the coverage is close to 100%, the conclusion is that the complete surface coverage of the graphene coating prevents wet corrosion of SS. However, the effect of the Ni seed layer on SS has been overlooked, although Nickel based coatings and alloys have already been proposed as corrosion-resistive bipolar plates in fuel cells [9,10]. Here, we report that both the Ni/SS and the G/Ni/SS exhibit a similar behaviour when subjected to twenty polarization scans under same experimental conditions (2-h test), and thus that a graphene coating does not give a significant contribution to the short-term corrosion resistance of steel. In the long term, however, there is indeed a positive effect of graphene; after 504 h of exposure to boiling seawater (Atlas cell test, see Experimental section for details), there is indeed a clear difference in SS protected by Ni with or without graphene.

2. Experimental

2.1. Fabrication of samples

2 inch diameter, 3 mm thick 304 stainless steel samples were glass blasted and sonicated for 20 min in Triton X before being pre-coated with a 150 μm nickel seed layer using a Technotrans electroplating system without any additives/brighteners.

The chemical vapour deposition (CVD) system used for graphene growth is based on a graphitic block heated by halogen light bulbs and a PID-temperature control. Before insertion into the CVD-chamber, the samples were sonicated in isopropanol and then rinsed in deionized water. As for the growth process, firstly the samples were kept at 850 °C in hydrogen atmosphere for 10 min after which a mixture of hydrogen (24 sccm) and acetylene (12 sccm) was injected for the graphene growth. The samples were cooled down at a fixed rate of 0.5 °C/s in low vacuum (base pressure around 10^{-1} mbar).

2.2. Electrochemical tests

The electrochemical tests were done using a platinum counter electrode, an Ag/AgCl reference electrode and a Quick WE working electrode holder [11] along with the Gamry Reference 3000 potentiostat. The scan rate was 5 mV/s, and 3.5 wt% NaCl solution was the chosen electrolyte. Twenty polarisation scans were performed on each sample and the open circuit potential was monitored to ensure stabilisation between each scan.

2.3. Atlas cell tests

The simulated seawater tests were also done in 3.5 wt% NaCl solution. These long term tests were done at Accoat A/S using an Atlas glass cell. It consists of a glass canister with a hole in both ends allowing two samples to be tested simultaneously (see Supplementary Materials). The samples are only partially immersed in the corrosive solution, thus testing both liquid- and vapour phase-induced corrosion. Heating the solution to the boiling point has two effects; reaction kinetics is accelerated and large temperature gradients arise over the samples with their backside being exposed to room temperature. This furthermore tests the tendency of the coating to delaminate due to condensation and bubble formation at the coating/sample-interface in case of a semi-permeable coating or poor adhesion.

It is worth noting that the corrosive environment at an elevated temperature of the Atlas test presents a scenario similar to a fuel cell in operation, including the temperature gradients due to the surroundings being at a lower temperature.

2.4. Characterisation

The structure and composition of the samples were investigated with Scanning Electron Microscopy and Energy Dispersive Spectroscopy using FEI Quanta 200 FEG and FEI Inspect. Focused Ion Beam milling was done using FEI Helios dual beam focused ion beam microscope. Raman spectra were obtained using a Thermo Scientific DXR confocal Raman Microscope with a 455 nm laser, 2 mW power and a spot-size of approximately 1 μm.

3. Results and discussion

Fig. 1(a) shows an averaged Raman spectrum recorded on several locations of the G/Ni/SS sample. The ratio of the intensities of the 2D-peak (~2750 cm^{-1}) to the G-peak (~1590 cm^{-1}) is ~0.26 ± 0.01, indicating the multi-layered character of the graphene film. The thickness was 25 nm–40 nm measured by SEM of Focused Ion Beam milled sections (see supplementary materials). The D-band, located at ~1370 cm^{-1}, indicates the presence of defects and structural imperfections in the graphene lattice, which could be related to the small size of polycrystalline graphene domains [12]. Additionally, the Raman map displayed in Fig. 1(b) shows the full coverage and high homogeneity of the multilayer graphene coating over a millimetre-sized area of the sample, confirming the well-known high catalytic activity of Ni towards the synthesis of graphene [13].

In Fig. 2(a) we report the results of a single polarization scan acquired for three sets of samples: (i) bare SS, (ii) Ni/SS and (iii) G/Ni/SS. For comparison, we report on the same graph the data for a G/Ni/SS sample taken from Ref. [8]. Firstly, observing the anodic part of the polarization curve for SS (black curve), it is possible to observe the passivation layer formation (red arrow) and its subsequent break-down (blue arrow). Such a passivating film reduces the conductivity of the surface due to the oxide phase, and thus results in being detrimental in view of applications as a bipolar plate for polymer electrolyte membrane fuel cell. Secondly, we can see that the G/Ni/SS sample of Ref. [8] (brown curve) is performing better than our G/Ni/SS sample (blue curve), with a lower corrosion rate indicated by the curve being located at a lower current density range. We explain the difference with respect to our data as due to the larger defect density in our graphene film compared with the one reported by Pu et al. [8], which can be seen by direct comparison of the Raman spectrum in Fig. 1(a) of this work and the one displayed in Fig. 1(a) of Ref. [8]. In fact, it is well established that ions (such as Cl^- ions), water and oxygen may diffuse through defects of graphene, like grain boundaries and cracks, until reaching the metal surface underneath the coating and beginning its corrosion [14]. Lastly, we want to point out that our Ni/SS sample (green curve) is showing similar performance to the G/Ni/SS sample in Ref. [8] and, therefore, better performance than our G/Ni/SS specimen. This finding is actually not surprising, due to the intrinsic strong corrosion resistance of nickel and nickel-based alloys [15,16].

In order to (i) investigate the medium-term behaviour of the

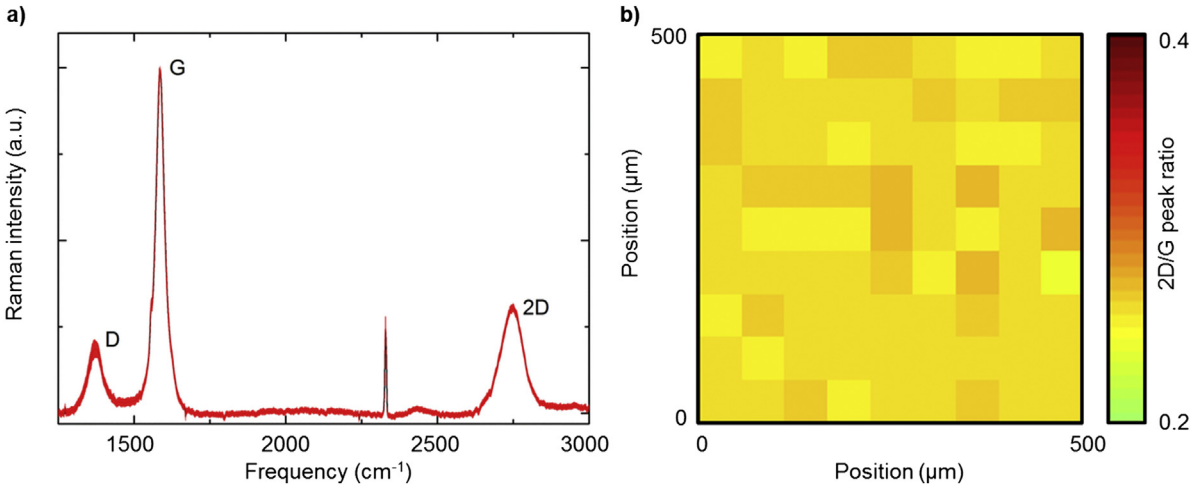

Fig. 1. a) Average Raman spectrum of the G/Ni/SS sample extracted from 100 spots over a millimetre sized area. The width of the graph represents the standard deviation. The sharp peak located at ~2350 cm^{-1} is related to N_2 b) Raman map highlighting the full coverage and high homogeneity of the graphene film.

samples under study and (ii) directly compare our data with that one reported in Ref. [8], we repeated the polarization curves twenty times and plotted our measurements along with the ones for G/Ni/SS of Ref. [8]. As illustrated in Fig. 2(b), the SS sample turned out to be highly degraded after twenty polarization scans, with the corrosion potential being significantly shifted at a lower value (−168 mV) with respect to the one after a single scan (−2 mV). This is ascribed to the breaking down of the metal oxide film passivating the surface of the SS, which is now "less noble" and thus more prone to be corroded [17]. The passivating oxide film breakdown can be seen on the first polarisation scan at an over potential of around 320 mV.

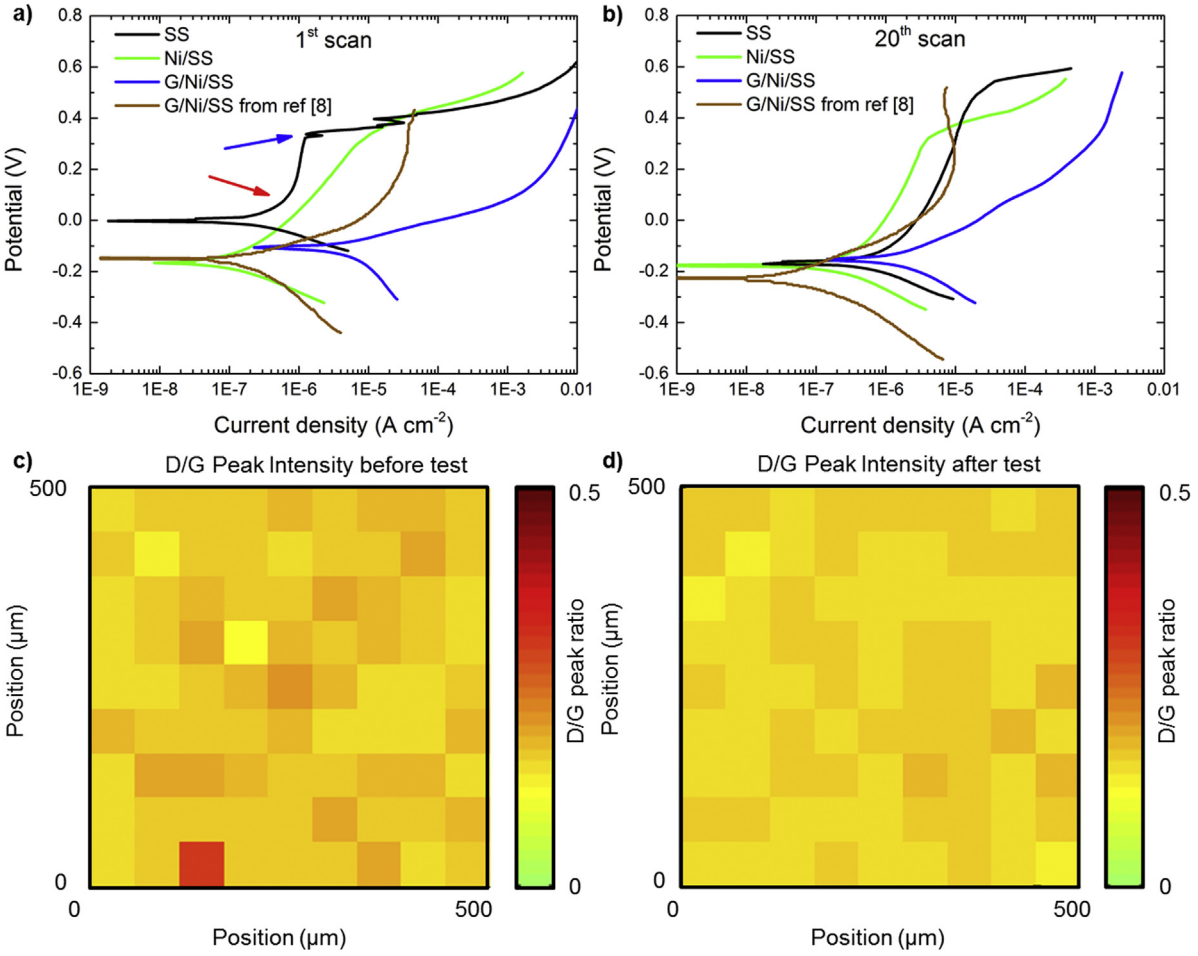

Fig. 2. Potentiodynamic study of SS (black curve), Ni/SS (green curve), G/Ni/SS (blue curve) and a G/Ni/SS from Ref. 7 (brown curve) after (a) one and (b) twenty polarisation scans. (c) and (d): Raman maps of the G/Ni/SS before and after the potendiodynamic study, respectively. The I(D)/I(G) peak which represents the defect density is almost unchanged. (For interpretation of the references to colour in this figure legend, the reader is referred to the web version of this article.)

Both the Ni/SS (green curve) measured by us and the G/Ni/SS (brown curve) from Ref. [8] exhibit strong corrosion resistance, low corrosion current and a trend to keep a constant line shape over 20 polarization scans (see Supplementary Materials). As a matter of fact, the corrosion potential of the Ni/SS is slightly higher than the one of the G/Ni/SS of Ref. [8]. As for our G/Ni/SS sample, the polarisation curve is still located at a higher current density compared to that of the two just-mentioned samples, however, it shows a trend to maintain the performance after twenty polarization scans, in contrast with bare SS (black curve) and similar to our Ni/SS and G/Ni/SS reported in Ref. [8]. It is worth noting that the presence of the graphene coating after the potentiodynamic analysis is confirmed by the Raman maps acquired on the G/Ni/SS before and after testing (Fig. 2(c) and (d), respectively). The D-to G-peak intensity ratio, I(D)/I(G), representing the density of lattice defects [18], is 0.16 ± 0.01 which is within the measurement uncertainty when compared to the 0.17 ± 0.02 obtained before the polarization tests.

Based on these data it is not possible to determine whether the corrosion resistance within the tested timeframe is due to the graphene coating, to the Ni seed layer or both in combination, as all are improving the anti-corrosion performance of steel.

In order to evaluate whether a graphene coating can lead to an actual improvement of SS's corrosion resistance, we apply a much longer test, the Atlas-cell test [19]. The samples are subjected to a harsh wet corrosive environment at an elevated temperature which accelerates the reaction kinetics and also represents a simulation of an environment relevant for polymer fuel cells [20]. The elevated working temperatures and the likelihood of NaCl contamination from *e.g.* ocean mist provide highly corrosive conditions for the cathode. The samples are half immersed in boiling simulated seawater for 504 h, with a large temperature gradient arising owing to their backside being exposed to room temperature.

Fig. 3 displays two samples, Ni/SS and G/Ni/SS before (Fig. 3(a) and (b), respectively) and after the Atlas-cell test (Fig. 3(c) and (d)). The Ni surface without graphene coating exhibits clear signs of corrosion including both Ni(II)oxide (green) as well as other nickel oxides in higher oxidation states (black), which are visible to the naked eye (Fig. 3(a) and c) [21]. The position of the water–vapour interface can easily be observed on the sample. While both the liquid-exposed and gas-exposed sides of the sample appear to be damaged, the latter appears to have suffered the most damage. This may be due to a higher oxygen concentration in the vapour phase than in the liquid phase, which bears resemblance with the working environment of bipolar plate inside a fuel cell where both the oxygen concentration and the temperature are high.

On the contrary, the surface of the graphene-covered sample does not show any sign of degradation when comparing visual appearance of the sample before (Fig. 3(b)) and after (Fig. 3(d)) testing. This is also confirmed by energy dispersive x-ray spectroscopy (EDS) of the samples after testing (see Supplementary Materials), where an oxygen peak is absent for G/Ni/SS, while present in the uncoated nickel reference.

After the Atlas-cell test we investigated the graphene coating, to verify whether it has been damaged or even removed by the

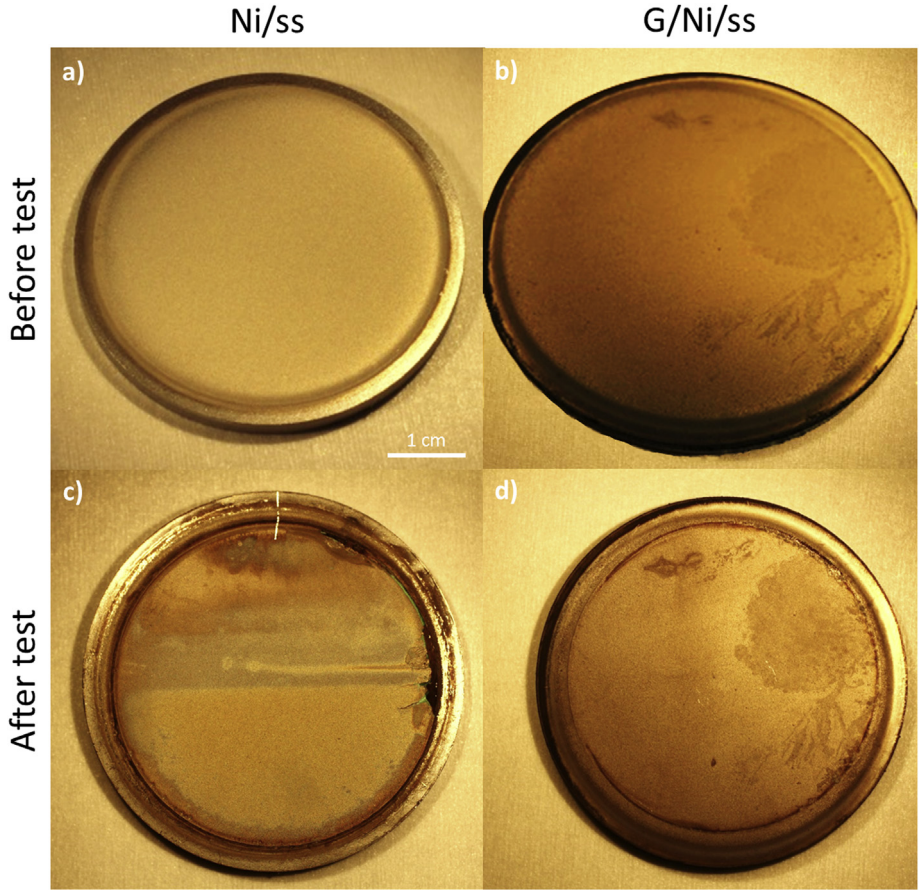

Fig. 3. Optical images of samples before and after test in boiling simulated seawater (i.e., Atlas cell test). a) and b) show Ni/SS and G/Ni/SS samples before testing, respectively. c) and d) display the samples in a) and b) after the test has been carried out, respectively. The graphene-uncoated sample is highly corroded, especially in the vapour side (highlighted by the scratch at the edge of the sample) due to the higher oxygen concentration than in the liquid phase. It is worth noting that the dark areas in the graphene-coated samples were present even before testing, and are the result of the annealing during CVD process.

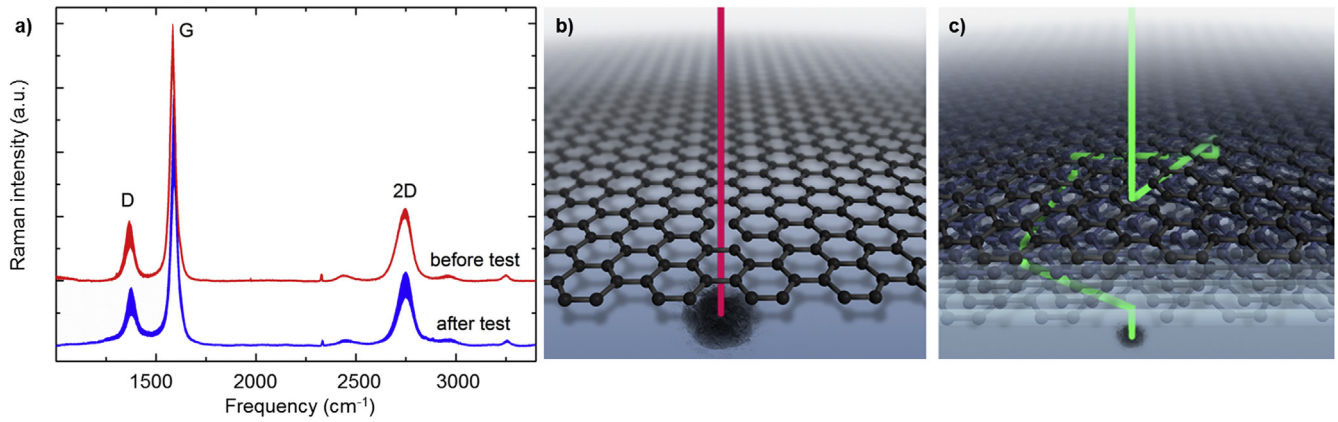

Fig. 4. a) Raman spectra of the graphene-coated sample before (red curve) and after (blue curve) testing in the boiling simulated seawater. The spectra are obtained away from the edge, averaging in different sample locations. The plotted data is the average value with standard deviation error bars being represented by the thickness of the lines. The I(D)/I(G) ratio before the test was 0.19 ± 0.07 while after the test 0.16 ± 0.04. b) and c): Schematic illustration of diffusion paths for single-layer (b) and multi-layer (c) graphene. In the case of a multi-layer film, the diffusion path for oxygen and water molecules is longer. (For interpretation of the references to colour in this figure legend, the reader is referred to the web version of this article.)

aggressive test. As illustrated in Fig. 4(a), comparison of the Raman spectra recorded before and after testing asserts that the graphene coating is still present and intact. Notably, the D-to G-peak intensity ratio, which was 0.19 ± 0.07 before test, is now 0.16 ± 0.04, and thus remains constant within the measurement uncertainty.

At first sight, the positive long-term action of graphene coating shown in this work might seem to be in disagreement with a recent study reported in Ref. [7]. However, it is worth noting that the scenarios are not immediately comparable. While Shiver et al. in Ref. [7] are reporting on the barrier properties of graphene in a dry oxidative environment, we are demonstrating the long-term protection in wet environment, where the reactions involved are different. In addition, while they are investigating the properties of a single-layer graphene coating, here we propose to use a multi-layer graphene film. This film is much thicker than single or few-layer graphene coatings previously reported in literature [22,23], but still extremely thin if compared to standard, industrially available composite coatings [24–26]. This greatly minimises the influence on mechanical tolerances of coated items. Despite the presence of defects, in case of a multi-layered graphene coating, oxygen and water molecules must traverse a complex combination of multiple intercalative paths between the layers, as well as penetrate to deeper layers through lattice imperfections in order to eventually reach the metal surface (Fig. 4(c)). Although producing a realistic simulation of such a system is very challenging, it is safe to assume that the diffusion time of corroding agents will scale with number of layers.

4. Conclusions

In summary, we have compared the corrosion resistance of three bipolar plates similar to those used for polymer fuel cells: (i) an SS substrate, (ii) an SS substrate with a Ni seed layer atop and (iii) an SS substrate with a Ni seed layer atop coated with graphene. We have shown that in the short-/medium-term, the performance of the latter two samples is in fact comparable and the stainless steel substrate is protected when subjected to electrochemical tests in corrosive electrolytes. From this alone, it is unclear whether the presence of the graphene film on top of the Ni seed layer is playing a role in the corrosion protection of steel as concluded by Pu et al. [8]. However, using a longer test in a very harsh environment (*i.e.*, the Atlas-cell test), it is evident that the graphene film is performing much better than just a Ni seed layer toward the protection of steel. This test has a 250 times longer duration than the potentiodynamic analysis reported in Fig. 2(c) and ref. [8] and features (i) accelerated reaction kinetics due to the high temperature as well as (ii) high temperature gradients, which increase the tendency of coatings to delaminate due to condensation and bubble formation at the coating/sample-interface, in case of poor adhesion, permeability or pinholes/cracks [19]. In addition, owing to the remarkable electrical properties of graphene [2], these results could boost the exploitation of graphene in fuel cell application.

Acknowledgement

We would like to thank A. Holm, Grundfos A/S for supplying the 2″ steel discs used for creating the samples. We would also like to thank N. Bild for help with figure 4 b) and c).

This project was supported by The Strategic Danish Research collaboration (DSF) with the DA-GATE project (12-131827) and through the High Technology Foundation (HTF) with the NIAGRA project (058-2012-4).

Appendix A. Supplementary data

Supplementary data related to this article can be found at http://dx.doi.org/10.1016/j.jpowsour.2015.06.009.

References

[1] K.S. Novoselov, A.K. Geim, S.V. Morozov, D. Jiang, Y. Zhang, S.V. Dubonos, I.V. Grigorieva, A.A. Firsov, Electric field effect in atomically thin carbon films, Science 306 (2004) 666–669.

[2] A.C. Ferrari, F. Bonaccorso, V. Falko, K.S. Novoselov, S. Roche, P. Boggild, S. Borini, F.H.L. Koppens, V. Palermo, N. Pugno, J.A. Garrido, R. Sordan, A. Bianco, L. Ballerini, M. Prato, E. Lidorikis, J. Kivioja, C. Marinelli, T. Ryhanen, A. Morpurgo, J.N. Coleman, V. Nicolosi, L. Colombo, A. Fert, M. Garcia-Hernandez, A. Bachtold, G.F. Schneider, F. Guinea, C. Dekker, M. Barbone, Z. Sun, C. Galiotis, A.N. Grigorenko, G. Konstantatos, A. Kis, M. Katsnelson, L. Vandersypen, A. Loiseau, V. Morandi, D. Neumaier, E. Treossi, V. Pellegrini, M. Polini, A. Tredicucci, G.M. Williams, B. Hee Hong, J.-H. Ahn, J. Min Kim, H. Zirath, B.J. van Wees, H. van der Zant, L. Occhipinti, A. Di Matteo, I.A. Kinloch, T. Seyller, E. Quesnel, X. Feng, K. Teo, N. Rupesinghe, P. Hakonen, S.R.T. Neil, Q. Tannock, T. Lofwander, J. Kinaret, Science and technology roadmap for graphene, related two-dimensional crystals, and hybrid systems, Nanoscale 7 (2015) 4598–4810.

[3] J.S. Bunch, S.S. Verbridge, J.S. Alden, A.M. van der Zande, J.M. Parpia, H.G. Craighead, P.L. McEuen, Impermeable atomic membranes, Nano Lett. 8 (8) (2008) 2458–2462.

[4] D. Prasai, J.C. Tuberquia, R.R. Harl, G.K. Jennings, K.I. Bolotin, Graphene: corrosion-inhibiting coating, ACS Nano 6 (2) (2012) 1102–1108.

[5] M. Topsakal, H. Şahin, S. Ciraci, Graphene coatings: an efficient protection from oxidation, Phys. Rev. B 85 (15) (2012) 155445.
[6] S. Chen, L. Brown, M. Levendorf, W. Cai, S.-Y. Ju, J. Edgeworth, X. Li, C.W. Magnuson, A. Velamakanni, R.D. Piner, J. Kang, J. Park, R.S. Ruoff, Oxidation resistance of graphene-coated Cu and Cu/Ni alloy, ACS Nano 5 (2) (2011) 1321–1327.
[7] M. Schriver, W. Regan, W.J. Gannett, A.M. Zaniewski, M.F. Crommie, A. Zettl, Graphene as a long-term metal oxidation barrier: worse than nothing, ACS Nano 7 (7) (2013) 5763–5768.
[8] N.-W. Pu, G.-N. Shi, Y.-M. Liu, X. Sun, J.-K. Chang, C.-L. Sun, M.-D. Ger, C.-Y. Chen, P.-C. Wang, Y.-Y. Peng, C.-H. Wu, S. Lawes, Graphene grown on stainless steel as a high-performance and ecofriendly anti-corrosion coating for polymer electrolyte membrane fuel cell bipolar plates, J. Power Sources 282 (0) (2015) 248–256.
[9] A. Hermann, T. Chaudhuri, P. Spagnol, Bipolar plates for PEM fuel cells: a review, Int. J. Hydrogen Energy 30 (12) (2005) 1297–1302.
[10] H. Tawfik, Y. Hung, D. Mahajan, Metal bipolar plates for PEM fuel cell – a review, J. Power Sources 163 (2) (2007) 755–767.
[11] A. C. Stoot, R. Birney and T. J. Booth, "Working electrode holder and electrochemical cell". Patent EP14178928, 2014.
[12] A.C. Ferrari, J.C. Meyer, V. Scardaci, C. Casiraghi, M. Lazzeri, F. Mauri, S. Piscanec, D. Jiang, K.S. Novoselov, S. Roth, A.K. Geim, Raman spectrum of graphene and graphene layers, Phys. Rev. Lett. 97 (Oct 2006) 187401.
[13] K.S. Kim, Y. Zhao, H. Jang, S.Y. Lee, J.M. Kim, K.S. Kim, J.-H. Ahn, P. Kim, J.-Y. Choi, B.H. Hong, Large-scale pattern growth of graphene films for stretchable transparent electrodes, Nature 457 (7230) (2009) 706–710.
[14] Y.-P. Hsieh, M. Hofmann, K.-W. Chang, J.G. Jhu, Y.-Y. Li, K.Y. Chen, C.C. Yang, W.-S. Chang, L.-C. Chen, Complete corrosion inhibition through graphene defect passivation, ACS Nano 8 (1) (2014) 443–448.
[15] R.A. Antunes, M.C.L. Oliveira, G. Ett, V. Ett, Corrosion of metal bipolar plates for PEM fuel cells: a review, Int. J. Hydrogen Energy 35 (8) (2010) 3632–3647.
[16] J. Sudagar, J. Lian, W. Sha, Electroless nickel, alloy, composite and nano coatings – a critical review, J. Alloys Compd. 571 (0) (2013) 183–204.
[17] L.L. Shreir, G.T. Burstein, Shreir's Corrosion, Elsevier, Cambridge, U.K, 2010.
[18] M.S. Dresselhaus, A. Jorio, M. Hofmann, G. Dresselhaus, R. Saito, Perspectives on carbon nanotubes and graphene Raman spectroscopy, Nano Lett. 10 (3) (2010) 751–758.
[19] Standard Test Method for Chemical Resistance of Protective Linings, ASTM, West Conshohocken, PA, 2012.
[20] W. Vielstich, Handbook of Fuel Cells: Fundamentals Technology and Applications, Wiley, 2009.
[21] N. Greenwood, A. Earnshaw, Chemistry of the Elements, the University of Michigan, Pergamon Press, 1984.
[22] L. Nilsson, M. Andersen, R. Balog, E. Lægsgaard, P. Hofmann, F. Besenbacher, B. Hammer, I. Stensgaard, L. Hornekær, Graphene coatings: probing the limits of the one atom thick protection layer, ACS nano 6 (11) (2012) 10258–10266.
[23] Y. Zhao, Y. Xie, Y.Y. Hui, L. Tang, W. Jie, Y. Jiang, L. Xu, S.P. Lau, Y. Chai, Highly impermeable and transparent graphene as an ultra-thin protection barrier for Ag thin films, J. Mater. Chem. C 1 (32) (2013) 4956–4961.
[24] K. Holmberg, H. Ronkainen, A. Matthews, Tribology of thin coatings, Ceram. Int. 26 (7) (2000) 787–795.
[25] J. Valli, A Review of Adhesion test methods for thin hard coatings, J. Vac. Sci. Technol. 4 (1986) 3007–3014.
[26] R.K.S. Raman, P.C. Banerjee, D.E. Lobo, H. Gullapalli, M. Sumandasa, A. Kumar, L. Choudhary, R. Tkacz, P.M. Ajayan, M. Majumder, Protecting copper from electrochemical degradation by graphene coating, Carbon 50 (11) (2012) 4040–4045.

Multilayer graphene for long-term corrosion protection of stainless steel bipolar plates for polymer electrolyte membrane fuel cell

*Adam C. Stoot*ǂ, *Luca Camilli*ǂ, *Susie-Ann Spiegelhauer*¤, *Feng Yu*ǂ, *Peter Bøggild*ǂ*.

ǂTechnical University of Denmark, Department of Micro- and Nanotechnology, Kgs. Lyngby, DK-2800, Denmark

¤Accoat, SP-Group A/S, Kvistgård, DK-3490, Denmark

ASSOCIATED CONTENT

Image of the Atlas cell test set-up used for long-term testing

S1: The cell is half filled with boiling simulated seawater. In either side of the cell (see black clamps), a sample is mounted with the liquid level crossing its centre so that half of the sample is exposed to liquid environment, half to vapour.

Energy dispersive X-ray spectroscopy (EDS) spectra of graphene-uncoated (Ni/SS) and graphene-coated nickel sample (G/Ni/SS).

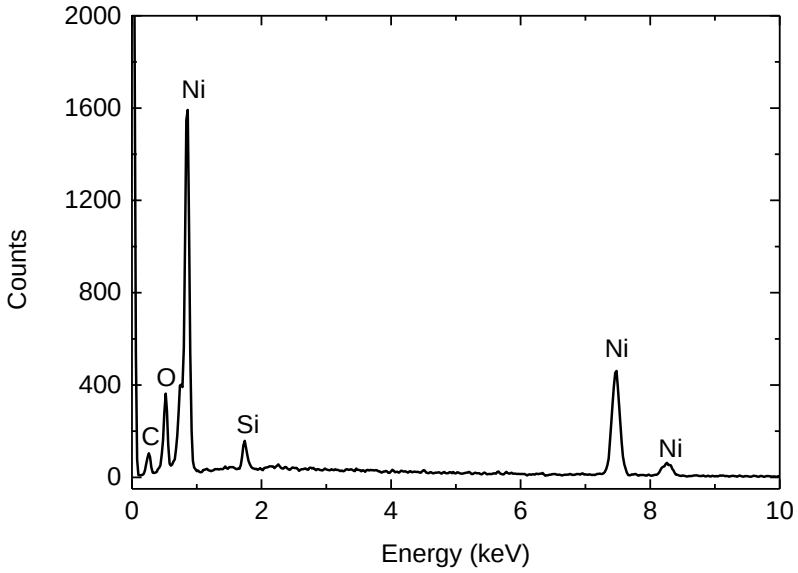

S2: EDS spectrum of the Ni/SS sample after the Atlas cell test.

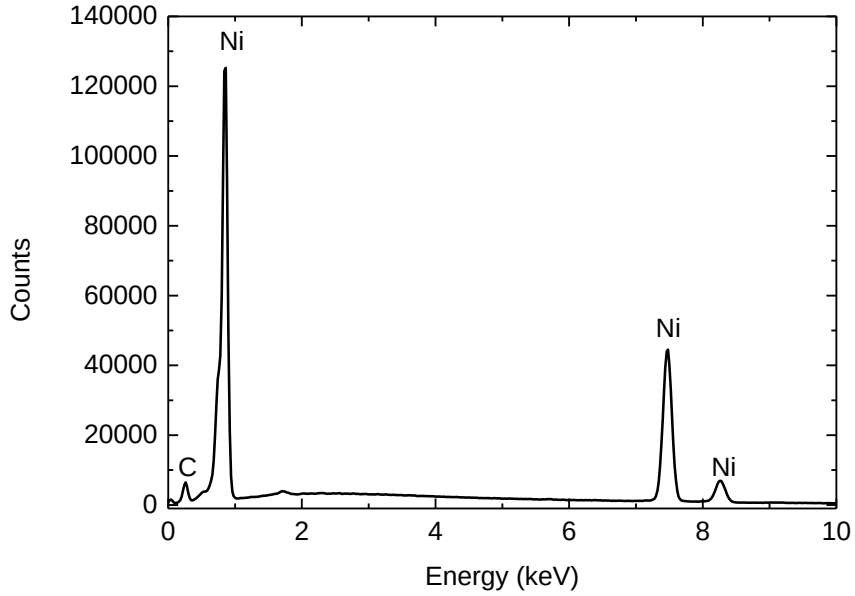

S3: EDS spectrum of the G/Ni/SS sample after the Atlas cell test.

Selected polarisation scans for bare stainless steel (SS), Ni/SS and G/Ni/SS sample

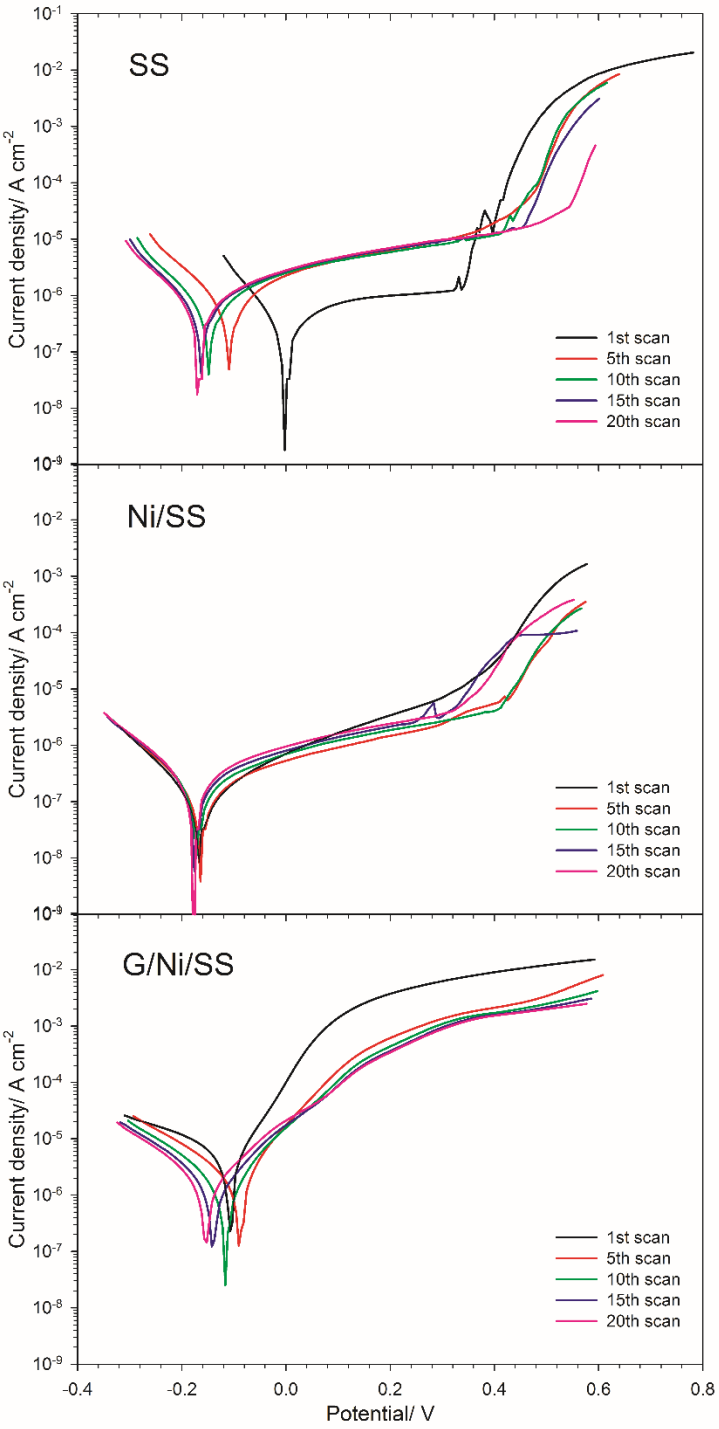

S4: Selected polarisation scans for SS, Ni/SS and G/Ni/SS samples.

The corrosion potential of bare SS304 sample was continuously shifted to lower values, indicating the sample was getting more susceptible to corrosion. This may stems from the formation and

breakdown of passive layer on the surface of SS304, which should also be responsible for the change in corrosion kinetics, as this corrosion process is under anodic control.

As for the Ni/SS, the corrosion potential and current density kept constant during the twenty scans, indicating excellent corrosion and passivation resistance of the carbon steel introduced by nickel seed layer.

In the case of graphene coating, the corrosion process turns out to be controlled by both cathodic and anodic reaction, different from the dominant anodic process seen for bare SS304 with or without the nickel seed layer. Besides, if compared to the bare SS sample, the difference in line shape, corrosion density and potential for the graphene-coated sample is considerably lower over the twenty consecutive scans.

Scanning electron image (SEM) of the G/Ni/SS after Fast Ion Beam milling (FIB)

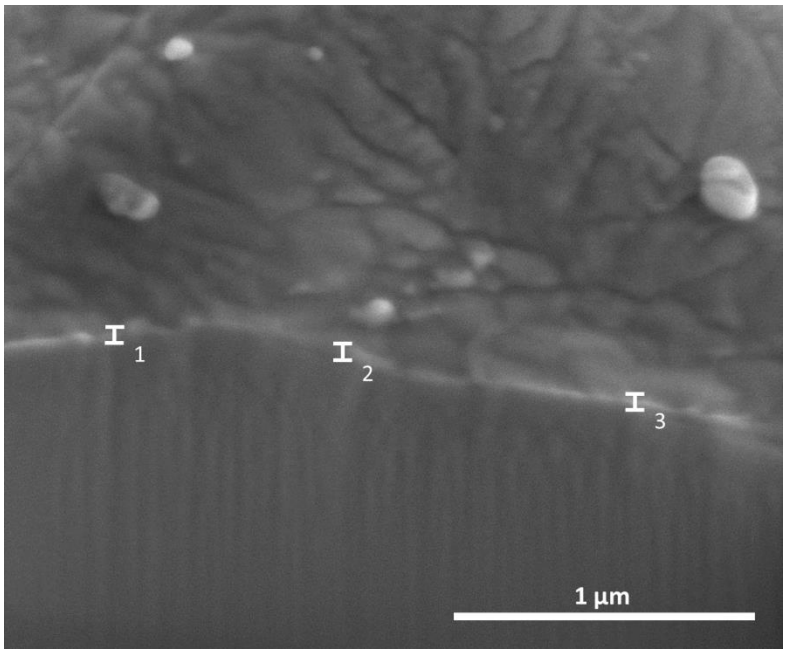

S 5: FIB SEM of G/Ni/SS. I_1, I_2 and I_3 are measurement points where thicknesses in the range of 25- 40 nm were measured. It corresponds roughly to a film with 75 to 120 layers of graphene.

X-ray diffraction characterisation of the (Atlas-cell) tested samples

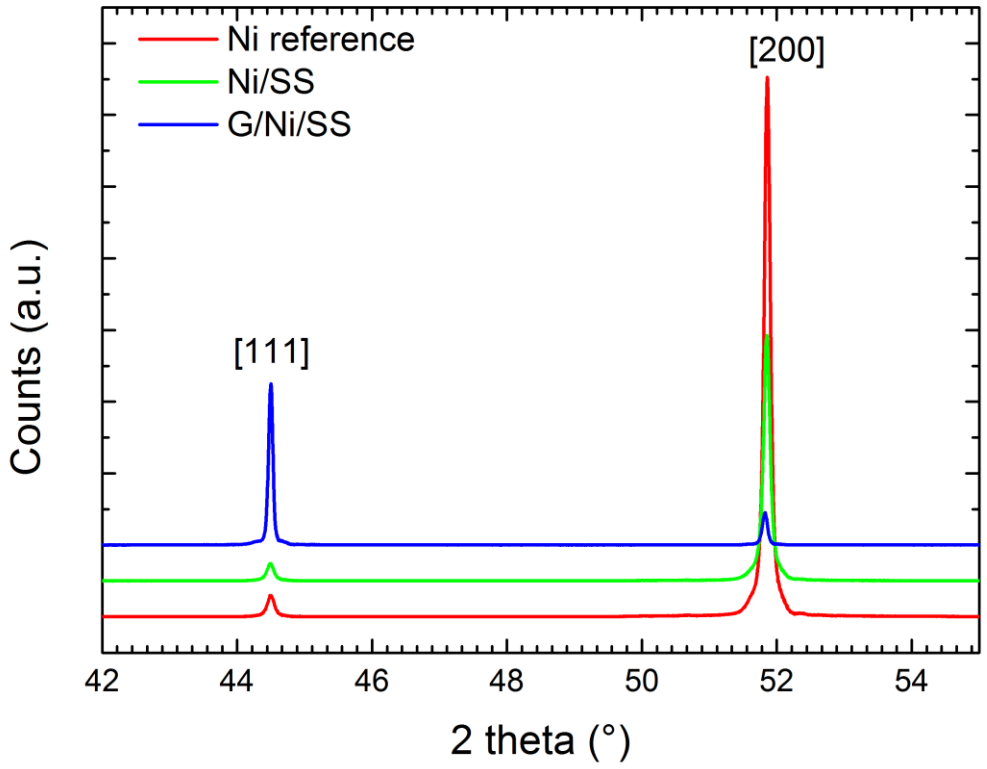

S6: X-ray diffraction spectra of a Ni/SS reference sample (red curve) along with Atlas-cell tested Ni/SS (green curve) and G/Ni/SS (blue curve). The peak width indicates µm-sized crystalline grains for all samples. The intensity from the [111] crystal orientation is larger for the G/Ni/SS sample, which is probably a result of the annealing process during graphene growth.

Appendix B

Failure of multi-layer graphene coatings in acidic media

Article published in RSC Advances

RSC Advances

PAPER

View Article Online
View Journal | View Issue

Cite this: *RSC Adv.*, 2016, **6**, 21497

Failure of multi-layer graphene coatings in acidic media†

F. Yu, A. C. Stoot, P. Bøggild and L. Camilli*

Being impermeable to all gases, graphene has been proposed as an effective ultrathin barrier film and protective coating. However, here it is shown how the gastight property of graphene-based coatings may indirectly lead to their catastrophic failure under certain conditions. When nickel coated with thick, high-quality chemical vapor deposited multilayered graphene is exposed to acidic solutions, a dramatic evolution of gas is observed at the coating–substrate interface. The gas bubbles grow and merge, eventually rupturing and delaminating the coating. This behavior, attributed to cathodic hydrogen evolution, can also occur spontaneously on a range of other technologically important metals and alloys based on iron, zinc, aluminum and manganese; this makes these findings relevant for practical applications of graphene-based coatings.

Received 18th January 2016
Accepted 15th February 2016

DOI: 10.1039/c6ra01556e

www.rsc.org/advances

Introduction

Corrosion, the gradual degradation of metals and alloys by interaction with the environment, is a problem of enormous significance. Costs due to corrosion represent 3–4% of the worldwide BNP.[1] Corrosion and oxidation cause waste of valuable resources, loss or contamination of product, reduction in efficiency and costly maintenance across many industries. Moreover, failure of critical metal parts is not just expensive, but potentially dangerous. Passivating and protective coatings comprise a widely applied approach to improve the surface properties of substrates and to protect materials from environmental degradation. To this aim, efficiently separating the substrate from the external environment is one of the most critical functions of a protective coating.

The hexagonal lattice of defect-free monolayer graphene has been proved both theoretically and experimentally to be impermeable to all liquids and gases including the smallest molecules, hydrogen and helium.[2–4] This outstanding feature has led to an enormous interest in employing graphene as an anticorrosion coating for metals and alloys.[5–7] Nevertheless, chemical vapour deposited (CVD) monolayer graphene generally exhibits defects through which molecules and radical species can diffuse, thus locally initiating metal corrosion.[8–10] In addition, it has been reported that once these local corrosion processes begin to take place underneath a monolayer graphene cover, they are actually even accelerated by the presence of graphene itself.[11] In this context, using a film made of several layers instead of a monolayer is one logical approach to improve performance of graphene-based protective coatings.[12–14] In this work, however, we report a so far unnoticed issue related to coatings with low permeability and high structural integrity. Indeed, when nickel coated with a thick, high-quality multilayered graphene is immersed in an acidic solution, the cathodic reaction spontaneously yields hydrogen at the nickel surface. The formed gas is not able to escape the high quality regions of the graphene film and therefore remains trapped and eventually forms bubbles, which can even lead to the delamination of the whole coating.

Experimental

Growth, transfer and characterization of MLG

Nickel foil (part no. 12722 from Alfa Aesar) was acetone ultrasonicated before graphene growth. Atmospheric pressure CVD growth was conducted with an AS-ONE CVD system from Annealsys. After loading the samples into the growth chamber, the chamber was evacuated with a rotary pump and then flushed with Ar three times before finally filling it up to atmospheric pressure. Next, the samples were heated at 950 °C for 15 min under the co-flow of 120 sccm and 100 sccm of Ar and H_2, respectively. The growth process was then carried out for 5 min at 950 °C with 2 sccm C_2H_2 and 100 sccm H_2. Lastly, the chamber was cooled down with a rate of 20 °C s^{-1} after the pressure was pumped down below 5 mbar.

Transfer of graphene coating onto glass slide or ~88 nm SiO_2 wafer was carried out *via* chemical etching of nickel in 5% HCl and 30% H_2O_2 mixed solution for 24 hours.

Optical images were taken with a Nikon Eclipse L200N optical microscope, while Raman spectra were collected by

Technical University of Denmark, Department of Micro- and Nanotechnology, Kgs. Lyngby, DK-2800, Denmark. E-mail: lcam@nanotech.dtu.dk

† Electronic supplementary information (ESI) available: Polarization curves, electrochemical impedance spectroscopy, further Raman characterizations of the coating and the video of the real-time microscope experiments. See DOI: 10.1039/c6ra01556e

a Thermo Fisher Scientific DXR Raman microscope (excitation wavelength 455 nm). Quanta 200 FEG environmental scanning electron microscope (SEM) and FEI Titan T20 G2 transmission electron microscope (TEM) were employed for the electron microscopy characterizations.

Electrochemical measurements

Polarization curves and electrochemical impedance spectroscopy (EIS) measurements were carried out with a three-electrode cell, using a AgCl/Ag reference electrode, a Pt foil as a counter electrode and a working electrode of tested samples, with a solution of 0.5 M HCl (aq) being the electrolyte. All measurements were repeated on three samples in a Faraday cage using a Gamry Reference 3000 potentiostat. Polarization curves were obtained after one hour of immersion by sweeping the potential from −300 mV to 300 mV *vs.* the open circuit potential (OCP) with a scan rate of 0.5 mV s^{-1}. EIS spectra were collected by applying a ±10 mV sinusoidal perturbation (*vs.* OCP) on tested samples at a frequency range from 100 000 Hz to 0.01 Hz with 10 points per decade.

Real-time microscopy experiments of hydrogen formation below the MLG coating

The *real-time* microscopy experiments were performed with a Nikon Eclipse L200N optical microscope and a Helios Nano Lab electron microscope. In both cases, the samples were exposed to 0.5 M HCl (aq) solution. The reader can refer to the next paragraph for more details of the performed *real-time* experiments.

Results and discussion

Fig. 1a reports an example of the bare nickel foil and the nickel foil coated with a CVD grown multilayered graphene (MLG) film, which have been the subject of this study. The MLG film is hydrophobic with a measured static water contact angle of 102.0° ± 0.4°, and floats as a monolithic piece on water after nickel being chemically etched (Fig. 1b), even though it is more than twice as dense as water. Raman spectroscopy provides information about the stacking order of the MLG[15] film and the density of defects.[16] For our samples, we find both AB-stacked and turbostratic regions (blue and red curve in Fig. 1c, respectively), with a higher prevalence of the former case, as expected for CVD graphene.[17] Regarding defect density, the small D-peak to G-peak ratio (0.040 ± 0.010) is the hallmark of the high quality film in terms of structural defects. X-ray diffraction analysis reveals an average interlayer distance of ~3.3 Å (See ESI†). The cross-sectional transmission electron micrograph (TEM) displayed in Fig. 1d gives insight into the total thickness of the MLG film (around 100 nm) and highlights the constant interlayer distance of the film, as shown by the Fourier transform displayed in the inset.

Nickel and its alloys are usually corrosion resistant in neutral, alkaline and diluted acidic media, while they deteriorate in aerated aggressive acidic environment. Hence, to investigate the corrosion performance of MLG coatings on nickel, we

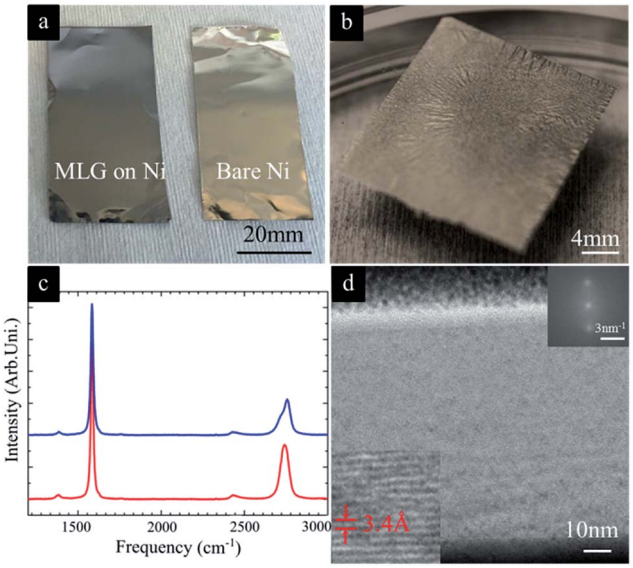

Fig. 1 (a) Multilayer graphene-coated (on the left) and bare (on the right) nickel foils. (b) Snapshot of the graphitic membrane floating on water after nickel substrate being chemically etched. (c) Two typical Raman spectra of the graphitic film showing the coexistence of regions with AB-stacking (top, blue curve) and turbostratic stacking (bottom, red curve). (d) Cross-section transmission electron microscope micrograph of the graphitic film on Ni foil. Insets: Fourier transform (top right corner) and high-resolution image (bottom left corner) both illustrating the high graphitization degree of the MLG film.

employ standard potentiodynamic polarization technique in 0.5 M HCl solution (pH = 0.3). With this method, by sweeping potential from negative to positive values with respect to the open circuit potential, the sample is electrochemically polarized, which allows us to obtain information about thermodynamics (*i.e.*, corrosion potential) and kinetics (*i.e.*, corrosion current density and corrosion rate) of the corrosion process.[18] Here, we estimate that the corrosion rate for the MLG-coated nickel is less than half that of the bare nickel specimen (see ESI† for more details). This trend is also confirmed by electrochemical impedance spectroscopy analysis (see ESI†) and is in agreement with previous studies on coatings based on few-layer graphene on nickel.[19] During the test, as expected, we could notice formation of hydrogen bubbles on the surface of both samples at the cathodic branch of the polarization curves (Fig. 2a), according to the reduction reaction:

$$2H_3O^+(aq) + 2e^- \rightarrow H_2(g) + 2H_2O(aq) \quad (1)$$

We further investigated the specimen surface by means of scanning electron microscopy (SEM). In Fig. 2b we report an example of an area where the MLG coating was locally delaminated. The approximately circular shape of the hole in the coating suggests that it has been caused upon rupture of a hydrogen bubble. However, the outward direction of the remaining MLG flakes at the surface near the edges of the hole suggests that the bubble was not located on the surface of the

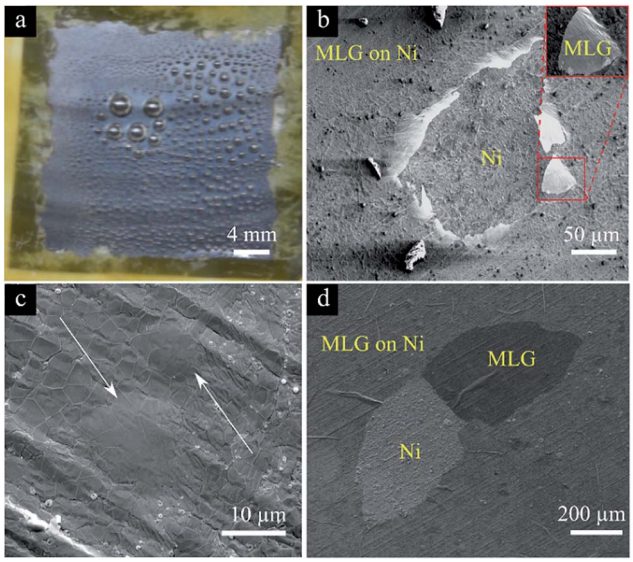

Fig. 2 (a) Snapshot of the MLG-coated nickel sample while being tested by potentiodynamic scanning at negative applied voltage (cathodic branch). Hydrogen bubbles can be observed on the surface of the sample. (b) SEM micrograph of the MLG-coated nickel foil after potentiodynamic scanning. At the center of the picture, the coating has been delaminated probably by a bursting hydrogen bubble; broken edges of the coating are now pointing outwards, suggesting that the burst bubble was located at the coating/substrate interface (inset). (c) SEM image of two bubbles – highlighted by the white arrows – found under the coating after applying constant negative potential (−0.6 V *vs.* Ag/AgCl) for 3 min to the MLG-coated nickel foil in 0.5 M HCl solution. (d) A portion of the MLG coating has been delaminated after 30 min of constant exposure to a potential of −0.6 V in 0.5 M HCl solution and still lies on the sample surface.

coating, but rather at the interface between it and the nickel substrate.

The formation of hydrogen bubbles at the interface between coating and substrate in aggressive acid environment is a known phenomenon in corrosion science.[20,21] Also, it is worth reminding that, though under different conditions, the evolution of hydrogen bubbles at the interface between graphene and metal substrate during the cathodic reaction is a method largely used for graphene transfer.[22]

To investigate whether the hydrogen bubbles are being generated both at the surface of the MLG film and underneath, we applied a fixed negative potential (−0.6 V *vs.* Ag/AgCl) to the coated nickel sample in 0.5 M HCl solution for only a short period of time (3 min). In this way, the bubbles can be observed at the interface before they become large enough to burst. As soon as the potential was applied, numerous hydrogen bubbles appeared at the surface of the coating. After this test, the sample was rinsed with water and gently blow-dried with nitrogen. Under the optical microscope, a few nearly circular protrusions of approximately 20 μm in diameter were found at seemingly un-correlated locations under the graphitic film. To prove that these protrusions are actually blisters, *i.e.* trapped gas underneath the graphene film and not particles or contaminants present on the surface, we characterized these structures by scanning electron microscopy. Fig. 2c displays two such protrusions that indeed seem to be blisters of the coating. Notably, the characteristic graphene wrinkles[23] at the base of the blisters gradually unfold near the center of the blister, as would be expected. To demonstrate that these blisters can become large enough to burst and locally delaminate the coating, we apply a fixed negative potential (−0.6 V *vs.* Ag/AgCl) to the coated nickel sample in 0.5 M HCl solution for 30 min. As displayed in Fig. 2d, SEM analysis shows that in many places, the coating is no longer covering the metal substrate, similar to what was found after the potentiodynamic scan experiment, which is another indication that the film has now ruptured and delaminated. Raman spectroscopy was also used to prove that no graphene is present in the delaminated areas (see ESI†).

Raman spectroscopy is also known to provide information regarding mechanical stress in the graphene lattice. A significant blue-shift of all the peaks in the spectrum has been indeed reported for the case of micro-balloons made of single and bi-layer graphene on a oxidized silicon substrate.[24] However, within our samples, we do not observe any remarkable shift of the peaks in the Raman spectra either recorded at the center of the blister, at its base, or away from the blister on a flat graphene region (see ESI†). This can be understood looking at Fig. 2c, where the wrinkles seem to unfold at the center of the blister, thereby relieving any stress caused by the trapped hydrogen. The wrinkles are naturally formed upon cooling after the growth process as a consequence of the different thermal expansion coefficients of graphene and nickel;[23] likewise the unfolding of wrinkles is a way to release the mechanical stress caused by the formation of the blisters.

To gain more insights into the formation of the hydrogen bubbles below the MLG film, we set up two experiments for real-time monitoring of the process. The first experiment consists of placing a droplet of 0.5 M HCl solution in the center of the MLG-coated Ni foil under an optical microscope. Already after 5 min, few blisters can be seen randomly distributed over the imaged area, initially with diameters ranging from 10 μm to 20 μm (Fig. 3a). These blisters grow over time due to a build-up of hydrogen at the interface between nickel and the coating until they eventually start to merge. This behavior continues as long as the HCl droplet is present on top of the MLG film. After two hours the blisters can be larger than 100 μm and locally lift up the coating (Fig. 3a). It is worth noticing that the time scale for hydrogen bubble formation actually varies depending on the sample under study. Interestingly, once the acid droplet is removed, the region of the sample under the droplet does not seem to be visibly corroded, *i.e.* there is no noticeable change in color or appearance. On the other hand, the region of the sample surrounding the droplet, which is thus not in immediate contact with the acid, exhibits remarkable signs of degradation (see Fig. 3b and c, respectively). If the acid is distributed all over the sample area, the blisters eventually cause delamination of the whole coating (see ESI†).

In the second experiment, SEM is used in order to study the hydrogen bubble formation in real-time with higher spatial resolution. A droplet of 0.5 M HCl solution is placed in the center of the MLG-coated nickel foil, and gently removed with a tissue.

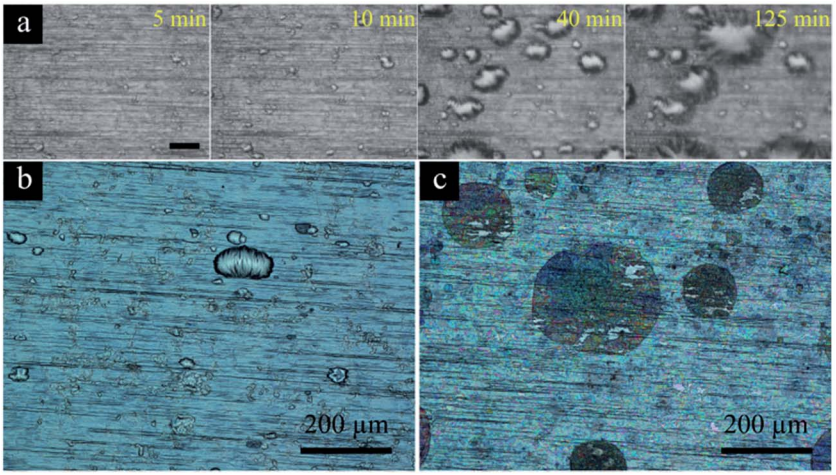

Fig. 3 (a) Sequence of optical microscope images taken from a MLG-coated nickel foil with a droplet of 0.5 M HCl solution on top. The pictures are recorded through the acid droplet – hence the low quality of the images. The scale bar is 100 μm. (b and c) Optical images of an area under the acid droplet (c) and away from it (c). The sample represented in (a) is different from the one reported in (b) and (c).

The sample is mounted inside the scanning electron microscope without prior rinsing or blow-drying. When the electron beam is focused on a flat region of the sample, a dramatic hydrogen evolution takes place below the MLG film (Fig. 4).

At first, a single micrometer-size blister is observed, then, other smaller blisters are formed all over the scanned area (Fig. 4b and c, respectively). At lower magnification, it is possible to see that the blister-like protrusions are mainly found in the area that was initially irradiated by the scanning electron beam (see ESI†). This might be explained by a monolayer of the acidic solution still being adsorbed on the surface[25] as well as within defects and crevices of the MLG film after the sample has being placed inside the microscope and evacuated. Then, the local heating and the creation of defects[26] induced by the electron beam trigger and accelerate the diffusion of water through the MLG coating thus giving rise to the hydrogen bubble formation. This experiment points out that (i) the fact that such gas evolution only occurs with samples that have been exposed to HCl solution rules out that this phenomenon is caused by the presence of residual gas trapped either between graphene and nickel or into the nickel itself during the CVD process; and (ii) the trapping of gas at the graphene–metal interface in vacuum conditions inside the SEM chamber indicates that the overall quality and integrity of the film is high, as also corroborated by Raman spectroscopy investigation (see Fig. 1c).

To explain why hydrogen is formed at the interface, we suggest that, even if few, local defects and inhomogeneities are intrinsically present in the coating. Notably, such inhomogeneities are areas with higher defect density, grain boundaries,[27,28] and sometimes also fewer layers (see ESI†). These areas may originate from local impurities on the nickel surface, temperature gradients during the synthesis process or different catalytic activity of the nickel grains, as already reported in the literature for CVD grown multilayer graphene.[29] In this scenario, as the coating is placed in contact with the acidic solution, water fills these defects and inhomogeneities thus forming a bridge which allows protons to shuttle from outside the coating to the nickel surface, through the hydrogen-bonding network (Fig. 5), similar to the case of proton transport through the channel of carbon nanotubes.[30,31] As water reaches the nickel, the cathodic reaction locally takes place. In fact, as described by the potential-pH diagram of nickel/water system, also known as Pourbaix diagram,[32] the evolution of hydrogen at the nickel–water interface is spontaneous at the low pH level used in this study. As the MLG coating on nickel shifts the open circuit potential of nickel by only −25 mV (see ESI†), the hydrogen evolution process for the MLG-coated nickel is still spontaneous, in accordance with our observations. Once hydrogen is formed at the coating-metal interface, we can assume it diffuses on the nickel surface, as observed in similar systems,[33] and

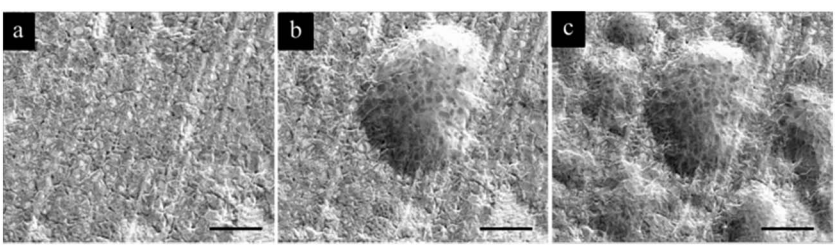

Fig. 4 Consecutive SEM micrographs recorded on a MLG-coated nickel foil after a droplet of 0.5 M HCl has been placed on top and subsequently removed. The formation of hydrogen blisters over time is reported. The scale bar is 20 μm.

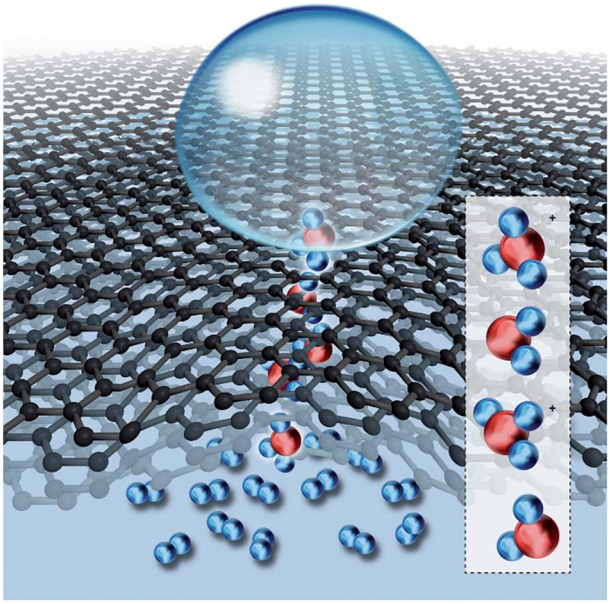

Fig. 5 Drawing of the proposed mechanism for hydrogen formation under a droplet of 0.5 M HCl solution. Once the solution reaches the nickel surface through defective areas in the coating, protons – which are carried by water molecules *via* the Grotthuss mechanism, jumping from a molecule to the next one (inset) – are spontaneously reduced to hydrogen. The red balls represent oxygen atoms, while the blue balls stand for hydrogen atoms.

merge, thus giving rise to the observed blisters. Since the majority of the coating is made of regions with very small apparent density of defects, a build-up of hydrogen occurs under the MLG film, produces bubbles that grow and merge, and eventually delaminate the coating. The formed hydrogen is not likely to pass through the coating *via* local defects and inhomogeneities, since these are clogged by water molecules, as previously suggested for helium-leak-tight coatings made of graphene oxide.[34] The fact that the formation of hydrogen bubbles takes place on a different time scale depending on the sample under study could be explained by varying density of inhomogeneous areas within the coating, which is easily accountable by variations of the nickel foil substrates or inevitable differences in the exact growth conditions commonly experienced for CVD graphene growth. Here, it is worth pointing out that proton transport through a defect-free single layer of graphene has already been observed, but not through a bilayer.[35] In this study we report on the performance of a coating comprised of hundreds of graphene layers, and therefore cannot immediately adopt the explanation proposed by Hu and co-workers,[35] where a tunnel mechanism was invoked.

The dramatic degradation of the sample in the regions surrounding the acid droplets can be ascribed to the formation of a galvanic cell between nickel and graphene. Every electrochemical reaction consists of a cathodic and an anodic part. In the case of the acid droplet deposited on the middle of the MLG-coated sample, the cathodic reaction (*i.e.*, reduction of protons to hydrogen) occurs under the droplet due to the abundance of

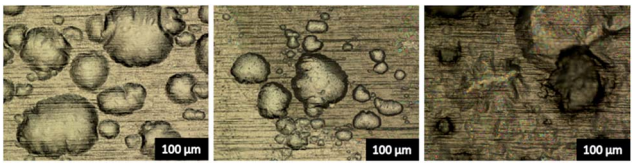

Fig. 6 Optical micrograph of three MLG-coated nickel foils exposed for 240 min to 0.5 M HCl (left picture), 0.5 M H_2SO_4 (center picture) and 0.5 M HNO_3 (right picture). In all cases, the MLG coating has been lifted in several areas due to evolution of hydrogen at the nickel-coating interface.

protons, while the anodic one (*i.e.*, oxidation of the nickel) takes place away from the droplet. While reducing protons to hydrogen, electrons are being continuously depleted in the region under the droplets. In this picture, electrons will move from the region surrounding the droplet, to the region below the droplet in compensation. Here, as already reported in the case of single layer graphene grown on copper foil,[11] the electrons may migrate through the graphene film due to its high conductivity, rather than through the passivated metal surface, thus giving rise to formation of a galvanic cell which spreads the oxidation of nickel to all regions in contact with graphene.

Ultimately, in order to verify that the formation of hydrogen beneath a graphene coating is a reaction occurring spontaneously in the system nickel/water at low pH values, regardless of the anions that are present in solution, we repeat the experiment of the droplet placed at the center of the coated substrate using different acids. At this aim, a MLG-coated nickel foil is cut into three pieces. The first piece is tested with HCl, the second one with H_2SO_4 whereas the third one with HNO_3, all solutions being at the same concentration (namely 0.5 M). As displayed in Fig. 6, after 240 min of exposure, the coating results in being lifted up in several areas by hydrogen in all the three cases, regardless of the acids that was used.

Conclusions

Our observations show that protective coatings based on CVD MLG might fail in certain chemical environments. Even for MLG consisting of hundreds of layers, with nominally very few defects, the few but inevitable inhomogeneities provide sufficient pathways for acid to reach the Ni surface, where hydrogen is spontaneously formed. We suggest that the very integrity and quality of the MLG coating prevents excess gas to escape at a rate that matches the rate of which it is formed, which thus leads to hydrogen build-up and eventually catastrophic delamination to the coating. This implies that coatings based on graphene and other two-dimensional materials, which are considered attractive for corrosion protection due to their impermeability, may fail for the same reason. Notably, the vulnerability to gas evolution below the coating may become increasingly severe as the thickness, quality and homogeneity of the coating is improved, as this will prevent gas from escaping in a non-destructive manner. Our findings may be relevant for

other electrochemically active metals and alloys made for instance of iron, zinc, manganese and aluminium.

On the other hand, however, it is also worth pointing out that (i) the possibility of spontaneously producing and effectively trapping hydrogen (or other gases) calls for further investigations of such MLG film in fields such as gas storage and production; and (ii) the capability of such membranes of being selectively permeable to water might be of great interest for particular environmental applications.[36]

Acknowledgements

The authors are grateful to Dr Rahul Raveendran Nair and Jijo Abraham for providing the XRD data and for the useful discussions. The authors also thank Dr David Mackenzie for help with the analysis of Raman data. This project was supported by The Strategic Danish Research collaboration (DSF) with the DA-GATE project (12-131827) and through the high technology foundation (HTF) with the NIAGRA project (058-2012-4). L. C. thanks funding support from The Danish Council for Independent Research | Technology and Production Sciences (FTP) through the Mobilex grant 'Atomically thin coatings'.

Notes and references

1 A. El-Meligi, *Recent Pat. Corros. Sci.*, 2010, **2**, 22–33.
2 J. S. Bunch, S. S. Verbridge, J. S. Alden, A. M. van der Zande, J. M. Parpia, H. G. Craighead and P. L. McEuen, *Nano Lett.*, 2008, **8**, 2458–2462.
3 O. Leenaerts, B. Partoens and F. M. Peeters, *Appl. Phys. Lett.*, 2008, **93**, 193107.
4 M. Miao, M. B. Nardelli, Q. Wang and Y. Liu, *Phys. Chem. Chem. Phys.*, 2013, **15**, 16132–16137.
5 S. Chen, L. Brown, M. Levendorf, W. Cai, S.-Y. Ju, J. Edgeworth, X. Li, C. W. Magnuson, A. Velamakanni and R. D. Piner, *ACS Nano*, 2011, **5**, 1321–1327.
6 D. Prasai, J. C. Tuberquia, R. R. Harl, G. K. Jennings and K. I. Bolotin, *ACS Nano*, 2012, **6**, 1102–1108.
7 N. T. Kirkland, T. Schiller, N. Medhekar and N. Birbilis, *Corros. Sci.*, 2012, **56**, 1–4.
8 D. L. Duong, G. H. Han, S. M. Lee, F. Gunes, E. S. Kim, S. T. Kim, H. Kim, Q. H. Ta, K. P. So, S. J. Yoon, S. J. Chae, Y. W. Jo, M. H. Park, S. H. Chae, S. C. Lim, J. Y. Choi and Y. H. Lee, *Nature*, 2012, **490**, 235–239.
9 I. Wlasny, P. Dabrowski, M. Rogala, P. J. Kowalczyk, I. Pasternak, W. Strupinski, J. M. Baranowski and Z. Klusek, *Appl. Phys. Lett.*, 2013, **102**, 111601.
10 Y.-P. Hsieh, M. Hofmann, K.-W. Chang, J. G. Jhu, Y.-Y. Li, K. Y. Chen, C. C. Yang, W.-S. Chang and L.-C. Chen, *ACS Nano*, 2013, **8**, 443–448.
11 M. Schriver, W. Regan, W. J. Gannett, A. M. Zaniewski, M. F. Crommie and A. Zettl, *ACS Nano*, 2013, **7**, 5763–5768.
12 N.-W. Pu, G.-N. Shi, Y.-M. Liu, X. Sun, J.-K. Chang, C.-L. Sun, M.-D. Ger, C.-Y. Chen, P.-C. Wang, Y.-Y. Peng, C.-H. Wu and S. Lawes, *J. Power Sources*, 2015, **282**, 248–256.
13 A. C. Stoot, L. Camilli, S.-A. Spiegelhauer, F. Yu and P. Bøggild, *J. Power Sources*, 2015, **293**, 846–851.
14 Y. Su, V. G. Kravets, S. L. Wong, J. Waters, A. K. Geim and R. R. Nair, *Nat. Commun.*, 2014, **5**, 4843.
15 R. Rao, R. Podila, R. Tsuchikawa, J. Katoch, D. Tishler, A. M. Rao and M. Ishigami, *ACS Nano*, 2011, **5**, 1594–1599.
16 A. Eckmann, A. Felten, A. Mishchenko, L. Britnell, R. Krupke, K. S. Novoselov and C. Casiraghi, *Nano Lett.*, 2012, **12**, 3925–3930.
17 A. W. Tsen, L. Brown, R. W. Havener and J. Park, *Acc. Chem. Res.*, 2013, **46**, 2286–2296.
18 C. Lefrou, R. P. Nogueira, F. Huet and H. Takenouti, in *Shreir's Corrosion*, Elsevier, Oxford, 2010, pp. 13–51.
19 X. H. Ye, F. Yu, M. Curioni, Z. Lin, H. J. Zhang, H. W. Zhu, Z. Liu and M. L. Zhong, *RSC Adv.*, 2015, **5**, 35384–35390.
20 M. L. White, H. Vedage, R. D. Granata and H. Leidheiser Jr, *Ind. Eng. Chem. Res.*, 1986, **25**, 129–132.
21 H. Leidheiser Jr and M. W. Kendig, *Ind. Eng. Chem. Res.*, 1978, **17**, 54–55.
22 L. Gao, W. Ren, H. Xu, L. Jin, Z. Wang, T. Ma, L.-P. Ma, Z. Zhang, Q. Fu and L.-M. Peng, *Nat. Commun.*, 2012, **3**, 699.
23 S. J. Chae, F. Güneş, K. K. Kim, E. S. Kim, G. H. Han, S. M. Kim, H.-J. Shin, S.-M. Yoon, J.-Y. Choi, M. H. Park, C. W. Yang, D. Pribat and Y. H. Lee, *Adv. Mater.*, 2009, **21**, 2328–2333.
24 J. Zabel, R. R. Nair, A. Ott, T. Georgiou, A. K. Geim, K. S. Novoselov and C. Casiraghi, *Nano Lett.*, 2012, **12**, 617–621.
25 D. Chakarov, L. Österlund and B. Kasemo, *Vacuum*, 1995, **46**, 1109–1112.
26 J. Jones, P. Ecton, Y. Mo and J. Perez, *Appl. Phys. Lett.*, 2009, **95**, 246101.
27 S. C. O'Hern, C. A. Stewart, M. S. Boutilier, J.-C. Idrobo, S. Bhaviripudi, S. K. Das, J. Kong, T. Laoui, M. Atieh and R. Karnik, *ACS Nano*, 2012, **6**, 10130–10138.
28 M. S. Boutilier, C. Sun, S. C. O'Hern, H. Au, N. G. Hadjiconstantinou and R. Karnik, *ACS Nano*, 2014, **8**, 841–849.
29 A. Reina, X. Jia, J. Ho, D. Nezich, H. Son, V. Bulovic, M. S. Dresselhaus and J. Kong, *Nano Lett.*, 2009, **9**, 30–35.
30 C. Dellago, M. M. Naor and G. Hummer, *Phys. Rev. Lett.*, 2003, **90**, 105902.
31 D. J. Mann and M. D. Halls, *Phys. Rev. Lett.*, 2003, **90**, 195503.
32 M. Pourbaix and R. W. Staehle, in *Lectures on Electrochemical Corrosion*, Springer, 1973, pp. 83–183.
33 E. Stolyarova, D. Stolyarov, K. Bolotin, S. Ryu, L. Liu, K. Rim, M. Klima, M. Hybertsen, I. Pogorelsky and I. Pavlishin, *Nano Lett.*, 2008, **9**, 332–337.
34 R. Nair, H. Wu, P. Jayaram, I. Grigorieva and A. Geim, *Science*, 2012, **335**, 442–444.
35 S. Hu, M. Lozada-Hidalgo, F. C. Wang, A. Mishchenko, F. Schedin, R. R. Nair, E. W. Hill, D. W. Boukhvalov, M. I. Katsnelson, R. A. Dryfe, I. V. Grigorieva, H. A. Wu and A. K. Geim, *Nature*, 2014, **516**, 227–230.
36 F. Perreault, A. Fonseca de Faria and M. Elimelech, *Chem. Soc. Rev.*, 2015, **44**, 5861–5896.

Supporting Information

Failure of graphene-based protective coatings in acidic media

*Feng Yu, Adam C. Stoot, P. Bøggild, Luca Camilli**

Technical University of Denmark, Department of Micro- and Nanotechnology, Kgs. Lyngby, DK-2800, Denmark

**email: lcam@nanotech.dtu.dk*

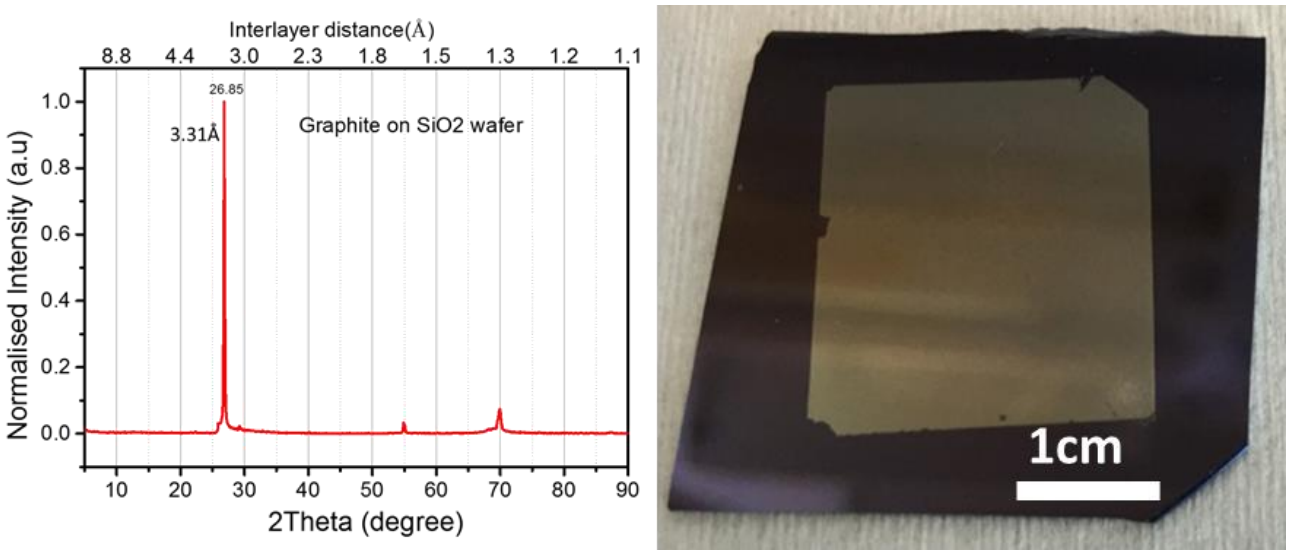

Figure S1. (left) X-ray diffraction pattern (CuKα excitation source) of a multilayer graphene (MLG) film deposited on a ~88nm SiO_2 substrate (right). The main peak, at around 27 degree, is due to the diffraction from the (002) planes of the graphitic film and gives an average interlayer distance of 3.31Å.

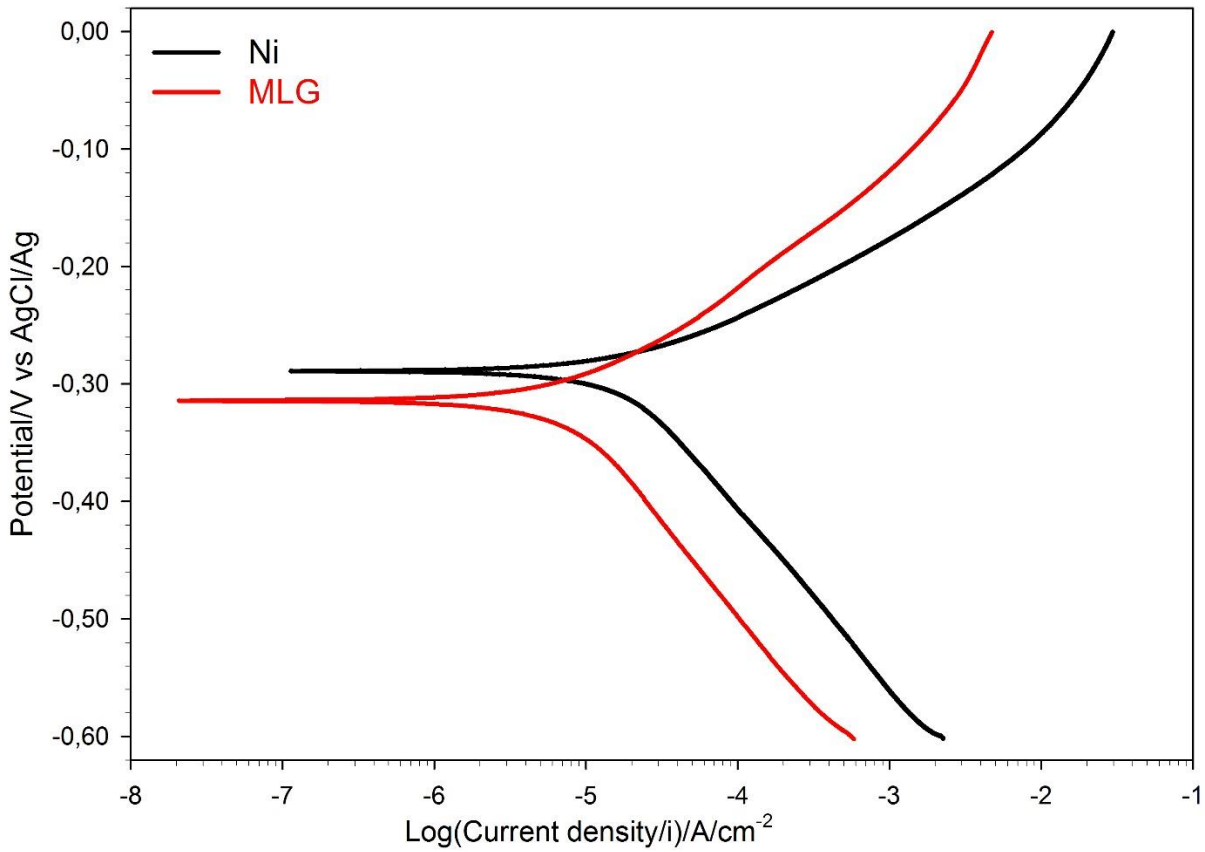

Figure S2. Polarization scans of both bare (dark curve) and MLG-coated (red curve) Ni samples after immersion in 0.5M HCl for 1 hour. The intersect between the extrapolation of the linear regions on both the cathodic and the anodic side of the current density minimum gives the corrosion potential (-290mV for bare nickel, -315mV for MLG-coated nickel) along with the corrosion current, I_{corr} (21μA/cm^2 and 9μA/cm^2 for bare and MLG-coated nickel, respectively). This, in turn, can be used to estimate the corrosion rate of the two systems: $CR = \frac{I_{corr} \cdot K \cdot EW}{\rho \cdot A}$ wherein K = 3272 mm/year, Nickel equivalent weight (EW) = 29g and the area is the expose working electrode area (A)[1]. The corrosion rates are calculated to be 0.226mm/year for bare nickel and 0.097mm/year for MLG-coated nickel.

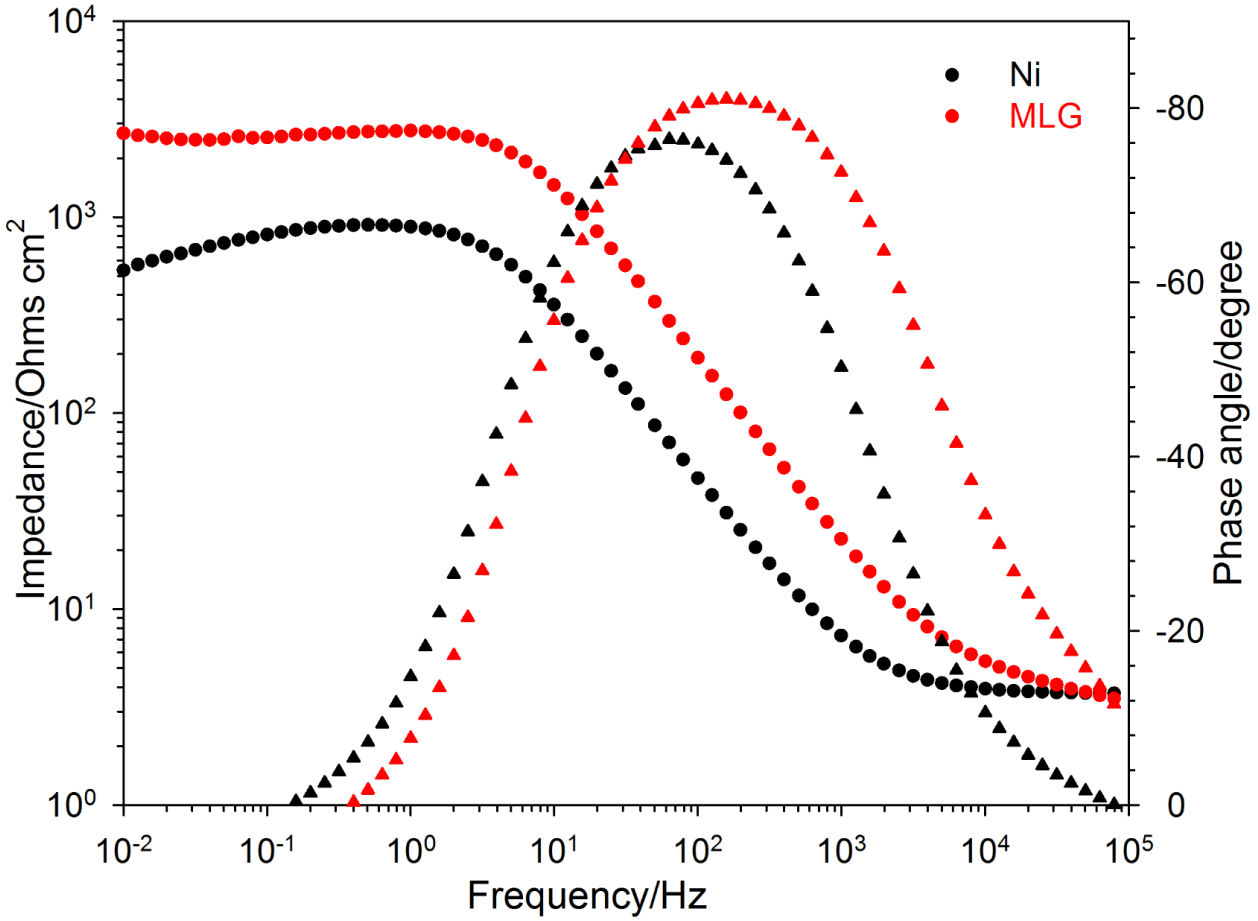

Figure S3. Electrochemical impedance spectroscopy of both Ni (black curves) and MLG-coated Ni (red curves) after immersion in 0.5M HCl for 1 hour. The magnitude of impedance (circles) at 10mHz for MLG-coated Ni samples is ~2700 Ω·cm^2, which is 5 times the value of ~540 Ω·cm^2 for bare Ni. This further indicates that MLG-coated Ni is more corrosion resistant than bare Ni. In the case of MLG-coated Ni, in the medium frequency region (10-1000Hz), both a shift to higher values of impedance (circles) and a shift to higher frequencies of time constant (triangles) can be observed when compared with bare Ni (with the time constant being the frequency where phase angle reaches the highest value on phase diagram). These features suggest that the double layer capacitance on MLG-coated Ni is lower than that of bare Ni, indicating that, to some extent, the MLG coating is acting as a barrier.

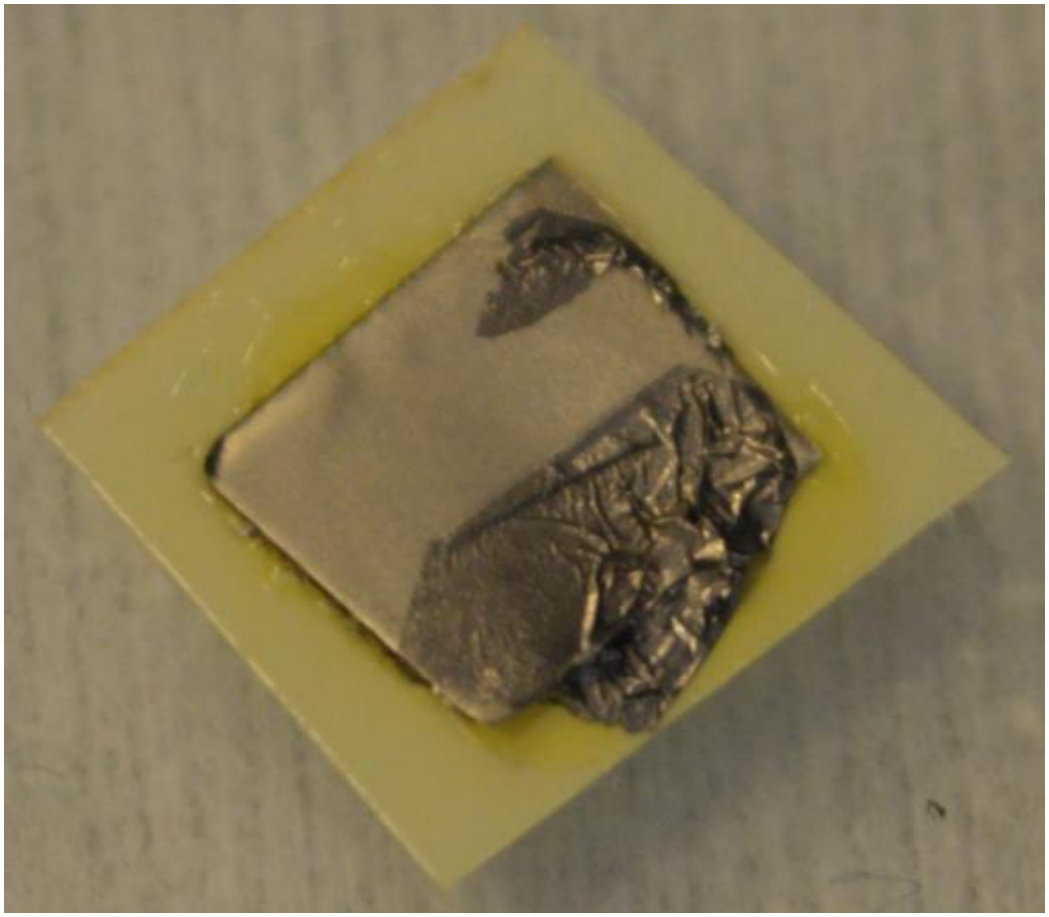

Figure S4. Delamination of the MLG coating from nickel substrate. A drop of 0.5M HCl solution was placed on a MLG-coated Ni sample, covering the whole surface. After 18 hours, the acid was removed by carefully absorbing it with a tissue, without touching the MLG coating. As can be seen from the picture, nearly the whole MLG film was delaminated from the nickel substrate due to the hydrogen bubbles formed at the MLG and Ni interface, with subsequent loss of adhesion of the coating.

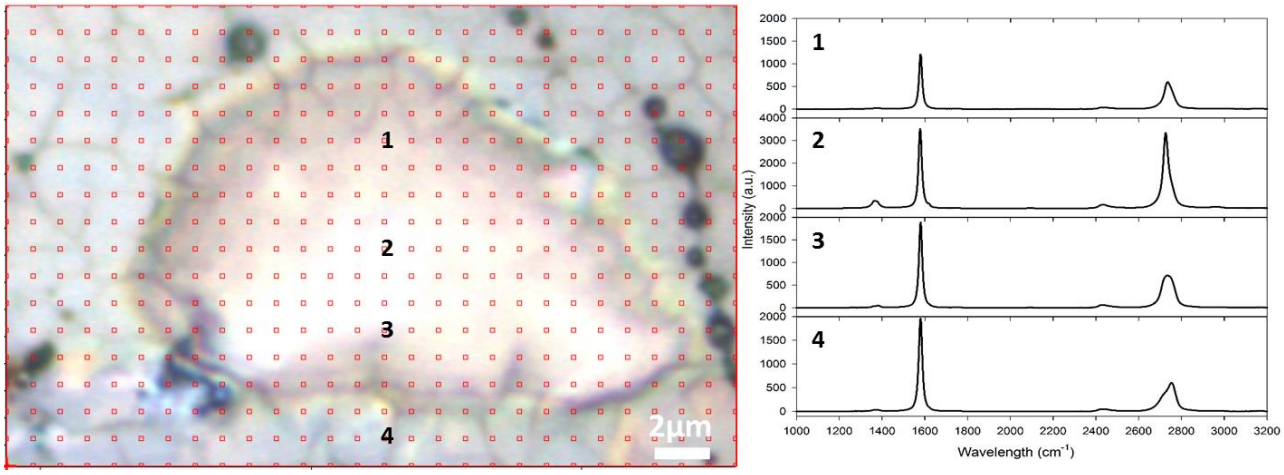

Figure S5. (left) Optical image and (right) Raman spectra of a blister formed under the MLG film. MLG-coated Ni sample was immersed in 0.5M HCl with an applied potential of -0.6V (vs. AgCl/Ag reference electrode) for 3min. Then, one of the blisters, which were found at the interface between MLG coating and nickel substrate, was analysed by Raman spectroscopy. The Raman spectra taken at different spots on top of the blister (point 1, 2 and 3) and outside (point 4) indicate the absence of any remarkable shift in the graphene peaks.

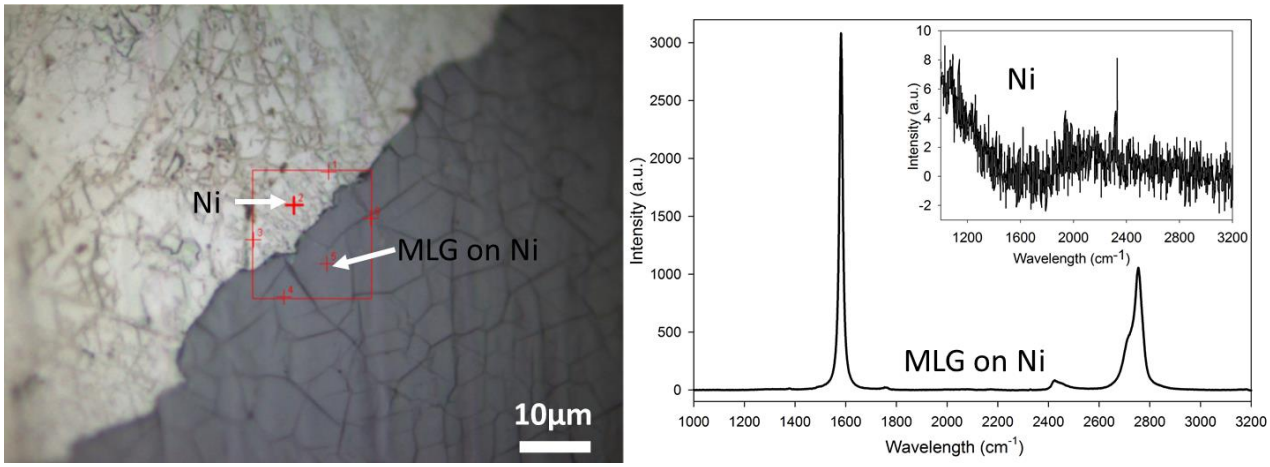

Figure S6. (left) Optical image and (right) Raman spectra of an area of the coated nickel sample where the MLG coating was partially delaminated. MLG-coated Ni sample was immersed in 0.5M HCl with an applied potential of -0.6V (vs. AgCl/Ag reference electrode) for 30min. The MLG coating was thus locally delaminated, showing some areas with no coating (left). The absence of the coating in this area is also proved by Raman spectroscopy (right).

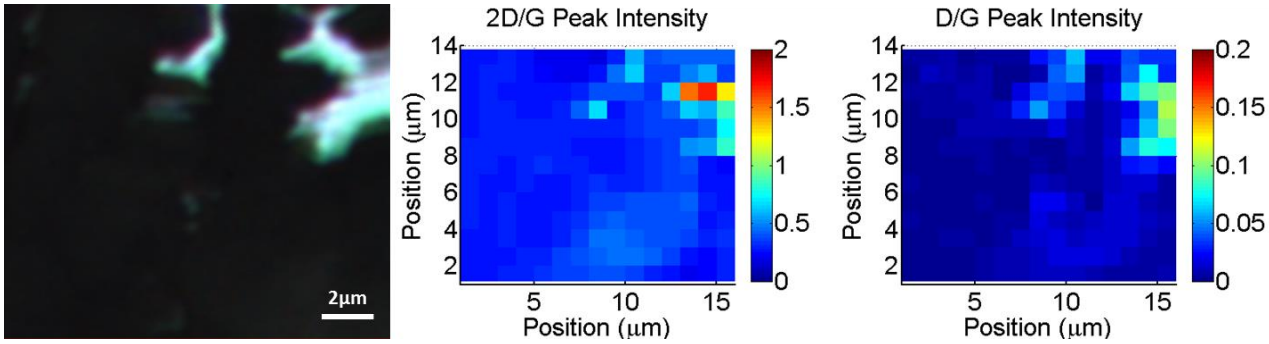

Figure S7. Optical image (left) with back illumination and relative Raman map (2D/G, at centre, and D/G, at right) of a transferred MLG film on a glass slide. The MLG is transferred on a glass slide and placed inside the Raman microscope. Back illumination is used to pinpoint the location of inhomogeneities in the MLG film (displayed as bright spots in the optical image at left). Raman map is then used to investigate the MLG film. The bright features found in the optical images show a higher defect density (see the D/G map, right panel) and a fewer number of layers (see 2D/G map, centre panel) with respect to the rest of the MLG film. These inhomogeneities are thought to be weak points in the coating and during the electrochemical tests they create paths for the acid, which can reach the nickel surface thus producing hydrogen.

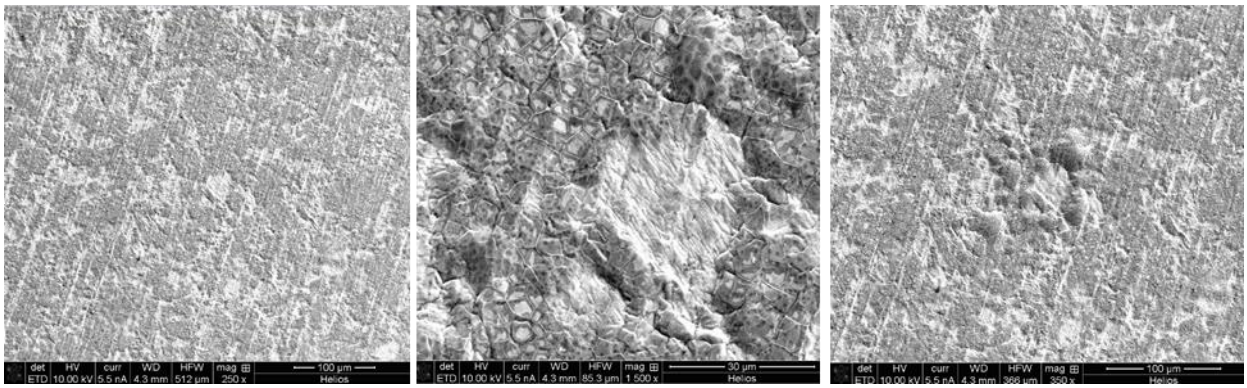

Figure S8. *In-situ* evolution of hydrogen in SEM. A droplet of 0.5 M HCl solution is placed in the centre of a MLG-coated nickel foil, and gently removed with a tissue. The sample is then mounted inside a SEM without prior rinsing or blow-drying. When the electron beam is focused on a flat region of the sample (left panel), some hydrogen bubbles are generated under the MLG coating (centre panel). At lower magnification, it is possible to see that the blister-like protrusions in the coating are mainly found in the area that was initially irradiated by the scanning electron beam (right panel).

References

1. Cottis, R. Shreir's Corrosion. Elsevier Amsterdam: 2010

Appendix C

Complete long-term corrosion protection with chemical vapor deposited graphene

Article published in Carbon

Carbon 132 (2018) 78–84

Contents lists available at ScienceDirect

Carbon

journal homepage: www.elsevier.com/locate/carbon

Complete long-term corrosion protection with chemical vapor deposited graphene

Feng Yu [a, *], Luca Camilli [a], Ting Wang [a], David M.A. Mackenzie [a], Michele Curioni [b], Robert Akid [b], Peter Bøggild [a, **]

[a] CNG – DTU Nanotech, Department of Micro- and Nanotechnology, Technical University of Denmark, Kgs. Lyngby, DK-2800, Denmark
[b] School of Materials, The University of Manchester, Manchester, M13 9PL, UK

ARTICLE INFO

Article history:
Received 30 November 2017
Received in revised form
25 January 2018
Accepted 6 February 2018
Available online 10 February 2018

ABSTRACT

Despite numerous reports regarding the potential of graphene for corrosion protection, examples of chemical vapor deposited (CVD) graphene-based anticorrosive coatings able to provide long-term protection (i.e. several months) of metals have so far been absent. Here, we present a polymer-graphene hybrid coating, comprising two single layers of CVD graphene sandwiched by three layers of polyvinyl butyral, which provides complete corrosion protection of commercial aluminum alloys even after 120 days of exposure to simulated seawater. The essential role played by graphene in the hybrid coating is evident when we compare the results from a polymer-only coating of the same thickness, which fails in protecting the metal after less than 30 days. With the emergence of commercially available large-area CVD graphene, our work demonstrates a straightforward approach towards high-performance anticorrosive coatings, which can be extended to other two-dimensional materials and polymers, for long-term protection of various relevant metals and alloys.

1. Introduction

The reliability and long-term durability of metal components is critical in many industrial sectors, such as aerospace, marine, transportation, construction, energy and manufacturing. Corrosion protection of metals is therefore vital to ensure useful component and system lifetimes, therein preventing economic loss, corrosion-induced catastrophic disasters and reducing negative impact on the environment. A well-established strategy for corrosion protection is to apply coatings on metal surfaces. Such anticorrosive coatings can consist of several layers, each with a specific function [1,2]. Barrier layers, in particular, serve to separate metals from the external environment. Graphene, being highly impermeable to gases [3] and chemically inert [4], has been long considered a promising candidate as a physical barrier for corrosion protection [5–9], following the seminal article by Ruoff's group [4]. While initial successes for graphene corrosion-inhibiting coatings have been reported [4–7,10], there are still several issues preventing the practical use of graphene in corrosion protection applications. For instance, high quality graphene is very challenging to grow directly on many commercially relevant metals and alloys (e.g., steel, Al and Mg alloys). Moreover, steels and other relevant alloys cannot in general withstand the high temperature needed for continuous graphene growth via CVD process, as they may undergo segregation when heated [11,12]. Alternatively, graphene coatings could be grown on a suitable growth substrate and subsequently transferred to a target metal surface. However, bare graphene coatings directly applied on metals show no or limited improvement in terms of corrosion protection [5,13–15] due to weak adhesion of graphene on metals [16,17], galvanic corrosion issues introduced by noble graphene [13,14,18,19] and direct corrosion attack at sites where graphene defects are located [20–22]. Using a graphene composite coating, where graphene-based nano-fillers (e.g. graphene oxide or reduced graphene oxide) are dispersed in a coating matrix is an alternative strategy [23–29]. Here, the fillers provide a tortuous diffusion pathway for corrosive species, thus enhancing the overall barrier performance of the coating. However, it is generally difficult to control the stacking of graphene-based nano-fillers in the coating matrix, and their agglomeration can ultimately limit the barrier performance of the coating by allowing, in fact, more

* Corresponding author.
** Corresponding author.
E-mail addresses: fengy@nanotech.dtu.dk (F. Yu), Peter.Boggild@nanotech.dtu.dk (P. Bøggild).

https://doi.org/10.1016/j.carbon.2018.02.035
0008-6223/

diffusion pathways through the matrix.

Here we report on hybrid anticorrosive coatings consisting of alternating CVD single layer graphene (SLGr) and polymer films. A systematic study performed on coatings with a different number and combination of layers allows us to understand the specific function of each layer comprising the hybrid coating and identify whether the behavior and performance of such hybrid coatings is critically dependent on its overall structure. In this study, a commercial aluminum alloy (AA) AA2024-T3 is the substrate of choice, as it is used extensively in the aerospace industry, due to its excellent strength-to-weight ratio [30]. We have found that the best performance is provided by coatings made up of two graphene layers sandwiched by three polymer layers. More specifically, when AA is coated with a polymer/SLGr/polymer/SLGr/polymer coating, its impedance at 0.01 Hz remains at $10^9\ \Omega\ cm^2$ for up to 120 days of immersion in 3.5 wt% NaCl solution. Although several discouraging reports have previously questioned the suitability of graphene-based coatings for corrosion protection in practical, long-term applications [13,14], here, by combining the adhesive [31] and insulating properties of polymer layers with the impermeability of continuous CVD-grown graphene sheets, we demonstrate a facile and ultimately scalable method, which can be applied to any realistic metal substrate, to make coatings that exploit graphene's excellent barrier properties, while avoiding its intrinsic drawbacks, such as poor adhesion, galvanic corrosion and fast diffusion through defects.

2. Experimental

2.1. Growth of graphene and preparation of polymer-graphene hybrid films

A copper foil (25 μm-thick, Part No. 13382, Alfa Aesar) was electrochemically polished in a solution with a volume ratio of 15% absolute ethanol (Millipore Corporation) and 85% concentrated phosphoric acid (Millipore Corporation) with magnetic stirring. A voltage of 4–5 V (corresponding to a current density of ~0.04 A cm^{-2}) was applied (Keithley 2400) on the copper foil for 3 min to reduce the surface roughness. The sample was then rinsed with deionized water and blow dried with nitrogen. The copper foil was loaded in a commercial rapid-thermal CVD system (AS-ONE, Annealsys), placed on a 4-inch graphite sample holder and thermal annealed at 1000 °C in Ar atmosphere (1000 sccm) for 10 min at 25 mbar. The graphene growth was carried out at atmospheric pressure for 15 min, with a co-flow of Ar (900 sccm), H_2 (60 sccm) and CH_4 (2 sccm). After growth, the samples were cooled down to room temperature at a rate of ~20 °C s^{-1}.

The polymer used to transfer graphene is a co-polymer of Polyvinyl butyral (PVB) (Mowital B 60 H, Kuraray Europe). The as-prepared graphene-covered copper foil was spin-coated with 12 wt% PVB ethanol solution at 1000 rpm for 1 min and cured at 60 °C for 2 h. The copper substrate was chemically etched in a mixed solution of 100 ml 5 wt% HCl (Millipore Corporation) and 3 ml 30 wt% H_2O_2 (Sigma-Aldrich). The polymer-graphene (P-G) films were then rinsed with deionized water to remove any residue of the etchant solution. The preparation process of P-G film is illustrated in Fig. 1. The quality of as-grown and transferred graphene on SiO_2 or PVB was assessed by optical microscopy and Raman spectroscopy (Figs. S1–4, Supplementary Material).

2.2. Fabrication of polymer-graphene hybrid coatings on aluminum alloy

Firstly, a clean AA surface was prepared. In particular, AA (Wilsons metals, UK) was ultra-sonicated in acetone, de-smutted (1 min at 60 °C) in 10 wt% NaOH (Sigma-Aldrich), etched (1 min at 25 °C) in 50 wt% HNO_3 (Millipore Corporation), rinsed with deionized water and finally blow dried with N_2. Then 12 wt% PVB ethanol solution was spin coated (1000 rpm, 1 min) on AA and cured at 60 °C for 2 h to coat the PVB primer on AA (AA-P). PVB is widely used for corrosion protection [30,32] and is chosen here as it exhibits strong adhesion to the surface of AA [31]. The P-G film obtained as described above was then dried and transferred onto either AA or AA-P, using a polydimethylsiloxane (Dow Corning Corporation) stamp for the mechanical transfer. Thermal annealing was then applied at 100 °C for 10–15 min to prepare AA-P-G, AA-G-P and AA-P-G-P. Two layers of P-G film could also be transferred onto AA-P to prepare AA-P-G-P-G-P (or AA-P-P-G-G-P). Fig. 1 shows the fabrication procedures of these coatings. The reference samples for AA-P-G-P and AA-P-G-P-G-P (or AA-P-P-G-G-P) were prepared by transferring one or two layers of PVB, which were obtained after etching the PVB spin-coated copper, to AA-P and then thermal annealed. Such reference samples are denoted as AA-P-P and AA-P-P-P, respectively. Both the PVB primer directly spin-coated on AA and the PVB layer used for graphene transfer have a similar thickness, ranging between 4 μm and 5 μm (Fig. S6, Supplementary Material).

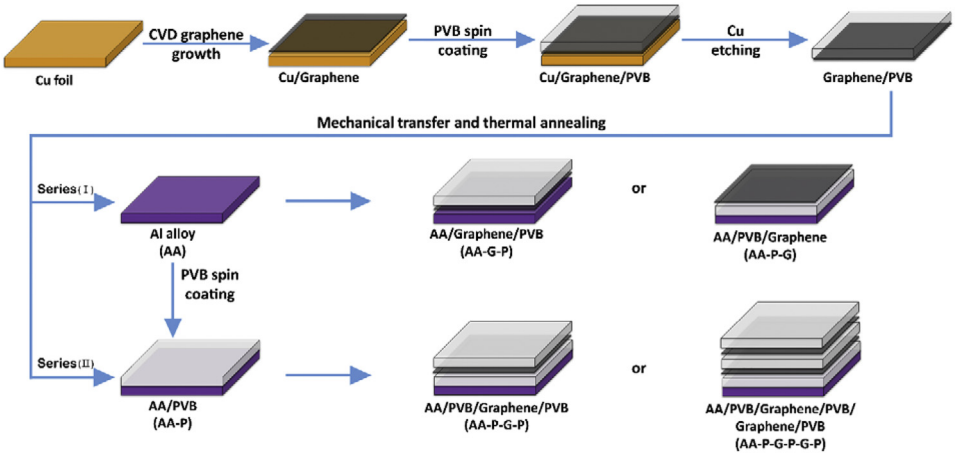

Fig. 1. Schematic illustration of preparation steps for the investigated polymer-graphene hybrid coatings on AA. (A colour version of this figure can be viewed online.)

2.3. Electrochemical tests

All electrochemical measurements were conducted at room temperature in a custom-made three-electrode Teflon cell using the studied samples as the working electrode, an Ag/AgCl reference electrode and a platinum counter electrode. The electrolyte of choice is a 3.5 wt% NaCl solution (i.e., simulated seawater). A Gamry Reference 3000 potentiostat and an ECM8 Electrochemical Multiplexer were used for the electrochemical measurements. Electrochemical impedance spectroscopy (EIS) were recorded at a frequency range from 100,000 Hz to 0,01 Hz with 10 points per decade under ±10 mV sinusoidal perturbation at the measured open circuit potential of the sample. Potentiodynamic scans (PDS) were performed with a scan rate of 1 mV/s starting from −500 mV (or −300 mV) to +500 mV (or +300 mV) vs OCP (or Ag/AgCl). Values of corrosion rate are calculated using Faradays' law from corrosion current density, which is obtained from Tafel analysis on PDS curves.

2.4. Additional characterization techniques

Optical images were collected using a Nikon Eclipse L200N optical microscope, whereas the scanning electron microscopy (SEM) images were taken with a Quanta 200 FEG environmental scanning electron microscope. While optical images were collected on the samples without removing the coating, SEM micrographs were obtained after all coatings were dissolved and removed with acetone. The Raman spectroscopy data were collected by a DXR Raman microscope (Thermo Fisher Scientific) using 455 nm laser with 8 mW power and 50X objective. The analysis of the Raman peaks was carried out as described by Larsen et al. [33].

3. Results and discussion

3.1. Electrochemical testing of the coating performance

Electrochemical impedance spectroscopy (EIS) is a powerful tool to evaluate the corrosion performance of coatings and provides insight into the corrosion behavior of coated metals as well as the barrier properties of anticorrosive coatings. A higher magnitude of impedance at low frequencies (e.g. $|Z|_{0.01Hz}$) is associated with increased anticorrosion performance, while a slow decrease of its value with elapsed time generally indicates high resistance to environmental degradation of the anticorrosive coatings [34].

As the thickness of SLGr is negligible when compared to the thickness of the polymer layers, in our tests we consistently compare bare PVB layered reference coatings to their graphene-enhanced counterparts of nominally same thickness (for instance, we use AA-P-P as a reference for AA-P-G-P and so on).

Fig. 2a and b shows respectively representative Bode and phase angle plots of both coated and uncoated samples after 1 day of immersion in 3.5 wt% NaCl solution (the complete set of data is provided in the Supplementary Material). The system AA-P-G-P, $|Z|_{0.01Hz}$ shows a value of $1.4 \times 10^7\,\Omega\,cm^2$, i.e., 500 times higher than uncoated AA ($2.8 \times 10^4\,\Omega\,cm^2$) and 20 times higher than the polymer-coated sample (AA-P-P) used as reference ($8.0 \times 10^5\,\Omega\,cm^2$). This result proves the enhancement provided by a single graphene sheet (which is one-atom-thick) to the overall barrier properties of a ~10 μm thick polymer coating at short-term. When the top polymer layer is absent (AA-P-G), we observe that $|Z|_{0.01Hz}$ decreases by an order of magnitude with respect to AA-P-G-P, ($|Z|_{0.01Hz} = 1.8 \times 10^6\,\Omega\,cm^2$), but is still 2 times higher than that of AA-P-P. Here it is worth pointing out that just replacing the 5 μm-thick PVB top-layer with a one-atom thick graphene sheet leads to slightly better short-term anticorrosion performance. When the polymer primer is absent (AA-G-P), the value of low-frequency impedance becomes lower than the bare AA ($|Z|_{0.01Hz} = 2.5 \times 10^4\,\Omega\,cm^2$). The reduced performance of AA-G-P is attributed to galvanic coupling between the AA and graphene. This last result is in apparent disagreement with that reported by Yu et al. [35], where a coating of CVD graphene covered with polymethyl methacrylate layer offered effective corrosion protection of a copper substrate. However, it is in agreement with recent findings [13,14,36] reporting that graphene layers directly in contact with metal substrates indeed accelerate the corrosion process due to the formation of a galvanic coupling between the noble and electron-conductive graphene sheet and the metal substrate. We therefore conclude that the insulating PVB, as it electrically separates graphene from the metal substrate, avoids the galvanic coupling.

Additionally, we test different coatings with two layers of graphene. An improvement of 50,000 times of the magnitude of $|Z|_{0.01Hz}$ with respect to uncoated AA is achieved by AA-P-G-P-G-P ($1.4 \times 10^9\,\Omega\,cm^2$) after 1 day of immersion. In contrast, the polymer-only reference sample of AA-P-P-P ($8.3 \times 10^7\,\Omega\,cm^2$) showed only 3000 times improvement over that of uncoated AA after 1 day of immersion. Once again, the significant improvement to the overall barrier performance of the hybrid coating provided by graphene is demonstrated. EIS data recorded after short-term exposure to a corrosive agent may reflect the intrinsic barrier performance of coatings, but long-term tests are needed to evaluate the environmental degradation of the coating and explore its potential for real applications. Therefore, EIS tests are performed on AA, AA-P-G-P, AA-P-P-P, AA-P-G-P-G-P at 30 days (Fig. 2c and d) and on AA-P-G-P-G-P at 120 days (Fig. 2e and f).

After 30 days of immersion, the magnitude of $|Z|_{0.01Hz}$ for AA-P-G-P drops to 7% of the value (from $1.4 \times 10^7\,\Omega\,cm^2$ to $9.2 \times 10^5\,\Omega\,cm^2$), while the value for AA-P-P-P drops to 3% (from $8.3 \times 10^7\,\Omega\,cm^2$ to $2.4 \times 10^6\,\Omega\,cm^2$), suggesting that both coatings undergo severe degradation and therefore are not effective for long-term corrosion protection of AA. On the other hand, AA-P-G-P-G-P shows only a minimal decrease of the magnitude of $|Z|_{0.01Hz}$, which even after 120 days of immersion remains in the $10^9\,\Omega\,cm^2$ range, indicating both excellent barrier performance and high resistance to environmental degradation.

We have also performed EIS measurements on some of our coatings applied to brass and steel. The data is reported in Supplementary Material (Fig. S13) and shows that our hybrid coating system can indeed provide effective protection when applied to other substrates as well. This clearly highlights the flexibility of the presented approach. A complete set of EIS data for all studied samples are presented in Supplementary Material (Figs. S8, S10, S12, S13, S15, S18).

From the phase spectra reported in Fig. 2b, d and f, one can notice that an additional time constant (evident as a peak in the medium frequency range in the phase spectrum and a plateau in the impedance modulus spectrum) is observed for AA-P-G-P and AA-P-G. This time constant appears to be associated with the presence of a graphene layer within the film, and is possibly related to the presence of the graphene-polymer interface. The specimens with three layers of polymer, even when they contain graphene layers, do not show such an additional time constant since they are considerably more resistive than the others and therefore the additional time constant cannot be resolved.

Although potentiodynamic scans (PDS) have intrinsic limitations when used on coated metals and should be used with caution in such cases, they have been carried out on all samples, as this technique has often been used to test corrosion inhibition performance of graphene-coated samples [5,7,26,27].

Representative PDS measurements for the samples AA, AA-P-P-P and AA-P-G-P-G-P after 1, 30 or 120 days of immersion in 3.5 wt%

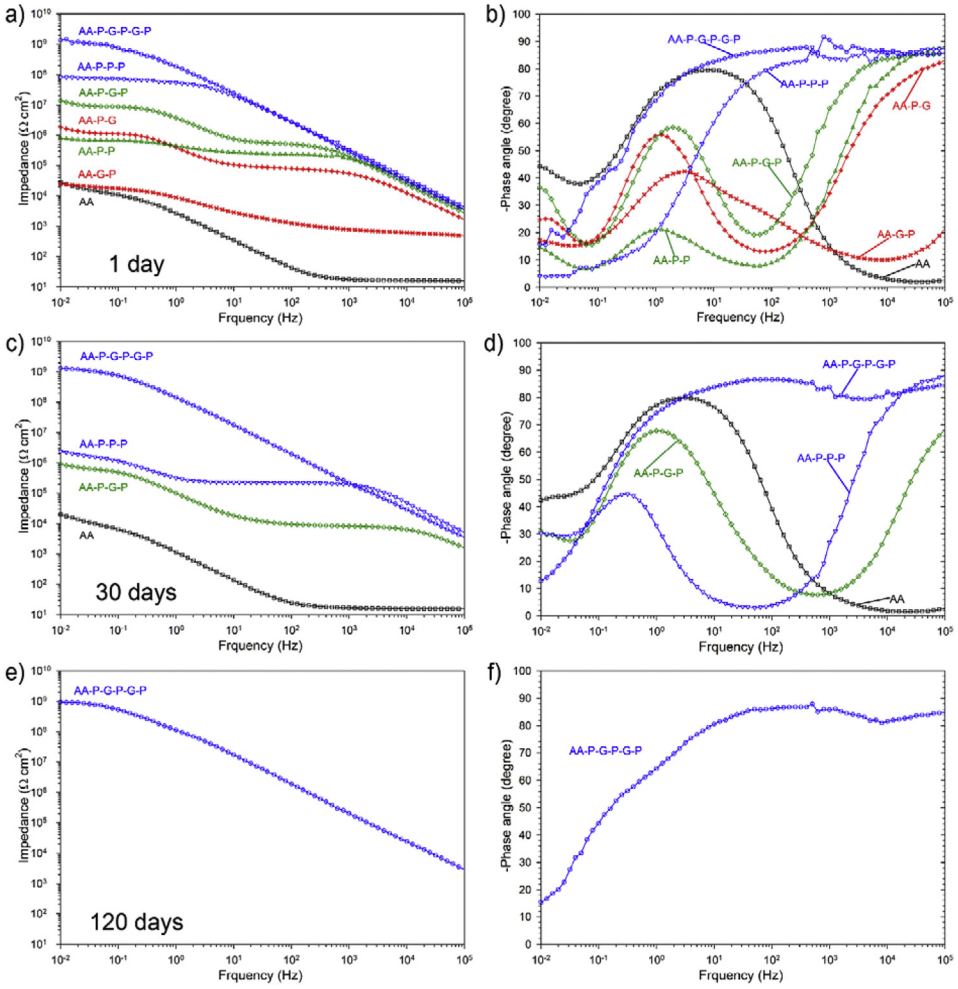

Fig. 2. Bode plots and phase diagram after 1 day (a and b, respectively), 30 days (c and d), and 120 days (e and f) of immersion in 3.5 wt% NaCl solution of tested samples. Note legends for each plot are identical: AA (black square), AA-G-P (red x), AA-P-G (red +), AA-P-P (green triangle up), AA-P-G-P (green diamond), AA-P-P-P (blue triangle down) and AA-P-G-P-G-P (blue circle). (A colour version of this figure can be viewed online.)

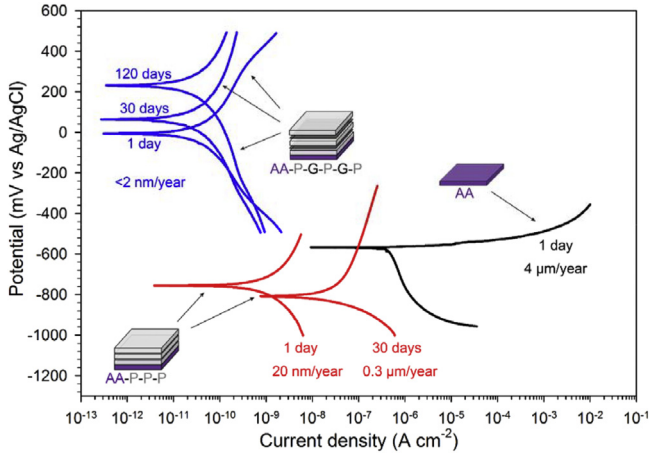

Fig. 3. Typical potentiodynamic scans for AA (black), AA-P-P-P (red) and AA-P-G-P-G-P (blue) after 1, 30 or 120 days of immersion in 3.5 wt% NaCl solution. (A colour version of this figure can be viewed online.)

NaCl solution are displayed in Fig. 3, while the complete set of data (for the other samples as well) is provided in the Supplementary Material. When AA is covered by P-P-P coatings, it exhibits a corrosion rate after 1 day of immersion that is two orders of magnitude lower than bare AA (20 nm/year for AA-P-P-P vs. 4 μm/year for bare AA). However, the corrosion rate of P-P-P coated AA increases by one order of magnitude after barely 30 days of immersion (0.3 μm/year for AA-P-P-P at 30 days vs. 20 nm/year for AA-P-P-P at 1 day), indicating the degradation of P-P-P coating. On the other hand, the PDS curves for AA-P-G-P-G-P remain in the relative low current range with the corrosion rate consistently below 2 nm/year over 120 days of immersion, suggesting no degradation of the coating within the tested timeframe. Overall, the PDS measurements are in agreement with the results from the EIS experiments.

To better visualize our results, we plot the open circuit potential (OCP) and the corrosion current density vs low frequency impedance ($|Z|_{0.01Hz}$) for coated and uncoated samples in Fig. 4. Both OCP and impedance values are obtained from raw data of the electrochemical measurements, while corrosion current densities (corrosion rates) are obtained from PDS curves with Tafel analysis.

One realizes that we can cluster our data into three groups. Group 1 consists of AA and AA-G-P. Both samples have no polymer in direct contact with the AA (i.e., they do not have the polymer primer layer), and are characterized by small $|Z|_{0.01Hz}$, large corrosion current density and OCP in the range −600 mV to −800 mV.

In Group 2 we have polymer-only coatings and hybrid coatings

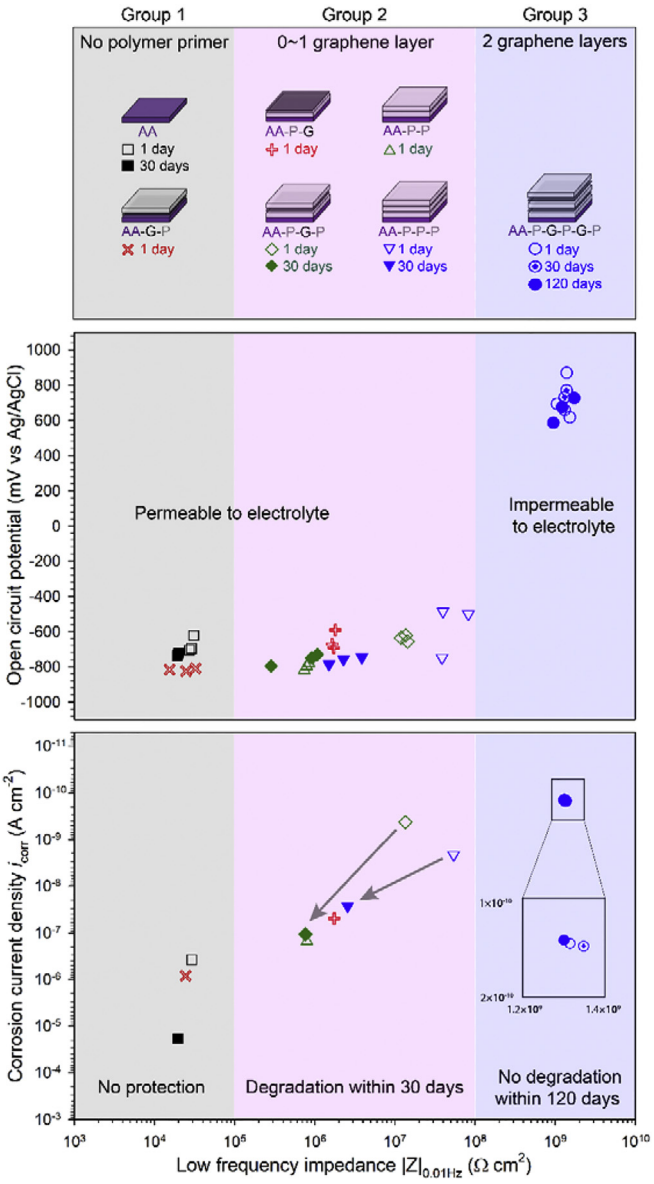

Fig. 4. Grouping of all tested samples and summary of the results from electrochemical tests. (A colour version of this figure can be viewed online.)

with only one graphene layer, that is AA-P-G, AA-P-P, AA-P-G-P and AA-P-P-P. Although they show some differences, their overall behavior is similar. In particular, they do offer some protection, but they cannot prevent the electrolyte from attacking the substrate, leading to OCP values comparable to that of uncoated sample. Furthermore, the arrows in this group indicate the degradation of AA-P-G-P and AA-P-P-P from 1 day to 30 days (empty *vs* filled symbols, respectively).

Group 3 consists of AA-P-G-P-G-P, which shows a behavior that is completely different from the samples in Group 1 and 2. Indeed, the P-G-P-G-P coating shows excellent barrier properties, with an OCP value in the range 600 mV–900 mV, approximately 1.5 V higher than that of AA. In addition, AA-P-G-P-G-P exhibits the highest $|Z|_{0.01Hz}$ values and lowest corrosion current density, which, most importantly, remain almost unchanged within the 120 day-long experiment.

We want to emphasize that AA-P-G-P-G-P is the first CVD graphene-based coating that maintains high-performance in terms of $|Z|_{0.01Hz}$, corrosion current density and OCP over 120 days or, in other words, it is the first successful long-term anticorrosive coating based on CVD graphene thus far developed.

3.2. Characterization of corrosion morphology

Furthermore, we characterized all samples using optical and scanning electron microscopy (SEM), in order to give additional information about the nature of corrosion. Notably, the corrosion morphologies of AA-P-G-P, AA-P-P-P after 30 days and AA-P-G-P-G-P after both 30 days and 120 days of immersion in 3.5 wt% NaCl solution are displayed in Fig. 5. Both optical and SEM images of AA-P-G-P and AA-P-P-P coatings after 30 days of immersion show heavy corrosion of the two samples, in agreement with electrochemical measurements. In all reported examples, the areas shown represent the highest level of damage found on the sample.

A complete set of images for all the samples is reported in Supplementary Material. While AA covered with P-G-P coating shows very mild corrosion at 1 day of immersion (Figs. S11b and e), the situation changes dramatically after 30 days of immersion, as concentrated pitting corrosion at millimeter scale is clearly observed. The corrosion for the sample AA-P-P-P develops on a large scale after 30 days of immersion, as seen from the filiform corrosion in Fig. 5b, f. Filiform corrosion is also observed for the sample AA-P-P at 1 day of immersion (Figs. S11a and d). For AA-P-G-P-G-P coatings at 30 and 120 days of immersion, as presented in Fig. 5c and d, no visible corrosion can be observed from the optical images. Even from SEM examination, the surface of P-G-P-G-P coated AA after 30 and 120 days of immersion is homogeneous and smooth, similar to that of unexposed AA surface. In summary, the morphological investigation further confirms the limited protection performance of AA-P-P-P and AA-P-G-P samples for long-term exposure, while highlighting the excellent performance provided by AA-P-G-P-G-P.

3.3. Corrosion protection mechanism

Defect-free graphene is known to be impermeable to any molecule [3]. CVD graphene, however, naturally exhibits defects and tears through which molecules and other chemical species can easily pass through. When CVD graphene is applied to a metal substrate to protect it from environmental degradation, the corrosive and oxidizing agents will pass through graphene's defects and start the corrosion of the underlying substrate (Fig. 6a). Owing to graphene's high electrical conductivity, the corrosion started locally under graphene's defects and will eventually spread throughout the whole metal substrate [13,14]. On the other hand, although they are insulating, thicker and may offer good adhesion to metal substrates, polymer anticorrosive coatings are not as impermeable as graphene, therefore they are finally bound to fail over time (Fig. 6b). Hence, adding a continuous single sheet of graphene to a polymer coating greatly enhances its barrier properties, and provides effective corrosion protection at short-term. Yet, over time, the corrosive species absorbed by the topmost polymer film will pass through graphene defects and tears, diffuse through the bottom polymer layer and eventually reach the metal surface, thus initiating its degradation (Fig. 6c). On the other hand, diffusion of corrosive species can be dramatically limited and retarded by adding two SLGr sheets to a polymer coating. (Such coatings can have either P-G-P-G-P or P-P-G-G-P structure, see Supplementary Material) The resulting coating indeed provides outstanding protection of aircraft aluminum for as long as four months of immersion in simulated seawater (Fig. 6d).

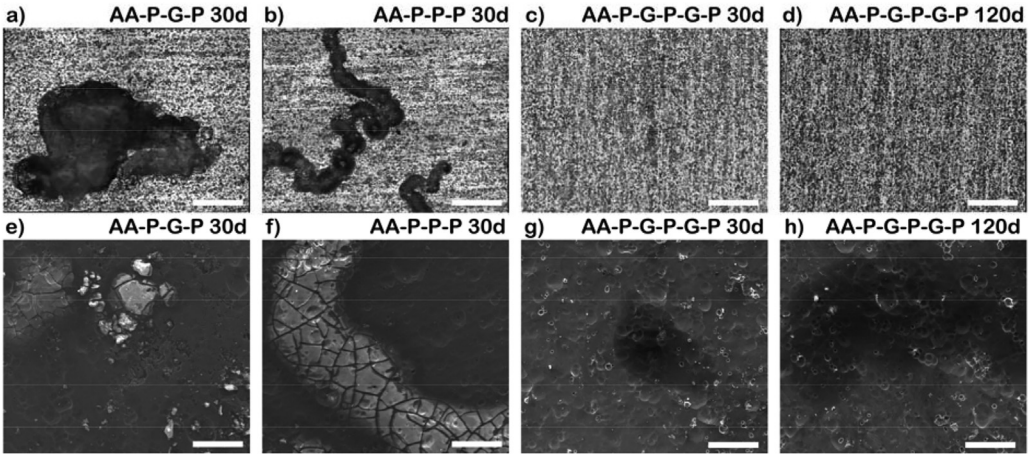

Fig. 5. Corrosion morphology of bare polymer and polymer-graphene hybrid coatings, where areas with most damage have been selected when possible a) – d) Optical and e) – h) SEM images of a), e) AA-P-G-P, b), f) AA-P-P-P and c), g) AA-P-G-P-G-P after 30 days and d), h) AA-P-G-P-G-P after 120 days of immersion in 3.5 wt% NaCl solution. Scale bars in a) – d) are 500 μm and e) – h) are 50 μm. (A colour version of this figure can be viewed online.)

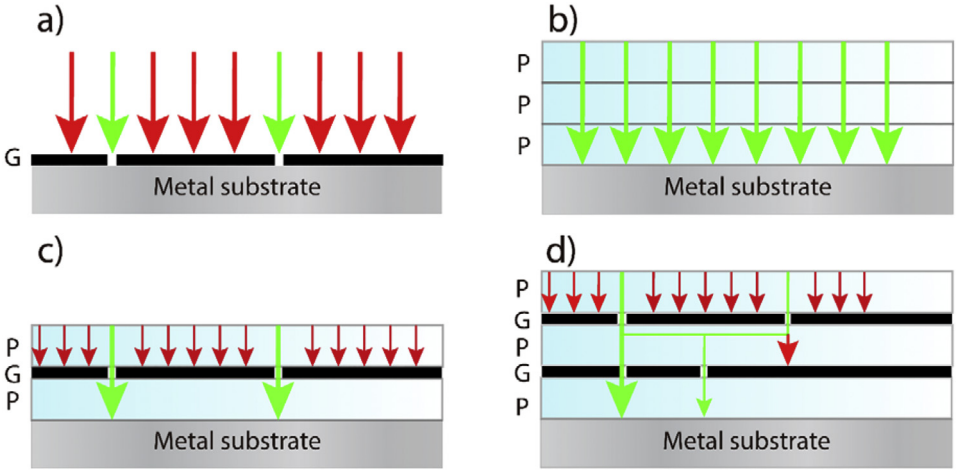

Fig. 6. Schematic illustration of the corrosion protection mechanism of a) as-grown graphene (G), b) bare polymer (P), c) P-G-P and d) P-G-P-G-P coatings on metal substrate. (A colour version of this figure can be viewed online.)

4. Conclusion

In summary, we have prepared a polymer-graphene hybrid anticorrosive coating that optimally exploits the impermeable nature of graphene, and studied in detail the importance and function of both graphene as well as polymer layers within the hybrid coating. While a single layer CVD graphene between two polymer films (P-G-P) provides corrosion protection only in the short-term (30 days), complete long-term (120 days) corrosion protection is achieved by sandwiching two single layers of CVD graphene between three polymer films (P-G-P-G-P or P-P-G-G-P). It may be argued that our coatings are, in essence, polymer coatings. However, the improvement of the graphene-containing coatings compared to the graphene-free variants used as reference, highlights the substantial contribution provided by graphene, which turns out to make a crucial difference after 120 days of exposure to 3.5 wt% NaCl solution.

Finally, by reporting for the first time effective long-term (four months) protection of anticorrosive coatings based on CVD graphene, our findings pave the way for the application of CVD graphene in the field of corrosion protection. In particular, since CVD graphene can be prepared via roll-to-roll processes, and roll-based lamination or processing has been demonstrated to work in practice [37], we envision that this type of polymer-graphene hybrid could provide a high performance coating that can be applied as a dry foil to a wide range of different surfaces.

Acknowledgements

This project was supported by The Strategic Danish Research collaboration (DSF) with the DA-GATE project (12-131827) and through the high technology foundation (HTF) with the NIAGRA project (058-2012-4), with additional support from the Danish National Research Foundation, Center for Nanostructured Graphene (DNRF103) and the EU Graphene Flagship (604391). L.C. acknowledges support from the European Union's Horizon 2020 research and innovation program under the Marie Sklodowska-Curie grant agreement No. 658327. This project has received funding from the EU Horizon 2020 research and innovation program under grant agreement No. 696656.

Appendix A. Supplementary data

Supplementary data related to this article can be found at

https://doi.org/10.1016/j.carbon.2018.02.035.

References

[1] R. Twite, G. Bierwagen, Review of alternatives to chromate for corrosion protection of aluminum aerospace alloys, Prog. Org. Coating 33 (2) (1998) 91–100.

[2] R.-G. Hu, S. Zhang, J.-F. Bu, C.-J. Lin, G.-L. Song, Recent progress in corrosion protection of magnesium alloys by organic coatings, Prog. Org. Coating 73 (2–3) (2012) 129–141.

[3] J.S. Bunch, S.S. Verbridge, J.S. Alden, A.M. Van Der Zande, J.M. Parpia, H.G. Craighead, et al., Impermeable atomic membranes from graphene sheets, Nano Lett. 8 (8) (2008) 2458–2462.

[4] S. Chen, L. Brown, M. Levendorf, W. Cai, S.-Y. Ju, J. Edgeworth, et al., Oxidation resistance of graphene-coated Cu and Cu/Ni alloy, ACS Nano 5 (2) (2011) 1321–1327.

[5] D. Prasai, J.C. Tuberquia, R.R. Harl, G.K. Jennings, K.I. Bolotin, Graphene: corrosion-inhibiting coating, ACS Nano 6 (2) (2012) 1102–1108.

[6] N. Kirkland, T. Schiller, N. Medhekar, N. Birbilis, Exploring graphene as a corrosion protection barrier, Corrosion Sci. 56 (2012) 1–4.

[7] R.S. Raman, P.C. Banerjee, D.E. Lobo, H. Gullapalli, M. Sumandasa, A. Kumar, et al., Protecting copper from electrochemical degradation by graphene coating, Carbon 50 (11) (2012) 4040–4045.

[8] A.C. Stoot, L. Camilli, S.-A. Spiegelhauer, F. Yu, P. Bøggild, Multilayer graphene for long-term corrosion protection of stainless steel bipolar plates for polymer electrolyte membrane fuel cell, J. Power Sources 293 (2015) 846–851.

[9] M.J. Nine, M.A. Cole, D.N. Tran, D. Losic, Graphene: a multipurpose material for protective coatings, J. Mater. Chem. A 3 (24) (2015) 12580–12602.

[10] Y.-P. Hsieh, M. Hofmann, K.-W. Chang, J.G. Jhu, Y.-Y. Li, K.Y. Chen, et al., Complete corrosion inhibition through graphene defect passivation, ACS Nano 8 (1) (2013) 443–448.

[11] X.-M. Chen, S.-H. Song, L.-Q. Weng, S.-J. Liu, Solute grain boundary segregation during high temperature plastic deformation in a Cr–Mo low alloy steel, Mater. Sci. Eng., A 528 (25) (2011) 7663–7668.

[12] A. Blesman, D. Polonyankin, D. Postnikov, The influence of the high temperature annealing on the small impurities segregation in J24056 grain steel, Procedia Eng. 113 (2015) 413–417.

[13] M. Schriver, W. Regan, W.J. Gannett, A.M. Zaniewski, M.F. Crommie, A. Zettl, Graphene as a long-term metal oxidation barrier: worse than nothing, ACS Nano 7 (7) (2013) 5763–5768.

[14] F. Zhou, Z. Li, G.J. Shenoy, L. Li, H. Liu, Enhanced room-temperature corrosion of copper in the presence of graphene, ACS Nano 7 (8) (2013) 6939–6947.

[15] X. Ye, F. Yu, M. Curioni, Z. Lin, H. Zhang, H. Zhu, et al., Corrosion resistance of graphene directly and locally grown on bulk nickel substrate by laser irradiation, RSC Adv. 5 (45) (2015) 35384–35390.

[16] T. Yoon, W.C. Shin, T.Y. Kim, J.H. Mun, T.-S. Kim, B.J. Cho, Direct measurement of adhesion energy of monolayer graphene as-grown on copper and its application to renewable transfer process, Nano Lett. 12 (3) (2012) 1448–1452.

[17] S. Das, D. Lahiri, D.-Y. Lee, A. Agarwal, W. Choi, Measurements of the adhesion energy of graphene to metallic substrates, Carbon 59 (2013) 121–129.

[18] V. Mišković-Stanković, I. Jevremović, I. Jung, K. Rhee, Electrochemical study of corrosion behavior of graphene coatings on copper and aluminum in a chloride solution, Carbon 75 (2014) 335–344.

[19] C. Cui, A.T.O. Lim, J. Huang, A cautionary note on graphene anti-corrosion coatings, Nat. Nanotechnol. 12 (9) (2017) 834–835.

[20] I. Wlasny, P. Dabrowski, M. Rogala, P. Kowalczyk, I. Pasternak, W. Strupinski, et al., Role of graphene defects in corrosion of graphene-coated Cu (111) surface, Appl. Phys. Lett. 102 (11) (2013), 111601.

[21] Y. Zhang, H. Zhang, B. Wang, Z. Chen, Y. Zhang, Y. Sui, et al., Role of wrinkles in the corrosion of graphene domain-coated Cu surfaces, Appl. Phys. Lett. 104 (14) (2014), 143110.

[22] Y. Zhu, C. Duan, H. Liu, Y. Chen, Y. Wang, Graphene coating for anti-corrosion and the investigation of failure mechanism, J. Phys. D Appl. Phys. 50 (11) (2017), 114001.

[23] Y.-H. Yu, Y.-Y. Lin, C.-H. Lin, C.-C. Chan, Y.-C. Huang, High-performance polystyrene/graphene-based nanocomposites with excellent anti-corrosion properties, Polym. Chem. 5 (2) (2014) 535–550.

[24] K.-C. Chang, W.-F. Ji, M.-C. Lai, Y.-R. Hsiao, C.-H. Hsu, T.-L. Chuang, et al., Synergistic effects of hydrophobicity and gas barrier properties on the anti-corrosion property of PMMA nanocomposite coatings embedded with graphene nanosheets, Polym. Chem. 5 (3) (2014) 1049–1056.

[25] W. Sun, L. Wang, T. Wu, M. Wang, Z. Yang, Y. Pan, et al., Inhibiting the corrosion-promotion activity of graphene, Chem. Mater. 27 (7) (2015) 2367–2373.

[26] K.S. Aneja, S. Bohm, A. Khanna, H.M. Bohm, Graphene based anticorrosive coatings for Cr (VI) replacement, Nanoscale 7 (42) (2015) 17879–17888.

[27] K. Qi, Y. Sun, H. Duan, X. Guo, A corrosion-protective coating based on a solution-processable polymer-grafted graphene oxide nanocomposite, Corrosion Sci. 98 (2015) 500–506.

[28] B. Ramezanzadeh, S. Niroumandrad, A. Ahmadi, M. Mahdavian, M.M. Moghadam, Enhancement of barrier and corrosion protection performance of an epoxy coating through wet transfer of amino functionalized graphene oxide, Corrosion Sci. 103 (2016) 283–304.

[29] J. Li, J. Cui, J. Yang, Y. Li, H. Qiu, J. Yang, Reinforcement of graphene and its derivatives on the anticorrosive properties of waterborne polyurethane coatings, Compos. Sci. Technol. 129 (2016) 30–37.

[30] F. Yu, R. Akid, Corrosion protection of AA2024-T3 alloy by modified hybrid titania-containing sol-gel coatings, Prog. Org. Coating 102 (2017) 120–129.

[31] B.C. Rincon Troconis, G.S. Frankel, Effect of roughness and surface topography on adhesion of PVB to AA2024-T3 using the blister test, Surf. Coating. Technol. 236 (2013) 531–539.

[32] G. Williams, H.N. McMurray, Anion-exchange inhibition of filiform corrosion on organic coated AA2024-T3 aluminum alloy by hydrotalcite-like pigments, Electrochem. Solid State Lett. 6 (3) (2003) B9–B11.

[33] M.B.B.S. Larsen, D.M.A. Mackenzie, J.M. Caridad, P. Bøggild, T.J. Booth, Transfer induced compressive strain in graphene: evidence from Raman spectroscopic mapping, Microelectron. Eng. 121 (2014) 113–117.

[34] A. Amirudin, D. Thieny, Application of electrochemical impedance spectroscopy to study the degradation of polymer-coated metals, Prog. Org. Coating 26 (1) (1995) 1–28.

[35] Y. Wang, Y. Zheng, X. Xu, E. Dubuisson, Q. Bao, J. Lu, et al., Electrochemical delamination of CVD-grown graphene film: toward the recyclable use of copper catalyst, ACS Nano 5 (12) (2011) 9927–9933.

[36] M. Galbiati, A.C. Stoot, D. Mackenzie, P. Bøggild, L. Camilli, Real-time oxide evolution of copper protected by graphene and boron nitride barriers, Sci. Rep. 7 (2017), 39770.

[37] S. Bae, H. Kim, Y. Lee, X. Xu, J.-S. Park, Y. Zheng, et al., Roll-to-roll production of 30-inch graphene films for transparent electrodes, Nat. Nanotechnol. 5 (8) (2010) 574–578.

Supplementary Material for

Complete long-term corrosion protection with chemical vapor deposited graphene

Feng Yu [a,*], Luca Camilli [a], Ting Wang [a], David M. A. Mackenzie [a], Michele Curioni [b], Robert Akid [b], Peter Bøggild [a,*]

[a] *CNG – DTU Nanotech, Department of Micro- and Nanotechnology, Technical University of Denmark, Kgs. Lyngby, DK-2800, Denmark*

[b] *School of Materials, The University of Manchester, Manchester, M13 9PL, UK*

*Address correspondence to fengy@nanotech.dtu.dk, Peter.Boggild@nanotech.dtu.dk.

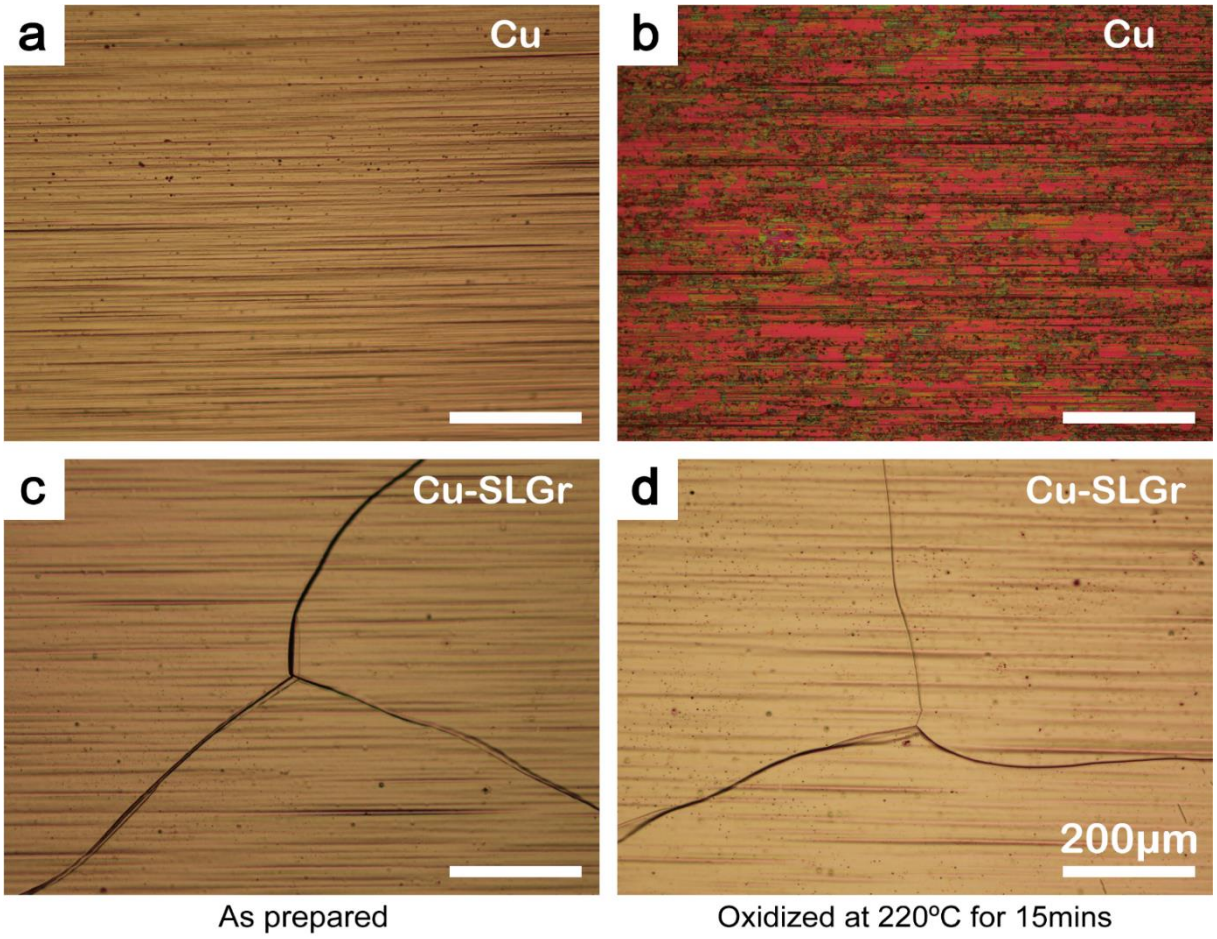

Fig. S1. Optical images of (a) fresh bare electrochemically polished copper (Cu), (b) Cu after oxidation in air at 200 ^{o}C for 15 minutes, (c) as prepared graphene covered copper (Cu-SLGr) and (d) Cu-SLGr after oxidation in air at 200 ^{o}C for 15 minutes.

After oxidation, bare Cu was severely oxidized to Cu_2O (red color in b), while SLGr covered Cu just showed minimal oxidation (microscale red dots in d), indicating both the excellent barrier properties of SLGr and its full coverage on Cu. Note that the horizontal trench lines are the rolling lines on Cu surface during the preparation of the foils and the intersecting lines in c, d are grain boundaries of Cu formed during the high temperature annealing process.

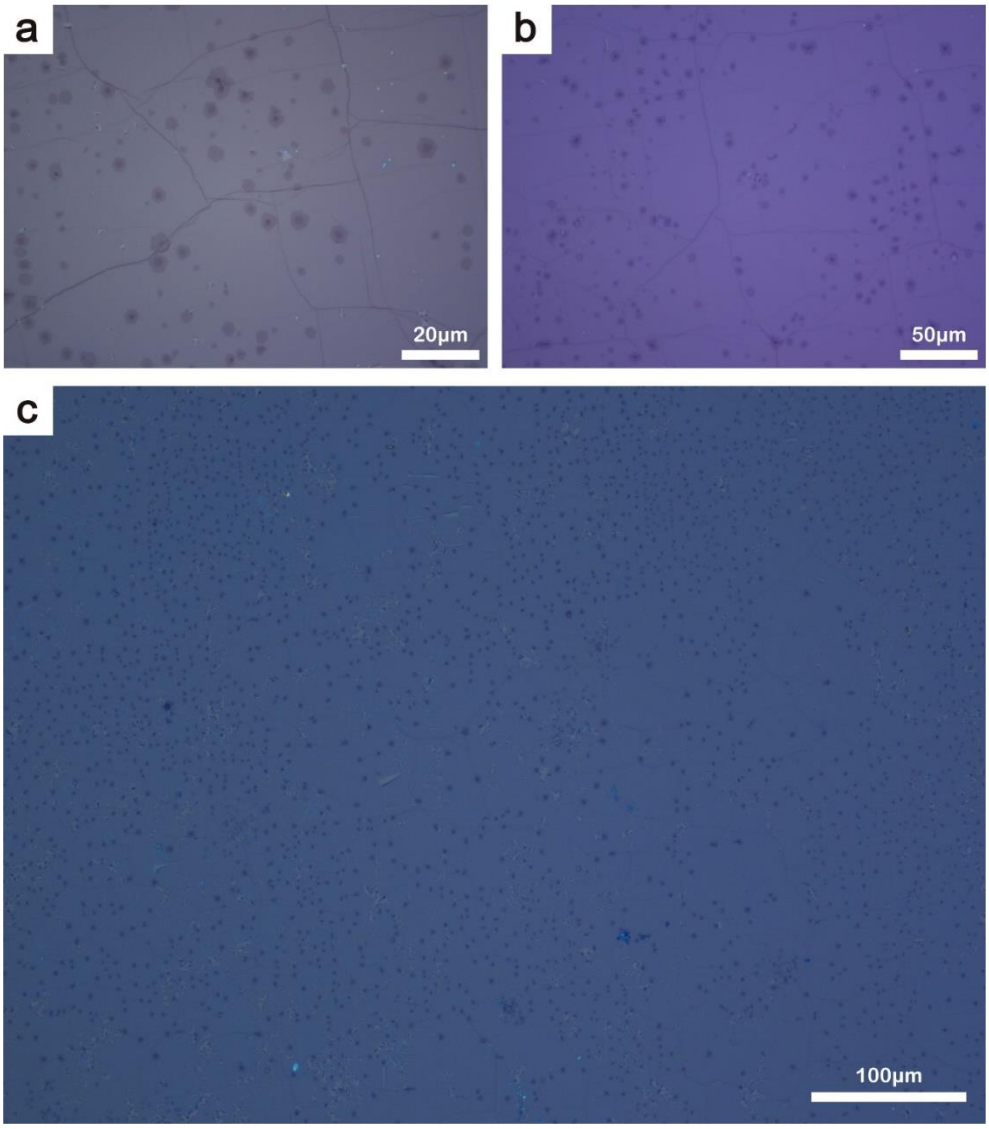

Fig. S2. Optical images of PVB transferred SLGr onto 90 nm thick SiO_2 wafer at (a) high, (b) medium and (c) low magnification.

CVD SLGr was transferred with PVB from a copper substrate to a SiO_2 wafer. However, a few micron sized pinholes (lighter areas in a, b, and c) were found on the transferred graphene layer, which may have originated from either the CVD growth process or the transfer process. Moreover, darker areas represent seeds of second or third graphene layers.

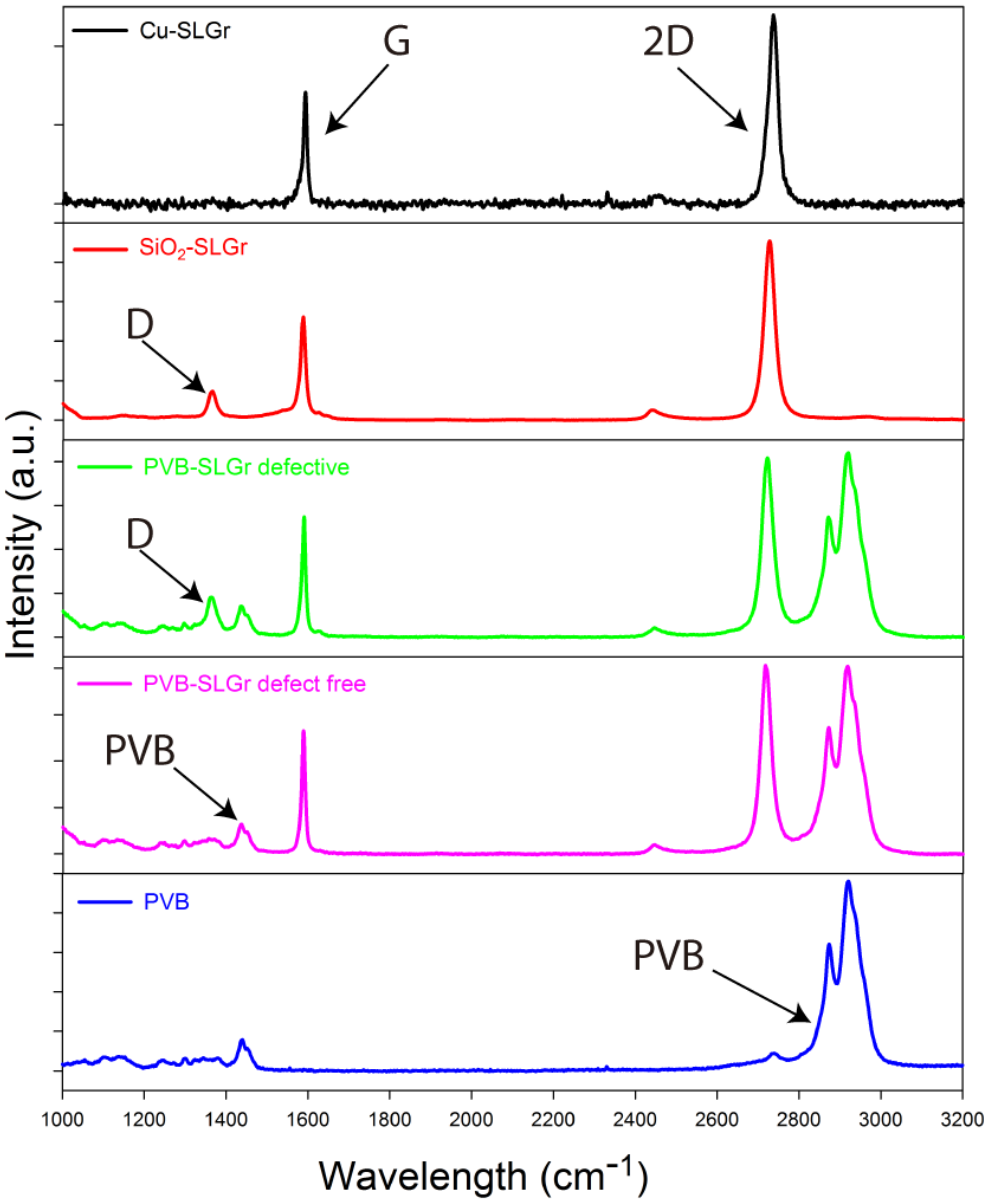

Fig. S3. Raman spectra of as-grown SLGr on copper (black), SLGr transferred onto SiO_2 (red), PVB supported SLGr with defects (green) and without defects (pink) and bare PVB (blue).

G (~1600 cm^{-1}) and 2D (~2750 cm^{-1}) peaks of graphene are presented regardless of the supporting substrate of copper, SiO_2 or PVB. However, defects from graphene are observed when supported on PVB or transferred onto SiO_2, as seen from the D peak (~1375cm^{-1}). The peaks between 2800 and 3000 cm^{-1} and between 1430 and 1450 cm^{-1} can be attributed to PVB.

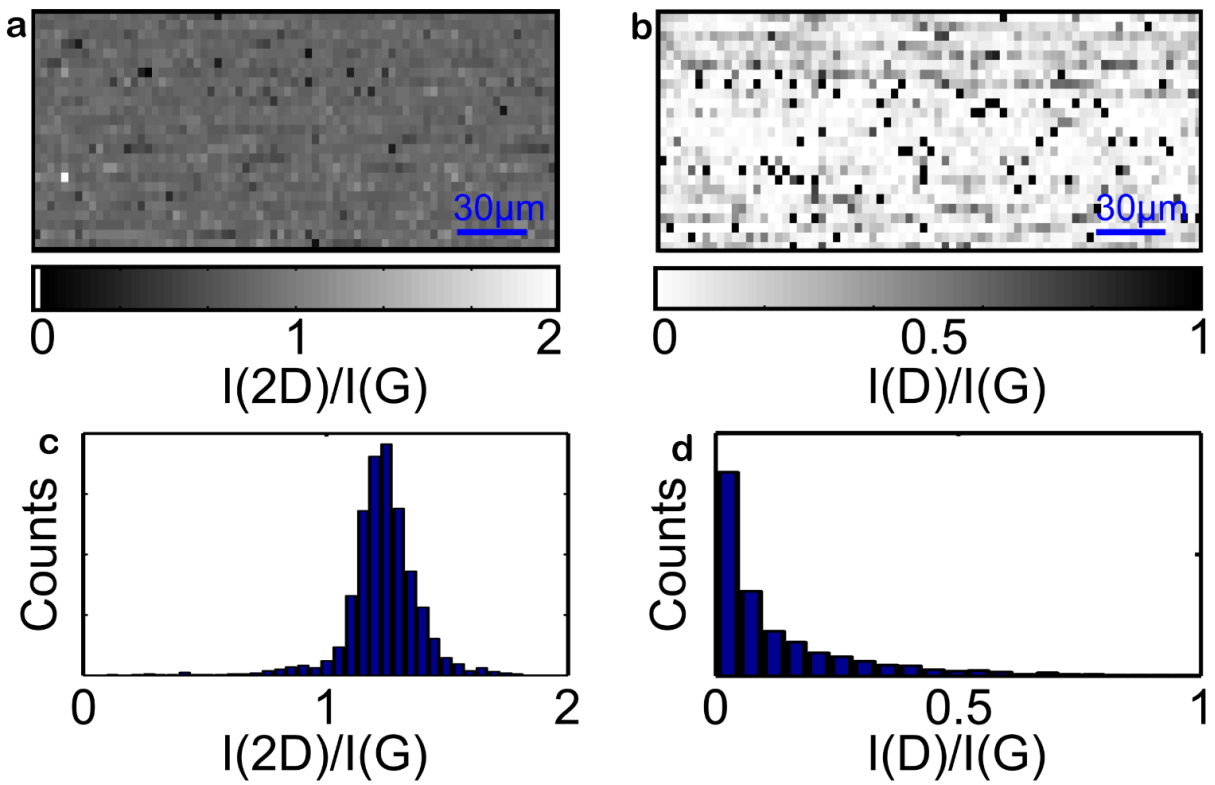

Fig. S4. Raman spectroscopic maps of the (a) I(2D)/I(G) and (b) I(D)/I(G) peak ratios of PVB supported graphene films on SiO_2 substrate. Statistical distribution of (c) I(2D)/I(G) and (d) I(D)/I(G) peak ratios.

The graphene/PVB layer is directly transferred to SiO_2 with the graphene layer facing up and then subject to thermal annealing. Micro-Raman spectroscopy study is directly carried out on the graphene layer in a representative 168 μm×102 μm area (a, b). The mapping is conducted with a step size of 3 μm using a 455 nm laser. Graphene is successfully transferred to PVB layer with a coverage of ~99%. The transferred graphene layer can be defective, as seen from the dark points in (b), with 8.1% spectra having a value of I(D)/I(G) higher than 0.5 (d). Moreover, we have demonstrated, for the first time, that the co-polymer PVB can be used as a graphene transfer support layer.

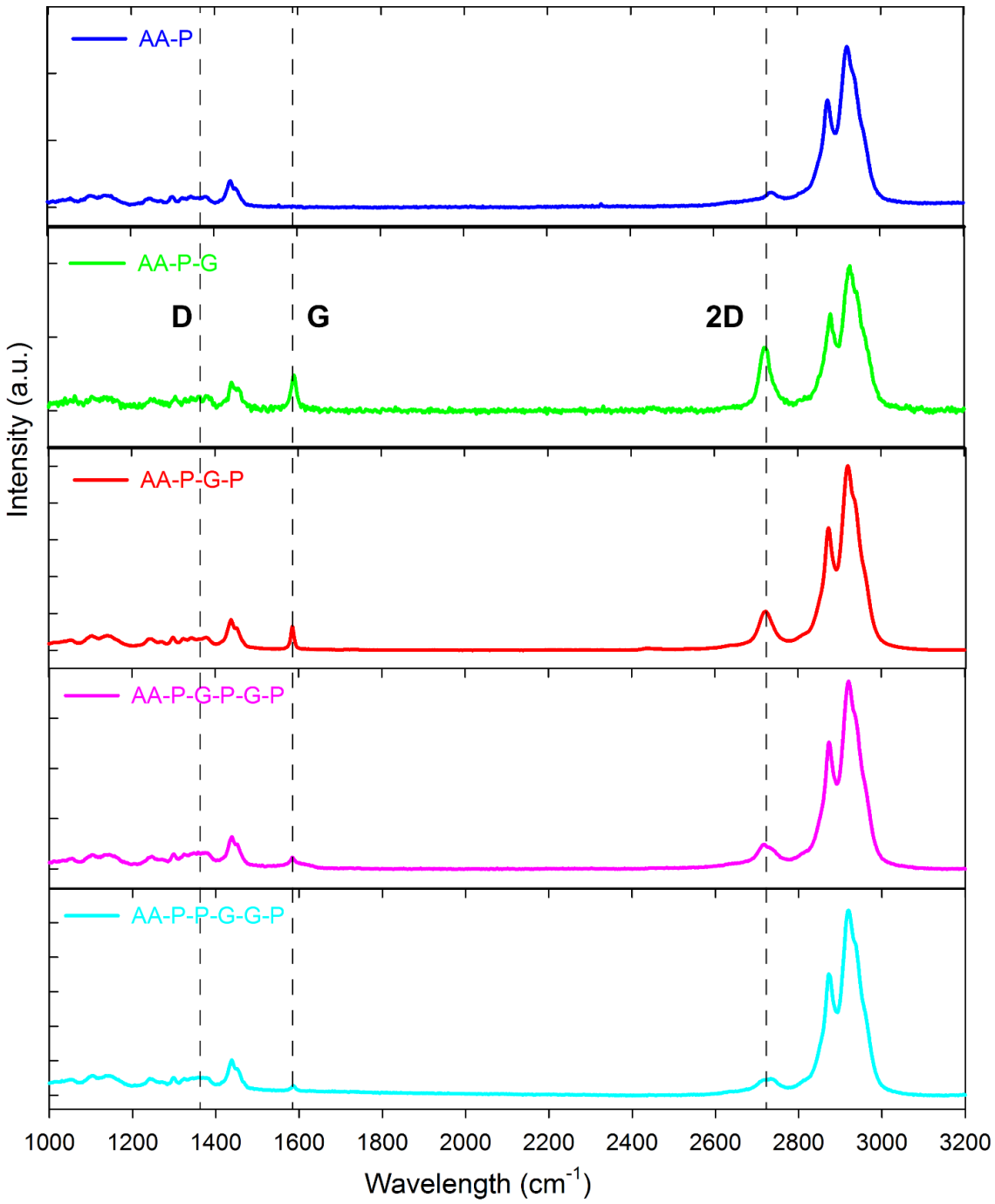

Fig. S5. Raman spectra of the samples after corrosion tests for AA-P (blue), AA-P-G (green), AA-P-G-P (red), AA-P-G-P-G-P (pink) and AA-P-P-G-G-P (cyan), respectively. Vertical dashed lines are used to highlight the characteristic D, G and 2D peaks for graphene.

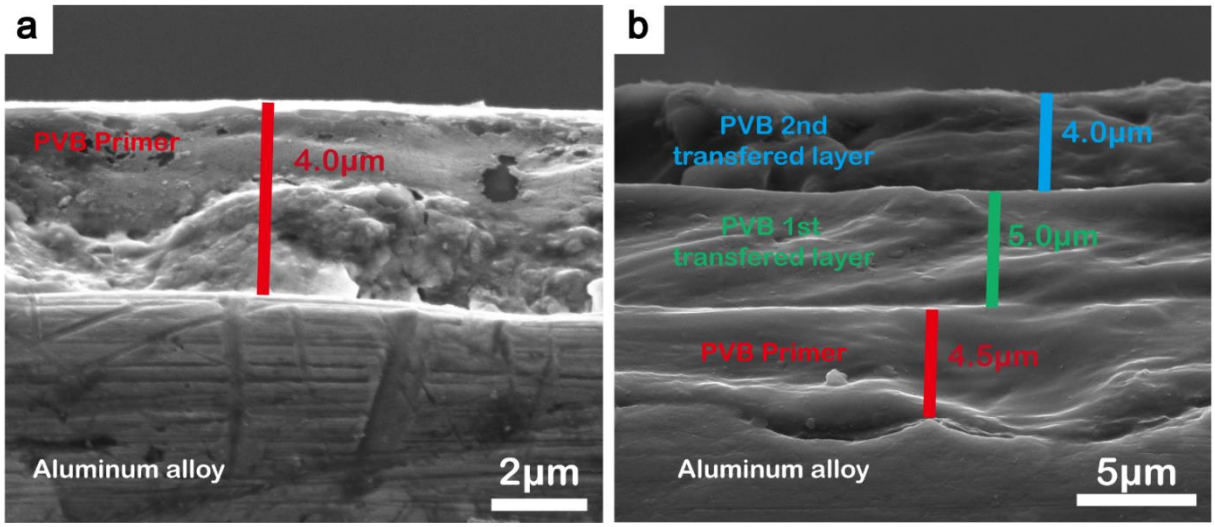

Fig. S6. Cross-section SEM images of (a) spin coated PVB primer on AA substrate and (b) two PVB layers transferred on a PVB primer coated AA substrate. When the PVB layer is either directly spin coated on AA or spin coated on copper and then transferred onto AA, it has a thickness of 4.5±0.5 μm.

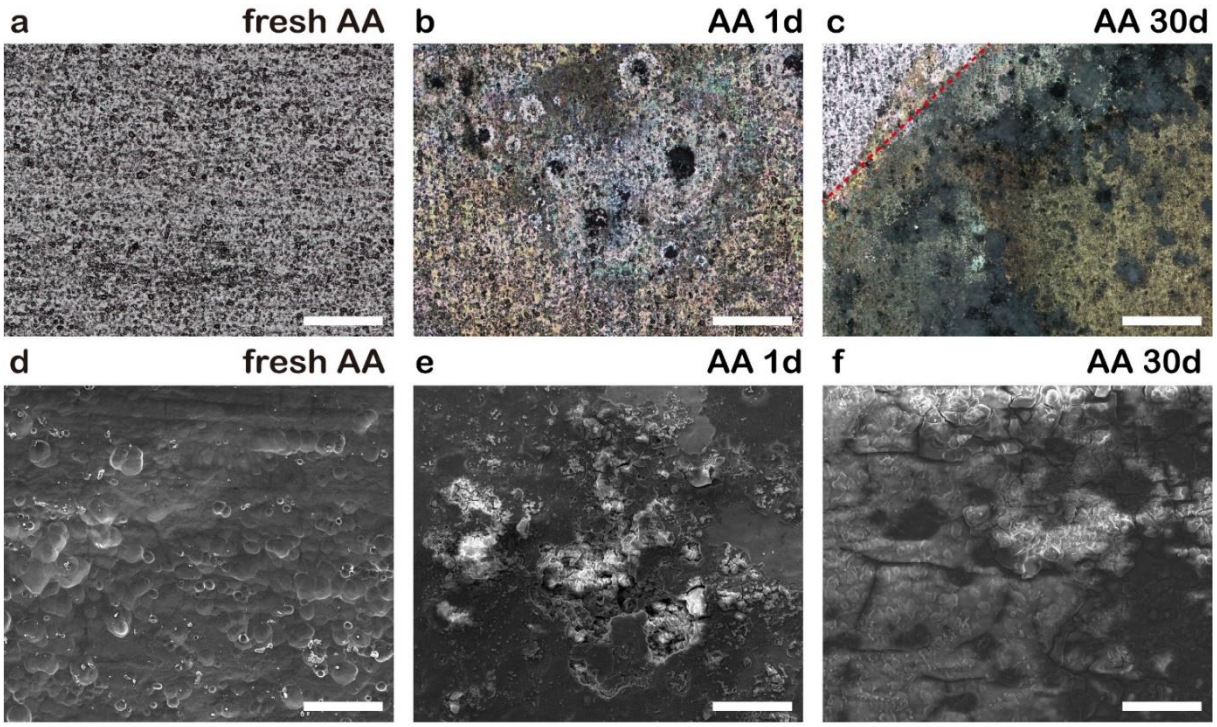

Fig. S7. (a,b,c) Optical images and (d,e,f) SEM images of (a,d) fresh AA, (b,e) AA at 1 day and (c,f) 30 days of immersion in 3.5 wt% NaCl solution. Red dashed line in (c) is to highlight the edge of the O-ring of the corrosion cell. Scale bars are 500 μm in (a,b,c) and 50 μm in (d,e,f).

Localised corrosion or pitting corrosion can be clearly observed on AA after 1 day of immersion in 3.5 wt% NaCl from (b) and (e). After long-term immersion for 30 days, AA is heavily corroded with corrosion products fully covered on its surface, as seen from (c) and (f).

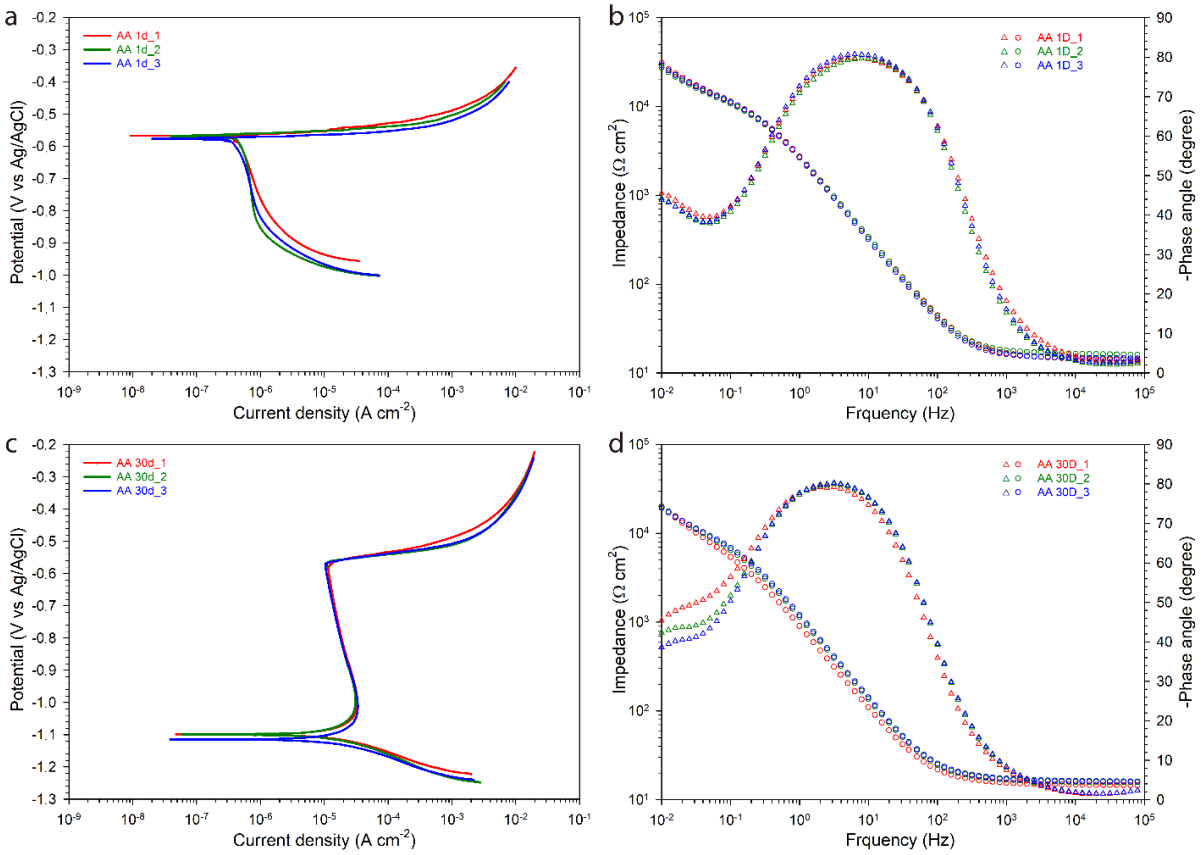

Fig. S8. (a,c) Potentiodynamic polarization curves and (b,d) electrochemical impedance spectra of uncoated AA after (a,b) 1 day and (c,d) 30 days of immersion in 3.5 wt% NaCl solution. For impedance spectra, circles and triangles are data for impedance module and phase angle, respectively.

Additionally, we have observed that results from both measurements for AA show no significant difference between 30 and 60 days of immersion, suggesting that the corrosion current density and impedance of AA are not significantly changed after 30 days of immersion.

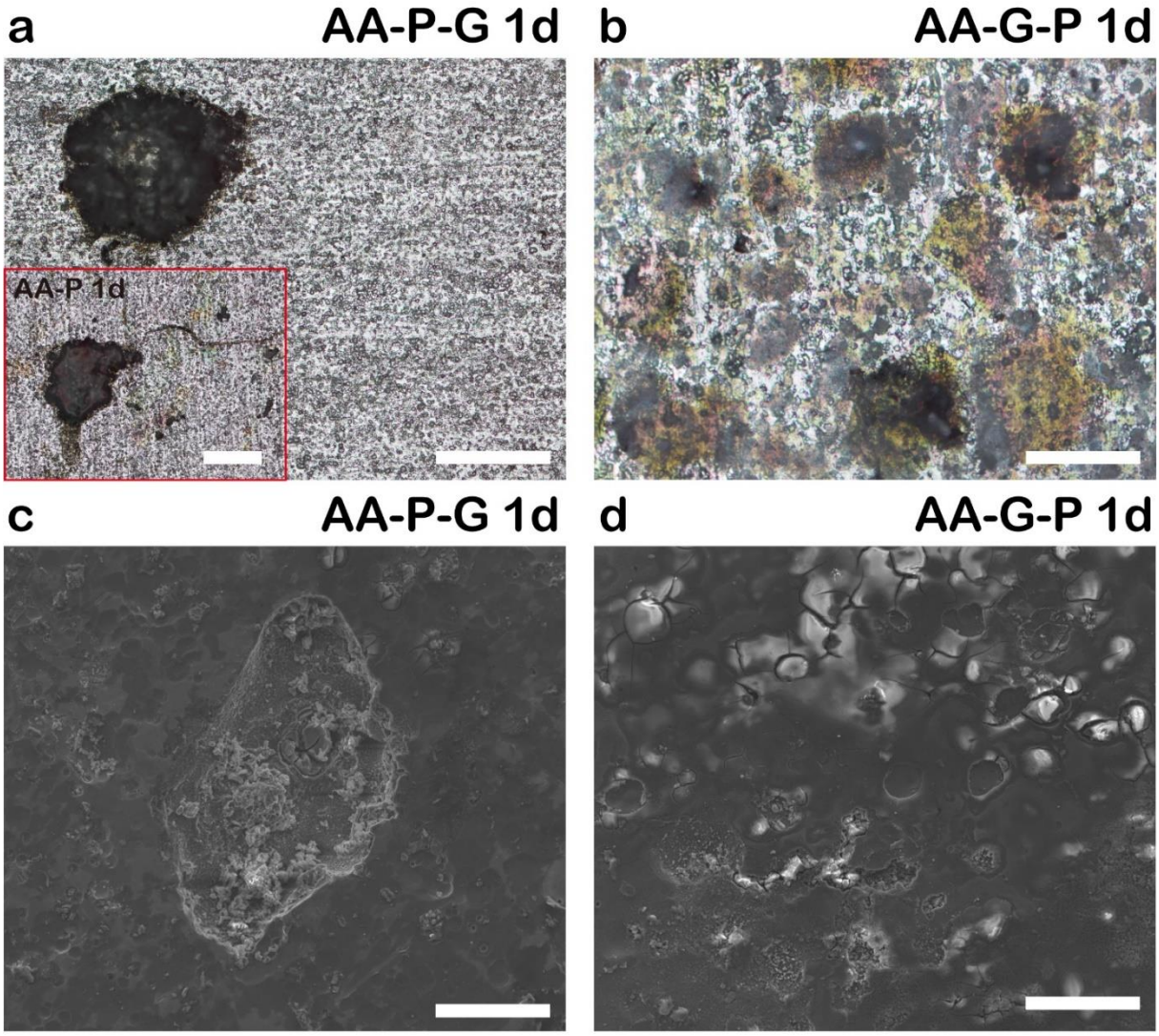

Fig. S9. (a,b) Optical images and (c,d) SEM images of (a,c) AA-P-G and (b,d) AA-G-P after 1 day of immersion in 3.5 wt% NaCl solution. Inset image in (a) presents an optical image of AA-P sample after 1 day of immersion. Scale bars are 500 μm in (a,b) and 50 μm in (c,d).

Localized corrosion can be clearly observed on the AA-P-G sample, as seen from (a, c). However, we notice that AA-P reference sample showed a greater number of dark pits, over a larger area, after 1 day of immersion (see inset of a), while AA-P-G sample corroded in only at a few local spots. This suggest that graphene layer on PVB can provide enhanced barrier performance.

Comparable or accelerated corrosion is observed for AA-G-P sample (c, d) respect to bare AA after 1 day of immersion, indicating that no benefit on corrosion protection is afforded by graphene when it was in direct contact with the AA surface, due to galvanic corrosion and poor adhesion.

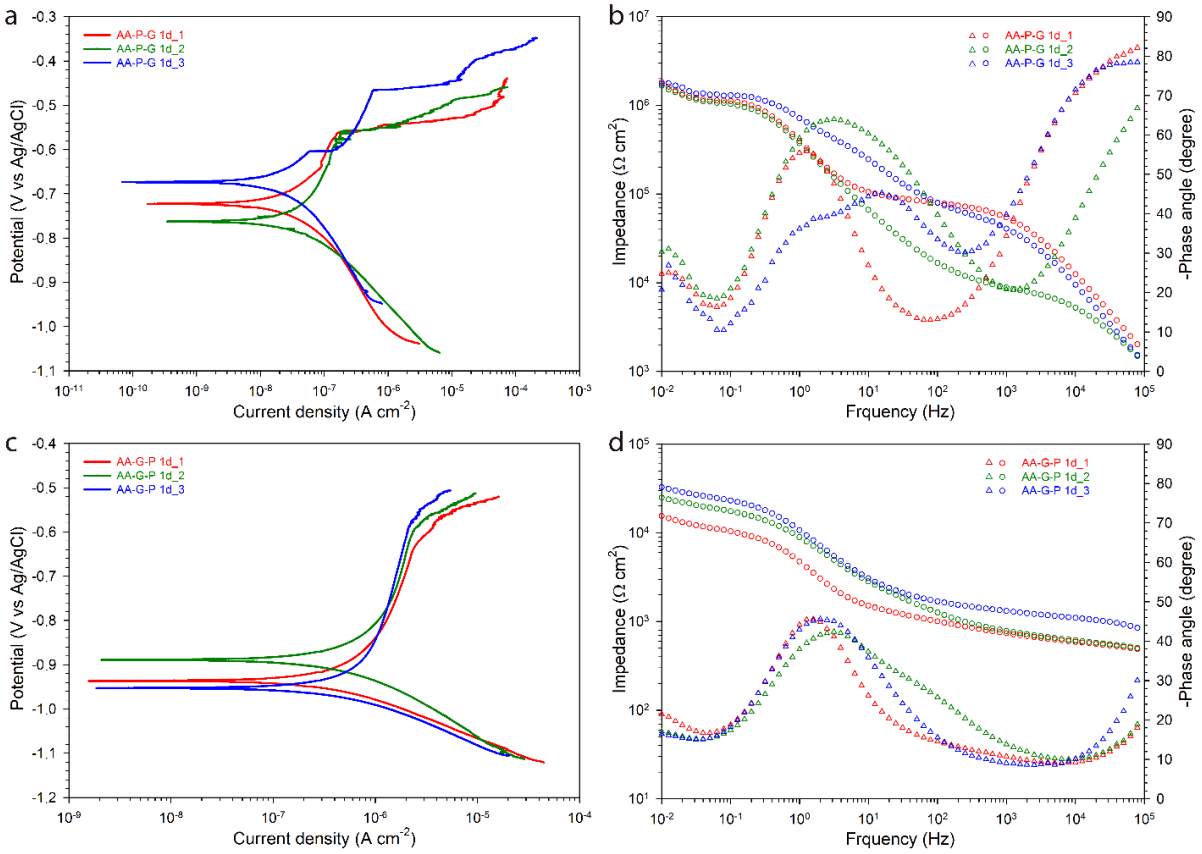

Fig. S10. (a,c) Potentiodynamic polarization curves and (b,d) electrochemical impedance spectroscopy of (a,b) AA-P-G and (c,d) AA-G-P after 1 day of immersion in 3.5 wt% NaCl solution. For impedance spectra, circles and triangles are data for impedance module and phase angle, respectively.

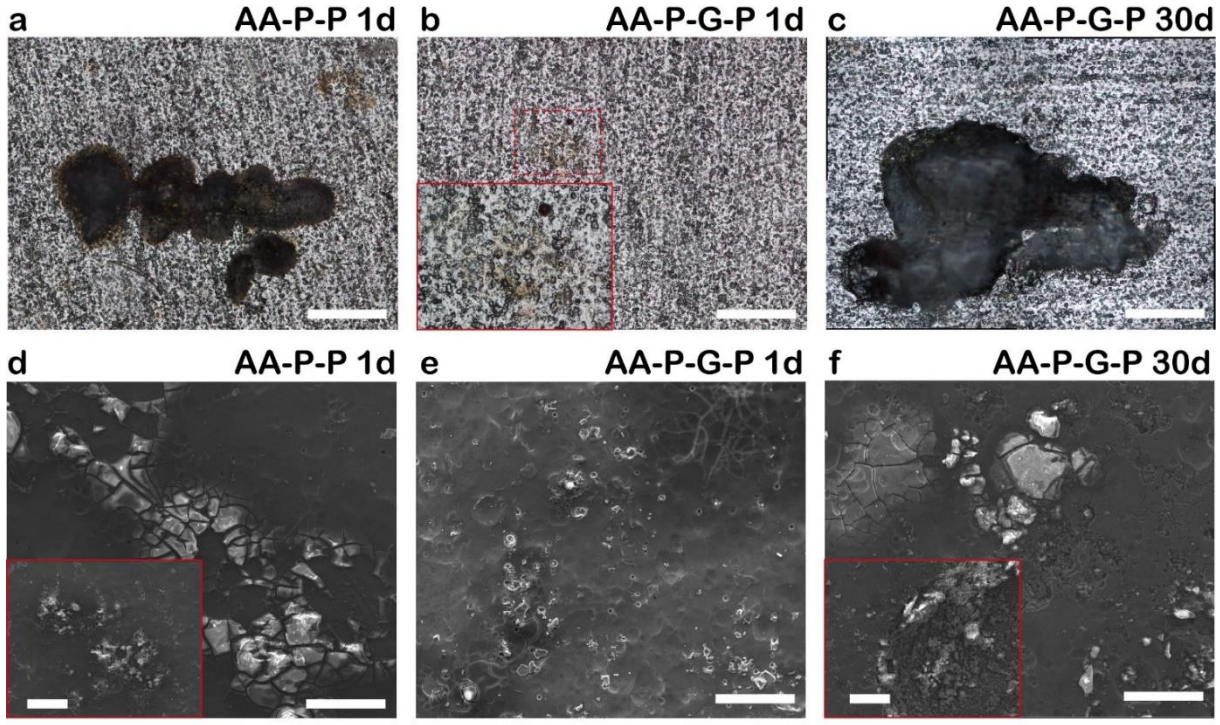

Fig. S11. (a,b,c) Optical images and (d,e,f) SEM images of (a,d) AA-P-P after 1 day and (b,e) AA-P-G-P after 1 day and (c,f) 30 days of immersion in 3.5 wt% NaCl solution. The inset of (b) is a high magnification image of red dashed line highlighted region and insets of (d) and (f) are another typical morphology from other area of the same sample. Scale bars are 500 μm in (a,b,c) and 50 μm in (d,e,f).

System AA-P-P also showed heavy corrosion attack, notably, induced local pitting, as seen from the dark area in (a). SEM observation revealed that a high degree of corrosion developed on AA-P-P, as seen from (d) and the inset image. Much less corrosion attack was observed for AA-P-G-P (b,e) compared with AA-P-P after 1 day of immersion. However, AA-P-G-P showed severe localised corrosion after 30 days of immersion (c,f), where pitting corrosion developed at local defective sites in the graphene. This suggests that AA-P-G-P could offer some effective corrosion protection for AA at short-term immersion of 1 day but not for long-term immersion after 30 days.

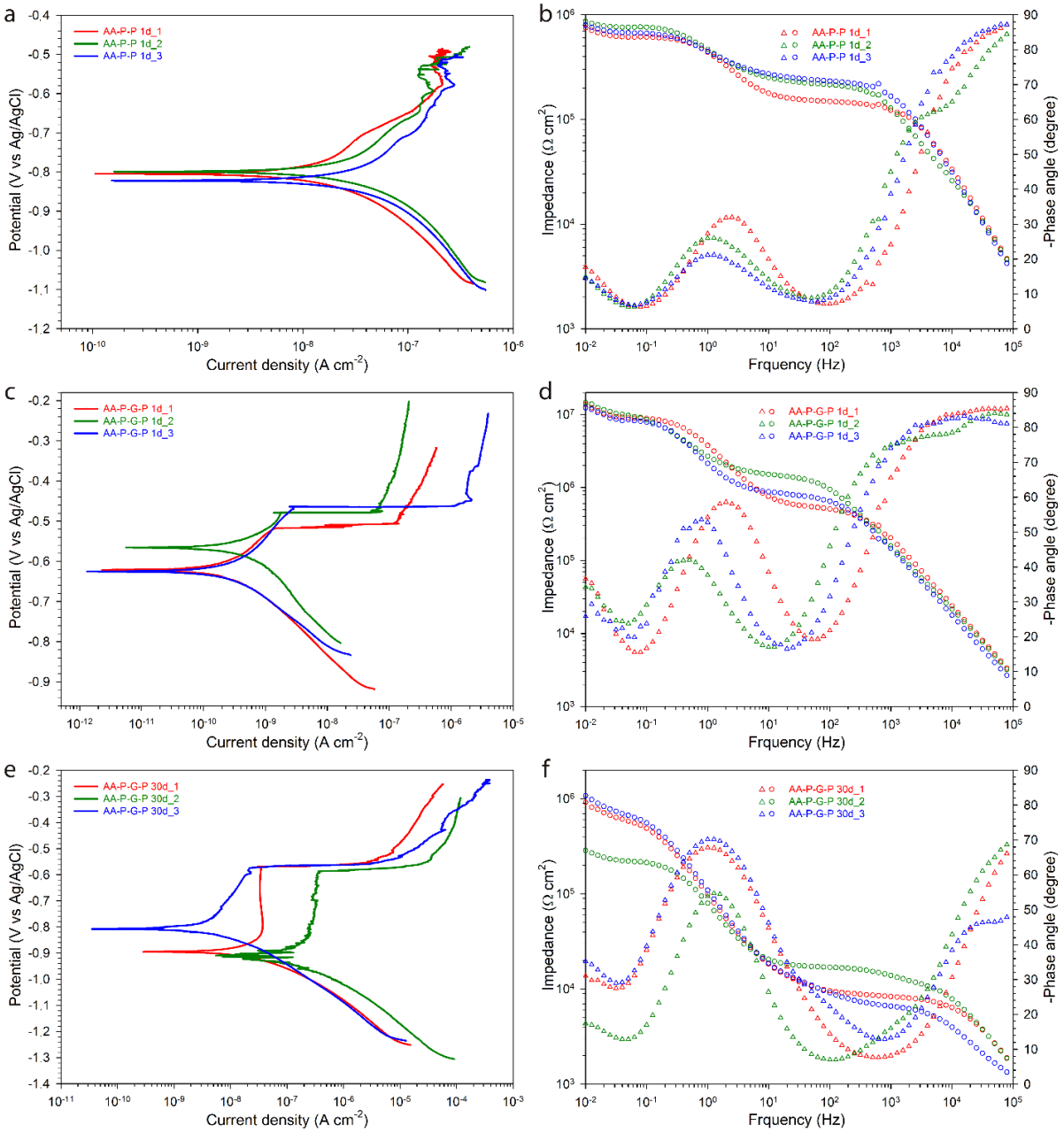

Fig. S12. (a,c,e) Potentiodynamic polarization curves and (b,d,f) electrochemical impedance spectroscopy of (a,b) AA-P-P at 1 day, AA-P-G-P at (c,d) 1 day and (e,f) 30 days of immersion in 3.5 wt% NaCl solution. For impedance spectra, circles and triangles are data for impedance module and phase angle, respectively.

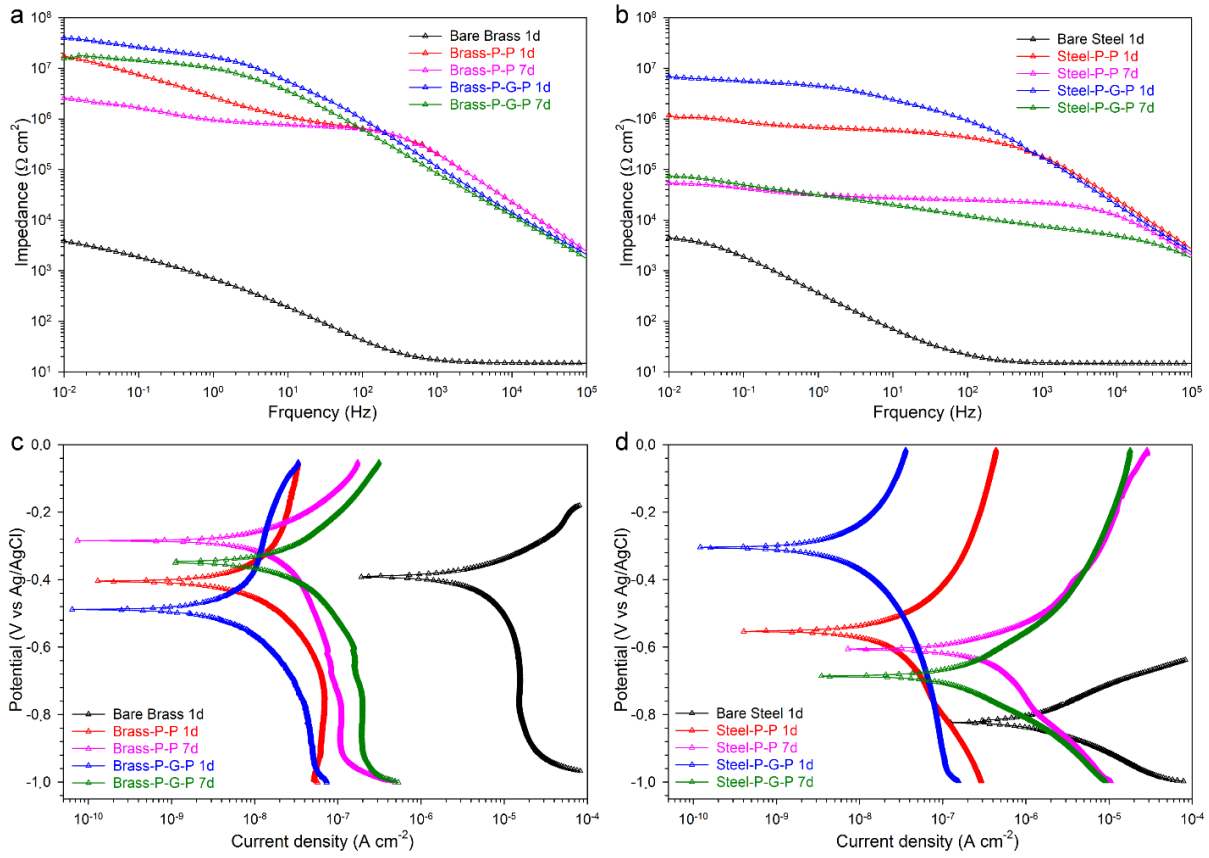

Fig. S13. (a,b) Electrochemical impedance spectroscopy and (c,d) potentiodynamic polarization curves of bare polymer (P-P) and polymer-graphene-polymer (P-G-P) coating on (a,b) carbon steel and (c,d) brass at different days of immersion in 3.5 wt% NaCl solution. Note that these are representive plots of the three reproducible samples.

From both measurements, Metal-P-G-P coatings provide better corrosion protection than Metal-P-P reference coatings for both steel (CXD-2.76.5.90-K, Q-LAB) and brass (Cu63/Zn37, GoodFellow) at 1 day of immersion. However, after 7 days of immersion, there is no significant difference between the performance of P-P and P-G-P coatings when applied on steel. On the other hand, the P-G-P coatings provide better protection than bare P-P ones even after 7 days of immersion when applied on brass.

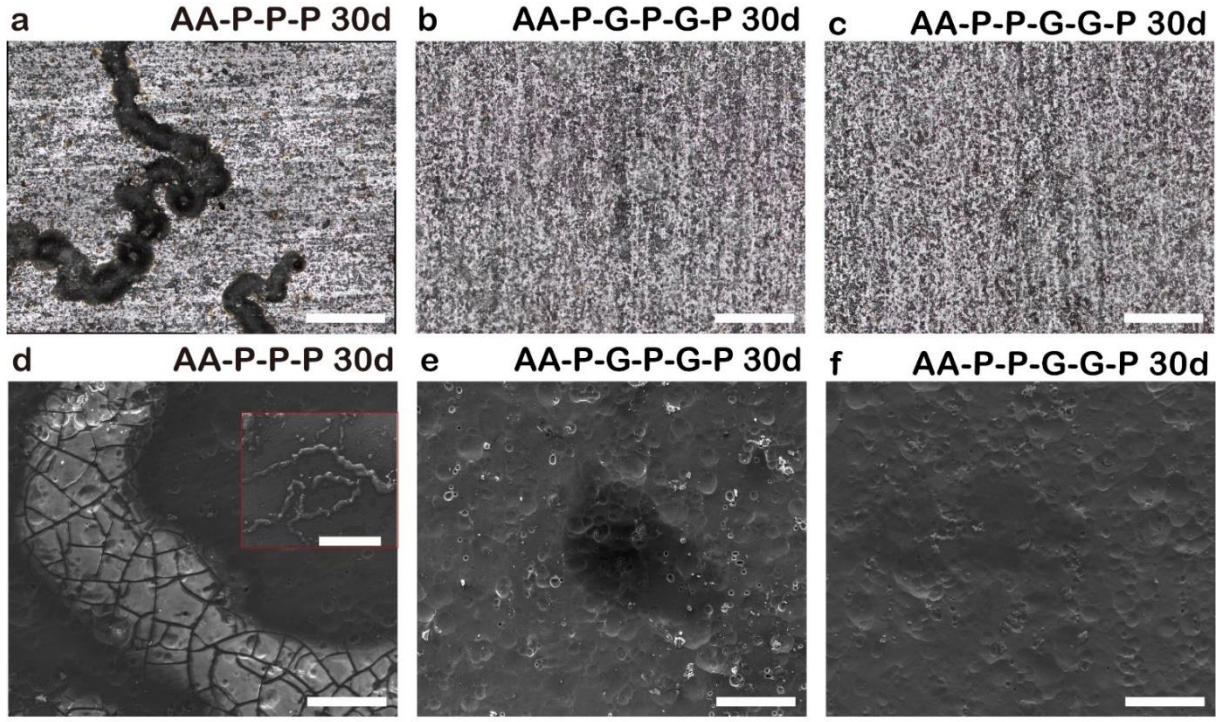

Fig. S14. (a,b,c) Optical images and (d,e,f) SEM images of (a,d) AA-P-P-P, (b,e) AA-P-G-P-G-P and (c,f) AA-P-P-G-G-P after 30 days of immersion in 3.5 wt% NaCl solution. The inset of (d) is a lower magnification image of the same sample. Scale bars are 500 μm in (a,b,c) and 50 μm in (d,e,f). The scale bar in the Inset in (d) is 500 μm.

At 30 days of immersion, bare polymer layer coated AA (AA-P-P-P) showed severe filiform corrosion with heavy corrosion attack at wide range spread across the whole surface, indicating that bare polymer layer could not provide effective corrosion protection for AA after 30 days of immersion. However, when two layers of graphene are sandwiched between three layers of polymer, for both AA-P-G-P-G-P and AA-P-P-G-G-P, after 30 days of immersion, no sign of corrosion was observed from both optical and SEM images.

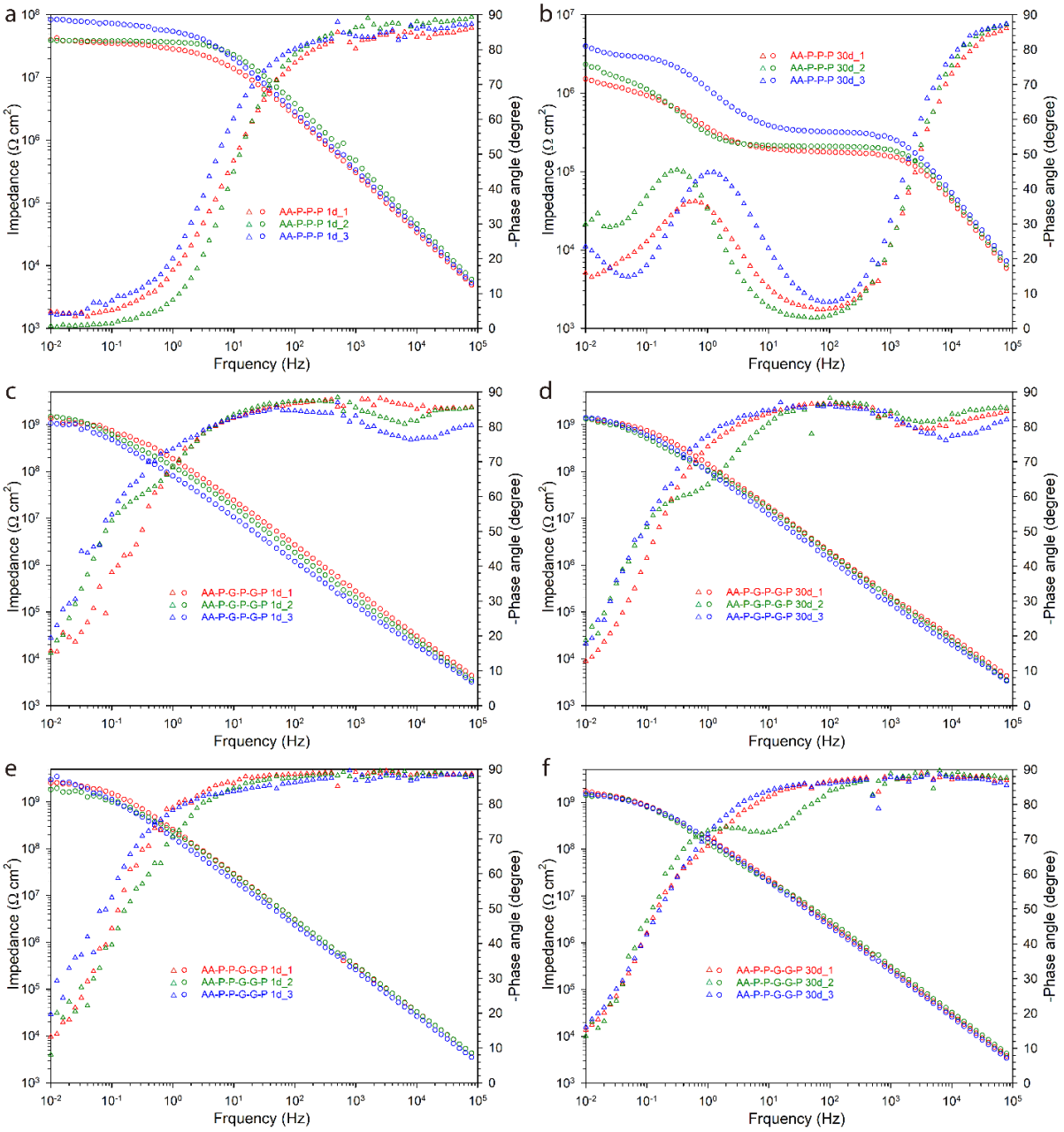

Fig. S15. Electrochemical impedance spectroscopy of (a,b) AA-P-P-P, (c,d) AA-P-G-P-G-P and (e,f) AA-P-P-G-G-G-P after (a,c,e) 1 day and (b,d,f) 30 days of immersion in 3.5 wt% NaCl solution. For impedance spectra, circles and triangles are data for impedance module and phase angle, respectively.

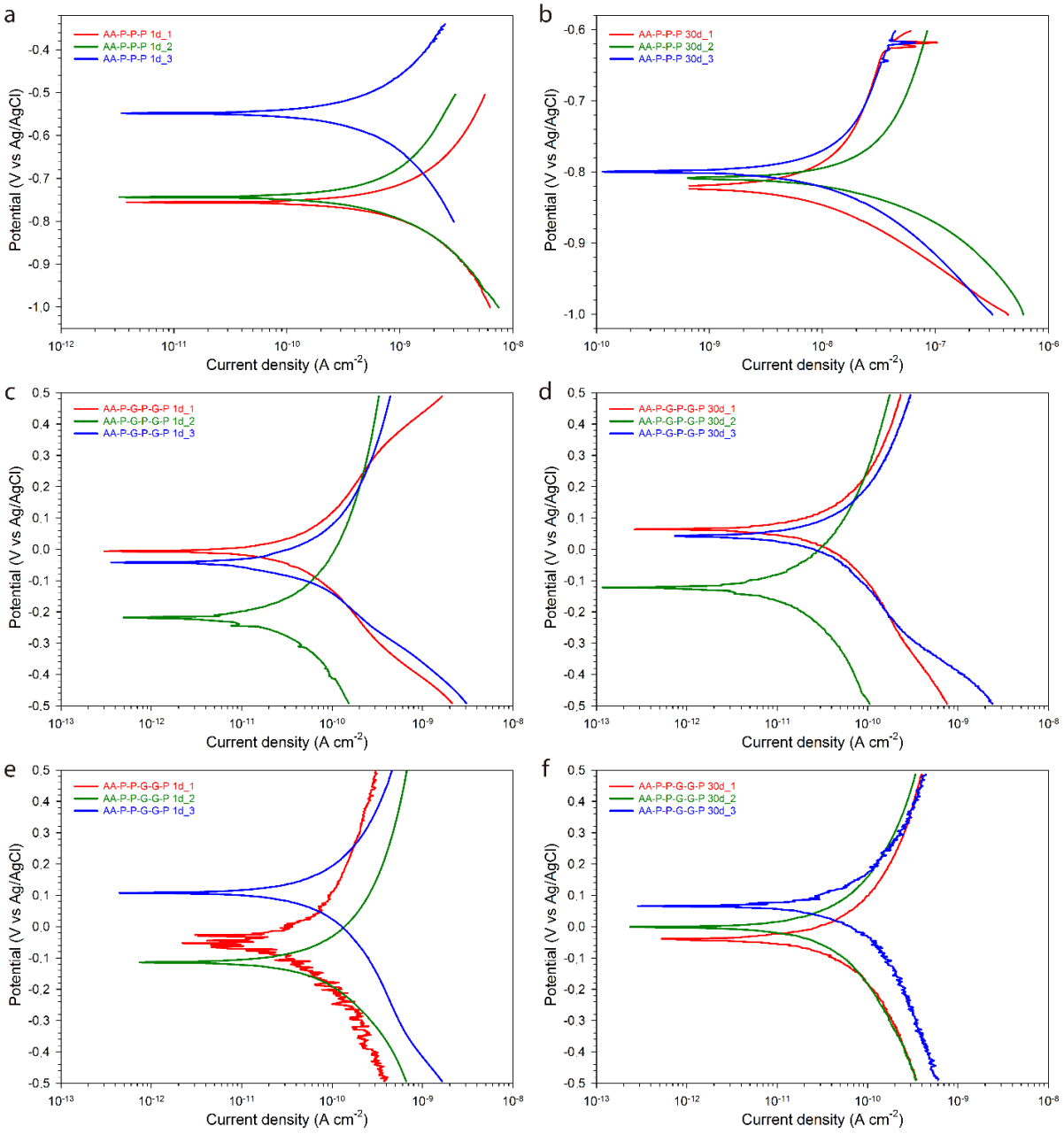

Fig. S16. Potentiodynamic polarization curves of (a,b) AA-P-P-P, (c,d) AA-P-G-P-G-P and (e,f) AA-P-P-G-G-G-P after (a,c,e) 1 day and (b,d,f) 30 days of immersion in 3.5 wt% NaCl solution.

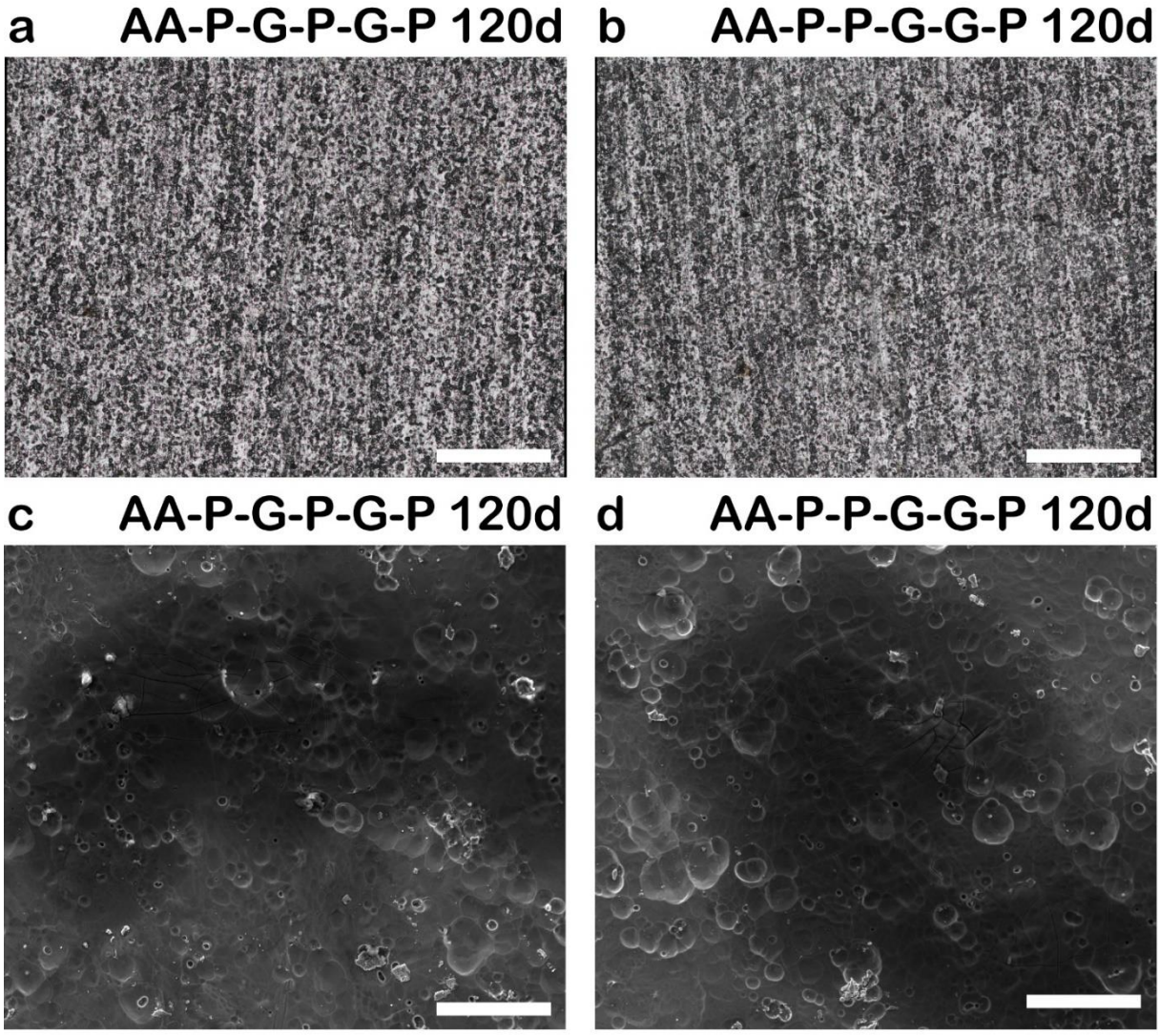

Fig. S17. (a,b) Optical images and (c,d) SEM images of (a,c) AA-P-G-P-G-P and (b,d) AA-P-P-G-G-P after 120 days of immersion in 3.5 wt% NaCl solution. Scale bars are 500 μm in (a,b) and 50 μm in (c,d).

No visible signs of corrosion on AA could be observed from both optical and SEM images for the two samples after 120 days of immersion.

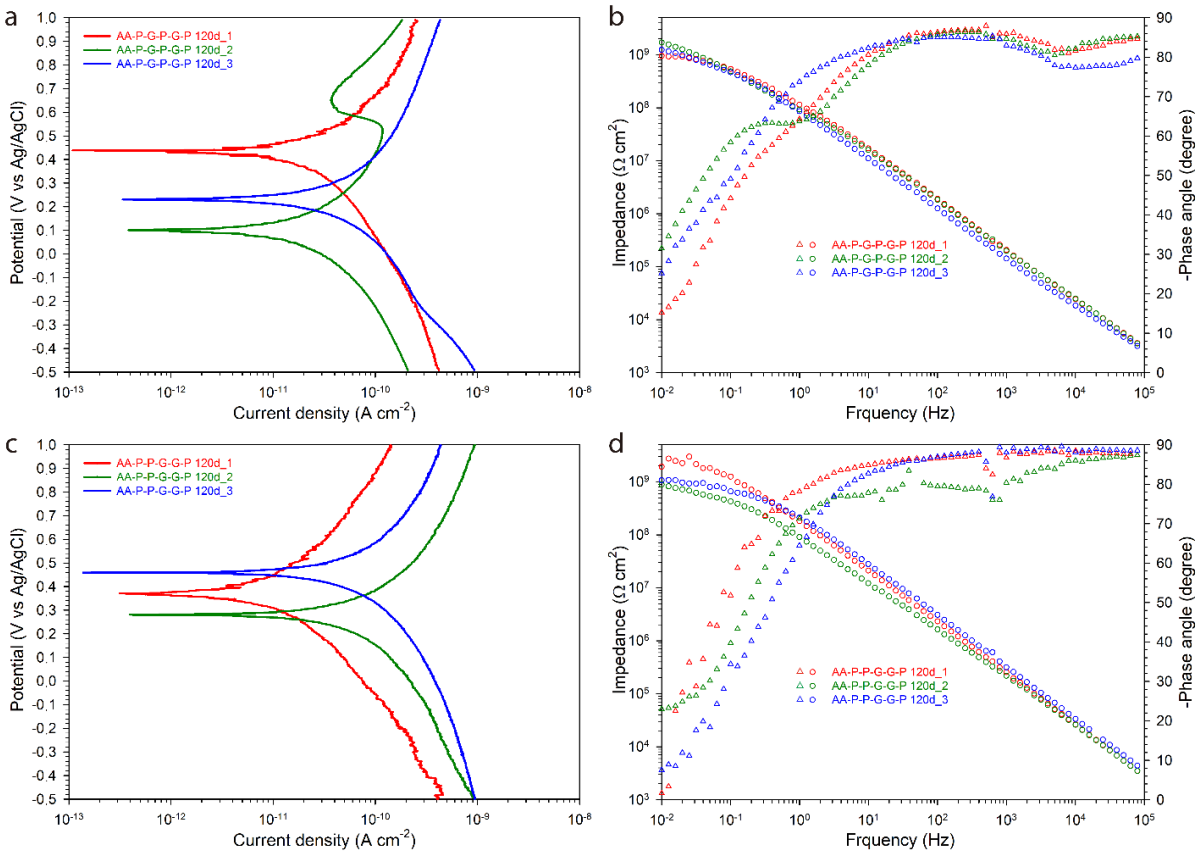

Fig. S18. (a,c) Potentiodynamic polarization curves and (b,d) electrochemical impedance spectroscopy of (a,b) AA-P-G-P-G-P and (c,d) AA-P-P-G-G-G-P after 120 days of immersion in 3.5 wt% NaCl solution. For impedance spectra, circles and triangles are data for impedance module and phase angle, respectively.

Sample	Open circuit potential OCP (mV vs Ag/AgCl)				Low frequency impedance $\|Z\|_{0.01Hz}$ (MOhms cm^2)			
	1	2	3	average	1	2	3	average
AA 1d	-623	-706	-697	-675	0.03	0.03	0.03	0.03
AA 30d	-732	-722	-738	-731	0.02	0.02	0.02	0.02
AA-G-P 1d	-817	-825	-810	-817	0.02	0.02	0.03	0.02
AA-P-G 1d	-591	-672	-693	-652	1.82	1.67	1.75	1.75
AA-P-P 1d	-820	-780	-797	-799	0.74	0.85	0.80	0.80
AA-P-G-P 1d	-635	-621	-657	-638	13.8	14.5	12.3	13.5
AA-P-G-P 30d	-751	-797	-732	-760	0.92	0.29	1.08	0.76
AA-P-P-P 1d	-750	-486	-501	-579	39	40	83	54
AA-P-P-P 30d	-787	-758	-747	-764	1.5	2.3	3.9	2.6
AA-P-G-P-G-P 1d	870	694	618	727	1364	1505	1077	1315
AA-P-G-P-G-P 30d	731	660	771	721	1319	1318	1408	1348
AA-P-G-P-G-P 120d	587	727	676	663	952	1709	1240	1300
AA-P-P-G-G-P 1d	746	487	686	640	2551	1830	2998	2460
AA-P-P-G-G-P 30d	230	448	405	361	1720	1408	1521	1550
AA-P-P-G-G-P 120d	401	204	337	314	1928	888	1073	1296

Table S1. Open circuit potential (OCP) and low frequency impedance ($|Z|_{0.01Hz}$) of all samples in this work after immersion times in 3.5 wt% NaCl solution. Values in this table are individual and average values of three samples listed with their corresponding electrochemical impedance spectroscopy.

Sample	Corrosion potential E_{corr} (mV vs Ag/AgCl)				Corrosion current density i_{corr} (nA cm^{-2})				Corrosion rate CR (μm/year)
	1	2	3	average	1	2	3	average	average
AA 1d	-567	-567	-576	-570	425	390	319	378	4
AA 30d	-1100	-1100	-1110	-1103	17700	19800	18200	18567	203
AA-G-P 1d	-936	-889	-953	-926	651	1020	837	836	9
AA-P-G 1d	-723	-762	-674	-720	38	75	35	49	0.54
AA-P-P 1d	-802	-799	-821	-807	52	195	206	151	1.6
AA-P-G-P 1d	-619	-564	-627	-603	0.39	0.53	0.34	0.42	0.005
AA-P-G-P 30d	-894	-912	-800	-869	124	182	12	106	1.2
AA-P-P-P 1d	-755	-736	-551	-680	1.3	1.9	3.2	2.1	0.02
AA-P-P-P 30d	-823	-808	-798	-810	15	43	22	27	0.29
AA-P-G-P-G-P 1d	-9	-219	-59	-96	0.08	0.27	0.09	0.15	0.0016
AA-P-G-P-G-P 30d	18	-158	-12	-51	0.13	0.04	0.28	0.15	0.0016
AA-P-G-P-G-P 120d	412	120	191	241	0.29	0.02	0.12	0.14	0.0016
AA-P-P-G-G-P 1d	-47	-115	32	-43	0.23	0.22	0.11	0.19	0.0020
AA-P-P-G-G-P 30d	-55	-36	26	-22	0.29	0.16	0.22	0.22	0.0024
AA-P-P-G-G-P 120d	371	234	461	355	0.01	0.15	0.32	0.16	0.0017

Table S2. Corrosion potential (E_{corr}), corrosion current density (i_{corr}) and calculated corrosion rate (CR) of all samples in this work after different days of immersion in 3.5% NaCl solution. Note that values in the table are individual and average values of three samples listed with their corresponding polarization curves. Corrosion rate are calculated following Faraday's law through equation of $CR=i_{corr}*K*E_w/d$, where i_{corr} is corrosion current density (A/cm^2), K is corrosion constant ($K=3272$ mm A^{-1} cm^{-1} $year^{-1}$), E_w is equivalent weight in (9g for Al), d is density ($2.7g/cm^3$ for Al).

Reference	Metal substrate	Coating system	Electrolyte	Immersion time	Relative corrosion rate improvement ($CR_{uncoated}/CR_{coated}$)	Relative corrosion impedance improvement ($|Z|_{coated}/|Z|_{uncoated}$)
[1]	Cu	CVD Gr	0.1 M Na_2SO_4	few hours	7	4
[2]	Cu	CVD Gr	0.1 M NaCl	1 hour	50	40
[3]	Cu	CVD Gr + ALD Al_2O_3	0.1 M Na_2SO_4	3 hours	100	500
[4]	Ni	Thermal annealing grown Gr	0.1 M NaCl	few hours	7	2
[5]	Ni-Fe alloy	Laser irradiation grown Gr	0.6 M NaCl	1 hour	9	7
[6]	Cu	CVD Gr	0.1 M NaCl	few hours	10	2
[7]	Cu	Electrochemically deposited graphene	3.5 wt% NaCl	1 hour	18	3
[8]	Cu	Polymer/graphene composites	3.5 wt% NaCl	few hours	11	3
[9]	NdFeB	Electrochemically deposited graphene	3.5 wt% NaCl	few hours	2	10
[10]	Steel	Electrochemically deposited Ni/graphene	3.5 wt% NaCl	5 mins	2	2
[11]	Al alloy	Spin coated graphene	3.5 wt% NaCl	few hours	2800	10
[12]	Steel	Polymer/graphene composites	3.5 wt% NaCl	30 mins	210	370
[13]	Steel	Nanocasted epoxy/graphene composites	3.5 wt% NaCl	few hours	70	3300
[14]	Steel	Polymer/graphene composites	3.5 wt% NaCl	30 mins	200	300
[15]	Cu	Polymer/graphene composites	3.5 wt% NaCl	100 hours	140	10
[16]	Steel	Electrochemically deposited graphene	3.5 wt% NaCl	30 mins	2	3
[17]	Zn	Electrochemically deposited graphene	3.5 wt% NaCl	1 hour	130	3
[18]	Fe	Polymer/graphene composites	3.5 wt% NaCl	24 hours	100	80
[19]	Steel	Epoxy/graphene composites	3.5 wt% NaCl	96 hours	120	10
[20]	Steel	Silane/graphene composites	3.5 wt% NaCl	few hours	2000	3000
[21]	Al	Dip coated graphene	0.5 M NaCl	30 mins	1200	200
[22]	Cu	Polymer/graphene composites	3.5 wt% NaCl	30 mins	110	1400
[23]	Fe	Polymer/graphene composites	3.5 wt% NaCl	24 hours	15	10
[24]	Steel	Ceramic/graphene composites	3.5 wt% NaCl	5 hours	500	50
[25]	Steel	Polymer/graphene composites	0.5 wt% NaCl	1 hour	35	150
[26]	Al alloy	Silane/graphene composites	3.5 wt% NaCl	30 mins	580	320
[27]	Al alloy	Silane/graphene composites	3.5 wt% NaCl	2 hours	10	6
[28]	Steel	Chitosan/graphene composites	3.5 wt% NaCl	6 hours	20	2000
[29]	Mg alloy	Silane/graphene composites	3.5 wt% NaCl	80 mins	80	15
This work	Al alloy	Polymer/graphene composites	3.5 wt% NaCl	30 days	127000	67000

Table S3. Comparison of corrosion protection performance between previously reported graphene based anticorrosive coatings[1-29] and this work. Relative corrosion rate (CR) improvement is calculated from the ratio $CR_{(uncoated)}/CR_{(coated)}$. Relative corrosion impedance ($|Z|$) improvement is calculated based upon the ratio $|Z|_{(coated)}/|Z|_{(uncoated)}$ at 0.01 Hz.

References

[1] D. Prasai, J.C. Tuberquia, R.R. Harl, G.K. Jennings, K.I. Bolotin, Graphene: corrosion-inhibiting coating, ACS nano 6(2) (2012) 1102-1108.
[2] R.S. Raman, P.C. Banerjee, D.E. Lobo, H. Gullapalli, M. Sumandasa, A. Kumar, et al., Protecting copper from electrochemical degradation by graphene coating, Carbon 50(11) (2012) 4040-4045.
[3] Y.-P. Hsieh, M. Hofmann, K.-W. Chang, J.G. Jhu, Y.-Y. Li, K.Y. Chen, et al., Complete corrosion inhibition through graphene defect passivation, ACS nano 8(1) (2013) 443-448.
[4] U. Mogera, N. Kurra, D. Radhakrishnan, C. Narayana, G.U. Kulkarni, Low cost, rapid synthesis of graphene on Ni: An efficient barrier for corrosion and thermal oxidation, Carbon 78 (2014) 384-391.
[5] X. Ye, Z. Lin, H. Zhang, H. Zhu, Z. Liu, M. Zhong, Protecting carbon steel from corrosion by laser in situ grown graphene films, Carbon 94 (2015) 326-334.
[6] L. Shen, Y. Zhao, Y. Wang, R. Song, Q. Yao, S. Chen, et al., A long-term corrosion barrier with an insulating boron nitride monolayer, J. Mater. Chem. A 4(14) (2016) 5044-5050.
[7] S.C. Sahu, A.K. Samantara, M. Seth, S. Parwaiz, B.P. Singh, P.C. Rath, et al., A facile electrochemical approach for development of highly corrosion protective coatings using graphene nanosheets, Electrochem. Commun. 32 (2013) 22-26.
[8] B.P. Singh, B.K. Jena, S. Bhattacharjee, L. Besra, Development of oxidation and corrosion resistance hydrophobic graphene oxide-polymer composite coating on copper, Surf. Coat. Technol. 232 (2013) 475-481.
[9] W. He, L. Zhu, H. Chen, H. Nan, W. Li, H. Liu, et al., Electrophoretic deposition of graphene oxide as a corrosion inhibitor for sintered NdFeB, Appl. Surf. Sci. 279 (2013) 416-423.
[10] C.P. Kumar, T. Venkatesha, R. Shabadi, Preparation and corrosion behavior of Ni and Ni–graphene composite coatings, Mater. Res. Bull. 48(4) (2013) 1477-1483.
[11] Y. Liu, J. Zhang, S. Li, Y. Wang, Z. Han, L. Ren, Fabrication of a superhydrophobic graphene surface with excellent mechanical abrasion and corrosion resistance on an aluminum alloy substrate, RSC Adv 4(85) (2014) 45389-45396.
[12] Y.-H. Yu, Y.-Y. Lin, C.-H. Lin, C.-C. Chan, Y.-C. Huang, High-performance polystyrene/graphene-based nanocomposites with excellent anti-corrosion properties, Polym. Chem 5(2) (2014) 535-550.
[13] K.-C. Chang, M.-H. Hsu, H.-I. Lu, M.-C. Lai, P.-J. Liu, C.-H. Hsu, et al., Room-temperature cured hydrophobic epoxy/graphene composites as corrosion inhibitor for cold-rolled steel, Carbon 66 (2014) 144-153.
[14] K.-C. Chang, W.-F. Ji, M.-C. Lai, Y.-R. Hsiao, C.-H. Hsu, T.-L. Chuang, et al., Synergistic effects of hydrophobicity and gas barrier properties on the anticorrosion property of PMMA nanocomposite coatings embedded with graphene nanosheets, Polym. Chem 5(3) (2014) 1049-1056.
[15] K. Qi, Y. Sun, H. Duan, X. Guo, A corrosion-protective coating based on a solution-processable polymer-grafted graphene oxide nanocomposite, Corros. Sci. 98 (2015) 500-506.
[16] M. Bagherzadeh, Z.S. Ghahfarokhi, E.G. Yazdi, Electrochemical and surface evaluation of the anti-corrosion properties of reduced graphene oxide, RSC Adv 6(26) (2016) 22007-22015.

[17] R. Li, J. Liang, Y. Hou, Q. Chu, Enhanced corrosion performance of Zn coating by incorporating graphene oxide electrodeposited from deep eutectic solvent, RSC Adv 5(75) (2015) 60698-60707.
[18] M. Mo, W. Zhao, Z. Chen, Q. Yu, Z. Zeng, X. Wu, et al., Excellent tribological and anti-corrosion performance of polyurethane composite coatings reinforced with functionalized graphene and graphene oxide nanosheets, RSC Adv 5(70) (2015) 56486-56497.
[19] L. Gu, S. Liu, H. Zhao, H. Yu, Facile Preparation of Water-Dispersible Graphene Sheets Stabilized by Carboxylated Oligoanilines and Their Anticorrosion Coatings, ACS Appl. Mater. Interfaces 7(32) (2015) 17641-17648.
[20] K.S. Aneja, S. Bohm, A. Khanna, H.M. Bohm, Graphene based anticorrosive coatings for Cr (vi) replacement, Nanoscale 7(42) (2015) 17879-17888.
[21] J. Liu, L. Hua, S. Li, M. Yu, Graphene dip coatings: An effective anticorrosion barrier on aluminum, Appl. Surf. Sci. 327 (2015) 241-245.
[22] H. Alhumade, A. Abdala, A. Yu, A. Elkamel, L. Simon, Corrosion inhibition of copper in sodium chloride solution using polyetherimide/graphene composites, Can. J. Chem. Eng (2016).
[23] M. Mo, W. Zhao, Z. Chen, E. Liu, Q. Xue, Corrosion inhibition of functional graphene reinforced polyurethane nanocomposite coatings with regular textures, RSC Adv 6(10) (2016) 7780-7790.
[24] J. Mondal, A. Marques, L. Aarik, J. Kozlova, A. Simões, V. Sammelselg, Development of a thin ceramic-graphene nanolaminate coating for corrosion protection of stainless steel, Corros. Sci. 105 (2016) 161-169.
[25] Y. Jafari, S.M. Ghoreishi, M. Shabani-Nooshabadi, Electrochemical deposition and characterization of polyaniline-graphene nanocomposite films and its corrosion protection properties, J. Polym. Res 23(5) (2016) 1-13.
[26] H. Zhu, L. Yue, C. Zhuang, Y. Zhang, X. Liu, Y. Yin, et al., Fabrication and characterization of self-assembled graphene oxide/silane coatings for corrosion resistance, Surf. Coat. Technol. 304 (2016) 76-84.
[27] A. Ahmadi, B. Ramezanzadeh, M. Mahdavian, Hybrid silane coating reinforced with silanized graphene oxide nanosheets with improved corrosion protective performance, RSC Adv (2016).
[28] E.M. Fayyad, K.K. Sadasivuni, D. Ponnamma, M.A. Al-Maadeed, Oleic acid-grafted chitosan/graphene oxide composite coating for corrosion protection of carbon steel, Carbohydr. Polym. (2016).
[29] A.B. Ikhe, A.B. Kale, J. Jeong, M.J. Reece, S.-H. Choi, M. Pyo, Perfluorinated polysiloxane hybridized with graphene oxide for corrosion inhibition of AZ31 magnesium alloy, Corros. Sci. (2016).

Appendix D

A coated metal product and a method to produce a coated metal product

EU patent application (EP16176135)

A COATED METAL PRODUCT AND A METHOD TO PRODUCE A COATED METAL PRODUCT

FIELD OF THE INVENTION

The present invention relates to a coated metal product having a reduced corrosion rate.

The present invention relates also to a method of producing the coated metal product and the use of the coating onto a metal substrate for reducing the corrosion rate of the metal substrate.

BACKGROUND OF THE INVENTION

Metals and metal alloys are of vital importance in several applications, ranging from outer space to deep sea. Preventing or protecting metals and alloys from environmental degradation is therefore of critical importance aiming at increasing the lifetime of material and decreasing eventually economic losses due to materials failure. Metals and metal alloys corrosion may lead to tragic disasters, such as leakage of toxic chemicals or collapse of infrastructures. Protection of metal surface aiming at complete separation of metals from external environment is therefore of primary importance in several technical fields.

Materials having high degree of impermeability, chemical inertness and thermal stability may be good candidates as protective layers for metals.
However, chemical, mechanical and electrical incompatibility between protective layers and metals or metal alloys substrates hinders the use of several of these good candidates.

For example, graphene is known for its outstanding impermeability, chemical inertness, thermal stability and transparency, and graphene has also shown great potential in the application of protective coatings.
However, protection of metals and alloys by graphene coatings is compromised by galvanic coupling effects with metals. These effects are due to graphene's higher nobility and conductivity than many metals. These conditions can lead to enhanced corrosion and oxidation of graphene coated metals.

In addition, graphene exhibits a very poor adhesion on some metal substrates (e.g. Cu, Pt), as adhesion takes place through relatively weak forces (such as van der Waals forces), thus making it not suitable for long-term protection in environments exposing the graphene coated metals to mechanical abrasion, or in situations where chemical species may intercalate (diffuse under) the graphene coating and further separate the graphene and the metal.
Another example of protective layers may be polymers based layers.
Polymer-based protective coatings may be applied on metal and alloy as barrier against aggressive species. However, due to the porous nature of polymeric networks, these polymer-based protective coatings generally do not offer good barrier properties, thus leading to significant limitation in the protection ability of polymer coatings for metals and alloys.

Hence, an improved coated metal product and an improved method of producing it would be advantageous. In particular, a more efficient and/or reliable method of producing a coating on a metal product would be advantageous.

OBJECT OF THE INVENTION

It may be seen as an object of the invention to provide a metal product having an increased resistance towards corrosion.
Thus, it may be seen as an object of the invention to provide a metal product with a reduced corrosion rate.

A further object of the invention may be seen as to provide a method for producing a coated metal product with improved resistance to corrosion.

In particular, it may be seen as a further object of the present invention to provide a metal product having an increased resistance towards corrosion that solves the above mentioned problems of the prior art by coating a metal product with a combination of one or more barrier elements.

It is an object of the present invention to wholly or partly overcome the above disadvantages and drawbacks of the prior art. More specifically, it is an object to reduce the corrosion rate of coated metal products.

An object of the present invention is to provide an alternative to the prior art.

SUMMARY OF THE INVENTION

The present invention offers a coating, which protects materials against degradation from the environment by a combination of at least one adhesion element, at least one barrier element and at least one upper element.
By combining the specific structure of the at least three elements respective disadvantages of the use of single adhesion, barrier and upper elements are overcome.
The elements herein referred to may also be referred to as components of the metal coating of the invention.

The present invention proposes a metal product having an anticorrosive coating made of at least one barrier element onto at least one adhesion element deposited onto a metal product and at least one upper element deposited onto the at least one barrier element.

Thus, the above described object and several other objects are intended to be obtained in an aspect of the invention by providing a coated metal product, comprising one or more metal surfaces and a coating deposited on said one or more metal surfaces, wherein the coating comprises: at least one adhesion element, deposited onto the one or more metal surfaces; a first barrier element deposited onto said at least one adhesion element; at least one upper element, deposited onto said first barrier element; and wherein the one or more metal surfaces comprise one or more metal elements and/or an alloy of metal elements.

The at least one adhesion element may comprise at least one first polymer layer.
The first barrier element may comprise one or more barrier layers, e.g. a first barrier layer.
The at least one upper element may comprise at least one second polymer layer.

The at least one adhesion element, is located directly on the surface of the metal to be protected. The primary function of the adhesion element is adhesion to the rest of the coating; the secondary function is to provide galvanic decoupling, i.e. reduction of galvanic corrosion through electrical insulation, in the case of the

barrier element being conductive; the tertiary function is that it may contribute to slowing down diffusion of undesired species.

The first barrier element may comprise graphene or other two-dimensional layers and has as main function the reduction of the diffusion of ions and liquids to the metal surface.

The at least one upper element may comprise the topmost layer of the coating. The primary function of the upper element is to provide protection of the rest of the coating, and secondary to limit diffusion of species towards or away from the metal surface.

Thus, the present invention offers a coating, which protects materials against degradation from the environment by a combination of at least one barrier layer and at least two or more polymer based layers. By combining a specific structure of two or more polymer based layers and one or more barrier layer respective disadvantages of the use of single barrier based layers or polymer based layers are overcome.

In one embodiments, the present invention proposes a metal product having an anticorrosive coating made of one or more barrier layers and two or more polymer based layers onto a metal product.

The coating covers, at least partially, the one or more metal surfaces.

The coating covers, at least partially, at least one surface of the one or more metal surfaces. The metal product or metal products may have a top and a bottom surface, wherein the top surface may be the external and the bottom may be the internal surface of the product. For example, a metal foil, such as a foil suitable for protecting materials may have a coating on both top and bottom surface, thus both surfaces in contact with the environment and with the material to be protected are coated.

A foil suitable for protecting materials may be a foil for packaging food e.g., fruit, and may as such replace, e.g., plastic food wrap.

In some other embodiments, the metal product may have the coating only on one of the one or more metal surfaces.

First and second polymer layer and first barrier layer are deposited onto, i.e. in contact with, the respective layers.

Onto the metal product, the coating may be defined as a coating unit of Polymer layer (POL), Barrier layer (BAR), Polymer layer (POL), thus POL/BAR/POL. In some embodiments, the coated metal product may comprise more than one repetitive coating unit POL/BAR/POL onto the same one or more metal surfaces.

Thus in one embodiment, the invention features a first barrier layer with a polymer layer on each side of the first barrier layer so as to form a polymer-barrier layer-polymer structure on a metal substrate.
In a more specific embodiment, the invention is further characterized in that the broad embodiment referred to above is placed on a metal or metallic alloy (MET-AL) so as to form a MET-AL/POL/BAR/POL structure.

The coating may enable protecting the metal, thus may have a protective function, e.g. may protect the metal from corrosion and/or abrasion.
The first polymer layer provides strong adhesion to the substrate surface, i.e. the metal or metal alloy surface, e.g. through chemical bonds.
The first polymer layer may also be highly adhesive on rough surfaces thus ensuring optimal adherence between the metal substrate and the first polymer layer.
The first polymer layer may also have the function of electrically separating the barrier layer from the metal surface thus avoiding galvanic coupling.
Indeed due to different electrode potentials between dissimilar metals and alloys and the material of the barrier layer, galvanic corrosion may occur between the metal surface and the barrier layer. The presence of the first polymer layer therefore may provide an insulating barrier between the barrier layer and the metal surface avoiding or reducing eventual electrochemical processes between the barrier layer and the metal surface.
The second polymer layer onto the barrier layer may protect the integrity of the barrier layer, such as protecting the barrier layer from mechanical abrasion, e.g. scratches.

The second polymer layer may also provide a diffusion barrier, thus reducing or completely stopping diffusion of compounds that can lead to corrosion, such as water or oxygen molecules to, towards and/or through the barrier layer.
In that, the second polymer layer may have a limited porosity that allows only diffusion of specific species and stops or at least reduces diffusion of other species.

In some embodiments, the coating further comprises a second barrier element deposited onto the at least one upper element.

The second barrier element may be the same as the first barrier element, however positioned onto the at least one upper element and not on the one or more metal surfaces.

The presence of a second barrier element may enhance the corrosion protection of the one or more metal surfaces.

In some further embodiments, the coating further comprises a top element deposited onto the second barrier element. The top element may comprise a third polymer layer.

The third polymer layer may be the same as the first and second polymer layer, however positioned onto the second barrier element and not on the one or more metal surfaces or onto the first barrier element.

The presence of the third polymer layer protects the second barrier element from mechanical abrasion and thus in turn enhances the corrosion protection of the one or more metal surfaces.

The one or more metal surfaces comprise one or more metal elements and/or an alloy of metal elements.
In some embodiments, the one or more metal surfaces may comprise a metal oxide.

Metal is herein referred to as a metal according to the periodic table, i.e. may be an Alkali metal, Alkaline earth metal, Transition metal, Post-transition metal, Lanthanide or Actinide.

In some embodiments, the one or more metal elements are Transition metals. For example, the one or more metal elements may be Cu, Fe, Zn, Cr, Ni or Mn. In some other embodiments, the one or more metal elements are Alkaline earth metals, such as Mg.

In some embodiments, the one or more metal elements are post-transition metals.

In some other embodiments, the alloy of metal elements comprises post-transition metals.

According to different classification example of post-transition metals may be Al, Cu, Ag, Au, Zn, Cd, Sn or Pb.

In some embodiments, the first barrier element comprises one or more barrier layers.

In some other embodiments, the second barrier element comprises one or more barrier layers.

The first and/or second barrier element may be formed by single layers, by multiple layers or by multiple overlapping layers.

The first barrier element may comprise one or more continuous layers.

The second barrier element may also comprise one or more continuous layers.

Being continuous layers, the first or second barrier elements may stop diffusion of specific species, such as water or oxygen gas, towards the one or more metal surfaces.

In some embodiments, the first barrier element comprises one or more discontinuous layers.

In some other embodiments, the second barrier element comprises one or more discontinuous layers.

The one or more discontinuous layers may be discontinuous overlapping layers. The one or more discontinuous layers may be defined as discontinuous overlapping layers, wherein overlapping layers are a series of layers overlapping on each other defining a structure that eventually retards, i.e. slows down or reduces, the diffusion of water or oxygen gas.

In some embodiments, the one or more discontinuous layers may be compressed discontinuous overlapping layers forming a structure defining a low diffusion pattern, i.e. a pattern producing a slow diffusion path for specific species, such as water or oxygen gas.

In some embodiments, the first barrier element comprises a layer having a form of a two-dimensional lattice of atoms.
For example, the first barrier element may comprise a layer having a two-dimensional, atomically thin material, which may have a honey comb lattice.

In some further embodiments, the second barrier element may comprise a layer having a form of a two-dimensional lattice of atoms.
The second barrier element may comprise one or more elements, for example one or more of the elements carbon, boron or nitrogen.
For example, the second barrier element may comprise a layer having a two-dimensional, atomically thin material, which may have a honey comb lattice.

The specific structure of the barrier element may reduce the diffusion towards the one or more metal surfaces.

In further embodiments, the first barrier element comprises graphene.

Graphene is a crystalline allotrope of carbon having the form of a two-dimensional, atomic-scale thick, honey-comb lattice in which one atom forms each vertex.
Carbon atoms in graphene are densely packed in a regular atomic-scale having hexagonal pattern and 2-dimensional properties.

Graphene is impermeable to very small molecule, e.g. helium and to a large variety of atoms and molecules. Besides the impermeability, other various properties of graphene, including chemical nobility, thermal stability, transparency, high surface area and mechanical strength may be beneficial for its use as barrier layer in a protective coating.
In some other embodiments, the second barrier element comprises graphene.

The first barrier element may comprise a single layer of graphene.

The second barrier element may also comprise a single layer of graphene.

A single layer of graphene may be referred to as mono-layer of graphene.

In some embodiments, the first and/or second barrier element may be formed by a plurality of mono-layers of graphene singularly deposited one onto the other.

The use of a single or few graphene layers, enables for cost savings, and furthermore allows the coating to be transparent.

The first barrier element may comprise a multi layer comprising graphene.

The second barrier element may also comprise a multi layer comprising graphene.

In some embodiments, the first and/or second barrier element may be grown so as to form a stack of multi-layers.

Graphene may be produced through a variety of techniques such as, for example, exfoliation, hydrothermal self-assembly and Chemical Vapour Deposition (CVD).

Graphene layers having good barrier properties may require to be of homogeneously high quality at a large scale and with a low number of defects. Thus, a preferred production method may be based on CVD processes that generally provide graphene of high quality having good mechanical and electrical properties.

CVD technology may be used to successfully prepare single-layer or multi-layer of impermeable graphene sheets with homogenously high quality and continuous at large scale on metal surface.

The inventors observed that CVD graphene on the surface of a metal substrate could effectively isolate the metal from environment and prevent corrosion. However, corrosion or oxidation could still be possible to start from defective area, such as point defects, wrinkles, cracks, grain boundaries, where aggressive species have access to the metal substrate. Moreover, due to the higher conductivity and nobility of carbon than most metals, accelerated corrosion of metal substrate would be possible, due to a galvanic coupling effect between graphene and metals, where electrons from metals can be easier transferred to cathodic sites for reduction reaction than those without graphene on surface, leading to enhanced anodic metal corrosion or oxidation. Adhesion of a protective coating on metal substrate is also critical for durability at long term protection. Graphene normally interact with metal substrate via Van Der Waals forces, and thus can easily be delaminated.

This can also be an advantage as for many metal alloys, where graphene cannot be grown directly on, such as carbon steel and aluminium alloys, graphene sheets may be transferred from the growth substrate.

Thus in some embodiments the graphene layers may be deposited onto the polymer layer from a growth substrate.

Multilayered as grown or transferred graphene layers may also be used offering a better barrier than single layer graphene by overlapping graphene defects for the protection of metals. However, still due to a weak adhesion on metal substrate and its galvanic coupling effects, at certain conditions both transferred and as grown multilayer graphene still have chances to be easily delaminated.

In order to overcome the drawbacks of deposition of direct barrier elements on metal or metal allow surface, the inventors devised the invention by combining polymer layers and barrier layers in a sandwich structure.

In general, the first or bottom polymer provides strong adhesion to the metal substrate surface, e.g. through chemical bonds and it may be more adhesive than graphene in itself on rough surfaces and separates graphene electrically from the substrate surface, thus avoiding galvanic coupling. The second or top layer of the polymer, which may also have been used to transfer the graphene from a growth substrate, helps keeping the integrity of atomic thin graphene layer e.g., protects the graphene from possible marks.

In some embodiments, the first and/or second barrier element comprises graphene based continuous or discontinuous layer, such as graphene oxide (GO), reduced graphene oxide (RGO), functionalised graphene, such as fluorizated CVD graphene or fluorizated graphene nano flakes.

For example, the first and/or second barrier element may comprise a series of continuous or discontinuous GO layers. For example, the barrier element may comprise a dispersion of a few layers flakes and monolayer flakes of GO.

One of the advantages of using graphene based nanoflakes (GO/RGO) is that the materials are low cost, easy to process, and more flexible compared to continuous CVD graphene layer.

Reduced graphene oxide (rGO) nano flakes may also be used in a barrier element for the protection of metals when CVD graphene is not applicable. CVD growth of graphene normally require carbon atoms to be rearranged on catalysis-active metal surface at high temperature. rGO based thin films may have similar properties as graphene layers, such as being impermeable to helium.
In some embodiments, the barrier element comprises rGO nano flakes or its composites in a matrix.
In the barrier element, the rGO nano flakes may be homogenously dispersed and compressed. In this way, diffusion pathway for molecules through the coating become more tortuous leading to a more impermeable coating.

In some embodiments, the first barrier element comprises boron nitride.

In some other embodiments, the second barrier element comprises boron nitride.

Boron nitride is a heat- and chemically resistant refractory compound of boron and nitrogen with the chemical formula BN. It exists in various crystalline forms that are isostructural to a similarly structured carbon lattice. In that, the hexagonal form corresponding to one of graphite may be used as a barrier element thus avoiding or reducing water and oxygen gas diffusion towards the one or more metal surfaces.

In general, first or second barrier element are dense, thin, e.g. atomically thin and chemical inert layers, such as more chemically stable in corrosive environment than uncoated metals, which are highly impermeable to corrosive species, e.g. impermeable to small molecule such as helium, oxygen gas and water and to protons , hydroxyl, halogen, and metal ions.

In some embodiments, the first and/or second polymer layer comprises one or more polymer layers.

In some other embodiments, the third polymer layer comprises one or more polymer layers.

The first and/or second polymer layer may be made of the same polymeric material.

The third polymer layer may also be made of the same polymeric material of said first and/or second polymer layer.

In some embodiments, first, second and other polymer layers are deposited and produced according to the same method leading thus to polymer layers made of the same polymer material.

In some embodiments, first, second and other polymer layers are produced using different polymeric materials.

In some embodiments, the first and/or second polymer layer comprise crossed linked polymers.

In some further embodiments, the third polymer layer comprises crossed linked polymers.

A synthetic polymer is herein defined to be "cross-linked" when the entire bulk of the polymer has been exposed to the cross-linking method producing modification of mechanical properties of the polymer.
Cross linking improves the polymer resistance to water diffusion.

Polymer may be referred herein as polymeric material.
Polymer layers are referred herein also as polymer based layers and are defined as layers comprising polymeric materials.

In some embodiments, the first and/or second polymer layer comprise Polyvinyl butyral (PVB).

In some further embodiments, the third polymer layer comprises PVB.

PVB, when used as first and second polymer layer, has shown to greatly enhance the corrosion resistance of the coated metal product.

In some other embodiments, the coated metal product further comprises a spacer element, such as one or more space elements.

The one or more spacer elements may comprise one or more spacer layers.

In some embodiments, the spacer element is the at least one upper element located in between the first barrier element and the second barrier element.

In some embodiments, the spacer element is the at least one upper element located in between the first barrier element and the second barrier element.

The function of the spacer layer may be to improve adhesion of the barrier elements, and secondary to limit diffusion of species between the metal surface and the environment.

In a second aspect, the invention relates to a method of producing the coated metal product according to the first aspect of the invention, the method comprising: depositing a first polymer layer onto the one or more metal surfaces; depositing a first barrier layer onto the first polymer layer; depositing a second polymer layer onto the first barrier layer.

In a third aspect, the invention relates to the use of a coating in reducing a corrosion rate of a metal substrate, the coating comprising: a first polymer layer deposited onto the metal substrate; a first barrier layer deposited onto the first polymer layer; a second polymer layer deposited onto the first barrier layer.

The first, second and third and other aspects or embodiments of the present invention may each be combined with any of the other aspects or embodiments. These and other aspects or embodiments of the invention will be apparent from and elucidated with reference to the embodiments described hereinafter.

BRIEF DESCRIPTION OF THE FIGURES

The coated metal product and the method to produce the coated metal product according to the invention will now be described in more detail with regard to the accompanying figures. The figures show one way of implementing the present invention and is not to be construed as being limiting to other possible embodiments falling within the scope of the attached claim set.

Figure 1 and figure 2 are schematic representation of the different components of the coated metal product according to some embodiments of the invention.
Figure 3 is a schematic representation of the preparation of a coated metal product according to some embodiments of the invention.
Figure 4 is a graphic representation of data related to measured corrosion potential and corrosion current density of some embodiments of the invention.
Figure 5 is a graphic representation of data related to measured electrochemical impedance spectroscopy for some embodiments of the invention.
Figure 6 is a graphic representation of data related to corrosion protection improvements including reported graphene based anticorrosive coating and the one developed in this work.
Figure 7 is a flow-chart of a method according to an aspect of the invention.

DETAILED DESCRIPTION OF AN EMBODIMENT

Figure 1 and figure 2 are schematic representation of the different components of the coated metal product according to some embodiments of the invention.
Figure 1 and figure 2 show also the symbols identifying the different samples tested. The results of the tests are showed in figures 4 and 5.
According to figure 1 and 2:
- AA is the Aluminium alloy having as symbol a solid circle and a hollow circle after 1 day and 1 month immersion in 3.5% NaCl solution, respectively;
- AA-P is the Aluminium alloy coated with PVB and has as symbol a square;
- AA-P-G is the Aluminium alloy coated with PVB on which a single layer of graphene is deposited or transferred and has as symbol a tringle pointing up;
- AA-G-P is the Aluminium alloy coated with a single layer of graphene on which a layer of PVB is deposited and has as symbol a tringle pointing down;

- AA-P2 is the Aluminium alloy coated with two layers of PVB having as symbol an hexagon;
- AA-P-SLG-P is the Aluminium alloy coated with PVB, a single layer of graphene and another polymer layer of PVB and it has as symbol a star;
- AA-P-MLG-P is the Aluminium alloy coated with PVB, a multilayer of graphene and another polymer layer of PVB and it has as symbol a diamond;
- AA-P3 is the Aluminium alloy coated with three layers of PVB having as symbol an "X" mark;
- AA-P-G-P-G-P is the Aluminium alloy coated with a two units of PVB and graphene, on top of which a further layer of PVB is deposited and has as symbol a plus;
- AA-P-P-G-G-P is the Aluminium alloy coated with a two layers of PVB and two layers of graphene, on top of which a further layer of PVB is deposited and has as symbol a cross.

Figure 3 is a schematic representation of the preparation 1 of a coated metal product according to some embodiments of the invention.
Electrochemically polished copper 2 is thermal annealed in Ar at 1000° C before graphene growth 3 with co-flow of Ar, H_2 and CH_4 at atmospheric pressure. Graphene coated copper foil 4 is then spin coated 5 with 12% Polyvinyl butyral (PVB) ethanol solution and cured at 60 °C for 2 hours leading to copper substrate coated with graphene and PVB 6. Copper substrate is etched 7 with a mixed solution of 5% HCl and 30% H_2O_2 for overnight and then washed with water to get PVB/graphene hybrid film 8 suspended on water. AA2024 aluminium alloys is successively treated with acetone, 10% NaOH (aq), 50% HNO_3 (aq) and water to prepare a clean and chemical active surface, where a PVB primer 10 is then spin coated on and cured as that of PVB layer for graphene transfer. The PVB/graphene hybrid film is then dried and transferred 9 with PDMS to the PVB primer with graphene layer between two PVB layers. Thermal annealing 11 at 100 °C and gentle pressure is then applied to obtain the final sandwich structure 12.

Reference coating of two PVB layer is following the same procedures as that of the sandwich without graphene growth, while multilayer graphene is CVD grown on nickel foil and its based hybrid coating is following the same procedure of single layer graphene sandwich.

The inventors have prepared coatings according to the specific embodiment, i.e., coated metal substrates with the polymer-graphene-polymer sandwich, and subjected them to testing of corrosion with promising results, which indicate that corrosion resistance of metals coated with the polymer-graphene-polymer sandwich is improved approximately 2 orders of magnitude with respect to a metal which is coated with a similar sandwich except that the graphene has been left out.

Figure 4 is a graphic representation of date related to corrosion potential vs corrosion current of some embodiments of the invention.

Figure 5 provides an indication of the resistance to corrosion.

For short term corrosion protection performance evaluation of the samples, electrochemical measurements on the corrosion potential and rate, and electrochemical impedance spectroscopy were conducted after 1 day of immersion in 3.5% NaCl solution for AA (solid circle), AA-P, AA-P-G, AA-G-P, AA-P2, AA-P-SLG-P, AA-P-MLG-P and after 1 month immersion of AA (hollow circle), AA-P3, AA-P-G-P-G-P, AA-P-P-G-G-P.

For AA-P sample, when one layer of polymer is deposited on the aluminium surface, it can be seen that the corrosion rate of the sample is reduced by 5 times, compared with bare AA samples. However, when a polymer-graphene thin film was deposited with polymer on AA surface, only 2 times of corrosion rate improvement is shown, indicating that graphene is not effectively working as a barrier when directly exposed to the corrosion environment. When graphene is placed on AA surface of the polymer-graphene hybrid thin film, an accelerated corrosion rate by 2 times was proved, due to the galvanic coupling effects between graphene and aluminium alloy. This also indicate that graphene is not only an ineffective barrier, but also a corrosion process catalyst in the sample of AA-G-P. When the thickness of polymer is increased for AA-P2 from AA-P1, it can be seen that no improvement of corrosion rate is observed at a comparable level of improvement of 3 times than AA sample, indicating the porous nature of the polymer, which have low resistance to corrosion species. However, when a single layer graphene is sandwiched between the two polymer layers, about 400times of corrosion rate reduction than AA sample is obtained and 100 times of improvement for multilayer graphene. This indicates that when the graphene layer, which is acting as the main barrier, is sandwiched between the two polymer layers, significant improvement of corrosion protection could be achieved. It is

noted that when the multilayer graphene is being sandwiched between the two polymer layers, a significant surface passivation effect is also observed when compared with AA sample with a 680mv of corrosion potential increase. The short term corrosion measurement indicate that effective corrosion protection than bare aluminium alloy is invalid in the case of both bare one or two polymer layers and a graphene polymer hybrid thin film is deposited on AA surface. It is essential that the graphene, either single layer or multilayer, is being sandwiched between the polymer layers that effective corrosion protection can be achieved.

For a long term corrosion protection measurement after 1 month of immersion in 3.5%NaCl solution, it can be seen that a significant degradation is clear with bare AA sample, where the corrosion rate has been increased by 55 times. When comparing AA-P3 sample with bare AA sample after one month immersion, 160 times of corrosion rate improvement was observed. However, when two layers of graphene is being sandwiched between three polymer layers of AA-P-G-P-G-P, AA-P-P-G-G-P samples, 300,000 and 200,000 times of corrosion rate improvement is achieved, indicating that a collaboration between two layers of single graphene layer could provide much more effective corrosion protection than a single layer of graphene being sandwiched. The lowest corrosion rate that calculated from AA-P-G-P-G-P and AA-P-P-G-G-P can reach a value of 0.8nm/year and 1.2nm/year after 1 month of immersion in 3.5% NaCl solution, suggesting that the superior corrosion inhibition of both structure has achieved, while the corrosion rate are 1.5μm/year for AA-P3 and 0.2mm/year for AA after 1 month immersion. Nearly 1000mV of increase of corrosion potential than bare AA sample has been achieved by both AA-P-G-P-G-P, AA-P-P-G-G-P samples, indicating that excellent surface passivation can be provided by both structures beyond excellent corrosion inhibition performance.

Fig 5 shows electrochemical impedance measurements of all the as mentioned samples immersed in 3.5% NaCl solution at 1 day for AA, AA-P, AA-P-G, AA-G-P, AA-P2, AA-P-SLG-P, AA-P-MLG-P and at 1 month for AA, AA-P3, AA-P-G-P-G-P, AA-P-P-G-G-P. Generally, the higher the magnitude of impedance at low frequencies of the sample, the higher resistance the coatings have to corrosion. In terms of the bare polymer or polymer-graphene hybrid thin films on AA for AA-P, AA-P-G, AA-G-P samples, it can be seen that the magnitude of impedance at

10mHz ($|Z|_{10mHz}$) for AA is just over 3.1×10^4 $\Omega\cdot cm^2$, while the values of $|Z|_{10mHz}$ are 7.5×10^5 $\Omega\cdot cm^2$, 1.2×10^5 $\Omega\cdot cm^2$ and 0.7×10^4 $\Omega\cdot cm^2$ for AA-P, AA-P-G, AA-G-P samples, respectively. These results indicate that polymer graphene thin film based coatings do not provide more effective corrosion protection than AA-P for AA-P-G, and accelerated corrosion than AA for AA-G-P. In terms of polymer graphene based sandwich coatings for AA-P-SLG-P and AA-P-MLG-P and reference sample of AA-P2 and AA, it can also be seen that AA-P2 sample can reach two orders higher the value of $|Z|_{10mHz}$ than AA at above 1.4×10^6 $\Omega\cdot cm^2$. This can be attributed to the non-conducting uniform polymeric network covered on Al alloy surface, acting as a thick barrier to electrolyte diffusion. Moreover, the value of $|Z|_{10mHz}$ is further increased to 1.4×10^7 $\Omega\cdot cm^2$ and 2.0×10^7 $\Omega\cdot cm^2$ for AA-P-SLG-P and AA-P-MLG-P, respectively, due to additional barrier properties introduced by graphene layers between the two polymer layers.

For the long term corrosion tests of AA, AA-P3, AA-P-G-P-G-P and AA-P-P-G-G-P samples at 1 month immersion in 3.5% NaCl solution, the magnitude of impedance at 10mHz are 2.0×10^4 $\Omega\cdot cm^2$, 4.2×10^6 $\Omega\cdot cm^2$, 1.5×10^9 $\Omega\cdot cm^2$ and 3.0×10^9 $\Omega\cdot cm^2$, respectively. These results also indicate that superior barrier properties have been achieved by two layers of graphene being sandwiched between three layers of polymer, while bare polymer coatings just showed limited corrosion protection at long term for aluminium alloys.

Moreover, all the electrochemical impedance spectroscopy measurements are well related with corrosion rate test results, indicating that all the conclusion have a solid proof.

Figure 6 also shows the corrosion resistance in term of corrosion improvements including corrosion protection system from as grown graphene coatings on metal surface and graphene oxide (GO) and reduced graphene oxide (RGO) based composite coatings on metal surface. It can be seen from the cycle points of as grown graphene based coatings that the majority of the reported results on corrosion rate improvement and corrosion resistance (from electrochemical impedance spectroscopy tests) improvement are below 1 order. Even though some high quality graphene can be synthesised on metal surface, the maximum of as reported results were 2 to 3 orders. In terms of coating systems from GO/RGO based composites, the maximum of reported corrosion rate and resistance improvement are 2000 times and 100,000 times, respectively. In this work, when a single layer graphene is sandwiched between two polymer layers, 2 to 3 orders

of corrosion rate and corrosion resistance improvement were achieved. Although, the graphene used in this work is defective especially after transfer, the corrosion protection improvement is comparable to high quality graphene directly synthesised on metal substrate. When two layers of graphene were sandwiched in the coating, about 100,000 times improvement of both corrosion rate and corrosion resistance were achieved than bare aluminium alloys at long term immersion in 3.5% NaCl solution. This generally shows that the coating system developed in this work provide much better corrosion protection performance than both as grown graphene coatings and GO/RGO based composite coating.

Example 1

Example 1 provides example of depositions step in preparation of the structure according some embodiments of the invention.

Pre-treatment of AA2024-T3 aluminium alloys

AA2024-T3 aluminium alloy panels from Wilsons Metals, UK were cut into 2*2cm with a thickness of 2mm. Cleaning process of as-received AA2024 coupons is following 3 steps:

1, ultra-sonicated in acetone for 1 hour;

2, immersed in 10wt% NaOH solution for 1 min at 60 $^{\circ}$C with magnetic stirring and rinsed with deionized water;

3, immersed in 50wt% HNO_3 solution for 1 min at 22 $^{\circ}$C with magnetic stirring and rinsed with deionized water.

Preparation of the polymer primer

Polyvinyl butyral (PVB) powders were supplied by Kuraray Europe GMBH. A PVB solution is prepared by dissolving 12wt% PVB in ethanol. PVB solution is then spin coated for 1 min onto the surface of aluminium alloy with a speed of 1000rpm and an acceleration rate of 1000rpm/s. The PVB coated aluminium alloys sample is cured at 60 $^{\circ}$C for 2 hours and the polymer primer is successfully deposited on metal surface.

Electro-polishing of copper foil

Copper foil (25um thickness from Alfa Aesar, Part No. 13382) was electro-polished in a solution of 15% v/v ethanol (99% purity) and 85% v/v phosphoric acid (85wt% concentration) for 3 mins under magnetic stirring. The copper foil subject

to CVD graphene growth was used as working electrode (anode) and another copper foil as counter electrode (cathode). A bias voltage of 4V is applied by Kethley 2000 to electro-polish the copper foil.

Chemical vapour deposition of single layer graphene (SLGr) on copper

Electrochemically polished copper is thermal annealed in Ar at 1000 °C for 20 mins. Graphene growth with co-flow of Ar, H_2 and CH_4 at atmospheric pressure for 15mins. Finally, the sample is cooled down with a rate of 20 °C/s to room temperature. The CVD growth is processed with AS-ONE CVD system from Annealsys.

Chemical vapour deposition of multilayer graphene (MLG) on nickel

Nickel foil (part No. 12722 from Alfa Aesar) was acetone ultra-sonicated before graphene growth. Atmospheric pressure CVD growth was conducted with AS-ONE CVD system from Annealsys. After loading the samples into the growth chamber, the chamber was evacuated with a rotary pump and then filled with Ar, up to atmospheric pressure. Next, the samples were heated at 950 °C for 15 min under the co-flow of Ar and H_2, respectively. The growth process was then carried out for 5 mins at 950 °C with a co-flow of C_2H_2 and H_2. Lastly, the chamber was cooled down with a rate of 20 °C/s.

Transfer of graphene coating onto glass slide or ~88 nm SiO_2 wafer was carried out via chemical etching of nickel in 5% HCl and 30% H_2O_2 mixed solution for 24 hours.

Transfer of graphene with polymer (PVB-SLGr hybrid film)

Graphene coated copper is placed on top of PDMS template, which was coated on Si wafer. 12% PVB solution is spin coated on graphene and cured with the same condition as that process for PVB primer. Copper substrate is then chemically etched in a mixed solution of 100ml 5% HCl and 1ml 30% H_2O_2 for overnight. The polymer-graphene hybrid film is then rinsed with deionized water to clean any residue ions and floated on water.

Preparation of polymer-graphene-polymer sandwich coating on aluminium alloy (AA-PVB-SLGr-PVB)

The as prepared polymer-graphene hybrid film was transferred on PDMS temperate and dried at 40 °C on a hot plate. The film is then transferred onto polymer primer on aluminium alloy surface with the graphene layer between the two polymer layers. Thermal annealing at 100 °C is applied on the polymer-graphene-polymer film on aluminium alloy for 15-30 mins and the PVB-SLGr-PVB sandwich coating is thus successfully prepared.

Preparation of other bare polymer or polymer-graphene based coatings on aluminium alloy

A single layer of transferred PVB on aluminium alloy (AA-PVB)

12% PVB solution is spin coated on electro-polished copper and then cured with the same condition as that of PVB primer on aluminium alloy. The copper is chemically etched and rinsed with deionized water to prepare free standing single layer PVB film. The PVB film is then dried and transferred with PDMS onto aluminium alloy and thermal annealed at 100 °C.

A single layer of polymer-graphene hybrid films on aluminium alloy (AA-PVB-SLGr, AA-SLGr-PVB)

A layer of PVB-SLGr hybrid film is transferred with PDMS onto aluminium alloy with either PVB layer directly contacted with aluminium alloy to prepare AA-PVB-SLGr structure or SLGr layer directly contacted with aluminium alloy to prepare AA-SLGr-PVB structure.

Two and three layers of PVB on aluminium alloy (AA-PVB-PVB, AA-PVB-PVB-PVB)

One or two layers of PVB free standing films were transferred onto PVB primer coated aluminium alloy and then thermal annealed at 100 °C to prepare bare polymer reference sample of AA-PVB-PVB and AA-PVB-PVB-PVB structure.

Multiple layer of polymer-graphene sandwiched coating (AA-PVB-SLGr-PVB-SLGr, AA-PVB-PVB-SLGr-SLGr-PVB)

One layer of polymer-graphene hybrid films was transferred onto PVB primer coated aluminium alloy with either graphene side or polymer side facing directly to the PVB primer ordering to prepare the AA-PVB-SLGr-PVB and AA-PVB-PVB-SLGr structure, respectively. Thermal annealing is applied before and after another layer of polymer-graphene hybrid film was transferred on to the as

mentioned two structures with both the PVB layers on the very top, so that both AA-PVB-SLGr-PVB-SLGr, AA-PVB-PVB-SLGr-SLGr-PVB structure were prepared.

Figure 7 is a flow-chart of a method 20 according to an aspect of the invention. In figure 7, the method of producing the coated metal product according to some embodiments of the invention comprises:

- (S1) depositing a first polymer layer onto the one or more metal surfaces;
- (S2) depositing a first barrier layer onto the first polymer layer;
- (S3) depositing a second polymer layer onto the first barrier layer.

Although the present invention has been described in connection with the specified embodiments, it should not be construed as being in any way limited to the presented examples. The scope of the present invention is set out by the accompanying claim set. In the context of the claims, the terms "comprising" or "comprises" do not exclude other possible elements or steps. Also, the mentioning of references such as "a" or "an" etc. should not be construed as excluding a plurality. The use of reference signs in the claims with respect to elements indicated in the figures shall also not be construed as limiting the scope of the invention. Furthermore, individual features mentioned in different claims, may possibly be advantageously combined, and the mentioning of these features in different claims does not exclude that a combination of features is not possible and advantageous.

CLAIMS

1. A coated metal product, comprising one or more metal surfaces and a coating deposited on said one or more metal surfaces,
wherein said coating comprises:
- at least one adhesion element deposited onto said one or more metal surfaces;
- at first barrier element deposited onto said at least one adhesion element;
- at least one upper element deposited onto said at least one barrier element;
and wherein said one or more metal surfaces comprise one or more metal elements and/or an alloy of metal elements wherein:
- said at least one adhesion element comprises a first polymer layer;
- said first barrier element comprises a first barrier layer;
- said at least one upper element comprises a second polymer layer.

2. A coated metal product according to any of the preceding claims, wherein said coating further comprises a second barrier element deposited onto said at least one upper element.

3. A coated metal product according to claim 2, wherein said coating further comprises a top element deposited onto said second barrier element.

4. A coated metal product according to claim 3, wherein said top element comprises a third polymer layer.

5. A coated metal product according to any of the preceding claims, wherein said one or more metal elements are post-transition metals, such as Al.

6. A coated metal product according to any of the preceding claims, wherein said first barrier element comprises one or more barrier layers.

7. A coated metal product according to any of the preceding claims, wherein said first barrier element comprises a layer having a form of a two-dimensional lattice of atoms, such as graphene.

8. A coated metal product according to any of the preceding claims 2-7, wherein said second barrier element may comprise a layer having a form of a two-dimensional lattice of atoms, such as graphene.

9. A coated metal product according to any of the preceding claims, wherein said first barrier element comprises boron nitride.

10. A coated metal product according to any of the preceding claims 2-9, wherein said second barrier element comprises boron nitride.

11. A coated metal product according to any of the preceding claims, wherein said first and/or second polymer layer comprises one or more polymer layers.

12. A coated metal product according to any of the preceding claims, wherein said first and/or second polymer layer comprise crossed linked polymers.

13. A coated metal product according to any of the preceeding claims further comprising a spacer element.

14. A method of producing said coated metal product according to any of the preceding claims, said method comprising:
- depositing a first polymer layer onto said one or more metal surfaces;
- depositing a first barrier layer onto said first polymer layer;
- depositing a second polymer layer onto said first barrier layer.

15. The use of a coating in reducing a corrosion rate of a metal substrate, said coating comprising:
- a first polymer layer deposited onto said metal substrate;
- a first barrier layer deposited onto said first polymer layer;
- a second polymer layer deposited onto said first barrier layer.

ABSTRACT

The present invention relates to a coated metal product having a reduced corrosion rate. The present invention relates also to a method of producing the coated metal product and the use of the coating onto a metal substrate for reducing the corrosion rate of a metal substrate.

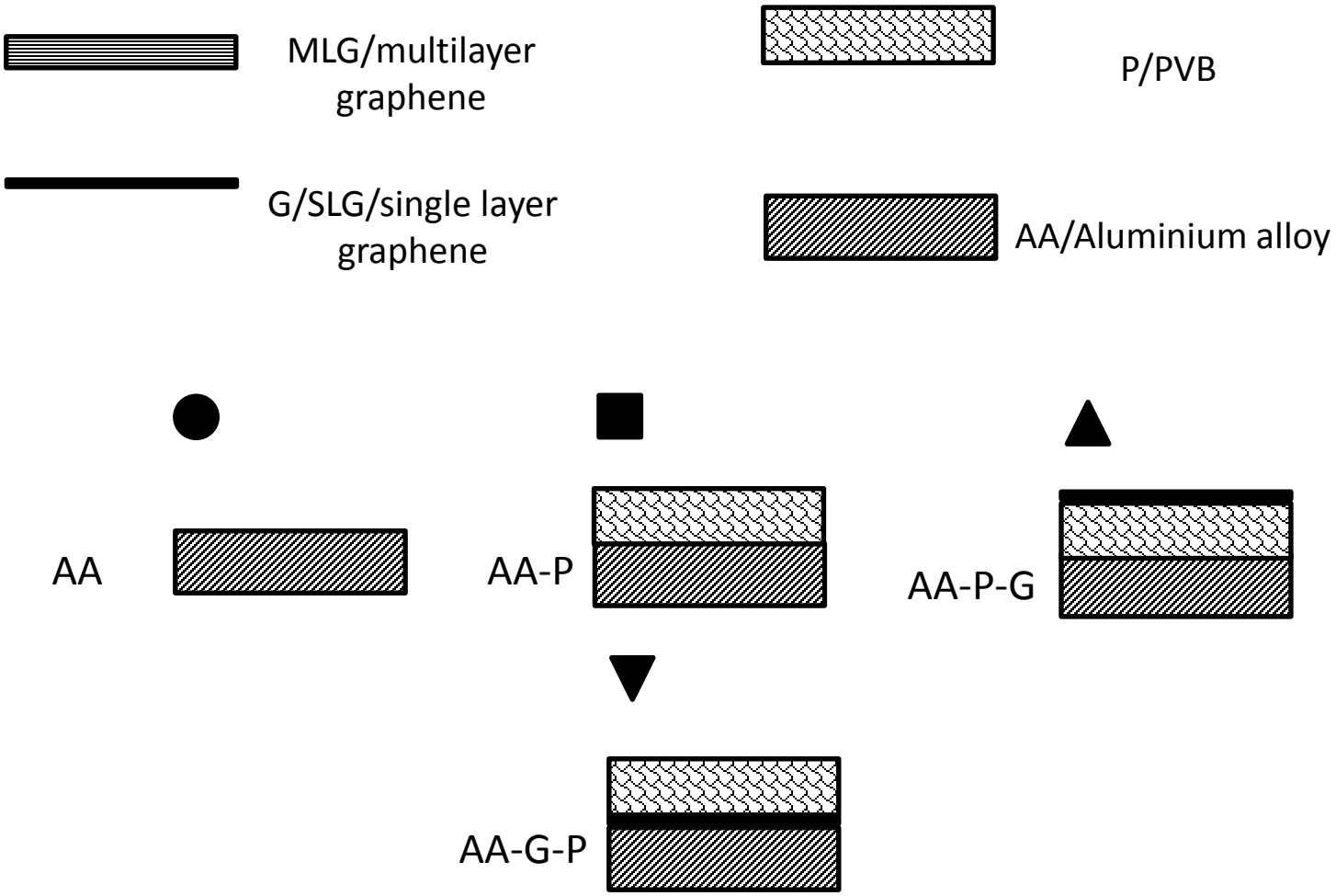
MLG/multilayer graphene
P/PVB
G/SLG/single layer graphene
AA/Aluminium alloy
AA
AA-P
AA-P-G
AA-G-P

FIG. 1

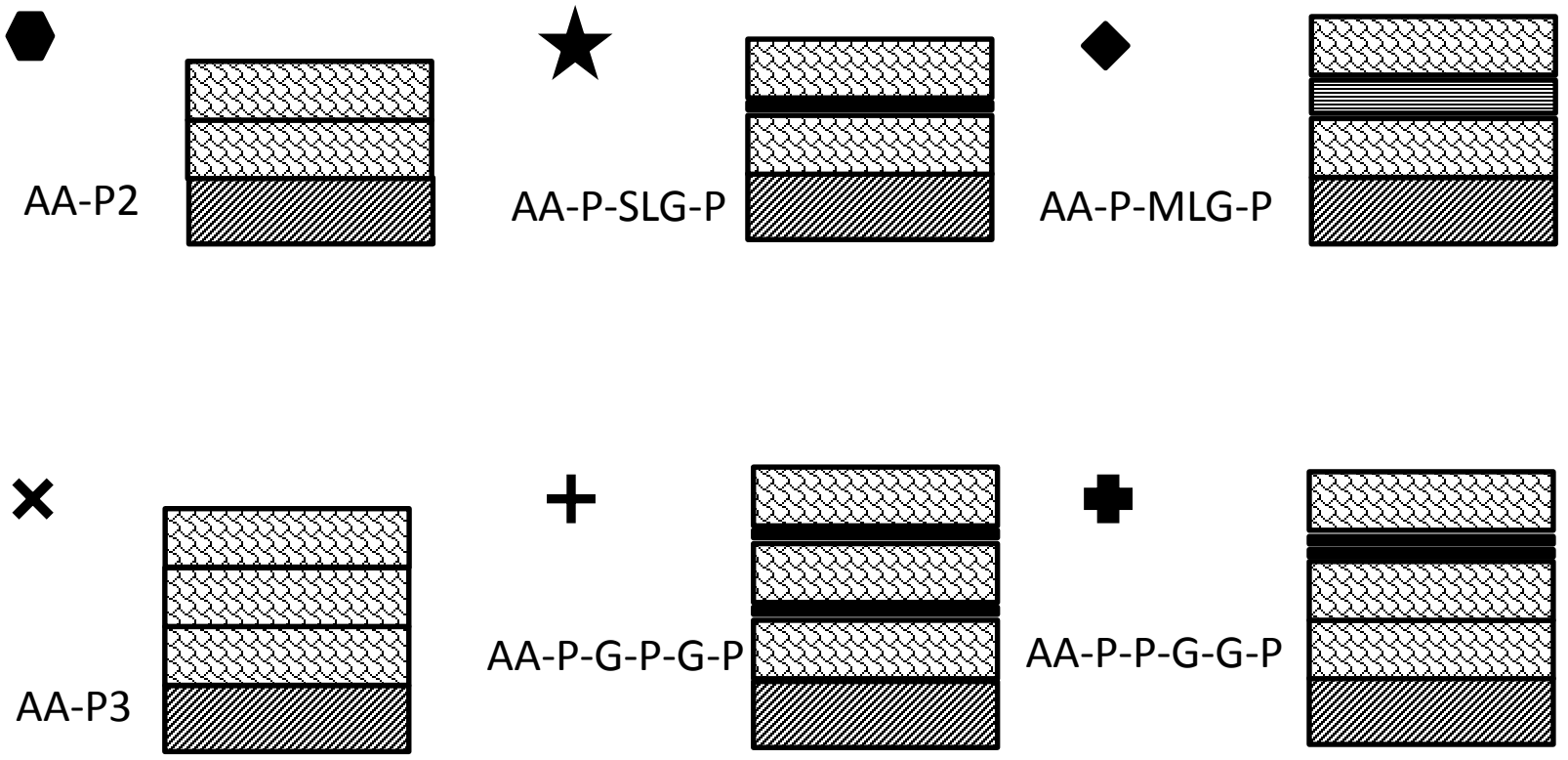

FIG. 2

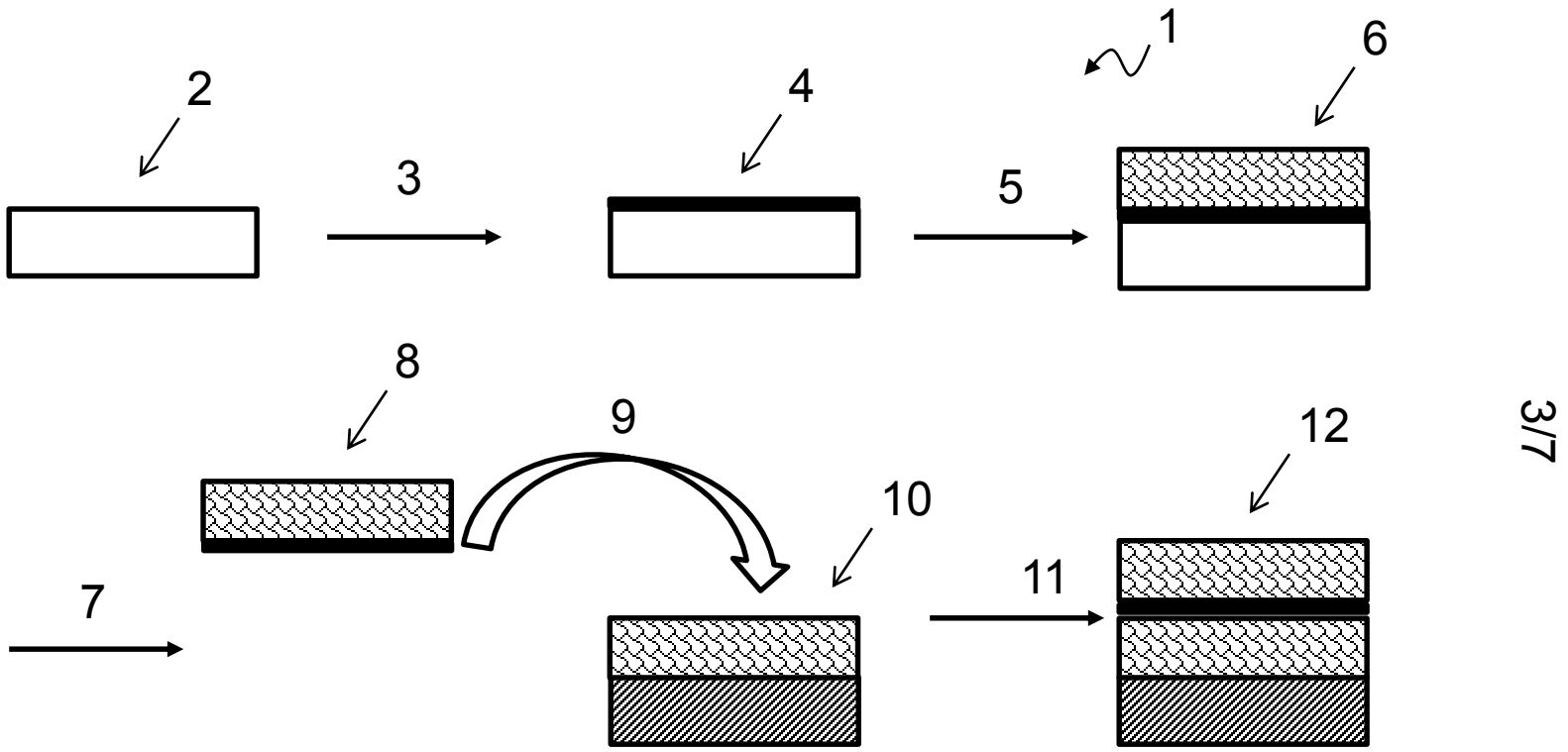

FIG. 3

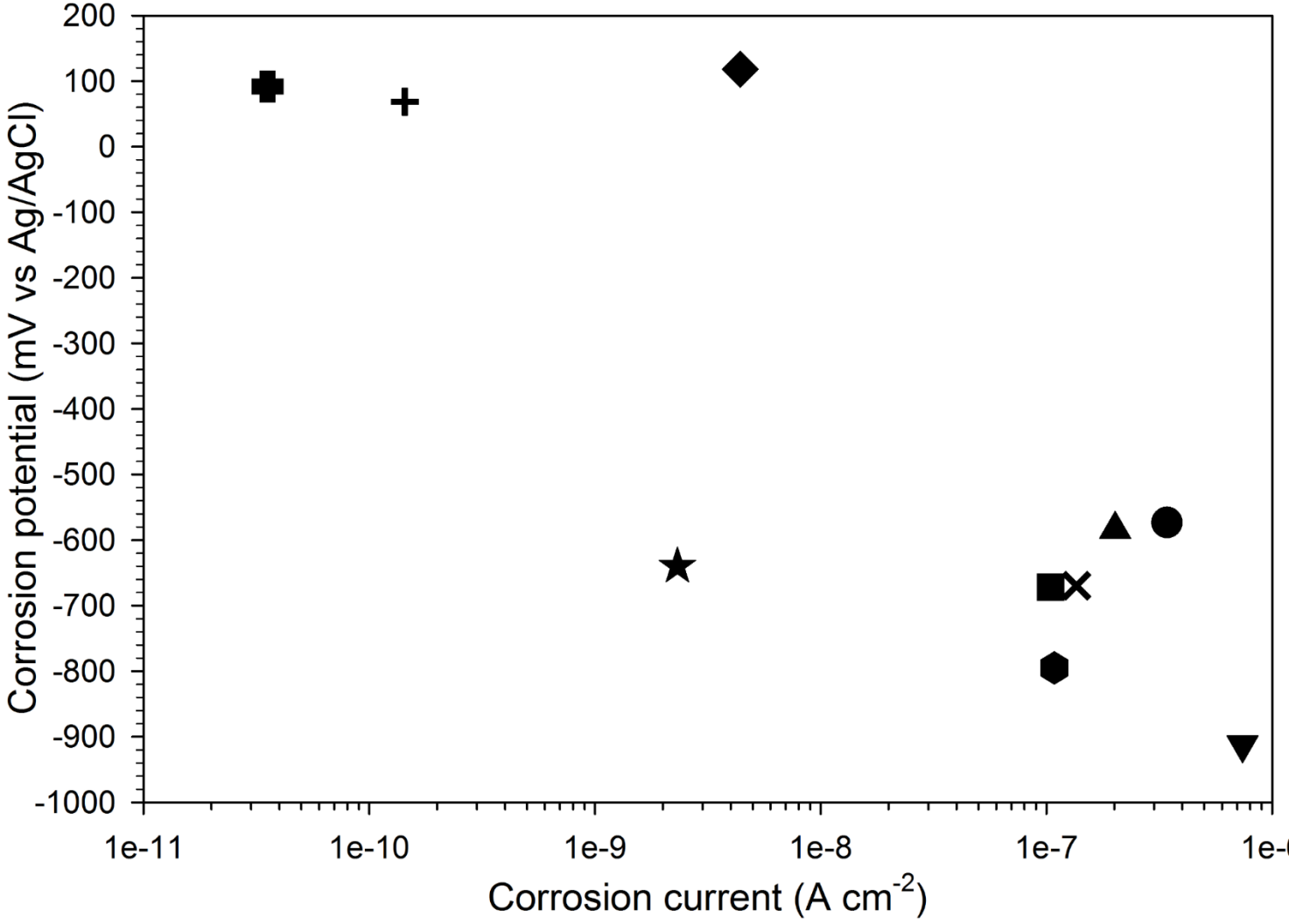
200
100
0
-100
-200
-300
-400
-500
-600
-700
-800
-900
-1000
Corrosion potential (mV vs Ag/AgCl)
1e-11
1e-10
1e-9
1e-8
1e-7
1e-6
Corrosion current (A cm-2)

FIG. 4

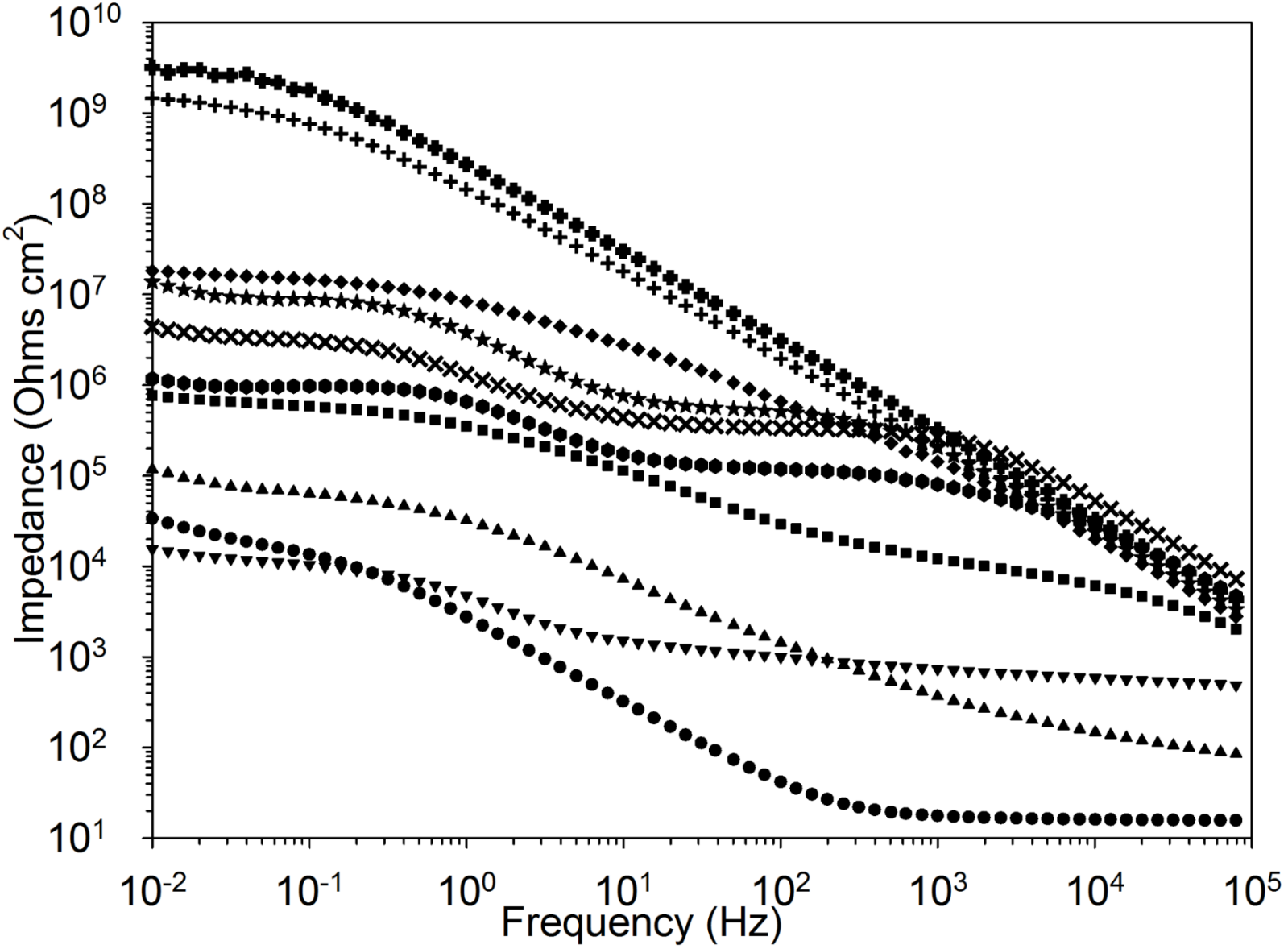
Impedance (Ohms cm^2)
10^{10}
10^{9}
10^{8}
10^{7}
10^{6}
10^{5}
10^{4}
10^{3}
10^{2}
10^{1}
10^{-2}
10^{-1}
10^{0}
10^{1}
10^{2}
10^{3}
10^{4}
10^{5}
Frequency (Hz)

FIG. 5

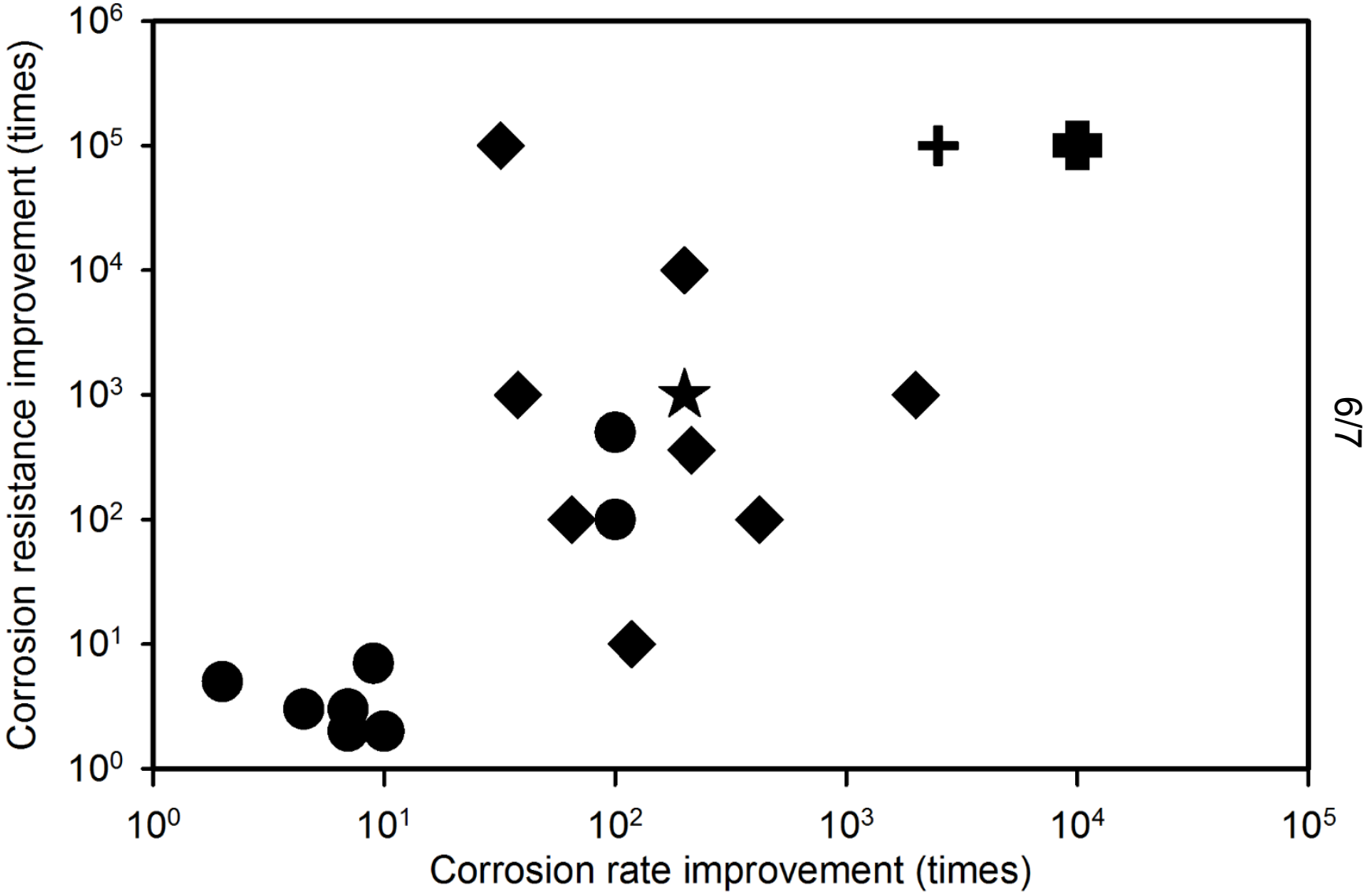
Corrosion resistance improvement (times)
10^6
10^5
10^4
10^3
10^2
10^1
10^0
10^0
10^1
10^2
10^3
10^4
10^5
Corrosion rate improvement (times)

FIG. 6

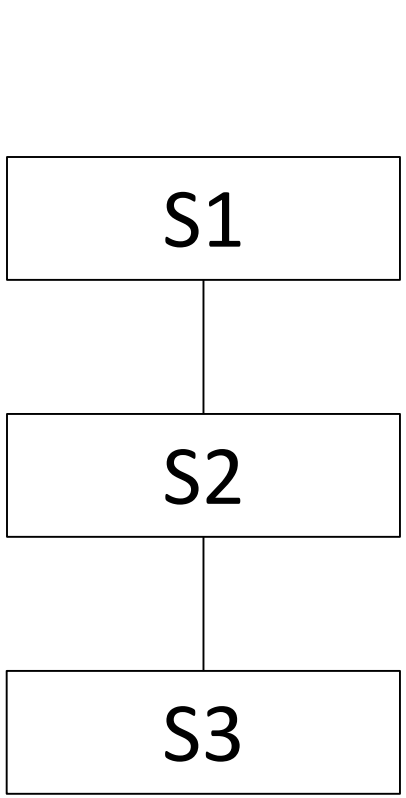

FIG. 7

Published by:
DTU Nanotech
Department of Micro- and Nanotechnology
Technical University of Denmark
Ørsteds Plads, building 345C
DK-2800 Kgs. Lyngby